# OPTIMIZATION OF SUB- AND SUPERCRITICAL WATER GASIFICATION OF RICE HUSK ENHANCED WITH IRON-DOPED ALKALINE-EARTH CATALYSTS

**Ramadhani Bakari**

**A Thesis Submitted in Fulfilment of the Requirements for the Degree of Doctor of Philosophy in Sustainable Energy Science and Engineering of the Nelson Mandela African Institution of Science and Technology**

**Arusha, Tanzania**

**May, 2022**

## ABSTRACT

Biomass is a promising renewable energy source widely available worldwide, particularly in developing countries where clean and affordable energy is a major problem. Biomass gasification is an attractive technology that can transform biomasses into a more versatile fuel known as syngas, tar (bio-oil) and biochar. Syngas is a hydrogen-rich gas that could promote a clean and green energy and promote the agriculture sector. The utilisation of syngas would reduce dependence on fossil-based fuels and eventually reduce the carbon footprints. The gasification technology faces operational challenges; one of the problems is tar formation, slow char gasification reaction, and poor performance of catalysts. These challenges are influenced by inappropriate operating conditions and the precursors employed in catalyst synthesis. In this study, the optimisation of noncatalytic and catalytic gasification of rice husk is reported. The rice husk biomass was gasified under subcritical and supercritical water conditions in a batch autoclave reactor. The effect of temperature (350-500°C), residence time (30-120 minutes), and feed concentration (3-10 wt%) is optimised. Moreover, the effect of the addition of natural, calcined and Fe doped limestone and dolomite catalysts on the gasification yield is studied using a response surface methodology. The catalyst was prepared by a facile incipient wetness process using chlorine- and sulphur-free iron (III) ammonium citrate precursor. Optimisation of operating conditions suggests a quadratic model for gasification efficiency, gas volume, char yield, and gravimetric tar. The findings revealed that higher temperatures, longer residence times and lower feed concentrations favoured high gas yields. The lowest tar yield obtained was 2.98 wt%, while the highest gasification efficiency and gas volume attained was 64.27% and 423 mL/g, respectively. The findings of the catalyst characterisation revealed that the predominant reactive site of Fe/limestone catalyst is iron oxide, calcium ferrite, and calcium oxide. Under all conditions tested, the manufactured catalyst was highly active in promoting char gasification, gas volume and gasification efficiency. Tar yield was substantially promoted at low temperatures and high feed concentrations, but at high temperatures and low feed concentrations (500$^{o}$C, 3 wt%), tar formation was suppressed by 22%, while char gasification was enormously enhanced by 65%. The maximum gas yield of 560 mL/g biomass was obtained under the catalytic conditions of 5%Fe/limestone, 15% catalyst loading, 500$^{o}$C, 120 minutes, and 3 wt% feed concentrations. Therefore, these findings revealed that the rice husk's energy content could be harnessed using supercritical water gasification to obtain substantial fuel products.

## DECLARATION

I, Ramadhani Bakari, do hereby declare to the Senate of the Nelson Mandela African Institution of Science and Technology that this dissertation titled *"Optimization of Sub- and Supercritical Water Gasification of Rice Husk Enhanced with Iron-doped Alkaline-Earth Catalysts"* is my own original work and that it has neither been submitted nor being concurrently submitted for degree award in any other institution.

Ramadhani Bakari

| | |
|---|---|
| Name and Signature of the Candidate | Date |

The above declaration is confirmed by:

Dr. Yusufu Abeid Jande Chande

| | |
|---|---|
| Name and Signature of Supervisor 1 | Date |

Dr. Thomas Kivevele

| | |
|---|---|
| Name and Signature of Supervisor 2 | Date |

## COPYRIGHT

## CERTIFICATION

The undersigned certify that they have read and hereby recommend for acceptance by the Senate of the Nelson Mandela African Institution of Science and Technology a dissertation entitled "*Optimization of Sub- and Supercritical Water Gasification of Rice Husk Enhanced with Iron-doped Alkaline-Earth Catalysts*" in Fulfilment of the Requirements for the Degree of Doctor of Philosophy in Sustainable Energy Science and Engineering at Nelson Mandela African Institution of Science and Technology, Arusha Tanzania.

Dr. Yusufu Abeid Jande Chande

| | |
|---|---|
| Name and Signature of Supervisor 1 | Date |

Dr. Thomas Kivevele

| | |
|---|---|
| Name and Signature of Supervisor 2 | Date |

## ACKNOWLEDGMENTS

I want to begin by thanking Allah, the Most Merciful, for his continuous protection, guidance, endurance, and spiritual healing since the beginning of my PhD programme.

I would like to thank the Nelson Mandela African Institution of Science and Technology (NM-AIST) and the African Centre of Excellence for Water Infrastructure and Sustainable Energy Futures (WISE-Futures) for providing financial support to my PhD studies. I am grateful to my employer, the University of Dodoma, for granting me the study leave to pursue PhD studies. I would like to express my gratitude to my supervisors: Dr. Yusufu Abeid Chande Jande and Dr. Thomas Kivevele, for their substantial contributions in the form of enthusiastic support, motivation, constructive critiques, invaluable counsel, and continuous supervision.

I would like to give special thanks to Prof. Xiao Huang for her generosity in donating the autoclave reactor utilised in this study, as well as her substantial assistance in reviewing drafts of my papers and thesis.

I would also like to thank my fellow students: Dr. Said Mateso, Mr. Kassim Ramadhani, Mr. Stanley Mtavangu, Ms. Sofia Bakili, Ms. Fina Lesafi, Ms. Tusekile Alfred, and Ms. Siri Abihudi for their courage and moral supports. I also extend my appreciation to the NM-AIST lab technicians, Mr. Emmanuel Lymo, Mr. Paulo Sanka, Ms. Irene Tesha, and Mr. Wilson Mahene, for their technical support when I was doing laboratory works.

It is an honour for me to express my heartfelt gratitude to my lovely wife Ms. Swaumu Mvungi for her patience, support, and lavish care for me and our daughters: Farhia and Farhat while I was away. I extend my sincere thanks to my mother, Ms. Fatuma Christopher, my sisters: Ms. Zehiria and Ms. Mwanaima Bakari, and my brothers: Mr. Mussa and Mr. Iddy Bakari, for their unwavering support, which has enabled me to pursue my PhD studies.

## DEDICATION

This work is dedicated to my mother, Fatuma Christopher, my lovely wife, Ms. Swaumu Mvungi, and my daughters, Farhia and Farhat.

**TABLE OF CONTENTS**

## LIST OF TABLES

## LIST OF FIGURES

## LIST OF APPENDICES

## LIST OF ABBREVIATIONS AND SYMBOLS

| | |
|---|---|
| µm | Micrometer |
| 3D | Three-Dimensional |
| a.u. | Arbitrary Unit |
| $Al_2O_3$ | Aluminium Oxide |
| ANOVA | Analysis of Variance |
| ASTM | American Society for Testing Materials |
| BBOT | 2,5-Bis(5-tert-butyl-2-benzo-oxazol-2-yl) thiophene |
| BET | Brunauer-Emmett-Teller |
| BJH | Barrett-Joyner-Halenda |
| C | Carbon |
| $Ca(OH)_2$ | Calcium Hydroxide |
| $Ca_2Fe_2O_5$ | Calcium Ferrite |
| $CaCl_2$ | Calcium Chloride |
| $CaMg(CO_3)_2$ | Dolomite |
| C–C | Carbon-Carbon Bond |
| CE | Carbon Efficiency |
| C-H | Carbon-Hydrogen Bond |
| $CH_3COONa$ | Sodium Acetate |
| $CH_4$ | Methane |
| CHN | Carbon, hydrogen, and nitrogen elemental analyser |
| Cl | Chlorine |
| C–N | Carbon-Nitrogen Radical |
| CO | Carbon Monoxide |
| Co | Cobalt |
| $CO_2$ | Carbon Dioxide |
| CPP | Calculated Percent Passing |
| Cr | Chromium |
| Cu | Cupper |
| CV | Coefficient of Variance |
| DTA | Differential Thermal Analysis |
| EDX/EDS | Energy-Dispersive X-ray |
| EES | Engineering Equation Solver |

| | |
|---|---|
| FC | Fixed Carbon |
| Fe | Iron |
| $Fe(NO_3)_3$ | Ferric Nitrate |
| $Fe_2O_3$ | Iron Oxide/ Hematite |
| $Fe_3O_4$ | Magnetite |
| $FeCl_3$ | Ferric Chloride |
| $FeMg(SiO_4)_2$ | Olivine |
| FeO | Wustite |
| FT | Fischer–Tropsch |
| FT-IR | Fourier-Transform Infrared Spectroscopy |
| GE | Gasification Efficiency |
| $H_2$ | Hydrogen |
| $H_2O$ | Steam |
| $H_2SO_4$ | Sulphuric Acid |
| HCL | Hydrogen Chloride |
| HCOOH | Formic Acid |
| HHV | Higher Heating Value |
| IAPWS | International Association for the Properties of Water and Steam |
| ICP-MS | Inductively Coupled Plasma Mass Spectrometry |
| IPR | Individual Percent Retained |
| IUPAC | International Union of Pure and Applied Chemistry |
| JCPDS | Joint Committee on Powder Diffraction Standards |
| $K_2CO_3$ | Potassium Carbonate |
| $KHCO_3$ | Potassium Hydrogen Carbonate |
| KOH | Potassium Hydroxide |
| LHV | Lower Heating Value |
| LiOH | Lithium Hydroxide |
| MC | Moisture Content |
| MgO | Magnesite |
| Min | Minutes |
| Mo | Molybdenum |
| MPa | Megapascal |
| MS | Mass Spectroscopy |
| $Na_2CO_3$ | Sodium Carbonate |

| | |
|---|---|
| NaOH | Sodium Hydroxide |
| $NH_3$ | Ammonia |
| Ni | Nickel |
| NOx | Nitrous Oxide |
| O | Oxygen |
| OFAT | One-Factor-at-a-Time |
| PCPP | Previous Calculated Percent Passing |
| Pd | Palladium |
| PID | Proportional, Integral, Derivative |
| PRESS | Predicted Residual Sum of Squares |
| Pt | Platinum |
| PTFE | Polytetrafluoroethylene |
| Rh | Rhodium |
| RH | Rice Husk |
| RHC | Rice Husk Char |
| RSE | Residual Standard Error |
| RSM | Response Surface Methodology |
| Ru | Ruthenium |
| $RuO_2$ | Ruthenium Oxide |
| SCW | Supercritical Water |
| SEM | Scanning Electronic Microscope |
| SS | Sum of Squares |
| SSR | Solid State Relay |
| TCD | Thermal Conductivity Detector |
| TEM | Transmission Electron Microscopy |
| TGA | Thermogravimetric Analysis |
| TOC | Total Organic Carbon |
| TPR | Temperature-Programmed Reduction |
| UART | Universal Asynchronous Receiver-Transmitter |
| USA | United States of America |
| Va- | Oxygen Vacancy |
| VAC | Volts of Alternating Current |
| Vc | Volume of Container |
| VM | Volatile Mater |

| | |
|---|---|
| Wc | Weight of Empty Container |
| WGS | Water-Gas Shift |
| Ws | Weight of Container and Sample |
| wt% | Weight Percent |
| XRD | X-ray Diffraction |

# CHAPTER ONE

# INTRODUCTION

## 1.1 Background of the Problem

Growing concerns about the price of fossil fuels, increased energy demand as a result of rapid industrialization and population growth, and the foreseen climate change through global warming pose a contemporary threat to the quality of life of populations, plants and animals (Boot-Handford *et al.,* 2018; Kumar *et al.,* 2018; Matin *et al.,* 2018; Sansaniwal *et al.,* 2017; Thomsen *et al.,* 2011). The global energy matrix is currently 85% dependent on fossil fuels as the primary energy source; but, depending on the country, this dependency can range from 32.1 to 100% (Devi *et al.,* 2003; Khatib, 2012). The combustion of fossil fuels accounts for approximately 70% of total global greenhouse gases (GHG) emissions in the form of $CO_2$ (Johnsson *et al.,* 2019). To ensure the society's long-term sustainability, the only option is to prioritize clean and green energy by searching for the appropriate renewable energy resources (Liu *et al.,* 2016; Tursun *et al.,* 2019). Among the available resources, it is worth noting that biomass is regarded as the primary form of energy capable of providing reliable energy in the same way that fossil fuels do (Cabuk *et al.,* 2019; Guan *et al.,* 2016).

Biomass is a green fuel that is widely available worldwide, and it can account for 14-15% of total energy consumption (Wang *et al.,* 2020). According to reports, biomass contributes more than 90% of the energy required in developing countries' rural and remote areas (Huang *et al.,* 2011; Sansaniwal *et al.,* 2017; Sheth & Babu, 2009). Biomass is a cleaner fuel, with lower sulphur, nitrogen, and carbon dioxide emissions (Reddy *et al.,* 2014). Furthermore, it is inexpensive and widely available in various forms, including agricultural residuals, wood and energy crops. Rice (*Oryza sativa*) is the world's second-largest cultivated crop, producing a substantial quantity of residuals. It is estimated that more than 150 million tons of rice husk (RH) are produced every year (Pinto *et al.,* 2017; Singh *et al.,* 2020). Tanzania, in particular, produces approximately 3.2 million tonnes of rice in the season 2018/19 (rice production statistics in Appendix 1 ) (Faria, 2021). Therefore, about 0.6 to 1.1 million tonnes of rice husk is produced annually based on 20-35% of rice paddy being rice husk (Pinto *et al.,* 2017). Literature shows that less than 17% of the RH is effectively utilised and the remaining portion is disposed to the environment or directly burned, contributing to significant greenhouse emissions (Adam *et al.,* 2012; Alvarez *et al.,* 2014; Olupot *et al.,* 2016; Vieira *et al.,* 2020). Reports on RH composition in the literature differ, with hemicellulose usually accounting for

11-29 %, cellulose accounting for 31-44 %, lignin accounting for 10-34 %, ash accounting for 15-29 % and other extractive compounds accounting for the remainder (Bakari *et al.*, 2020).

Thermochemical and biochemical conversion are two convenient methods for transforming biomass into gaseous, liquid, or solid biofuels. Thermochemical conversion includes pyrolysis, liquefaction, gasification and combustion, while fermentation and digestion are examples of biochemical conversion. A slow reaction marks the latter, and its typical residence times are almost 2–4 weeks. Besides, the fermentation sludge and wastewater from the reactors should further be processed before disposal (Yakaboylu *et al.*, 2015). Gasification is a favourable option that transforms biomass energy values to permanent gases ($H_2$, CO, and $CH_4$) known as syngas, a hydrogen-rich gas with stable energy content comparable to fossil fuels (Al-Rahbi & Williams, 2017; Boot-Handford *et al.*, 2018). Syngas from biomass is more valuable than its source biomass, it can be directly burned to produce heat, used to generate electricity in gas turbines, or in synthesizing chemicals and other fuels (Wang *et al.*, 2008). To date, hundreds of thousands of biomass gasifiers have been installed for rural electrification worldwide, with varying degrees of success (Banerjee, 2006; Wu *et al.*, 2002). Tar formation and removal, slow char conversion, the cost of biomass drying and processing, and high costs for construction materials are just a few of the obstacles that hamper the development of biomass gasifiers (Baker *et al.*, 1988; Guo *et al.*, 2018; Hervy *et al.*, 2019; Miccio *et al.*, 2009; Sansaniwal *et al.*, 2017; Tursun *et al.*, 2019).

Supercritical water (SCW) gasification is a novel and effective thermochemical technique with high reaction efficiency and $H_2$ selectivity among nearly any type of biomass feedstock (Kruse & Gawlik, 2003; Matsumura *et al.*, 2005). This method does not involve drying and has a much shorter residence time, just a few minutes (Yakaboylu *et al.*, 2015). Supercritical water gasification is regarded as the most cost-effective thermochemical conversion technology for converting biomass to hydrogen (Hosseini *et al.*, 2015). Most of the studies carried out on SCW gasification used biomass model compounds, including cellulose (Guan *et al., 2008;* Huang *et al.*, 2017; Minowa *et al.*, 1998; Osada *et al.*, 2006; Williams & Onwudili, 2005), lignin (Meier *et al.*, 1992; Osada *et al.*, 2006; Sato *et al.*, 2006), starch (Williams & Onwudili, 2005), fructose (Kabyemela *et al.*, 1999; Nanda *et al.*, 2015), and glycerol (Bühler *et al.*, 2002; S. Guo *et al.*, 2012). The use of model biomasses enhances understanding of the reaction processes that occur during the SCW gasification process. However, during gasification, lignocellulosic compounds in actual biomass undergo complex interaction reactions that cannot be predicted using model biomasses. A few studies have published results for actual biomass to date (Rodriguez Correa & Kruse, 2018). The few available studies include SCW gasification of sugarcane bagasse (Cao

*et al.*, 2018; Kumar & Reddy, 2019), cornstalk (Wang *et al.*, 2020), food waste (Chen *et al.*, 2020), mosambi peels (Kumar & Reddy, 2019), eucalyptus chips (Borges *et al.*, 2019), rice straw (Sun *et al.*, 2020) and rice husk (Basu *et al.*, 2009). As a result, further study on actual biomass is needed to understand its decomposition behaviours in SCW conditions and foresee problems in large-scale operations (Okolie *et al.*, 2019).

The efficiency of the supercritical water gasification is affected by various operating and design factors, including reaction temperature, reaction pressure, feed concentration, residence time, feed flow rate, reactor type, reactor material, and catalyst. The optimization of these factors will significantly increase gasification yield and, consequently, a higher syngas yield (Ferreira-Pinto *et al.*, 2019). Previously, some researchers investigated SCW gasification parameters; these include: (a) SCW gasification of eucalyptus chips at temperatures between 400 and 500°C, pressures ranging from 20-22 MPa, 22-25 MPa to 25-30 MPa, and various residence time (30, 45, or 60 minutes) (Borges *et al.*, 2019); (b) examination of gasification mechanism of cornstalk in SCW at temperatures between 500-800°C, residence time between 1 to15 minutes and a feed concentration of 1-9 wt% (Wang *et al.*, 2020); (c) production of $H_2$-rich gas from gasification of unsorted food waste in SCW at temperatures between 420-480°C, a residence time of 30-75 minutes and a feed concentration of 5-15 wt% (Su *et al.*, 2020); (d) investigation of in-situ SCW gasification of sugarcane bagasse at different temperatures (300, 350, 400, 450 and 500), biomass ratios (0.125, 0.167, 0.25 and 0.5) and a constant residence time of 50 minutes (Kumar & Reddy, 2019); and finally (e) gasification of RH in SCW at temperatures between 400-680°C, a biomass concentration between 2-14 wt%, a biomass particle size ranging from 250 to1500 microns and a constant residence time of 1 hour (Basu *et al.*, 2009).

An effort to improve gasification efficiency by using catalysts has been widely published in the literature. Hundreds of catalysts with favourable catalytic efficiency have been extensively developed over the decades, though challenges have accompanied them, the most common of which is catalyst deactivation caused by contamination, sintering, and coke deposition (Hervy *et al.*, 2019; Liu *et al.*, 2019). The nickel-based catalyst, in particular, has been widely used due to its high syngas yield, favourable tar reforming behaviour, and low cost compared to noble metals (Guo *et al.*, 2018; Peng *et al.*, 2017; Shen *et al.*, 2014). However, its key drawback is rapid deactivation due to coke deposits and poisoning caused by the presence of impurities such as sulphur, nitrogen, and chlorine-containing biomass (Tan *et al.*, 2020). Furthermore, the environmental and safety concerns associated with nickel toxicity render them unsuitable for gasification (Boot-Handford *et al.*, 2018; Guan *et al.*, 2016; Shen & Yoshikawa, 2013; Virginie

*et al.,* 2012). Noble-metal-based catalysts have demonstrated high catalytic activity, long-term stability, and resistance to carbon deactivation, but they are expensive (Boot-Handford *et al.,* 2018).

Alternatively, alkali-earth-based catalysts such as dolomites, olivine, and limestone have piqued the interest of many researchers due to their abundance and reasonably good catalytic activity (Boot-Handford *et al.,* 2018; Gusta *et al.,* 2009; Wang *et al.,* 2005). An additional factor to consider is that the cost and availability of these materials may be such that catalyst recovery is unnecessary (Orío *et al.,* 1997). Dolomite is exceptionally soft and chlorine sensitive, making it unsuitable for high-temperature reactions (above 850$^{o}$C) and biomass containing traces of chlorine (Guan *et al.,* 2016; Nordgreen *et al.,* 2012). On the other hand, coke is reported to deactivate olivine significantly, thereby blocking active sites and reducing surface area (Shen & Yoshikawa, 2013). Furthermore, since the active sites of olivine are deeply buried on its matrix, it quickly loses its catalytic nature (loss of pore structure) at temperatures above 850$^{o}$C and behaves as inert materials (Abu-El-Rub *et al.,* 2004). In general, the alkali-earth-based catalysts are generally found to be marginally weaker due to rapid deactivation but with promising activity when used at low gasification temperature (< 800$^{o}$C) and when doped with other active metals (Ramadhani *et al.,* 2020).

According to the studies, the SCW gasification process's severity operating factors are temperature, feedstock concentration, residence time, and catalyst. Unfortunately, most of the published studies used the classic one-factor-at-a-time (OFAT) experiment method, which changes only one variable at a time while holding the other variables constant. Using this method, it is difficult to identify the optimum combination of operating parameters, which necessitates a function expression between the variables and responses predicting gasification outcomes. Compared to the OFAT approach, statistically designed experiments that vary several factors concurrently and judiciously are more effective when studying the effect of more than one parameter because it involves the interaction(s) among factors (Czitrom, 1999). Response surface methodology (RSM) is a combination of mathematical and statistical methods that can be used for studying the effect of many parameters at a different level and hence their effects on each other, overcoming the limitation of the classic OFAT approach. Moreover, RSM is advantageous in minimising the number of experiments, expenses and time spent on physical experiments while providing sufficient statistically relevant results. Just a few studies on the use of RSM in SCW gasification have been published to date. A few published studies includes optimisation of H2 production from crude oil SCW gasification Yang *et al.* (2013), optimisation

of effect of temperature, feed loading and reaction time on gaseous production of the microalgae in SCW gasification Samiee-Zafarghandi *et al.* (2018), parametric optimisation of SCW gasification of food waste Chen *et al.* (2020), and optimisation of noncatalytic gasification of lignin in SCW using central composite design Kang *et al.* (2015). Therefore, it is critical to investigate further the optimisation of SCW gasification parameters focusing on specific biomass and reactor type. Currently, to the best of our knowledge, no single study exists on the parametric optimisation of subcritical and SCW gasification of RH enhanced with alkaline earth catalyst using RSM.

## 1.2 Statement of the Problem

The use of catalysts to enhance biomass conversion has been proposed as an environmentally, economically, and efficiently method of biomass gasification. However, the rapid deactivation of catalysts, high cost, and disposal issues coupled with the poisonous nature of many metals make them unsuitable for gasification. Iron is a promising metal for gasification catalysis due to its abundance, inexpensive and less toxic; yet it is largely neglected compared to other metals (Ali *et al.,* 2016; Maheshwari, 2011). Iron precursors based on ferrous chloride and sulphate have been widely employed during iron synthesis (Guo *et al.,* 2018; Hao *et al.,* 2014; Noichi *et al.,* 2010). The use of these precursors results in a substantial amount of contaminated wastewater, and the sulphate and chloride residues potentially poison the catalyst and contribute to its rapid deactivation. Iron precursors based on acetate, citrate, oxalate, or formate could give a feasible alternative iron synthesis to circumvent this barrier. Nonetheless, based on the knowledge of the author no information available in literature on utilization of these precursors in subcritical and SCW biomass gasification. Therefore, this study investigates the feasibility of employing an alternative iron precursor based on iron (III) ammonium citrate to synthesise a catalyst to promote biomass gasification via sub- and SCW. Furthermore, the study will employ RSM to optimize the operational parameters of gasification of varieties of rice husks. For the first time, an RSM based on a computer-aided design known as the I-optimality criterion is used in this study. In contrast to other conventional RSM approaches (Box-Behnken and Central-Composite), optimal designs are effective and precise for assessing the optimisation problem, and it can fit any model (first, second, quadratic, or cubic orders) (Mohamed *et al.,* 2016; Ranade & Thiagarajan, 2017). Besides this, the I-optimality design allows for fewer experimental runs than classic RSM types and has a confined design space.

## 1.3 Rationale of the Study

Concerns about the price of fossil fuels, energy security, and climate change, combined with the world's growing population, necessitate the research of alternative renewable energy sources. Biomass is a potential renewable energy source; however, its exploitation practices, such as landfilling and incinerating, are highly detrimental to the environment. The research to replace fossil fuels focuses on hydrogen generation from biomass because it is a sustainable renewable type and one of the cleanest energy routes. Therefore, biomass gasification via hot compressed (sub- and supercritical) water serves as an efficient energy conversion technology that can convert nearly any kind of biomass to a valuable product like $H_2$-rich gas, bio-oil, and biochar. Furthermore, because the reaction occurs in the water phase, sub- and SCW gasification can directly utilize the high moisture content biomass and avoid the energy-intensive drying process.

## 1.4 Objectives of the Study

### 1.4.1 General Objective

To optimize the sub- and supercritical water gasification of rice husk biomass enhanced with iron-doped alkaline earth catalysts.

### 1.4.2 Specific Objectives

(i) To investigate the properties of rice husk variants in terms of their viability for waste-to-energy utilization through gasification.

(ii) To develop optimized empirical models using response surface methodology that can mimic the influence of operating parameters on subcritical and SCW gasification of rice husk.

(iii) To fabricate and characterize limestone and dolomite catalysts supported Fe synthesized using an iron (III) ammonia citrate precursor.

(iv) To develop optimized empirical models using response surface methodology that can simulate the influence of catalyst on SCW gasification of rice husk

## 1.5 Research Questions

(i) What are the characteristics of rice husks which make them appropriate for subcritical and SCW gasification?

(ii) To what extent does the developed optimized empirical models predict the gasification output of subcritical and SCW gasification of rice husk?

(iii) What is the impact of iron (III) ammonia citrate precursor on metal dispersion and catalyst selectivity toward gasification yield?

(iv) To what extent does the developed optimized empirical models predict the influence of addition of catalyst in SCW gasification yield?

## 1.6 Significance of the Study

The use of RH, an agricultural byproduct of rice farming, to produce syngas, a stable fuel analogous to fossil fuels, is crucial for the long-term sustainability of clean energy. This research presents optimization options for the SCW gasification of RH using a facile iron-doped alkaline earth catalyst. The findings of this study will contribute to the existing knowledge on subcritical and SCW gasification of biomass to optimize gasification output. The use of RH as a renewable energy source will add value to the bulk RH produced in rice processing plants while also helping to mitigate climate change caused by its combustion management. Furthermore, the produced syngas can be used as an alternative to fossil fuels, helping to reduce carbon emissions.

## 1.7 Delineation of the Study

This study investigates the feasibility of using RH, a pervasive agricultural waste, to produce a hydrogen-rich gas called syngas. This study presents the characterisation of RH varieties, the empirical models that can predict the interaction of operating conditions on gasification outputs and predict the impact of addition of alkaline earth catalysts enhanced with iron. This dissertation is organized into five chapters. Chapter one includes background information, the purpose of the study, objectives, research questions, and the significance of the study. The second Chapter provides a detailed assessment of the literature on subcritical and SCW gasification, catalytic gasification, the role of iron-based catalysts, and their redox behaviour under gasification conditions. The third Chapter (materials and methods) covers the procedures for subcritical and SCW gasification, optimisation protocol for gasification operations, synthesis of iron supported dolomite and limestone, and the optimisation of catalytic SCW gasification. The fourth Chapter includes the results and discussion on the optimisation of multiple gasification operating parameters and catalysts on the subcritical and SCW gasification yield of various rice husks. The conclusion and recommendations are presented in Chapter five. The study thought to improve the production of $H_2$-rich gas by employing an easy-to-prepare and

recoverable iron-doped alkaline earth catalyst. It is worth noting that no gas characterisation, catalyst recoverability, or catalyst after use characterisation was carried out. This is one of the study's shortcomings, and it leaves a gap for future studies of this nature. The scope of this study spanned optimizing subcritical and SCW gasification conditions, determining the interrelationships between the various properties of rice husks and their gasification yield, and optimizing the gasification yield using an easy-prepared iron-doped alkaline earth catalyst. Furthermore, this work was primarily based on a lab-scale gasification system. As a result, further research into the technology's economic potential for the use of low-cost agricultural residue is necessary.

# CHAPTER TWO

# LITERATURE REVIEW

## 2.1 Introduction

Gasification is the thermochemical processing of biomass to $H_2$, CO, $CO_2$, and $CH_4$ at high temperatures (normally >700$^oC$) in the presence of controlled oxygen or steam. A supercritical water gasification is a form of biomass gasification in which the reaction medium is SCW (374$^oC$ and 22.1 MPa). As a result, the primary distinction between SCW gasification and other thermochemical gasification approaches is the gasification medium, which can be SCW, inert gas, or steam (Rodriguez & Kruse, 2018). Supercritical water serves as both a reactant and a medium in the gasification of biomass. The likelihood of generating $H^+$ and $OH^-$ ions at high density increases under supercritical conditions, creating an environment for hydrolysis and pyrolysis reactions (Kruse & Dinjus, 2007b). Free radicals are also generated at high temperatures above supercritical temperatures (Kruse & Dinjus, 2007a). The production of $H_2$ from biomass via SCW gasification, regardless of biomass compositions, outperforms other conventional thermochemical routes. The added benefit of SCW gasification of biomass is its high-pressure $H_2$ production, which reduces the cost for compression energy during storage (Demirbas, 2009). Water can form ions at the supercritical point, which helps decompose biomass components (Guo *et al.*, 2010). At high temperatures and pressures, SCW dissolves lignocellulosic biomass, which consists of lignin, hemicellulose, and cellulose. By increasing the reaction temperature and pressure, the produced cellulose and hemicellulose are further broken down into simple sugars, which are further gasified into permanent gases. On the other hand, Lignin transforms into phenolic compounds, which are then reformed into simple gases like $H_2$, CO, $CO_2$, and $CH_4$ (Fang *et al.*, 2008; Kruse, 2008).

## 2.2 Subcritical and Supercritical Water

### 2.2.1 Thermophysical Property of Subcritical and Supercritical Water

Water, the planet earth's most abundant liquid, has been extensively researched and used widely near atmospheric conditions. Little is reported about fluids in extreme states, such as those found in the supercritical zone. A supercritical fluid is any substance that exists at temperatures and pressures higher than its critical point, where specific liquid and gas phases do not exist. Water has a critical temperature of 374.1°C and a pressure of 22.1 MPa, as shown in Fig. 1. Above the critical point, there is usually no further phase transformation, and the water is classified as a

homogeneous supercritical fluid rather than a liquid or gas. Supercritical water has both liquid-like and gas-like characteristics (Kritzer, 2004). Due to these exceptional behaviours, SCW exhibits many exceptional thermophysical properties suitable for different industrial applications. Supercritical water has become an exciting medium for reactions in many industries such as hydrothermal synthesis (Rabenau, 1985), waste oxidation (Kritzer & Dinjus, 2001; Shaw & Dahmen, 2000), plastic degradation (Hayashi *et al.*, 1998), synthesis of nano-particles (Poliakoff *et al.*, 1999), and biomass conversion (Yakaboylu *et al.*, 2015). Under supercritical conditions, the physicochemical properties of water, such as density, ion product, viscosity, and dielectric constant, vary significantly from either the extreme state of the gas phase or the liquid phase.

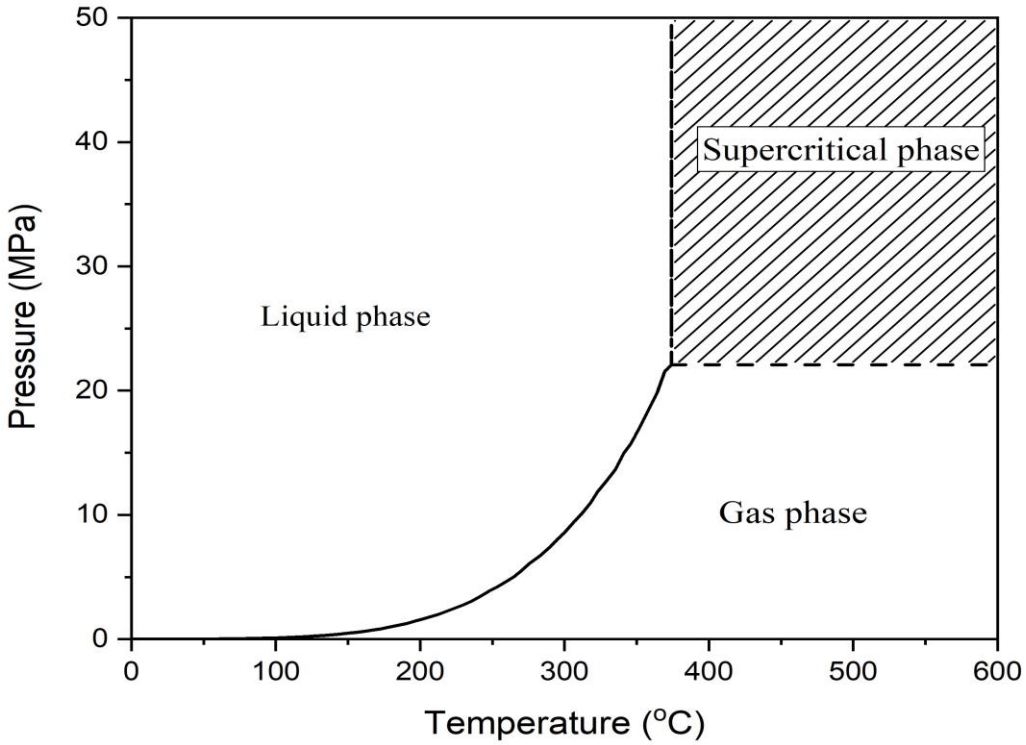


**Figure 1: Schematic phase diagram of water (Yakaboylu *et al.*, 2015)**

### (i) Density, Ionic Product, and Viscosity

In theory, the density of water decreases gradually as the temperature rises around the ambient conditions. Then again, it falls precipitously near the critical point. After entering the supercritical regime, the density declines moderately. On the other hand, the amount of ionic product, which represents the ions in a specific solution, decreases sharply near the critical point. Under ambient conditions, liquid water self-dissociates into $H^+$ and $OH^-$ ions. Since the equilibrium is an endothermic reaction, increased temperature promotes ion formation. As

shown in Fig. 2, near the critical point, water density and ion product are lower than in normal conditions. The density varies with temperature and pressure, ranging from liquid (1 g/cm$^3$) to low-pressure vapour (0.0011 g/cm$^3$). On the other hand, the ion product is related to both temperature and density, but density has a more significant influence. The ion product increases with an increasing density below the critical point, suggesting that the ionic reaction mechanism is advantageous in this situation. The decrease in water density induces a drop in ion product because the temperature increment is beyond the critical point, implying that the free-radical mechanism is preferable in this case (Henrikson *et al.*, 2003).

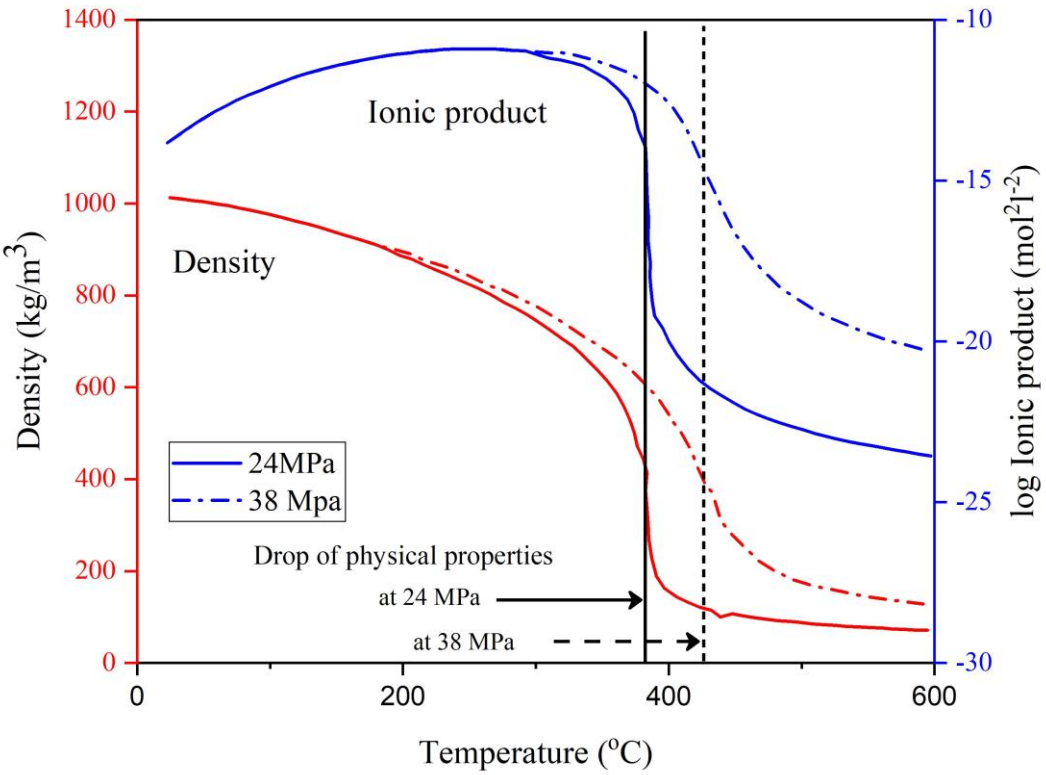


**Figure 2: Physical properties of water against temperature at 24 MPa and 38 MPa (Kritzer, 2004)**

### (ii) Hydrogen Bonding, Dielectric Constant, and Viscosity

Water has a high polarity at room temperature due to a dipole created by a large difference in the electronegativity of hydrogen and oxygen atoms. The dielectric constant is used to express the degree of polarity (Kutz, 2007). Water molecules form hydrogen bonds between hydrogen atoms and oxygen atoms, which are electronegative. The hydrogen bond is thought to be responsible for water's unique behaviours. For example, intermolecular hydrogen bonding is liable for water's high boiling point compared to other hydrides that lack hydrogen bonds. The

polarity of water molecules can also influence the solubility of various inorganic compounds or salts in water. The chemical structure of water at room temperature may be altered or destroyed by temperature increases. Because of the strong influence of the hydrogen bond in water, the dielectric constant is relatively high (approximately 80) at standard temperature and pressure. Nonetheless, as temperature and pressure rise, the dielectric constant of water decreases precipitously (Fig. 3).

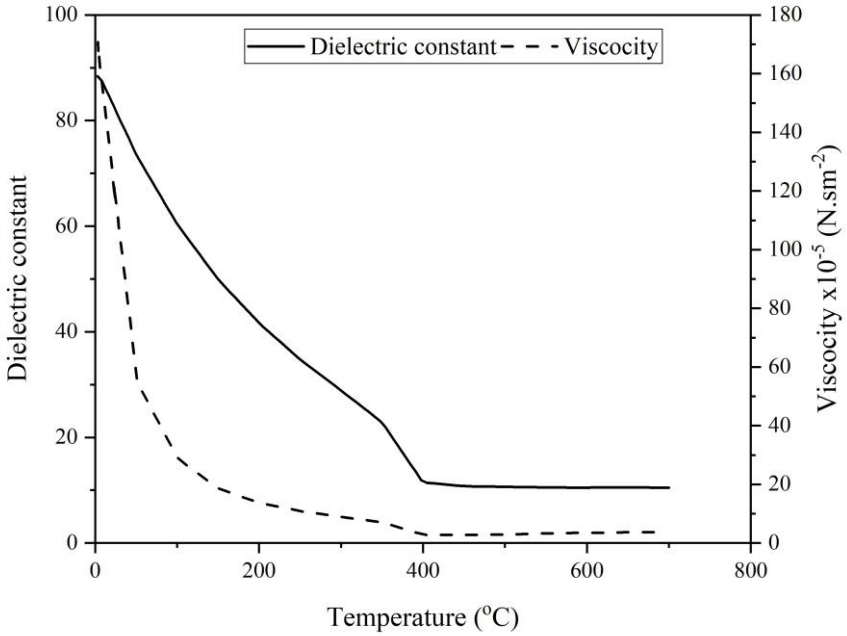


**Figure 3: Changes in the viscosity and dielectric constant properties of water with the temperature at a constant pressure of 22.1 MPa (Okolie *et al.*, 2021)**

A change in the dielectric constant can cause a change in the dissolving ability of water. Supercritical water has a dielectric constant that is approximately equivalent to that of typical organic compounds (Guo *et al.*, 2010). Supercritical water can perform similarly to nonpolar organic compounds, so its strong solubility makes it a solvent for nonpolar organic compounds. On the contrary, the dissolving potential of highly polar inorganic compounds decreases significantly, resulting in the isolation of dissolved organic compounds from water. The SCW becomes essential in gasification because it can dissolve organic compounds and improve their breakdown into permanent gases. On the other hand, the increase in temperature can also induce a change in water viscosity. At the critical point, the viscosity of water ($2.98 \times 10^{-5}$ N·s $m^{-2}$) approaches that of vapour ($2 \times 10^{-5}$ N·s $m^{-2}$), Fig. 3. Lower viscosity can give water a high diffusion coefficient, leading to the ideal reaction conditions for a high reaction rate (Guo *et al.*, 2010).

### 2.2.2 Role of Water as Reactant and Catalyst in the Reaction

Supercritical water has a different structure than ordinary water, resulting in an ionic product with two orders of magnitude greater than at room temperature. The Sub- and SCW contains a high concentration of $H^+$ and $OH^-$, making it possible to create an ideal environment for acid- or base-catalyzed reactions (Kritzer, 2004). Supercritical water gasification is a thermochemical conversion that involves complex hydrolysis and pyrolysis reactions. Water has a significant impact on the SCW gasification reaction process as a reactant involved in the reaction and as a catalyst (Guo *et al.,* 2010). Water and salt can yield acid or alkali during the hydrolysis reaction, influencing the bond cracking of organic compounds. Many experiments using model compounds were carried out to test the effect of water in the SCW reaction. Ogunsola and Berkowitz (1995) investigated the breakdown of heterocyclic sulfur and nitrogen from oil precursors using SCW extraction. According to the findings, protons supplied by SCW can promote heterocycle saturation and the formation of alkyl and C–N radicals. Compared to normal hydrolysis, interaction with SCW can expedite the removal of S and ring-opening of heterocycle rings. Benjamin and Savage (2004) investigated the reactivity of methylamine in SCW at temperatures ranging from 386 to 500°C and discovered that amine and amide conversion is a combination of pyrolysis and hydrolysis mechanisms. When temperatures are high, the pyrolysis mechanism is preferred, and when water density is high, the hydrolysis mechanism is preferred. Furthermore, autocatalysis of hydrolysate can be used to boost the reaction of organic compounds in subcritical water because the acid and alkali produced during the hydrolysis process can have a catalytic effect on the reaction path (Penninger *et al.,* 1999, 2000).

## 2.3 Subcritical and Supercritical Water Gasification

### 2.3.1 Reactions during Sub- and Supercritical Water Gasification

Understanding the reactions of decomposition of each biomass component in subcritical or SCW is invaluable for optimising and improving the efficiency of SCW gasification process. The first decomposition reaction that occurs during the hydrothermal processing of lignocellulosic materials is hydrolysis. As a result of these reactions, hemicelluloses degrade to form glucuronic acid and xylose, cellulose to glucose, and lignin to phenolics (Okolie *et al.*, 2019). Supercritical water gasification entails complex reactions that promote the thermal breakdown of biomass into permanent gases ($H_2$, $CH_4$ and CO). A few examples of such reactions include Boudouard reaction, water–gas shift reaction, steam reforming reaction,

decarboxylation, methanation reaction, hydrogenation, dehydration, and decarbonylation, as shown in Equation 1-7 ( Rana *et al.*, 2017; Rodriguez & Kruse, 2018).

Water-gas shift reaction:

$$CO + H_2O \longleftrightarrow CO_2 + H_2 \quad (1)$$

Steam reforming reaction:

$$CH_xO_y + (1-y)H_2O \longrightarrow CO + (1 - y + \frac{x}{2})H_2 \quad (2)$$

Syngas composition is heavily influenced by x and y, where x and y reflect the elemental molar ratios H/C and O/C in biomass, respectively (Guo *et al.*, 2007).

Methanation reaction for CO and $CO_2$:

$$CO + 3H_2 \longleftrightarrow CH_4 + H_2O \quad (3)$$

$$CO_2 + 4H_2 \longleftrightarrow CH_4 + 2H_2O \quad (4)$$

Hydrogenation reaction:

$$CO + 2H_2 \longrightarrow CH_4 + 0.5O_2 \quad (5)$$

Boudouard reaction:

$$2CO \longrightarrow CO_2 + C \quad (6)$$

$$CO_2 \longrightarrow O_2 + C \quad (7)$$

The water-gas shift reaction (Equation 1) is a chemical reaction that uses CO and $H_2O$ to generate $CO_2$ and $H_2$. The reaction is promoted at high temperatures and low feed concentrations (Rana *et al.*, 2017; Susanti *et al.*, 2010). Steam reforming is another significant reaction during SCW gasification of biomass to form CO, $CO_2$ and $H_2$ (Equation 2). Hydrogenation and methanation reactions are considered secondary reactions that need a more extended residence period and primarily use $H_2$, $CO_2$ and CO to generate $CH_4$, as shown in Equations 3-5 (Nanda *et al.*, 2015; Reddy *et al.*, 2014). The Boudouard reaction, on the other hand, produces carbon in the form of char or coke from CO and $CO_2$ Equations 6 and 7.

### 2.3.2 Effects of Process Parameters on Gasification

#### (i) Reaction Temperature and Pressure

Subcritical and SCW gasification have been investigated over a broad range of temperature and pressure conditions of 200 – 700$^{o}$C and 4.3–50 MPa. There are three operating regions that are

often considered: Region-I (500-700$^{o}$C, > 25 MPa), region-II (374-500$^{o}$C, 22 – 30 MPa), and region-III (< 374$^{o}$C, <22 MPa). The typical reaction routes in both SCW gasification regions are entirely governed by the thermo-physical characteristics of SCW, which can be represented by the ionic and free radical mechanisms shown in Fig. 4. In region-I gasification, the free-radical mechanism such as pyrolysis reaction dominates, correlates with high temperatures and low density, and the reaction is second order. In this gasification region, low-cost activated carbon and alkali catalysts are appropriate as catalysts for the inhibition of char formation. However, the circumstances necessitate high energy input. At gasification temperatures ranging from 374 to 500$^{o}$C, the reaction mechanism shifts with rising water density from one that follows free-radical mechanisms to one that promotes ionic reaction mechanisms. Hydrolysis is an essential ionic reaction that stimulates cellulose and lignin degradation. Cellulose degradation is primarily accomplished through hydrolysis, dehydration, and retro-aldol condensation. Watanabe *et al.* (2002) conducted a batch experiment for $H_2$ production from cellulose and glucose at 400 to 440$^{o}$C and 30 to 35 MPa and observed the char formation during decomposition of cellulose. According to Fang *et al.* (2004), as the temperature rises, char is formed by a dehydration reaction of low molecular weight compounds that were originally produced from cellulose in the subcritical zone. Lignin degradation to alkylphenols via hydrolysis in SCW at 400$^{o}$C has previously been documented in the literature (Ehara *et al.,* 2002; Yokoyama *et al.,* 1998). The production of char from lignin is thought to occur in the following order: Hydrolysis produces phenolic compounds and formaldehyde, and then a condensation reaction occurs between the phenolic compounds and formaldehyde to produce char (Okuda *et al.,* 2004; Saisu *et al.,* 2003). Since char gasification is a slow reaction, especially in this gasification regime, inhibition of its formation by using a catalyst is critical.

At low temperatures and high densities, the ionic process dominates, and both a vapour and a liquid phase will exist (Osada *et al.,* 2006). In this area, the equilibrium composition of gases derived from biomass is generally methane and carbon. Since the reaction rate of hydrolysis in subcritical water is slower than that in SCW (Sasaki *et al.,* 2004), it is difficult to gasify high molecular weight components of biomass such as lignin and cellulose. However, gasifying biomass in this temperature range is beneficial because the energy input is low even though the gasification rate is slow.

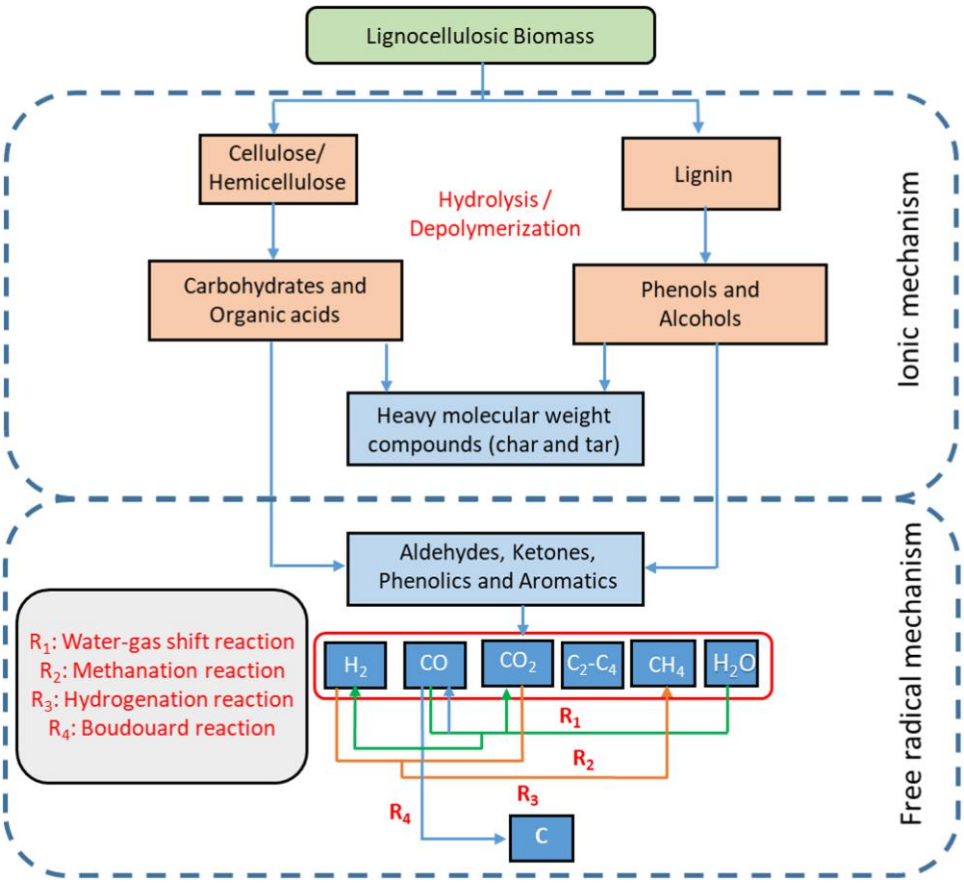


**Figure 4: Reaction pathways involved in the subcritical and supercritical water gasification of lignocellulosic biomass (Okolie *et al.*, 2021)**

The reaction temperature is the most critical factor influencing product yield during sub- and SCW gasification of biomass, mainly when the reaction occurs in the absence of a catalyst. Guo *et al.* (2007) conducted a systematic experimental and analytical study on hydrogen production by biomass gasification in SCW. Figure 5 depicts the equilibrium gas yield as a function of reaction temperature (400 - 800ºC) at a pressure of 25 MPa and feed concentration of 5%. At the steady chemical state, the yields of $H_2$ and $CO_2$ increase with temperature, but the yield of $CH_4$ decreases rapidly. The equilibrium CO yield is meagre, about $10^{-3}$ mol/kg dry biomass. As the temperature rises from 400 to 800ºC, the CO yield rises and then falls. When the reaction temperature rises above about 650°C, biomass gasification is complete, and the equilibrium gas product is $H_2$ and $CO_2$.

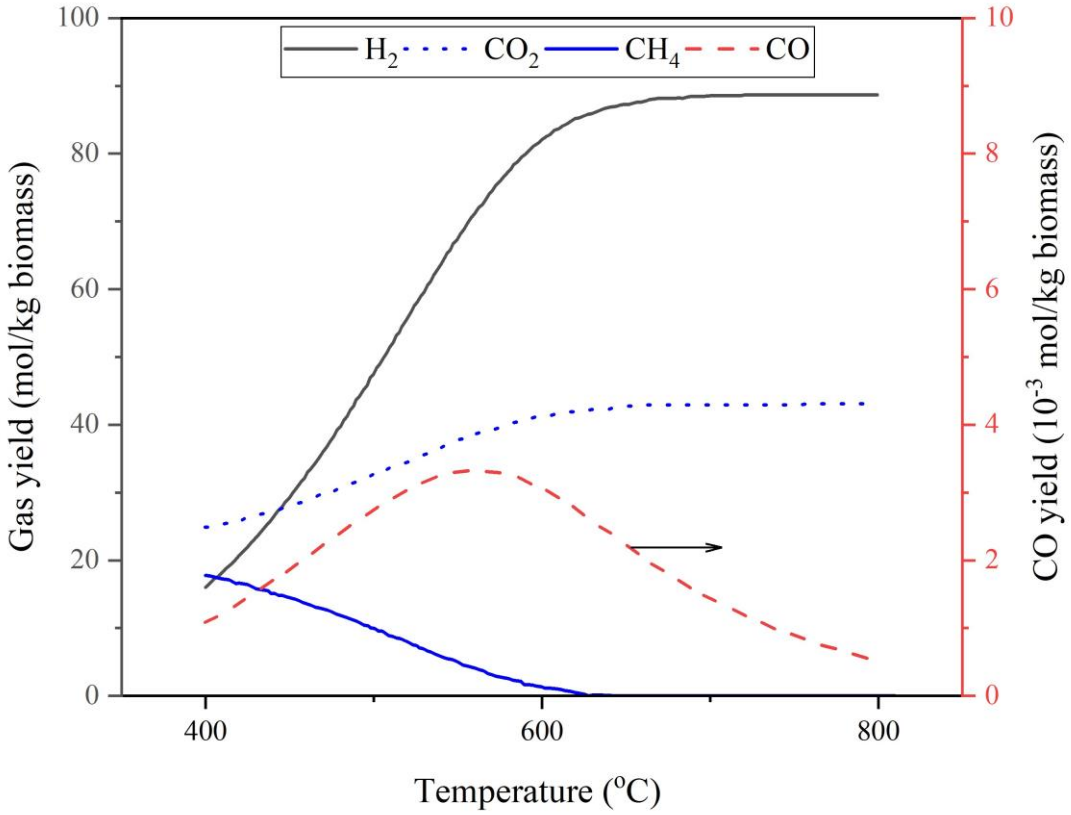


**Figure 5: The effect of temperature on the equilibrium gas yields from super critical water gasification at 25 MPa and 5 wt% wood sawdust concentration (Guo *et al.*, 2007)**

In order to explain the effect of pressure, it is essential to consider Le Chatelier's principle and competing chemical reactions involved in gasification. According to Le Chatelier's theorem, increasing the pressure shifts the equilibrium to the side of the reaction with fewer moles of gas. There are three major competitive reactions in hydrothermal gasification: Water–gas-shift, methanation, and steam reforming, as listed in section 2.3.1. As a result, as pressure rises, the methanation reaction shifts to the right, enhancing the formation of $CH_4$ with the concurrent consumption of $H_2$, $CO_2$ and CO. Furthermore, an increase in pressure can increase water density, dielectric constant, and ionic product (Basu & Mettanant, 2009). Free-radical and ionic reactions start competing as water density varies with pressure (Anikeev & Fan, 2014). However, due to ionic stabilisation at high water density, the ionic reaction becomes dominant at high pressure, as stated by Bühler *et al.* (2002). As pressure increases the rate of ionic reactions increases while the rate of free radical reactions declines. As a result, the rate of ionic reactions increases as pressure increases, while free radical reactions decrease (Okolie *et al.*, 2019).

Pressure effects on the overall equilibrium gas yield of SCW gasification remain uncertain (Rodriguez & Kruse, 2018). A study conducted by Kang *et al.* (2015) shows that the efficiency of the sub- and SCW gasification processes increase with decreasing temperature and increasing pressure. In contrast, as shown in Fig. 6, Guo *et al.* (2007) and Kang *et al.* (2015) found no significant influence of pressure on product yield. In another parametric analysis, Lu *et al.* (2006) found that as pressure rises, $H_2$ and $CO_2$ concentrations rise, while $CH_4$ and CO yields fall (Fig. 7a). They concluded that while higher pressure favours the water-gas-shift reaction, it can also slow down the decomposition reaction rate, as seen with increasing TOC concentration and decrease in GE Fig. 7b. Basu and Mettanant (2009) published an SCW gasification of RH at various pressures (22-34 MPa) and temperatures (500-700$^{o}$C). They found that pressure has a more pronounced impact on the equilibrium gas yields of SCW gasification of biomass at higher temperatures.

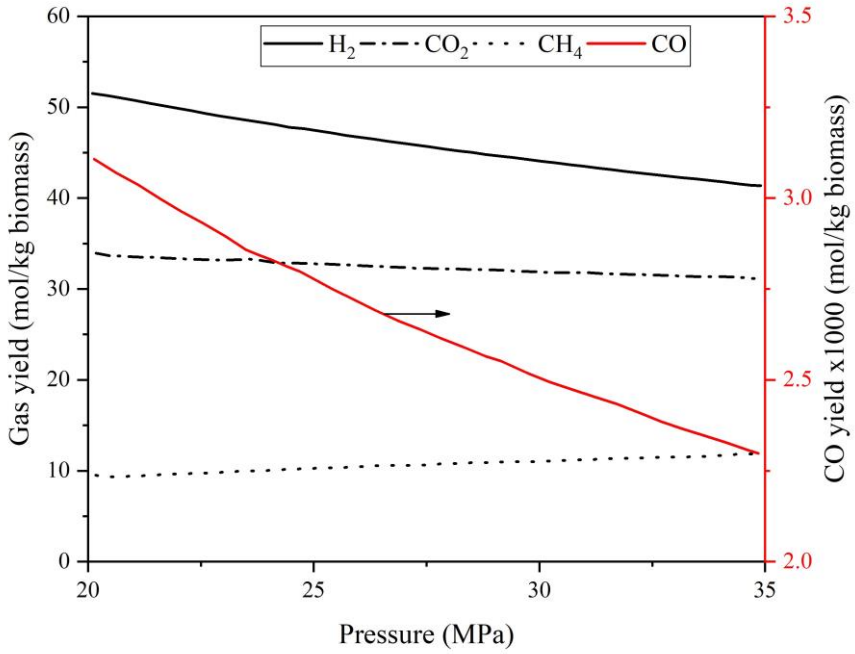


**Figure 6: Equilibrium gas compositions in the reactor as a function of pressure for biomass gasification at 500°C with a feed concentration of 5% (Guo *et al.*, 2007)**

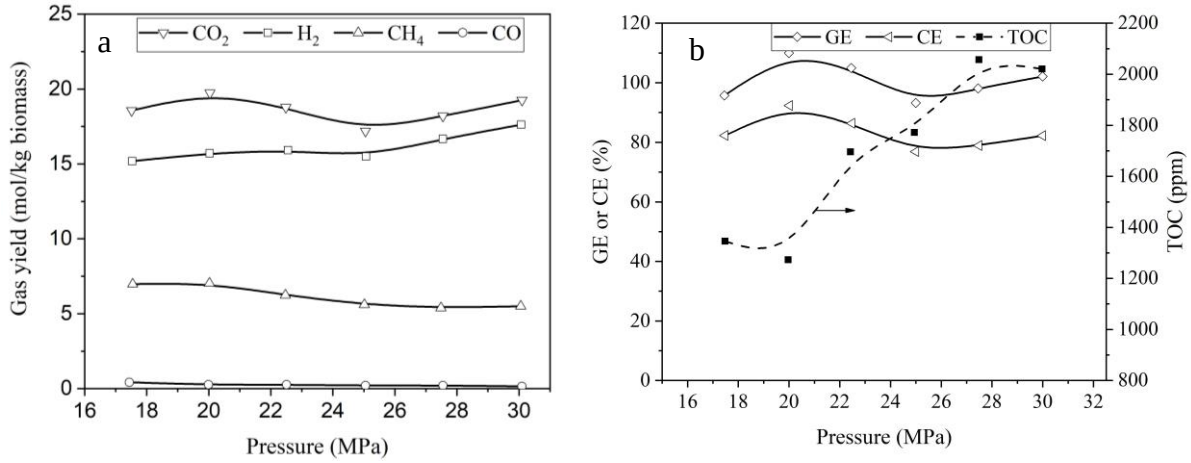


**Figure 7: Effects of pressure on wood sawdust gasification in super critical water at 650°C, feed concentration 4 wt% and residence time 27 s. (a) equilibrium gas yields; (b) GE, CE, and TOC (Lu *et al.*, 2006)**

### (ii) Feed Concentration

The feed for SCW gasification is primarily a blend of solid biomass and water. The proportion of biomass and water in the feed has a significant impact on gasification. Supercritical water is used as a medium for gasification to help cleavage the large molecules of biomass into simpler molecules, primarily CO, $H_2$, $CO_2$, and $CH_4$. Water serves as a reaction media as well as a source of hydrogen for the hydrolysis process. It is necessary to consider the role of the water-gas shift reaction and methanation in explaining the impact of feed concentration on gas yield during SCW gasification. Since the feedstock in SCW gasification reactor is made up of both biomass and water, the feed concentration is also regarded as the water-to-biomass or biomass-to-water ratio. When the concentration ratio is high, it indicates that the amount of water is small compared to biomass. Through the water–gas shift reaction (Equation 1), an increase in feed concentration would shift the reaction equilibrium to the left, thus impeding the formation of $H_2$ and $CO_2$. At low feed concentrations, the yields of $H_2$ and $CO_2$ generally increase due to increased biomass-to-gas conversion efficiency induced by the higher amount of water than the feedstock (Nanda *et al.*, 2017). Deniz *et al.* (2015) investigated the SCW gasification of marine biomass at 400°C, 4-12 wt% feed concentration, and a residence time of 60 minutes. The results reveal that when the biomass loading increased from 4 to 8 wt%, the hydrogen and methane yields increased, but the carbon dioxide yield declined, and the GE rose remarkably from 17 to 47.5%. However, as biomass loading increased from 8 to 12 wt%, $H_2$ yield declined sharply from 6.41 to 3.88%, $CH_4$ yield decreased from 3.26 to 2.31%, $CO_2$ yield increased from 84.37% to 88.83%, and GE increased marginally. Guo *et al.* (2007) investigated and published the impact of biomass concentration on equilibrium gas yield at 600°C and 25 MPa. When low

concentration biomass feedstock is gasified, the output gas is primarily $H_2$ and $CO_2$, but when high concentration feedstock is gasified, the $CH_4$ yield is very high, as shown in Fig. 8.

In SCW process, the interrelationships between low feed concentrations and high temperatures are best described by a decline in water density, ionic product formation, and dielectric constant as well as an elevation in the free-radical formation and solubility potential (Savage, 2009). At lower feed concentrations, the low water density combined with fewer moles of feed results in enhanced thermal conversion of organic compounds into products.

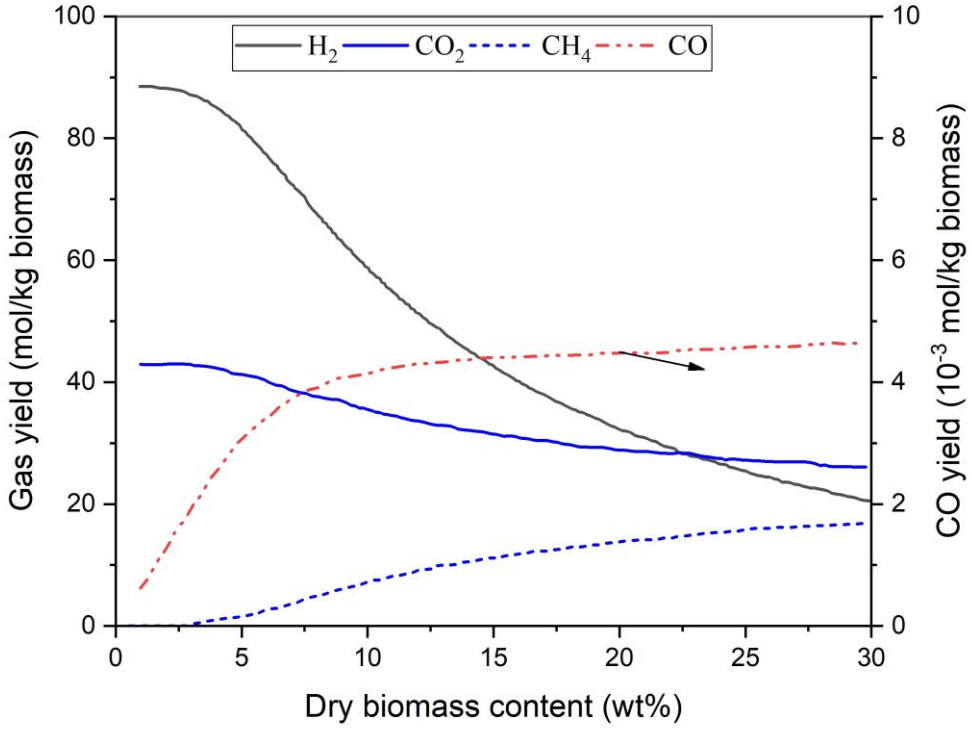


**Figure 8: Effect of wood sawdust concentration on super critical water gasification equilibrium gas yields at 25 MPa and 600°C (Guo *et al.* 2007)**

**(iii) Residence Time**

The period during which the reactants remain within the reactor after reaching the target temperature is referred to as residence time. Gas yields from SCW gasification are typically high at more extended residence periods and high temperatures due to enhanced biomass-to-gas thermal cracking reactions (Chen *et al.*, 2003). Since CO is consumed as a reactant across many reactions, such as hydrogenation, methanation, and the water–gas shift reaction, the concentration of CO usually decreases with longer residence times. As a result, $H_2$ and $CO_2$ yields are higher in the gas phase since they are the main products of the water–gas shift reaction, and $CH_4$ concentrations are also improved from hydrogenation and methanation reactions

(Reddy *et al.,* 2014). Residence time is strongly dependent on the reaction temperature, with a more substantial effect at lower temperatures and a slight effect at higher temperatures. Lu *et al.* (2006) investigated the impact of rising residence time on gasification of wood sawdust at 650$^{o}$C and 25 MP and discovered that the $H_2$ and $CH_4$ yields increase dramatically as residence time increases from 9 to 46s (Fig. 9a). At the same time, the CO yield decreases with increasing residence time. Moreover, as residence time increases, gasification efficiency (GE) and carbon efficiency (CE) increase, while unconverted total organic carbon (TOC) in the liquid residual decreases (Fig. 9b). Lee *et al.* (2002) reported that regardless of residence time, the yields of all gases remained virtually constant at 700$^{o}$C, except for the shortest residence time of 10.4s when gasifying the 0.6 M glucose at 28 MPa. Basu and Mettanant (2009) published a review study on biomass gasification in SCW and concluding that biomass conversion and $H_2$ yields increase with residence time up to a certain time and then exhibit no considerable change. Williams and Onwudili (2005) investigated the effect of long residence time on $H_2$ yield in SCW gasification of glucose and found that it increased slightly from 1.26 wt% at 30 minutes to 1.27 wt% at 120 minutes, with a slight decrease in oil yield and an increase in char yield. The effect of residence time on gas products is also affected by the interaction of other operating parameters such as temperature, pressure, feed concentration, reactor configuration and biomass type.

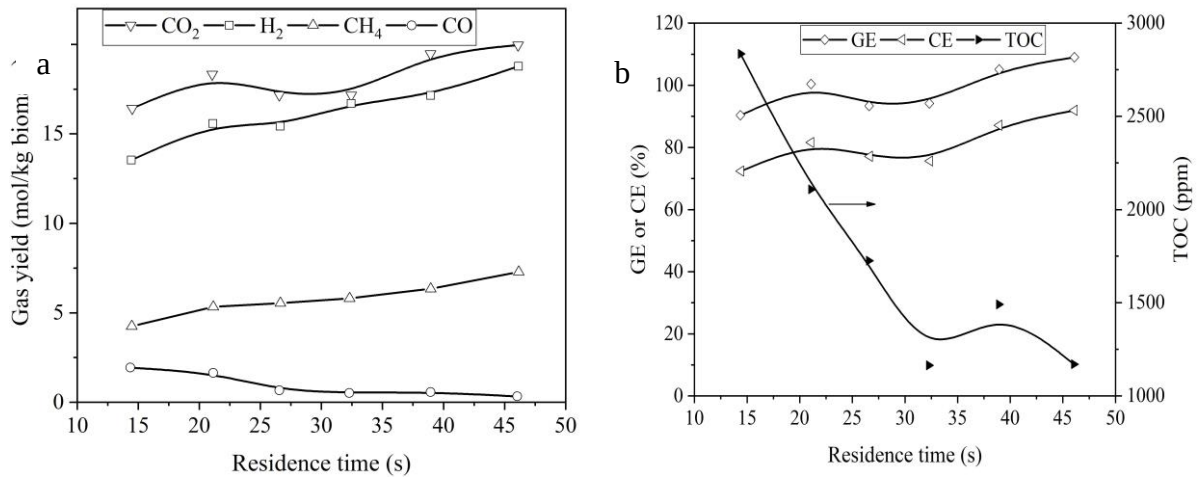


**Figure 9: The effects of residence time on the gasification of wood sawdust in super critical water. (a) Gas yield; (b) GE, CE, and TOC. (Operating conditions: temperature, 650 $^{o}$C; pressure, 25 MPa; feed concentration, 4 wt%) (Lu *et al.*, 2006)**

### (iv) Biomass Particle Size

Few studies have been conducted to investigate the effects of biomass particle size on gas yield through hydrothermal gasification (Basu *et al.,* 2009; Okolie *et al.,* 2019). The low mass transfer

resistance of SCW can counteract the effects of biomass particle size, even though the latter affects both heat and mass transfer. Furthermore, it is undeniable that biomass with smaller particle sizes has a larger surface area, allowing SCW to degrade and solubilize it more effectively. It is essential to consider the influence of surface area per unit mass of biomass to understand the impact of particle size on gas yield during SCW gasification. Smaller particle size biomass has a larger surface area per unit mass, exposing it to the reaction environment and promoting heat and mass transfer between the particles. This could boost the hydrothermal decomposition and subsequent gas yields by increasing the efficiency of the gasification reactions. Lu *et al.* (2006) reported SCW gasification results at 650$^{o}$C, 25 MPa, 4 wt% feed concentration, residence time 30 s, and biomass particle sizes ranging from 180 to 400 micron. Biomass with smaller particle sizes, < 180 microns, yielded higher $H_2$ yields of 17 mol/kg and GE of 93.2% than larger biomass particle sizes of 180-400 microns, which recorded a $H_2$ yield of 13.7 mol/kg and GE of 56.51%. Basu *et al.* (2009) investigated SCW gasification of rice with particle sizes ranging from 250 to 1500 micron and found no clear trend of GE for different particles under gasification conditions of 500°C, pressure 30 MPa, biomass concentration 10%, and residence time 1 hr. It could be concluded that, while smaller particles generate more hydrogen when gasified and the optimal particle size should be determined while taking both economy and feasibility into account.

## 2.4 Process Parameters Optimization

Engineers and scientists often use the OFAT experiments approach in which just one factor is changed at a time while the rest are held constant (Czitrom, 1999). However, statistically designed experiments that vary several factors simultaneously are more efficient when studying two or more factors. A statistically designed experiment is a more effective technique than an OFAT experiment for determining the impact of two or more variables on a response, and it generates mathematical models that can describe the process behaviour. Response surface methodology (RSM) is a set of mathematical and statistical techniques for establishing an appropriate functional relationship between control variables (factors) and the response of interest (products) (Khuri & Mukhopadhyay, 2010). The RSM is important in designing, developing, and analysing new scientific studies and products. It is also effective in improving existing products or designs. Response surface methodology is most commonly used in industrial, clinical and biological science, food science, social science, and physical and engineering sciences. The advantage of the design of experiment over OFAT experiment includes: (a) It uses minimal resources (experiments, materials, time, etc.) for the amount of

information obtained. This is especially important in industries where trials can be costly and time-consuming, (b) The estimations of the effects of each variable are more precise. All the observations are used to estimate the effect of each factor and each interaction resulting in higher precision (reduced variability), (c) The interaction between variables is estimated systematically, and (d) There is experimental information in a larger region of the factor space. This enhances the predictability of the response in the factor space by minimizing the variability of the estimates of the response in the factor space and improves the efficiency of process optimization since the optimal solution is sought over the entire factor space (Baş & Boyacı, 2007; Czitrom, 1999).

Optimization research can be divided into six stages using RSM as an optimization technique: (a) the selection of independent factors with significant effects on the system through screening analyses and the demarcation of the experimental region, based on the study objectives and the researcher's knowledge; (b) the selection of the experimental design and the execution of the experiments using the selected experimental sequence; (c) the mathematical-statistical treatment of the obtained experimental data via the fit of a polynomial function; (d) the assessment of the model's fitness; (e) the confirmation of the necessity and potential of conducting a displacement in direction to the optimal region; and (f) the determination of the optimum values for each studied variable (Bezerra *et al.*, 2008).

The relationship between the response and the variables is given in Equation 8.

$$Y = f(x_1, x_2, \dots\dots, x_n) + \varepsilon \tag{8}$$

Where $Y$ is the response, $f$ is the unknown function of response, $x_1$, $x_2$, ..., $x_n$ denote the independent variables, $n$ is the number of the independent variables, while $\varepsilon$ is the random error representing other sources of variability not accounted for by $f$, such measurement error. It is generally assumed that the random error has a normal distribution with a zero mean and variance (Baş & Boyacı, 2007). The model employed in RSM is generally a full quadratic equation or reduced form, as shown in Equation 9. Factorial design is a first-order design that estimates the linear functions of variables on outputs. These designs do not account for curvature. Second-order designs, such as Central Composite and Box-Behnken, and optimal designs, estimate the curvature-interaction of the variables and present it as a quadratic equation (Ranade & Thiagarajan, 2017).

$$Y = \beta_o + \sum_{i=1}^{n} \beta_i X_i + \sum_{i=1}^{n} \beta_{ii} X^2{}_i + \sum_{i=1}^{n} \sum_{j=i+1}^{n} \beta_{ij} X_i X_j + \varepsilon \quad (9)$$

Where $\beta_o$ is the intercept, $\beta_i$ is the linear coefficient of terms, $\beta_{ii}$ is the square effect terms, $\beta_{ij}$ is the interactive coefficient of terms, and $X_i$ and $X_j$ are the coded value of independent variables.

The central composite design (CCD) was invented in 1951 by Box and Wilson (1951). The CCD is made up of factorial points, centre points, and star points. Star points represent the extreme values of the variables. There are a few studies in the literature that use the central composite design in gasification optimization. Yang *et al.* (2013) used RSM and CCD to optimise $H_2$ output from SCW gasification of crude glycerol. Three variables were investigated: glycerol concentration (1 to 5 wt%), reaction temperature (300 – 600°C), and KOH concentration (0 to 3 molL$^{-1}$). The findings revealed that high temperatures and KOH concentrations promoted $H_2$ generation. Further, the study revealed that too high glycerol concentration had a negative influence on $H_2$ generation. The optimal reaction conditions for producing $H_2$ were found to be 500°C, 7 wt% glycerol concentration, and 2.39 mol L$^{-1}$ KOH concentration. Ibtissem *et al.* (2019) used CCD to optimize the hydrogen production in SCW gasification of glycerol using a mini autoclave reactor. The effect of five operating conditions namely, temperature (400-600° C), residence time (5 -124 minutes), feed concentration of glycerol (3-25 wt%), pressure (20.21-29.76 MPa) and KOH catalyst quantity (0-2 wt%) was studied. The results showed that a high temperature and a long residence time are preferable for hydrogen production and gasification efficiency, with temperature having the most significant effect on both responses. According to the created mathematical models, the operating settings for optimum hydrogen yield and gasification efficiency are temperature = 599.9°C, residence time = 60.8 minutes, pressure = 21.3 MPa, glycerol concentration = 3.79 wt%, and KOH = 0.102 wt%. Bai *et al.* (2020) employed CCD in RSM for the optimisation of temperature (500-800ºC) and residence time (2-60 minutes) in SCW gasification of polypropylene (PP) plastics. The results show the effect of temperature on gasification was more important than time, and the optimal condition was 750°C and 60 minutes.

Box and Behnken (1960) proposed a method for selecting points from the three-level factorial arrangement, allowing for the efficient estimation of first- and second-order coefficients of the mathematical models called Box and Behnken design (BBD). When constructing the BBD, the midpoints of the edges of the variables region and the centre point are considered. In the Box-Behnken design, all variable levels must be adjusted only at three levels (−1, 0, +1) with evenly

spaced intervals between these levels. In fact, this design is more economical and efficient than CCD (Bezerra *et al.*, 2008). This experimental design has been extensively used for process optimization; however, its applicability in supercritical water gasification is still much limited than that of the CCD. Samiee-Zafarghandi *et al.* (2018) investigated the effects of temperature (355-405°C), feed loading (1-8 wt%) and reaction time (15-45 minutes) on gaseous product's composition of the microalgae in SCW gasification using RSM and BBD. The temperature was discovered to be the most critical variable, followed by reaction time and microalgal biomass loading. The optimum condition for the highest $H_2$ production of 21.1 mol% was observed to be feed loading 1.4 wt%, temperature 405$^{o}$C and reaction time 45 minutes. Kang *et al.* (2015) used a BBD to optimise noncatalytic gasification of lignin in SCW. Three variables were chosen: Temperature (399−651°C), pressure (23−29 MPa), and biomass ratio (3−8 %). The results revealed that pressure had a minor effect on gas yield and that the maximum hydrogen yield can reach 1.60 mmol/g biomass when optimal temperature, water to biomass ratio, and pressure were 651°C, 3.9%, and 25 MPa, respectively. Chen *et al.* (2020) designed experiments for investigating the interactive effects of temperature (650–850°C), time (5–15 minutes) and concentration (5–15 wt%) on the SCW gasification of food waste using RSM based on BBD. The results showed that complete gasification was essentially achieved, with carbon gasification efficiency reaching 98% for the operational parameters of temperature, concentration, and residence time of 850°C, 5%, and 10 minutes, respectively. The authors observed that temperature is the most influential factor, followed by residence time and feed concentration. The discrepancy in the order of severity among different factors in the published literature could be attributed to the degree of operating condition studied, the types of biomasses used, and the type and configuration of the reactor used. Seçer *et al.* (2021) employed RSM and BBD to assess the impacts of process parameters such as reaction time (0-100 min), initial water volume (0-70 mL), feedstock amount (1-6 g), and catalyst amount (0.01-0.2 g) on total gasification and hydrogen production yield by low-temperature hydrothermal gasification of Sorghum biomass at 250°C. Water volume should not be raised above a particular threshold to enhance the overall gas volume produced from the processes. Also, the reaction time can be decreased by increasing the amount of catalyst, or it can be kept longer if a large volume of gas is desired by using less catalyst. The optimum parameters for maximum hydrogen production were determined to be a residence time of 58.6 minutes, a water volume of 24.5 mL, and a catalyst quantity of 0.02 g.

Optimal designs are generated based on computer algorithms and are called computer-aided designs. The optimal designs are not orthogonal like traditional CCD and BBD, and the variables' effects are correlated in these designs. The key benefit is that it may be used to fit any

model (first and second orders, quadratic, cubic) or for any specific research purpose such as screening or generating a response surface. Furthermore, optimal designs allow for fewer experimental runs than traditional RSM types and offer a constrained design space. The "I" in I-optimal designs stands for integrated. The I-optimality is an experimental design criterion that reduces the estimated variance across the region of experimentation. The I-optimal provides significant benefits in terms of enhanced prediction while also performing very well in respect of the precision of variable effect estimates (Jones & Goos, 2012). Ranade and Thiagarajan (2017) used generated experimental trials to compare CCD, BBD and optimal design and concluded that optimal design had fewer experimental runs and the highest mean R-square value. Optimal designs have mainly been applied in pharmaceutical and chemistry studies (Barot *et al.,* 2012; Holm *et al.,* 2006; Mohamed *et al.,* 2016). To the best of the author's knowledge, no single article has yet been published that employs optimal design for the optimization of subcritical or SCW gasification of biomass.

## 2.5 Catalytic Gasification of Biomass

### 2.5.1 Homogeneous Catalyst

Subcritical or SCW gasification is an energy-demanding process that necessitates high temperatures and pressures, resulting in increased operating costs. Catalysts are used in SCW gasification to lower the reaction temperature, shorten the reaction time, enhance hydrogen selectivity, minimize tar and char yields, and reducing energy requirements. Alkali and hydroxide catalysts such as $Na_2CO_3$, $K_2CO_3$, NaOH, $Ca(OH)_2$, $KHCO_3$ and KOH are examples of homogeneous catalysts that have received the most attention in the literature (D'Jesús *et al.,* 2006; Guo *et al.,* 2012; Kruse *et al.,* 2000; Ramsurn *et al.,* 2011; Xu *et al.,* 2013). Xu *et al.* (2013) examine the catalytic effects of alkali salts (KOH, NaOH, $Na_2CO_3$, $K_2CO_3$ and $Ca(OH)_2$) on the SCW gasification of dewatered sludge and observes that $H_2$ concentration and char suppression significantly increases with the addition of catalyst except for $Ca(OH)_2$. Only the $CO_2$ concentration was found to be affected by $Ca(OH)_2$. Nanda (2016) investigated the effects of homogeneous alkali catalysts such as carbonates ($K_2CO_3$ and $Na_2CO_3$) and hydroxides (KOH and NaOH) on timothy grass SCW gasification to maximize hydrogen yield. A non-catalytic SCW gasification of timothy grass at 650$^o$C for 45 minutes with a feed concentration of 11.1 wt% yielded high concentrations of $H_2$ (5.15 mol/kg) and total gases (17.2 mol/kg). The addition of catalyst substantially increased $H_2$ concentrations in the following sequence: KOH (8.91 mol/kg) > $K_2CO_3$ (7.84 mol/kg) > NaOH (6.68 mol/kg) > $Na_2CO_3$ (6.39 mol/kg) > no catalyst (5.15 mol/kg). According to Jin *et al.* (2014), the addition of $Ca(OH)_2$ increased $H_2$ yield by

125% compared to non-catalytic experiments. The order of catalytic impact on hydrogen yield of biomass gasification followed the following pattern: KOH > $Ca(OH)_2$ > $K_2CO_3$ > LiOH > NaOH > $Na_2CO_3$, which agrees with Nanda and Kozinski (2016) but contrasts with Xu *et al.* (2013). The type of biomass used, the reactor type and configuration, and the variations of operational conditions could all have caused the controversy.

It is confirmed that alkali catalysts, especially KOH and $K_2CO_3$, assist in the scission of C–C bonds and speed up the water–gas shift reaction, resulting in the production of $H_2$ and $CO_2$ rather than CO (Kruse, 2008; Xu *et al.*, 2009). On the other hand, $Na_2CO_3$ causes the decarboxylation of formic acid (HCOOH), an intermediate component of the water–gas shift reaction, enhancing the $H_2$ yields (Kruse *et al.*, 2005; Xu *et al.*, 2009). Furthermore, $Na_2CO_3$ precipitates particles in SCW, providing a larger surface area for many catalytic reactions. In comparison, NaOH enhances $CH_4$ yields by promoting the methanation reaction even at near-critical conditions (< 374$^o$C). Sodium acetate ($CH_3COONa$) is generated as an intermediate product of biomass hydrolysis by NaOH, which breaks down further to $CH_4$ and sodium bicarbonate ($NaHCO_3$) (Onwudili & Williams, 2009). Homogeneous catalysts are advantageous due to their reduced cost, high and efficient conversion rates, and versatility in continuous and batch gasification systems (Juan *et al.*, 2011). Even though homogeneous catalysts are often more active than heterogeneous catalysts, they can cause serious operational challenges in some situations, such as reactor plugging and corrosion problems caused by the low solubility of alkali salt in SCW (Anikeev & Fan, 2014; Kang *et al.*, 2017). Furthermore, it is challenging to recycle and reuse homogeneous catalysts after SCW gasification application, and it only offers a few options for reuse with additional expenses (Okolie *et al.*, 2019).

### 2.5.2 Heterogeneous Catalyst

Heterogeneous catalysts such as metal oxides and transition metal offer high selectivity, catalytic activity, and recyclability and are more effective for SCW gasification of biomass (Reddy *et al.*, 2014; Rodriguez & Kruse, 2018). Researchers conducted intensive research in screening the active metal and supporting materials to identify a catalyst with high $H_2$ selectivity, hydrothermal stability, and tolerance to coke formation (Wu & Williams, 2009). Nickel-based catalysts are commonly used in SCW gasification due to their low-cost relative to other noble metal catalysts (Hossain *et al.*, 2017; Kang *et al.*, 2017; Li *et al.*, 2018). Catalysts based on Cu, Co, and Ru have also been used (Byrd *et al.*, 2011; Zhang *et al.*, 2011). Elliott et *al.* (1993) used a batch reactor to test different Ni and Cr catalysts for biomass conversion in a hot water system at 350$^o$C and 17–23 MPa. It is found that Ni has excellent catalytic activity,

and the main product of gas steam is $H_2$ and $CH_4$, whereas Cr showed little activity. Resende and Savage (2010) reported that Ni and Cu loadings of 5 wt% could maximize $H_2$ yields, with nickel providing the highest $H_2$ yields at 1.0 wt% loading for lignin gasification in SCW. It is further observed that the presence of metals adds no significant effect on $CH_4$ yields. Sato *et al.* (2003) gasified alkylphenols as lignin model compounds in SCW at 400°C in the presence of assisted noble metal catalysts. The catalyst's activity was in the following sequence: Ru/γ-alumina > Ru/carbon, Rh/carbon > Pt/γ-alumina, Pd/carbon, and Pd/γ-alumina. The key gas composition was mainly methane, carbon dioxide, and hydrogen. Park and Tomiyasu (2003) used stoichiometrically insufficient amounts of $RuO_2$ in SCW to achieve nearly complete gasification of organic compounds, resulting in $CH_4$, $CO_2$, and $H_2$. Jin *et al.* (2014) prepared various Raney-Ni doping elements for $H_2$ production through SCW gasification of a peanut shell. Raney-Ni doping with Fe produces the most hydrogen as compared to Mo and Cr doping.

The noble metal Ru has excellent catalytic activity in the biomass SCW gasification process, has a high selectivity to $H_2$, and is more resistant and less susceptible to hydrothermal sintering than Ni catalysts. However, the expense of industrial implementation is exceptionally high (Huang *et al.*, 2019). Although nickel can result in higher total gas yields and improved carbon gasification performance, $H_2$ production is limited due to its utilisation in hydrogenation reactions. Furthermore, hydrothermal instability, rapid deactivation, toxicity, and sintering caused by the presence of sulphur, nitrogen, coke, or any other heteroatom-containing compound continue to be significant issues in the development of Ni-based catalysts (Azadi *et al.*, 2013; Zhang *et al.*, 2012).

Elements in the eighth group are thought to have high chemical absorption for reactants, allowing them to catalyze SCW gasification reactions at low temperatures (Jin *et al.*, 2014). Iron is one of the elements in the eighth group that can increase the catalytic activity of SCW gasification, but it has received less attention than other elements in its group. The potential and role of iron as a catalyst to improve SCW gasification is discussed in detail in sections 2.6 - 2.8.

## 2.6 Iron-based Catalyst

Iron is the second-most common element in the Earth's crust, and it occurs in various oxidative states. The most common oxidative states found in nature are ferric $Fe^{3+}$ and ferrous $Fe^{2+}$. For several decades, iron and iron oxides in granule or nanoparticle form have been used as industrial catalysts for various reactions, including tar conversion in gasification, Fischer–Tropsch synthesis, and the Haber-Bosch method for ammonia synthesis (Karim *et al.*, 2016).

Iron is a low-cost, non-toxic substitute for other metals such as nickel, gold, and copper, often used as catalysts in gasification. Mineral-ore-based catalysts are naturally occurring homogeneous rocks with a definite but not permanently fixed chemical composition and an ordered atomic arrangement. Mineral rock catalysts can be used directly in a gasification system or in conjunction with physical treatment. Mineral rocks like dolomite, olivine, and limestone have been used as primary gasification catalysts (Boot-Handford *et al.*, 2018). These rocks benefit from being used as a bed guard to protect expensive metals from tar or other impurities such as $H_2S$ deactivation (Abu-El-Rub *et al.*, 2004; Shahbaz *et al.*, 2017).

### 2.6.1 Dolomite

Dolomite is a calcium magnesium ore with the general formula $CaMg(CO_3)_2$. This catalyst is abundant and is regarded as the most popular and least expensive naturally occurring catalyst for tar conversion (Abu-El-Rub *et al.*, 2004). Dolomite also contains trace minerals such as potassium and iron oxides, which are catalytically active in gasification reactions such as steam/dry-reforming and steam/thermal-cracking (Aznar *et al.*, 1998). Jin *et al.* (2014) investigated the production of $H_2$ from SCW gasification using olivine and dolomite catalysts. The findings show that olivine and dolomite have a catalytic impact on biomass gasification, raising hydrogen yield by 46.2 and 37.8%, respectively, compared to the no-catalytic reaction condition. Gusta *et al.* (2009) investigated the catalytic conversion and overall gas yield of various dolomite catalysts and discovered that at 750$^{o}$C, tar conversion to gaseous products increased by an average of 21% over the non-catalytic reaction.

Similarly, it was discovered that traces of iron in dolomite affected tar conversion and water gas shift reaction, with optimum tar conversion of 66% for dolomite with higher iron concentration (0.9 wt%). Furthermore, the catalyst was found to be stable after 15 hrs of cyclic use at 800$^{o}$C. Orío *et al.* (1997) investigated whether the origin of four different calcined dolomites influences their behaviour for tar removal in a hot flue gas coming from a biomass gasifier. The highest activity was observed in dolomite with the highest content of iron, mostly $Fe_2O_3$. Boot-Handford *et al.* (2018) investigated the feasibility of using calcined limestone and dolomite as a primary catalyst for downdraft gasification of RH. The catalytic effect of the calcined limestone contained bed was visible at 700°C and 800°C by 25% and 43% tar conversion. Similarly, at 700°C and 800°C, calcined dolomite was slightly more effective than calcined limestone, increasing tar conversion by 35% and 47%, respectively. The higher catalytic cracking of Dolomite is attributed to its larger surface area. The BET analysis revealed that calcined dolomite had a significantly larger surface area than calcined limestone across all temperature

ranges investigated. When the temperature was raised to 900°C on the dolomite-containing bed, approximately 98% of the primary tar was converted to permanent gases, demonstrating the effective catalytic action of dolomite for gasification. However, as the temperature rose, the particles fractured and fragmented. Dolomite particle fragmentation was more severe than limestone particle fragmentation. It is worth noting that high-temperature gasification reactions may favour the polymerization of primary tar to more complex structures and aerosols that are difficult to convert or detect. Furthermore, dolomite has been reported to be soft and, as a result, easily eroded in high-temperature gasification (Abu-El-Rub *et al.*, 2004). Furthermore, dolomite is highly sensitive to chlorine, which means that it may not function properly if the biomass contains traces of chlorine. Dolomite is more likely to react with chlorine at higher temperatures, producing calcium chloride ($CaCl_2$), which blocks the catalyst pore matrix and thus becomes utterly inactive in catalytic activity (Nordgreen *et al.*, 2012).

### 2.6.2 Olivine

Olivine ($FeMg(SiO4)_2$) has slightly lower catalytic activity in tar conversion than dolomite but is more resistant to wear and tear (Rapagnà *et al.*, 2000). The magnesite (MgO) and iron oxide ($Fe_2O_3$) contents of olivine are primarily responsible for its catalytic activity for tar elimination, with the latter being significantly higher in olivine than in dolomite. Olivine's catalytic activity has been shown to increase with gasification time due to the formation of calcium oxide layers (Rapagnà *et al.*, 2018). Rauch *et al.* (2004) compared the performance of various olivine catalysts for biomass gasification and found that their activity is dependent on the concentration of iron oxide. Rapagnà *et al.* (2011) studied iron-olivine catalyst for tar conversion and found that when 10%Fe/olivine was fed in the gasifier at 800–830°C, the average gas yield rose by 40% and the $H_2$ yield by 88% while the tar yield decreased by 46%. Furthermore, naphthalene and toluene, which are difficult to crack/reform, were reduced by 48% and 59%, respectively. Kirnbauer *et al.* (2012) prepared and tested a Fe/olivine catalyst in bubbling fluidised beds at 850°C and discovered a 65% reduction in gravimetric tar compared to non-catalytic. Virginie *et al.* (2012) investigated the effect of Fe/olivine on the catalytic conversion of pinewood in dual fluidised bed gasification and discovered a catalytic conversion of 65% at 850ºC. They also reported that when using Fe/olivine, toluene conversion and hydrogen production were nearly three times higher than when using olive alone. These experimental findings confirm that iron-supported natural olivine can significantly increase olivine's catalytic activity. Due to its low cost compared to other metals such as nickel, iron impregnation could not raise the catalyst cost (Shen & Yoshikawa, 2013). Courson *et al.* (2000) reported contentious results showing almost

no activity (methane conversion around 1% and hydrogen yield close to zero) when olivine alone was used as a bed catalyst at 800$^{o}$C. Coke has been shown to significantly deactivate olivine, thereby blocking active sites and reducing surface area (Shen & Yoshikawa, 2013). Furthermore, at temperatures above 850$^{o}$C, they lose their catalytic nature (pore structure) and act as inert materials (Abu-El-Rub *et al.,* 2004). It should be noted that mineral-based catalysts perform slightly weaker due to rapid deactivation but with promising activity when accompanied by other active metals. These mineral rocks have been commonly used as catalyst supports rather than in-situ application in their natural state. Nevertheless, mineral-based catalysts are associated with difficulties in regeneration of the deactivated catalysts (Shen *et al.,* 2014).

### 2.6.3 Supported Iron Catalyst

Supported iron catalysts have gained interest in many researchers due to the ability to control the size of particles and loading and dispersion in catalyst support. Recent research has focused on the production of nanoparticle catalysts for various reactions. The nanoparticle catalysts increase the number of surface sites per unit weight of the metal, resulting in more active catalysts (Munnik *et al.,* 2015). Nano-iron-based catalysts have caught the interest of researchers due to their mechanical stability, environmental friendliness, high catalytic efficiency and low cost. Miccio *et al.* (2016) developed Fe/$Al_2O_3$ catalysts by wet impregnation and compared their activity to Ni/$Al_2O_3$ catalysts in a fluidized bed reactor, reporting comparable activity in tar conversion for both catalysts at 780$^{o}$C with tar concentrations of 8.4 g/$Nm^3$ and 8.0 g/$Nm^3$, respectively. When compared to Ni/$Al_2O_3$, Fe/$Al_2O_3$ was found to be less active in hydrocarbon reforming; this phenomenon is essential when biomass gasification is used to produce methane. During 100 minutes of continuous testing, their analysis revealed no activity loss for the developed catalysts. Guo *et al.* (2018) used impregnation and one-step pyrolysis to make Fe-RHC catalyst for tar removal in biomass pyrolysis/gasification. The ICP-MS measurements revealed an iron loading of 8.85 wt% in the catalyst support. The tar conversion efficiency differed with gasification temperature during testing with a biomass to catalyst ratio of 5:3 (g:g), with a maximum value of 92.6% at 800°C. Furthermore, the catalyst remained stable after three cycles of experimental runs, suggesting that it is stable in coke deposition. Uddin *et al.* (2008) produced an iron-based catalyst using $FeCl_3$ and $Fe(NO_3)_3$ as precursors, with the goal of complete tar destruction and a regenerable catalyst. Since the amount of biomass used in their research was too tiny (about 0.04 g) to obtain tar samples, the extracted producer gas analysis was used to understand the catalytic conversion better. For the

$FeCl_3$ catalyst, the total volatile matter gasified, which was called tar conversion, reached more than 90%.

Yu *et al.* (2006) produced a nano-iron catalyst supported coal char for a water-gas-shift-reaction in a fluidised bed reactor. At temperatures below 300ºC, the prepared catalyst was found to be very active. They concluded that the developed catalyst could effectively be used in gasification to perform the integrated role of hot gas and pollutant cleaning. David (2015) created a novel nanoparticle coal char-supported iron catalyst and compared its catalytic efficiency to ilmenite, native iron-containing mineral rock with well-dispersed iron oxide and titanium oxide. Ion-exchange with $Fe/Cl_3$ aqueous solution was used to create an iron char catalyst. The results showed that tar conversion of ilmenite catalyst was on average 70%, while Fe/coal-char conversion was between 82% and 95% at 800ºC and 850ºC, respectively. Furthermore, the char-supported iron catalyst remained stable for up to 60 minutes of operation, whereas the ilmenite catalyst exhibited high coke deposition. Some researchers have considered synthesising metallic iron with other metals to improve its stability and conversion efficiency. Ahmed *et al.* (2018) investigated the effect of iron on the promotion of monometallic Ni catalysts synthesised in zeolites. Ni-Fe/zeolite (0.71 wt% Fe) exhibited a preliminary conversion of 63%, stabilised at 60% before decreasing slightly. Alternatively, the initial conversion of Ni-Fe/zeolite (0.77 wt% Fe) was 72%, peaking at 74% after 60 minutes and then dropping and hovering around 72%. These results show that increasing the iron promotes the steam reforming reaction in the range of the molar ratio of Ni to Fe (Ni/Fe) $\leq 0.7$, which reduces the amount of tar and promoted the gasification yield. The effect of addition of iron on coke tolerance was also observed in comparison to monometallic Ni/zeolite. Furthermore, contrary to many other studies, Fe/zeolite activity was low under these experimental conditions.

## 2.7 Preparation and Characterization of Iron-supported Catalysts

### 2.7.1 Catalyst Preparation

Heterogeneous catalysis, which takes part in gas, liquid, or solid-phase reactions, have been at the core of many chemical reactions in industry. In general, during gasification, a gas mixture stream reacts on the surface of a solid catalyst, which is primarily supported by transition metals. Catalyst preparation is the process of developing a suitable catalyst composition and structure for the necessary reactions. Several methods for catalyst preparation have been widely published, including incipient wetness (Ahmed *et al.,* 2018; Miccio *et al.,* 2016; Shen *et al.,* 2014) and co-precipitation (Kumagai *et al.,* 2015; Liu *et al.,* 2012; Uddin *et al.,* 2008). The

incipient wetness method is a common and straightforward method that uses a pore filling technique and is suitable for low metal loadings. However, it is important to note that the intensive washing procedures utilized during synthesis to remove residual chlorine, sulphate, and nitrate result in contaminated wastewater. Similarly, the use of chloride- or sulphate-based precursors may result in the retention of traces of sulfur or chlorine on the catalyst surface (Guo *et al.,* 2018), which can poison the catalyst and cause it to deactivate quickly.

Traces of nitrogen can trigger a large concentration of $NH_3$ in the exhaust gas of a gasifier, resulting in an environmental violation (Asadullah, 2014). Furthermore, during combustion, $NH_3$ can be converted to NOx, which is also strictly prohibited (Sullivan *et al.,* 2002). On the other hand, traces of sulfur could frequently be converted into hydrogen sulfide and sulfur dioxide compounds, which have a high affinity to adsorb permanently on the active site of the catalyst (Visconti *et al.,* 2007). As a result, the active sites acquired by the sulfuric compound become dormant and wholly deactivated. Chlorine traces, on the other hand, will react with trace metals in the catalyst to form inorganic salts that block the active site and deactivate the catalyst completely. Chlorine can also be converted to HCL, which can corrode downstream equipment (Asadullah, 2014). Because of the nature of iron behaviours, it is anticipated that the iron supported catalyst could enhance gasification to a significant level at a low temperature ($\leq 800^{o}C$). Meanwhile, the iron precursors used in many studies deter the non-toxic characteristics of iron and therefore need to be avoided (Baerns, 2013). As a result, further research into appropriate iron precursor is critical to utilise its abundance, low toxicity, and valuable catalytic properties.

### 2.7.2 Catalyst Characterisation

The interaction of metals and catalyst support is critical to the effectiveness of a catalyst. The catalyst support not only facilitates metal dispersion but also enhances the catalytic reaction. To avoid reducing the catalyst's effectiveness, the catalyst precursor should not cause contamination or react with the catalyst support. It has been observed that the precursor used for iron-based catalyst synthesis can leave traces of chlorine, sulphate, or nitrate at the formed catalyst, potentially reducing the catalyst's effectiveness. Guo *et al.* (2018) investigated the catalytic cracking of biomass pyrolysis tar over char-supported iron catalysts prepared with $FeCl_3.6H_2O$ as a precursor. The surface of the catalyst support is abrasive, with a corrugated outer epidermis, as shown in Fig. 10a. The energy-dispersive x-ray (EDX) in Fig. 10b demonstrates the existence of inorganics on the catalyst's surface (mainly potassium, oxygen, and silicon). The obtained catalyst showed a destroyed globular structure and the creation of

several cavities after high-temperature pyrolysis of iron impregnated catalyst (Fig. 10g). The EDX (Fig. 10h) shows the enhanced Fe and Cl characteristic peaks, indicating the interaction of the precursor with the catalyst support. Specifically, the chlorine residue is caused by the type of precursor used. Nonetheless, the textural properties suggest that Cl can be used as an activating agent for the porous catalyst support, potentially increasing surface area.

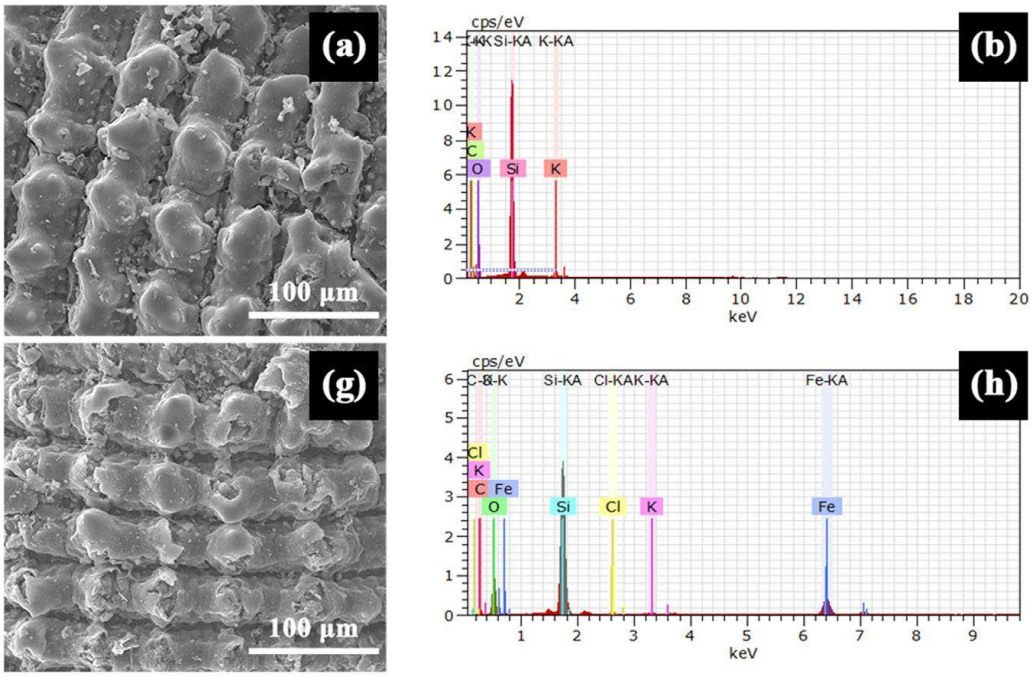


**Figure 10: SEM-EDX images of the fresh catalyst: (a) catalyst support-SEM; (b) catalyst support-EDX; (g) Fe-supported-SEM; (h) Fe-supported-EDX (Guo *et al*., 2018) copyright (2018), with permission from Elsevier**

Zhang *et al.* (2015) investigated $CO_2$ gasification of a sub-bituminous Wyodak coal in a fixed bed laboratory gasifier at atmospheric pressure using $FeCO_3$ as an in-situ catalyst precursor. The $FeCO_3$ and coal particles were mixed using the incipient wetness impregnation method. The scanning electron microscope (SEM) image (Fig. 11a) of a 3 wt% Fe/char sample and dispersion of iron clusters after 5 minutes of gasification at 900°C shows that the catalyst was not distributed homogeneously among the coal particles but agglomerated in certain char particles. The agglomeration of iron resulted in an unequal distribution of the gasification rate in char samples and a low efficiency of the added catalyst. Higher magnification (scale bar of 5 µm) in Fig. 11b shows that the coal particle with a high concentration of iron was significantly eroded, indicating that iron had a significant catalytic effect on char gasification. Furthermore, much smaller (0.1 µm diameter) lighter coloured spheroids appeared across the particle surface, implying that the active sites formed by iron promoted the consumption of adjacent carbon.

$FeCO_3$ has demonstrated excellent catalytic efficiency, and it exist abundantly; however, further research into iron distribution improvement is required.

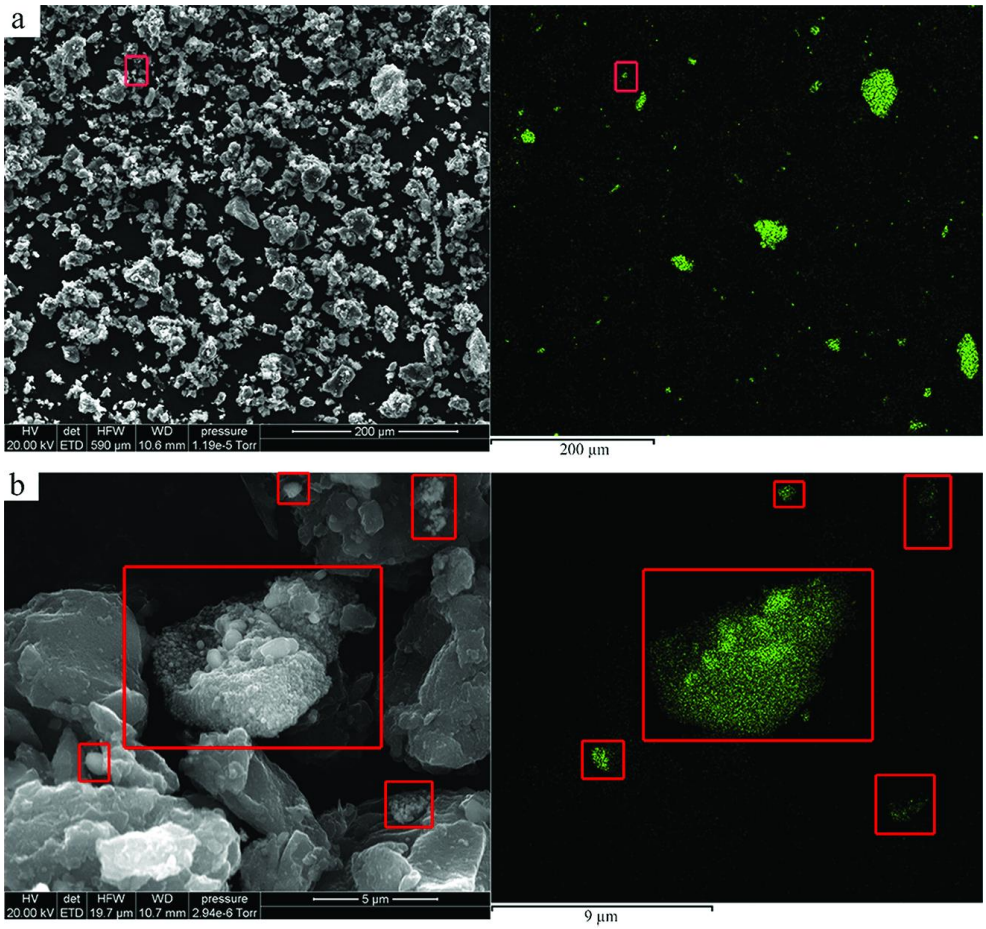


**Figure 11: Figure 5: SEM image of the char sample with 3 wt% Fe after 5 min gasification at 900°C and the corresponding distribution of iron atom clusters from EDS: (a) 200 µm scale bar and (b) 5 µm scale bar for the marked area in (a) (Zhang *et al.*, 2015), copyright (2015), with permission from Elsevier**

Huang *et al.* (2012) investigated biomass gasification in a fluidized bed reactor using a Fe/CaO catalyst at 730ºC. The catalyst was produced by impregnating CaO with a precursor of iron nitrate ($Fe(NO_3)_3H_2O$). The results show that Fe reacted with CaO to form a $Ca_2Fe_2O_5$ phase and that as the Fe content increased, this phase gradually became the catalyst's main reactive phase while CaO decreased. The $Ca_2Fe_2O_5$ particles decomposed polyaromatic tar compounds as the primary reactive sites; however, char gasification was ineffective at the studied conditions. The Fe/CaO ratio of 15% appears to be adequate for polyaromatic tar decomposition and increased $H_2$ production by 24.7%, implying that Fe and CaO can be used as a low-cost catalyst to enhance gasification. Guo *et al.* (2018) investigated the thermal stability of Fe-supported rice husk char (RHC) at 600 to 800°C and compared it to the thermal stability of Cu

and K. The mass fraction of their residues in the range of 93.3–95.7% was observed for char and char-supported catalysts, with Fe-RHC exhibiting the highest thermal stability. The thermal stability of the catalyst was further demonstrated by a 1.5% mass loss of the catalyst after tar reforming, confirming the iron-based catalyst's stability for multiple circles activity.

## 2.8 The Catalytic Reactions of Iron Catalyst

### 2.8.1 Nature and Activity of Iron

The use of an iron-based catalyst in the gasification process is motivated by its lower toxicity and abundance and its water-gas-shift action. Owing to variations in its oxidation states, iron is known to occur in numerous forms, including metallic iron, various iron oxides (magnetite ($Fe_3O_4$), hematite ($Fe_2O_3$), and wustite (FeO)), and iron carbides, which also exist in multiple forms. The formation of these different iron phases is influenced by various factors, including catalyst preparation methods such as supported or unsupported, reduced or unreduced, temperature, particle size, and precursors. Nonetheless, the intrinsic function of each phase in catalytic gasification reactions remains debatable. The debate surrounding iron activity arises from the fact that its activity phase varies during the reaction due to changes in temperature, time of exposure, the structure of the reactor, feed conditions, and product yield. According to an earlier study by Blanchard *et al.* (1982), magnetite is the active phase of an iron catalyst in a Fisher-Tropsch-synthesis, specifically in a water-gas-shift-reaction (WGS). Ohtsuka and Asami (1991) and Asami and Ohtsuka (1993) found that magnetite is an active and stable phase of all oxides in the experiment, regardless of the catalyst preparation process. Their claim was a follow-up to Dictor and Bell (1986) suggestion that the active site is a mixture of carbides and a trace of metallic iron.

In the early 1990s, Butt (1990) compared reduced, unreduced, and carbided iron catalysts and proposed that magnetite could be an active phase for synthesis even in the absence of a carbide phase. They proposed two compelling models for the activity of the iron-based catalyst on WGS: the carbide model proposed that the activity is due to active sites on the surface of the bulk carbide. On the other hand, the competition model suggests that a surface iron atom causes the activity and that there is a competition of CO molecules between bulk carbidization and hydrocarbon. According to the findings published by Jung and Thomson (1992), metallic iron is not initially active but rapidly carbidizes, causing the catalytic activity to steadily increase and then decline as it completely transforms to carbide. This assertion implies that the iron-based catalyst may favour the Boudouard backward reaction of carbon formation. They

concluded that, while catalytic activity increases primarily with carbide formation, its deactivation was observed to correlate with iron carbide phase formation, with smaller size being more stable to deactivation. Tamhankar *et al.* (1985) investigated the catalytic behaviour of reduced and unreduced iron oxide catalysts in benzene conversion. Their findings revealed nearly 100% benzene conversions on both unreduced iron oxide in the presence of hydrogen and pre-reduced iron oxide in the absence of hydrogen. Mössbauer's study of the surface of the unreduced catalyst showed that the iron oxide was first reduced to its metallic state by hydrogen before reacting with benzene, confirming the activity of metallic iron. Nordgreen *et al.* (2012) investigated iron granules as a tar reduction catalyst in biomass gasification. They investigated the impact of metallic iron and iron oxide (wustite) in tar cracking at two different temperatures, 800 and 850$^{o}$C. In comparison to iron oxide, the findings showed that metallic iron has a higher tar decomposing capability. However, when the catalyst was held oxidised, multiple iron phases were observed (Fig. 12). The existence of these phases can be demonstrated by looking at the Ellingham lines of iron and the Boudouard reaction (Fig. 13), which shows that the presence of a reducing agent (CO) can determine the existence of different iron phases. It is worth noting that the limited window of opportunity for iron to exist in its metallic state will make it difficult to exist.

Matsuoka *et al.* (2006) clarified the presence of various iron phases as being correlated with redox reactions rather than coke reforming during $H_2$ formation at higher temperatures. In this case, CO produced during steam reforming was used to reduce iron oxide before it was combined with steam to form $H_2$. An X-ray diffraction (XRD) analysis of the Fe-impregnated alumina before and after steam reforming was performed to evaluate the form of the iron oxide present on the catalyst surface. In the raw sample, the analysis discovered firm γ-alumina peaks as well as hematite ($Fe_2O_3$) peaks (before the steam reforming). Following the steam reforming reactions, the hematite peak disappeared, and small magnetite ($Fe_3O_4$) peak was observed. After the steam reforming, no distinct peaks for wustite (FeO) or metallic iron (Fe) were detected. The peaks for γ-alumina were quite sharp, and the positions of the peaks for wustite and metallic iron were close to the alumina peaks. The study concluded that magnetite was a stable iron-containing species following the steam reforming reaction but did not suggest whether magnetite was further reduced.

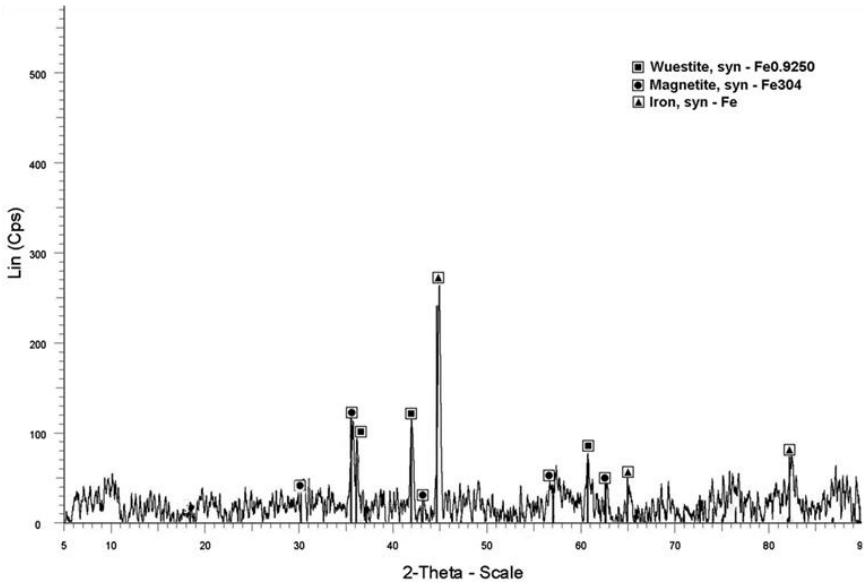


**Figure 12: XRD measurement of the iron catalyst after applied in the reactor at gasification temperature 850ºC (Nordgreen *et al.*, 2012), copyright (2012) with permission from Elsevier**

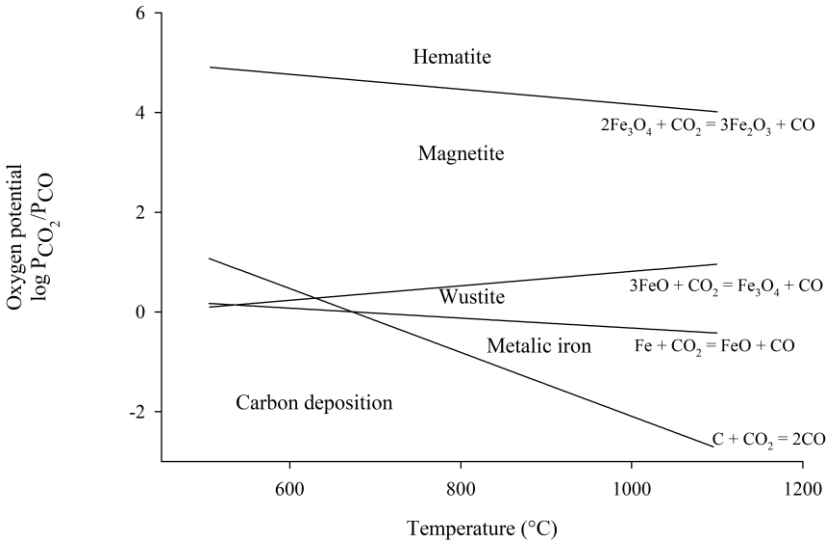


**Figure 13: The Ellingham lines of different iron phases (oxygen potential versus time) (Nordgreen *et al.*, 2012) copyright (2012), with permission from Elsevier**

Miccio *et al.* (2016) recently investigated the behaviour of various iron oxide phases. The temperature-programmed reduction (TPR) profile of fresh iron catalysts shown in Fig. 14 shows two peaks at 460°C and 700°C, which correspond to hematite to magnetite and magnetite to metallic iron reductions, respectively. Jozwiak *et al.* (2007) explained a similar phenomenon. They did, however, observe two overlapping peaks in the high-temperature regions of TPR, indicating two-step magnetite reduction: From magnetite to wustite to metallic iron, as shown by Equation 10. Furthermore, Ahmed *et al.* (2018) demonstrated that at 700°C, almost all iron

species in their prepared catalyst were reduced to a metallic state. According to the studies reviewed, the active catalytic phase can be: Fe > $Fe_2O_3$ > $Fe_3O_4$ > FeO.

$$Fe_3O_4 \longrightarrow 6FeO \longrightarrow 6Fe \quad (10)$$

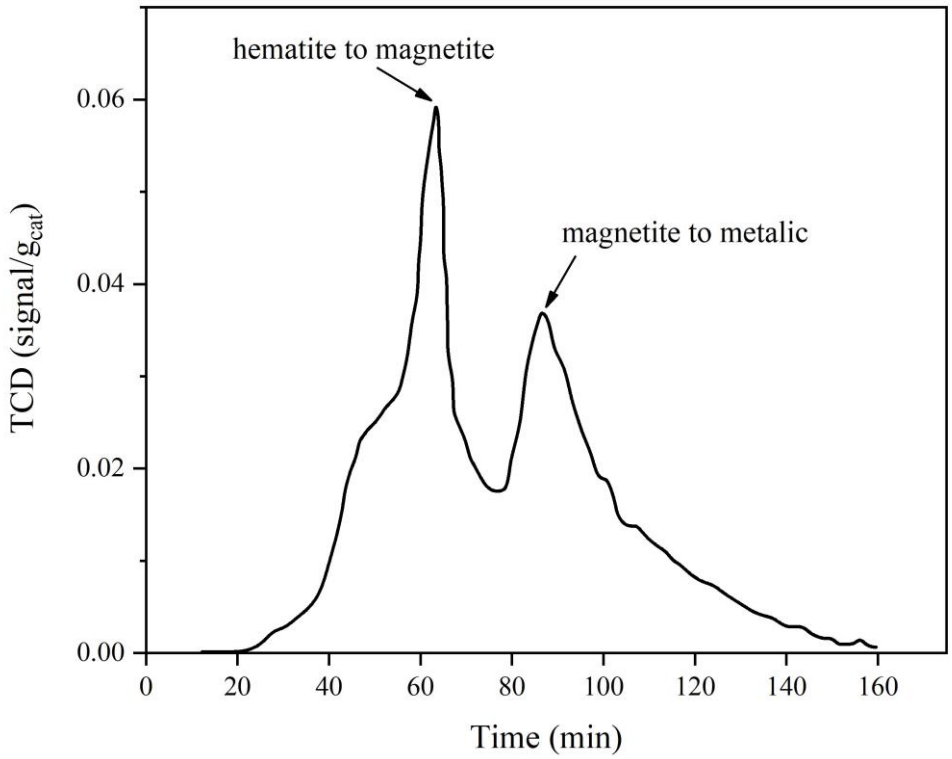


**Figure 14: Temperature-programmed reduction analysis of the fresh $Fe/Al_2O_3$ catalyst (Miccio *et al.*, 2016), copyright (2016) with permission from Elsevier**

In general, metallic iron is thought to be active in breaking C-C and C-H bonds, implying catalytic activity towards aromatic hydrocarbon compounds (Virginie *et al.*, 2010), though its existence window is very narrow. However, in an oxidation/reduction environment, $Fe_3O_4$ and $Fe_2O_3$ are the most stable existing phases, whereas FeO is thermodynamically unstable (Fig. 13). As a result, understanding the intrinsic role and oxidation/reduction behaviour of metallic iron and iron oxide in catalysis is necessary. The influence of different particle sizes of iron particles, ranging from bulk to different nano-sized particles, has been reported less frequently in gasification catalysis in general. According to the reviewed literature, as summarized graphically in Fig. 15, the presence of various compounds (reducing and oxidising agents) in gasification reactors can affect the catalyst's existence, nature, and performance, highlighting the importance of iron redox behaviour studies.

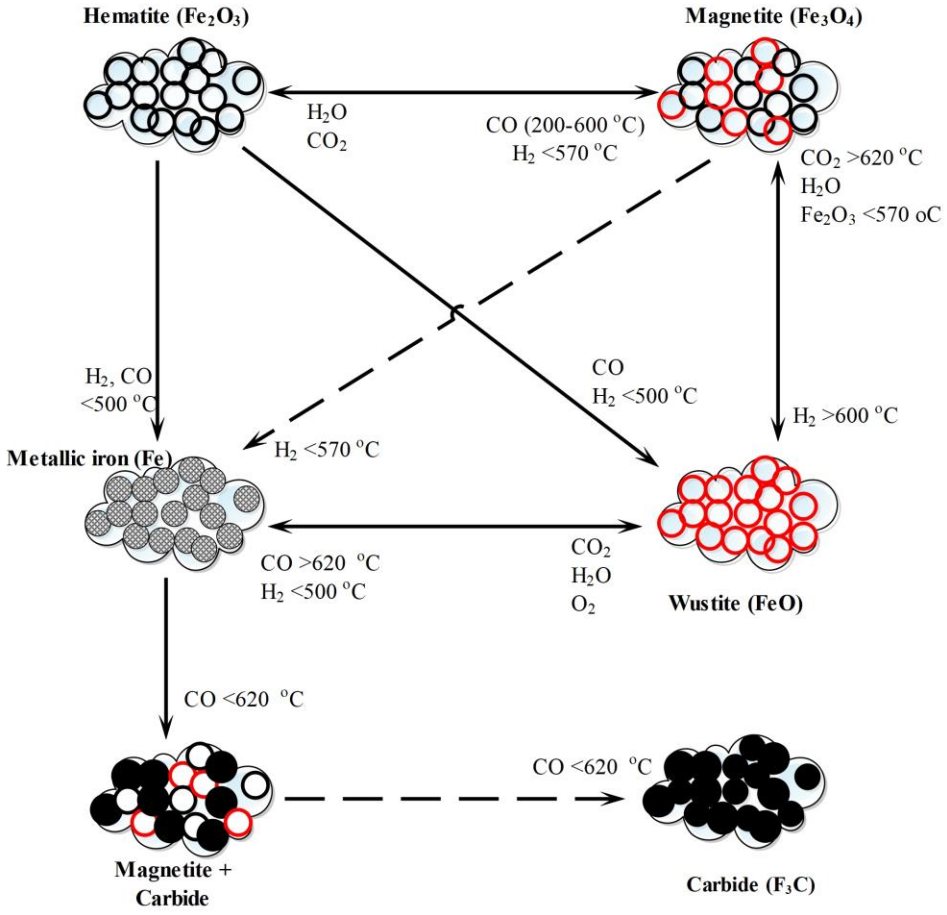


**Figure 15: A cartoon representation of the formation of metallic and iron oxides under various oxidising and reducing agents and temperatures**

### 2.8.2 Redox Characteristics of Iron

Karim *et al.* (2016) investigated the size-dependent redox behaviour of iron nanoparticles and bulk iron in forming various oxide phases. Compared to iron in nanoparticle form, the formation rate of oxides in bulk iron was significantly different. The FeO is formed as soon as oxidation begins; however, the process is transient and quickly converts to phases with higher oxidation states. For nanoparticles and bulk iron, there was a significant difference in conversion from FeO to $Fe_3O_4$ or $Fe_2O_3$. As shown in Fig. 16a, as bulk iron oxidation starts, the metallic iron concentration drops, and FeO (wustite) forms on the surface, then oxidised to $Fe_2O_3$ and $Fe_3O_4$. Bulk iron has a much more substantial build-up of $Fe_3O_4$ than nanoparticles, and it remains the dominant species in the oxidation process. The oxidation behaviours of nanoparticles are noticeably different, with FeO rapidly forming on the surface during the initial stage of oxidation and then oxidising almost entirely to $Fe_2O_3$. The concentration of $Fe_2O_3$ continues to increase with a decrease in metallic iron concentration, and at the later stage, the evolution of $Fe_3O_4$ is observed. As the growth of $Fe_2O_3$ saturates, the concentration of $Fe_3O_4$ increases with the

decrease in FeO and metallic iron. As nanoparticle size decreases (probably less than 10 nm), the transition between FeO and $Fe_2O_3$ is stated to occur more quickly (Fig. 16b-d).

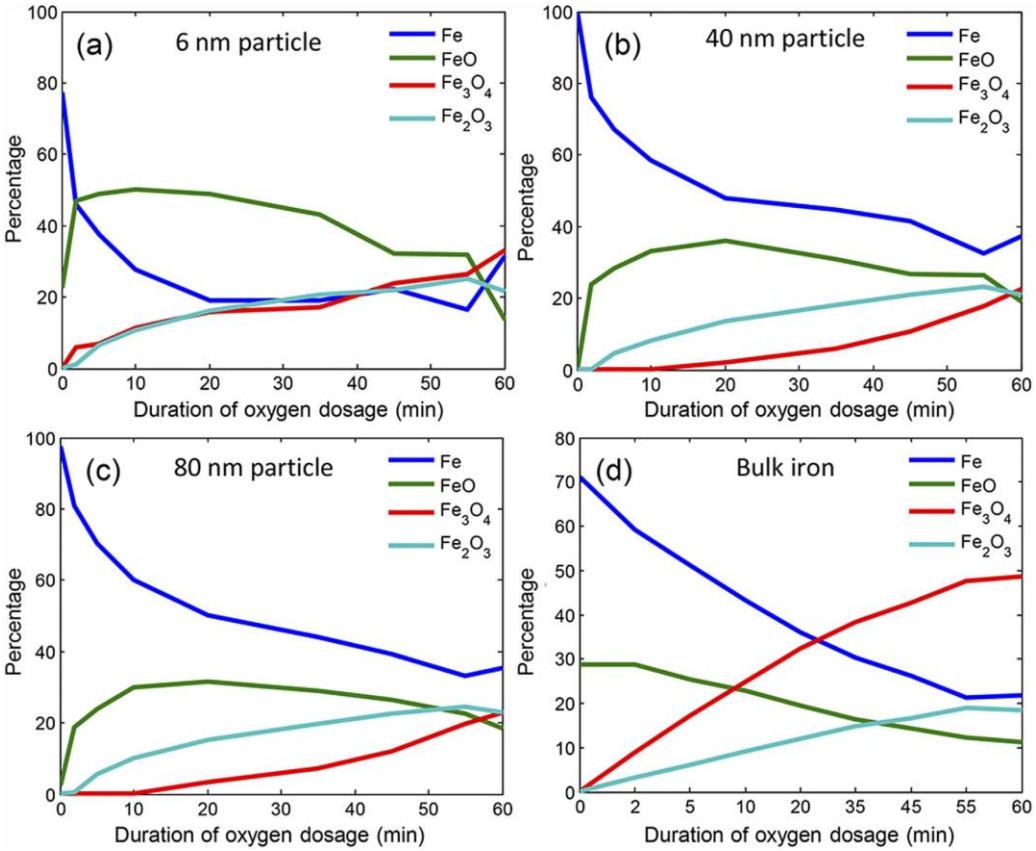


**Figure 16: Transition of Fe, FeO, $Fe_2O_3$ and $Fe_3O_4$ during oxidation over oxygen dosage time (Karim *et al.*, 2016), copyright (2016) with permission under a Creative Commons Attribution 4.0 International License**

The presence of CO and $H_2$ in the syngas, according to the studies, could facilitate the reduction of iron oxides during reactions. Iron oxides, such as $Fe_2O_3$, $Fe_3O_4$, and FeO, vary in oxidation and reduction. The form of the reduction process, on the other hand, is highly complex and can vary depending on the physicochemical properties of iron oxide or the conditions of reducing agents (temperature and partial pressure) (Jozwiak *et al.*, 2007). The iron oxide reduction pathway can be radically different. However, the three-step reduction of hematite, magnetite, and wustite to metallic iron is often proposed. Khader *et al.* (1991) investigated the kinetic reduction of $Fe_2O_3$ in the presence of hydrogen. At 300–400$^oC$, $Fe_2O_3$ reduces, thus forming an oxygen vacancy, which serves as an anion dopant for the remaining $Fe_2O_3$ (Equation 11). Later on, the $Fe_2O_3$ is wholly reduced to FeO, a thermodynamically unstable compound that easily re-oxidizes to $Fe_3O_4$ when exposed to air (Equation 12). It was also stated that Fe(II) could only exist in the subsurface region beneath the $Fe_2O_3$ lattice. Figure 17a depicts the X-ray diffraction pattern of $Fe_2O_3$ before reduction, while Fig. 17b depicts the reduced product after exposure to

air (reduction was performed at 400°C for 1 hr). The graph shows that the $Fe_2O_3$ peak (at 2θ = 33.2°) completely disappears in the pattern of the reduced sample. On the other hand, the diffraction pattern in Fig. 10(b) is identical to the pattern of $Fe_3O_4$, indicating that some of the FeO have been oxidised back to $Fe_2O_3$. According to Equation 13, exposing $Fe_3O_4$ to $H_2$ for a more extended time could reduce it to metallic iron (Fe). In theory, the metallic iron formation described by Equation 13 can be described by combining the two subsequent steps, Equations 14 and 15.

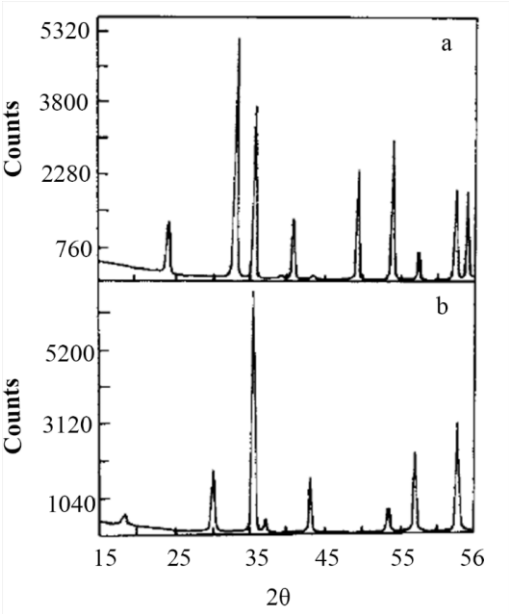


**Figure 17: XRD patterns of (a) $Fe_2O_3$ before reduction (b) reduction product after exposed to air (Khader *et al.*, 1991), copyright (1991) with permission from Elsevier**

$$3Fe_2O_3 + H_2 \longrightarrow 2FeO[V_a^-] + H_2O \quad (11)$$

$$FeO[V_a^-] + Fe_2O_3 \longrightarrow Fe_3O_4[V_a^-] \quad (12)$$

Where $V_a^-$ means oxygen vacancy

$$Fe_3O_4 + 4H_2 \longrightarrow Fe + 4H_2O \quad (13)$$

$$2(Fe_3O_4 + H_2 \longrightarrow FeO + H_2O) \quad (14)$$

$$6(FeO + H_2 \longrightarrow Fe + H_2O) \quad (15)$$

The temperature of 570°C is the lowest limit for the thermodynamic stability of FeO, according to Jozwiak *et al.* (2007). When the FeO disproportionation reaction temperature falls below this threshold:

$4FeO \longrightarrow Fe_3O_4 + Fe$ is shifted toward products.

When the temperature rises above this threshold:

$Fe_3O_4 + Fe \longrightarrow 4FeO$ dominates.

The reducibility of FeO was observed at temperatures up to 620°C in the presence of CO. The main unreduced wustite phase was dominated by metallic iron in an X-ray powder diffraction (XRD) study. The TG–DTA–MS measurements revealed that CO reduction of hematite occurs in the temperature range 200–600°C and is accompanied by a highly exothermic process of carbon deposit formation on the surface of the reduced sample, Equation 16 (Boudouard reaction). At temperatures above 600°C and a high concentration of CO in the gas stream, the formation of iron carbide ($Fe_3C$) may occur, reducing the effectiveness of the catalyst.

$$2CO \longrightarrow CO_2 + C \tag{16}$$

The carbon deposit appears to be auto-catalyzed by metallic iron formed in the final step of hematite reduction, which is heavily influenced by CO concentration. A high-temperature operation is required to minimise carbon deposition caused by the Boudouard reaction; otherwise, the material will lose its mechanical stability (Lorente *et al.*, 2011). According to the reviewed studies, bulk iron (granules) may be a less active catalyst material because of the high concentration of $Fe_3O_4$, which is less active in tar cracking and promotes carbon formation and deposition. Shroff *et al.* (1995) and Galvis *et al.* (2012) previously claimed that bulk irons are mechanically unstable when reacting at high temperatures, favouring the Boudouard backward reaction, which results in carbon deposition. Therefore, as mentioned in section 2.6.3, nano-sized iron particles could be the best candidate material for catalyst in terms of mechanical stability, environmental friendliness, and efficiency

# CHAPTER THREE

# MATERIALS AND METHODS

## 3.1 Materials

Five different RH samples from 4-agro ecological zones in Tanzania were collected from small rice processing plants. The type of rice husks was selected based on the popularity to the farmers for cultivation in respective regions and availability from the local rice mills. In this thesis, samples were named as Dodoma (agro-ecological zone: semi-arid lands, paddy name: *Super Zambia*, sample collected at Dodoma district), Arusha (agro-ecological zone: Northern highland, paddy name: *Magugu*, sample collected at Arumeru Arusha), Iringa (agro-ecological zone: Semi-arid lands, paddy name: *Saro-5*, sample collected at Iringa town), Shinyanga (agro-ecological zone: Semi-arid lands, rice name: *Super*, sample collected at Kahama town) and Morogoro (agro-ecological zone: Plateaux, paddy name: *Mbawa mbili*, sample collected at Morogoro town). Other geographical characteristics for the five regions are shown in Appendices 2 and 3. The dolomite and limestone mineral rocks were collected from Dar es Salaam and Tanga region, respectively. The rice husk samples were dried at 105°C overnight in the oven and stored in airtight plastic bags for further analysis. All the chemicals used in this study were bought from Sigma Aldrich and were of analytical grade. The chemicals used include iron (III) ammonium citrate (18-20% Fe basis), acetone (>99% purity), n-hexane (>99% purity), anhydrous sodium sulphate (>99% purity), and anhydrous calcium chloride (> 97% purity).

## 3.2 Characterization of Rice Husk

### 3.2.1 Bulk Density and Moisture Content

Bulk densities of the different varieties of RH were determined according to the ASTM standard test procedure for the bulk density of densified particulate biomass fuels E873-83 (American Society for Testing and Materials [ASTM], 2013). In brief, an empty cylindrical container of 500 mL was weighed within 0.1 mg using a computerized analytical balance of the type Ohaus Explorer (Ohaus, New Jersey, USA). The RH sample (as received) was filled in a container by pouring from a height approximately 610 mm above the top edge of the container. Then the container was carefully dropped to a non-resilient surface five times from a height of 150 mm to allow for setting. Additional samples were added to fill the container, and the excess was struck off with the top edge. Then the total weight of the container and sample was recorded to within 0.1g. The bulk density was then determined using Equation 17.

$$bulk\ density, {}^{g}/_{cm^3} = \frac{W_s - W_c}{V_c} \quad (17)$$

Where: $W_c$ is the weight of an empty container, $W_s$ is the weight of container and sample, and $V_c$ is the volume of the container

The moisture content was determined by following the standard test method for moisture analysis of particulate wood fuels (ASTM E871-82) (ASTM, 2013). In short, the crucible was cleaned and fired in a muffle furnace (ColeParmer Instrument Co) at 600ºC for 1 hr and then cooled in a desiccator to room temperature. Then the crucible was placed in the oven for 30 minutes at 103 ± 1ºC then cooled in a desiccator to room temperature, and then weighed to the nearest 0.1mg ($W_c$). A minimum of 1 g of sample was placed in the crucible, and the total weight of the crucible and sample was recorded in nearest 0.1 mg ($W_i$). Then the sample and crucible were placed in the oven for 16 hours at 103 ± 1ºC and then cooled to room temperature in a desiccator. After cooling to room temperature, the sample was immediately removed from the desiccator and weighed to the nearest 0.1 mg and recorded its weight. The sample and crucible were then returned to the oven at 103 ± 1ºC for 2 hrs, and the procedure above was repeated until the total weight change between weights varies less than 0.2%, and the final weight was recorded ($W_f$). The moisture content of the sample was determined by Equation 18.

$$Moisture\ content, \% = \frac{W_i - W_f}{W_i - W_c} x100 \quad (18)$$

Where: $W_c$ is the crucible weight (g), $W_i$ initial weight (g), and $W_f$ is the final weight (g).

### 3.2.2 Particle Size Distribution

The particle size distribution of a RH sample was determined by sieving following the ASTM C136/C136M-14 standard test procedure for sieve analysis of fine and coarse aggregates. In brief, the sample was dried to constant mass at a temperature of 105ºC. Standard U.S. sieves No. 10, 14, 18, 28, 35 and a bottom pan were chosen and nested in decreasing the size of the opening from top to bottom. The bottom pan collects everything that passes through the fifth sieve. Then a sample of 500 ± 0.1g was put on the top sieve, covered by a sieve lid and mounted in a mechanical sieve shaker. The shaker was operated for 30 minutes. The RH particles retained in each sieve was carefully removed and weighed at the nearest 0.1 mg, and the percentage of weight retained was calculated by dividing the weight retained in each sieve by the total sample mass (Equation 19). The per cent passing was then calculated by using Equation 20.

$$IPR, \% = \frac{Individual\ mass\ retained}{Total\ dry\ \ sample\ mass} x100 \quad (19)$$

$$CPP, \% = \text{PCPP} - \text{IPR} \quad (20)$$

Where: IPR is Individual Percent Retained, CPP is Calculated Percent Passing and PCPP is Previous Calculated Percent Passing

### 3.2.3 Proximate Analysis

The proximate analyses of a variety of RH samples were conducted according to the ASTM standard test method for chemical analysis of wood charcoal D1762-84 (ASTM, 213). In brief, empty crucibles and covers were firstly fired in the muffle furnace at 600°C for 2 hrs and then cooled to room temperature in a desiccator. The sample of RH was air-dried, then rapidly pulverized in a grain grinding mill and sieved to pass a sieve of 850 µm. The muffle furnace was heated to 750°C, and the previously fired porcelain crucibles and covers were placed in the furnace for 10 minutes and then cooled in the desiccator for 1 hr. Then the crucibles were weighed and added approximately 1 g of the grounded sample weighed to the nearest 0.1 mg. The samples were placed for 2 hrs in the oven at 105°C, then dried in a desiccator for 1 hr before being weighed. When the decrease in weight of consecutive weighings is 0.0005 g or less, the samples were considered oven dry. Then the muffle furnace was heated to 950 ± 5°C, and the crucible with lids in place and containing the sample was preheated as follows: With the furnace door open, for 2 minutes on the outer ledge of the furnace (300°C) and then for 3 minutes on the edge of the furnace (500°C). Then the samples were moved to the rear of the furnace for 6 minutes with the muffle door closed. Finally, the samples were cooled in a desiccator for one hour and weighed. Then the crucibles were uncovered and placed together with lids in the furnace at 750°C for 6 hrs, and then the residuals cooled with its lids in place in a desiccator for one hour and weighed. The burning of the sample was repeated until a subsequent 1-hr period of heating results in a loss of less than 0.0005 g. The volatile matter was calculated using Equation 21, while the per cent ash in the samples was calculated by Equation 22. The percentage content of fixed carbon was calculated by difference, as shown in Equation 23.

$$Volatile\ matter, \% = \frac{B - C}{B} x100 \quad (21)$$

$$Ash, \% = {}^{D}/_{B}\, x100 \quad (22)$$

$$Fixed\ carbon, \% = 100 - volatile\ matter\ (\%) - ash(\%) \quad (23)$$

Where B is grams of the sample after drying at 105°C, C is grams of the sample after drying at 950°C, and D is grams of residue.

### 3.2.4 Ultimate Analysis

Elemental analysis of RH was performed on fine-grounded (<250 μm) samples using the organic elemental analyser (Thermo Scientific Flash 2000 series CHN/S analyser) with a thermal conductivity detector (TCD). The technique used followed the ASTM standard test methods for the determination of carbon, hydrogen, and nitrogen in analysis samples of coal and carbon D5373-16 (ASTM, 2016). Helium gas was used as a carrier gas, and a reagent grade 2,5-Bis(5-tert-butyl-2-benzo-oxazol-2-yl) thiophene (BBOT) was used for equipment calibration. Approximately 0.3 to 0.4 mg of samples were weighed into a tin cup and loaded into a CHNS-O instrument. A blank analysis to establish carbon, hydrogen and nitrogen levels in the combustion and carrier gases was established by loading an empty tin cup. Due to the lack of a simple, direct method for evaluating oxygen in biomass fuels, the value was estimated by difference, as shown in Equation 24. The average elemental composition of three samples was reported for each RH variety.

$$O, \% = 100 - (C(\%) + H(\%) + N(\%) + S(\%) + Ash(\%)) \quad (24)$$

### 3.2.5 Calorimetric Analysis

The heating values of the RH biomass was characterized according to the ASTM standard test method for gross calorific value of refuse-derived fuel E711-87 (ASTM, 2013) using a digital bomb calorimeter (model: IKA C 2000). The bomb calorimeter calculates the heat dissipated by the combustion of fuel with oxygen. Difficulties were encountered in the combustion of RH samples in the bomb calorimeter. The sample particles were expelled from the combustion crucibles due to rapid devolatilization, resulting in partial combustion. To overcome this problem, the RH particles were grounded using a grain grinding mill and sieved to pass 180 μm. The finely grounded samples were moisturized and compacted into 0.5 to 1.0 g pellets using a specially modified 10 mL syringe barrel. The pellets were then oven-dried at 105$^{o}$C for 2 hrs before testing in the bomb calorimeter.

A bomb was rinsed with distilled water and left undried before adding 1 mL of distilled water with the help of a pippet. The pellets were then weighed to the nearest 0.1 mg and placed in a crucible before being loaded into the bomb. Approximately 2 to 3 MPa of pure oxygen was charged into the bomb calorimetry and maintained to allow complete combustion of the sample under an adiabatic environment. The higher heating value (HHV) was established using the incorporated bomb calorimeter software. Additionally, the empirical model developed by Sheng and Azevedo (2005) (Equation 25) was also used to compute HHV based on the ultimate analysis data, and the results were compared with those of the experimental. On the other hand, a low heating value (LHV) was computed using empirical correlation developed by Mansaray and Ghaly (1997) (Equation 26).

$$HHV, MJ/kg = -1.3675 + 0.3137C + 0.7009H + 0.0318O \quad (25)$$

$$LHV, MJ/kg = (1 - MC)\left[HHV - Y\left(\frac{MC}{1 - MC}\right) + \frac{18H}{200}\right] \quad (26)$$

Where C, H, O, N, S and Ash are the composition of carbon, hydrogen, oxygen, nitrogen, sulphur, and ash; MC is moisture content, and Y is the latent energy of vaporization of water (MJ/kg).

### 3.2.6 Lignocellulosic Composition

Rice husk samples were analysed for their extractives, cellulose, lignin, and hemicelluloses content using Chesson (1978) method. The samples were oven-dried at 105ºC for 2 hrs and then grounded and sieved to particles size 250<d<350 μm before analysis. One gram of sample and 150 mL of $H_2O$ was placed in a 250 mL heat resistant bottle with a screw cap lid and then refluxed at 100°C in an oil bath for one hour. The result was filtered by a vacuum filtration unit using a cloth filter, and the residue was washed with hot water (300 mL). The residue was then dried at 105ºC in the oven for 2 hrs and then weighed. The drying process was repeated for intervals of 1 hr until constant and then weighed. The residue was then placed back into the bottle and added 150 mL of 1 N $H_2SO_4$ then refluxed in an oil bath at a temperature of 100°C. The results were filtered by filtration unit and washed by hot water (300 mL) to neutral and then dried. The dried residue was placed back in the bottle, added with 10 mL of 72% $H_2SO_4$, and soaked at room temperature for 4 hrs. The residue was then added 150 mL of 1 N $H_2SO_4$ and refluxed on an oil bath at 100ºC for one hr. The residue was filtered using a filtration unit and then washed with 400 mL of hot $H_2O$ to neutral and then dried in an oven at 105ºC until constant weight and weighed. The residual was then ashed in the muffle furnace at 580ºC (according to

ASTM 1102-84) and then cooled in a desiccator to room temperature and weighed. Extractives content was calculated according to Equation 27 while hemicellulose (Equation 28), cellulose (Equation 29) and lignin (Equation 30).

$$Extractive, \% = \frac{a-b}{a} x100 \quad (27)$$

$$Hemicellulose, \% = \frac{b-c}{a} x100 \quad (28)$$

$$Cellulose, \% = \frac{c-d}{a} x100 \quad (29)$$

$$Lignin, \% = \frac{d-e}{a} x100 \quad (30)$$

Where, *a* is the original weight of sample, *b* dry sample after water reflux, *c* dry sample after refluxing in 1N $H_2SO_4$, *d* dry sample after soaking in 72% $H_2SO_4$, *e* weight of ash

### 3.3 Sub- and Supercritical Water Gasification System

A supercritical water gasification system was developed for gasification studies of varieties of rice husks under various gasification conditions. Several runs were carried out in the beginning to establish reactor calibration and work-up protocols. Reactor leakage, premature burst-ring rupture, inaccurate pressure control, and safety precautions due to high pressure and temperature operation are the most common challenges encountered during the initial testing of the sub- and SCW water systems. As detailed in sections 12.13.3.1 to 12.13.3.5, many of these challenges were overcome during this study.

#### 3.3.1 Sub- and Supercritical Water System

The SCW system used in this study is a non-stirred pressure vessel Parr 4650 series (Parr Instruments Co., Inc. USA) with an internal volume of 500 mL and the maximum operating conditions of temperature and pressure of 600°C and 35 MPa, respectively. The reactor comes with a pressure cylinder, a 3-kW ceramic heater, Parr reactor controller model 4838 (Parr Instruments Co., Inc. USA), J-type thermocouple, pressure transducer, analogue pressure gauge, universal asynchronous receiver-transmitter (UART) communication system for data synchronisation, parrcom temperature controller communication software ver.1.0.0.9 (Parr Instruments Co., Inc. USA) and parr data converter tool. Other systems had to be designed and assembled to get the SCW system fully operational; these include a master system controller for controlling reactor controller (slave controller) through temperature signal from transducer,

coolant loop for the pressure transducer, safety enclosures to contain possible burst disc rupture, and a purge and gas sampling system. The autoclave controller was designed for USA standard voltage and frequency (110 V and 60 Hz); therefore, to avoid overvoltage damage to the reactor, a 220 V to 110 V step-down transformer was used. Figure 18 shows the schematic diagram of the SCW gasification system.

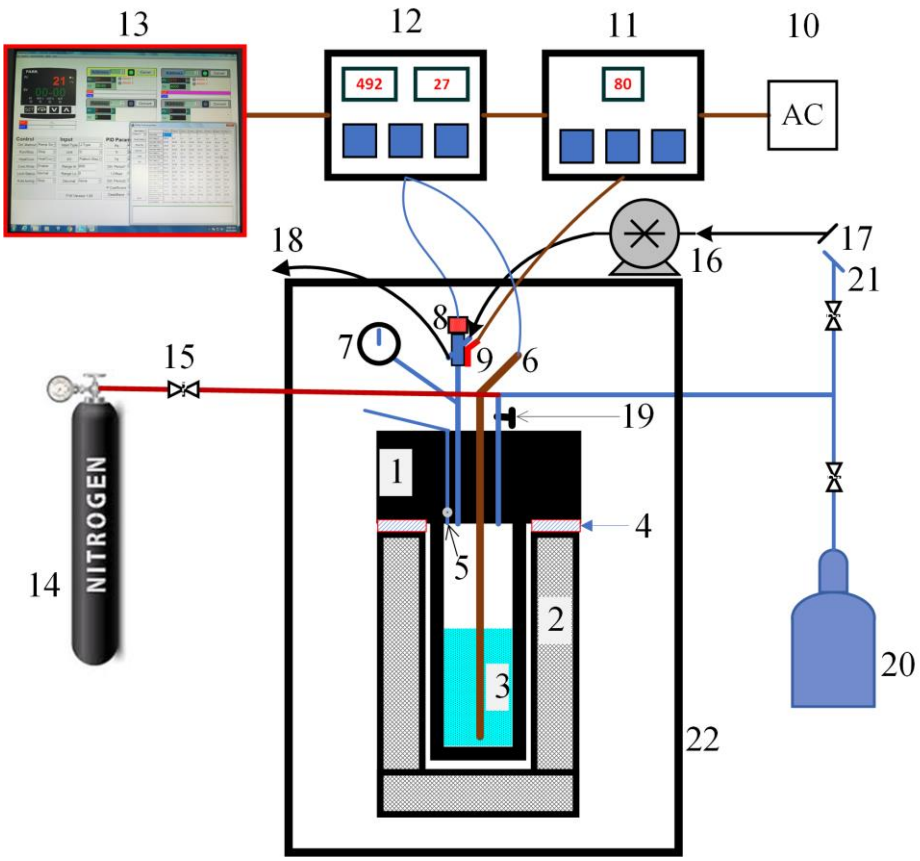


**Figure 18: Scheme diagram of the supercritical water gasification system**

**1. reactor head 2. furnace 3. reaction mixture 4. graphite gasket 5. safety burst disc 6. thermocouple (internal temperature measurement) 7. analogue pressure gauge 8. transducer 9. thermocouple (transducer temperature) 10. the power source (110 VAC) 11. master controller 12. slave controller (reactor controller model 4838, parr instrument) 13. communication software 14. nitrogen cylinder 15. valve 16. water pump 17,18. coolant line 19. needle valve 20. gas collection 21. venting line 22. safety cabin**

### 3.3.2 Reactor Pressure Monitoring and Control

Although the maximum working temperature of the pressure transducers is 120°C, it was discovered that the output pressure value varies slightly with transducer temperature. As a result, it is critical to keep the pressure transducers at a low and stable temperature to ensure pressure accuracy. To accomplish this, tape water was connected by Tygon tubing to the cooling sleeve of the pressure transducer. A K-type thermocouple was connected to the pressure transducer

and used as the master controller's signal. A master controller was built using a proportional, integral, derivative (PID) temperature controller model SYL-2352P (Auber Instruments Inc, USA) and a 25A solid state relay (SSR). For transducer temperatures below and above 80°C, the master controller was set to turn on and off the slave controller, respectively. This means that the SCW system cannot operate when the transducer temperature exceeds 80°C. At all experimental conditions, tape water was effective in keeping the transducer temperature below 80°C. On the other hand, an analogue pressure gauge was mounted using a T316 Bourdon tube mounted on the bomb head using a standard attachment fitting to measure the internal pressure of the reactor.

### 3.3.3 Safety Burst Discs and Containment

To protect the reactor from over pressurization and premature disc rupture, safety burst discs with a pressure capacity of 55 MPa and a temperature of 600°C were mounted. Furthermore, when the internal pressure reaches 30 MPa, the reactor controller is programmed to turn off the reactor. Moreover, for all experiments, the maximum reactor temperature does not exceed 500°C. A reactor enclosure was also designed in addition to this passive protection measure. The enclosures were constructed from 3.2 mm mild steel panels that were welded to an angle iron frame. All cables and coolant tubing were connected to the reactor via a small hole drilled on the sidewall of the enclosure. When the reactors were pressurized, the enclosure always remained closed.

### 3.3.4 Estimation Amount of Water Loading

One of the most subtle and common hazards in SCW gasification operations is overfilling the vessel. When water is heated beyond critical temperature in an overfilled closed vessel with insufficient free space to accommodate its expansion, destructive and lethal pressure can develop suddenly and unexpectedly. The pressure of heated water can rise to more than three times its original volume when heated from room temperature to 374°C. The required amount of water loading in each operating condition was carefully selected to ensure a safe operation of the reactor. Supercritical water pressure of up to 22 MPa was selected for temperatures operation below 374°C, and a range of 22 to 30 MPa was selected for operation between 374 and 500°C. With the aid of the Engineering equation solver F-chart program V9.457-3D (EES), the appropriate amount of water loading and estimated internal pressure with respect to operating temperature were calculated. Steam_IAPWS function issued by the International Association for the Properties of Water and Steam (IAPWS) was coded in the EES software to calculate

steam pressure. The Steam_IAPWS calculates thermodynamic properties of water with high accuracy (Wagner & Pruß, 2002). A trial and error of the amount of water loading were implemented at temperature 374°C to find the amount of water loading that gives a steam pressure of 22 MPa, and the same amount was used for all temperatures below 374°C. However, for temperatures between 374 to 500°C, the assumption was made that steam pressure varies linearly from 22 to 30 MPa. Temperature and pressure data were generated randomly and entered into the EES software to estimate the corresponding water loading. The generated temperature and water loading conditions were then tested experimentally to ensure that the pressure between EES estimation and experimental correlates.

### 3.3.5 Reactor Assembly and Leakage Control

Working with a high-pressure autoclave encompasses a series of complex activities, including reactor assembly, leakage management, and component disassembly for each experimental run. The reactor was loaded with the required amount of materials, fitted with flexible graphite or polytetrafluoroethylene (PTFE) gasket, lubricating all bolts and the thermowell with ant seize compound, tightening all bolts to an appropriate torque and test for system leakage. During initial runs, the pressure was observed decreasing with time, indicating the system leakage. After multiple trials, the primary leakage was from thermowell, whereby the pressure decreases while the temperature increases. Also, a significant loss of water was observed due escaping of steam from the reactor. The thermowell leakage was solved using a flexible graphite gasket and increasing the torque on the thermowell bolts to 50 newton-meter. Figure 19 shows the pressure and temperature profiles of the reactor with 70 mL water loading at a heating rate of 4ºC/minutes. A low standard deviation of pressure at holding times indicate that the reactor leakage was maintained.

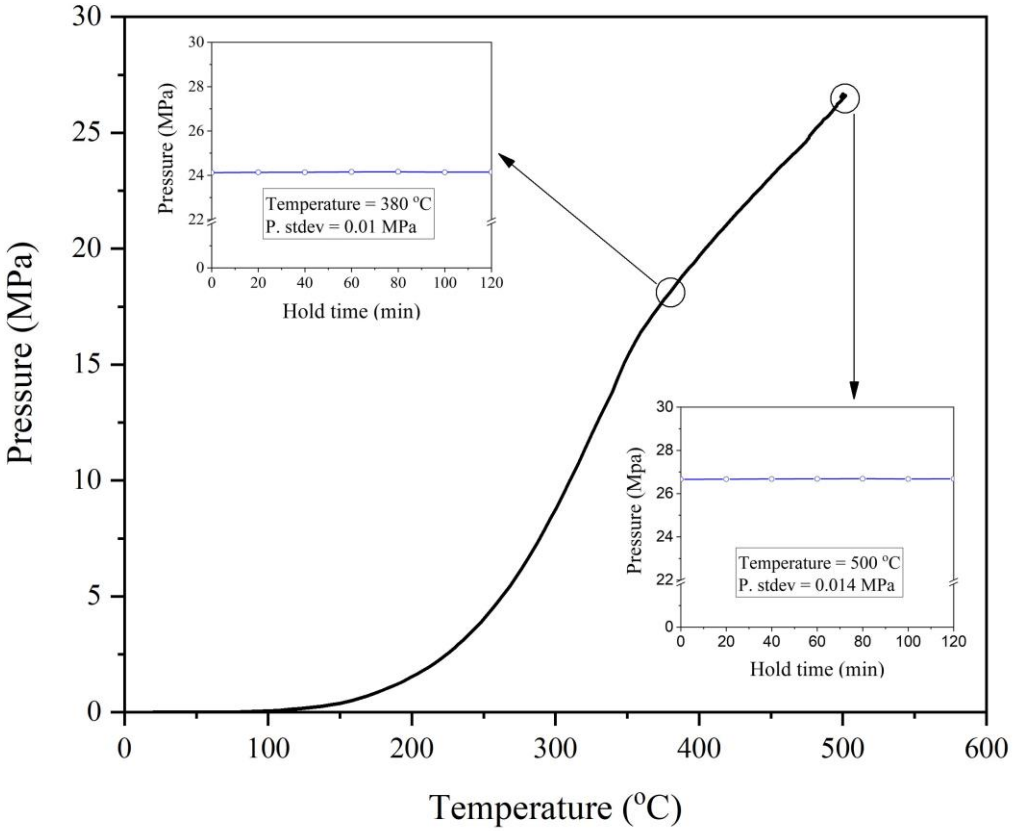


**Figure 19: Temperature and pressure profiles of the reactor. Water loading 70 mL, holding time 120 minutes at 380 and 500°C**

### 3.3.6 General Experimental Procedure

The dried rice husk sample was crushed in a grain milling machine and sieved to obtain a particle size between 0.25 and 0.35 mm. The RH sample was mixed well with deionised water for each experimental run according to feed concentration requirement (details in section 3.3.8) before being loaded into the reactor. Then the reactor was sealed by using a flexible graphite gasket and carefully tighten by applying 50 Nm torque to each closure bolt. The air inside the reactor was expelled by purging nitrogen gas. The nitrogen pressure of 2 MPa was purged four times to ensure all the air is evacuated. During the purging process, a pressurised reactor was held for 1 hr to observe any decrease in pressure due to leakage. Afterwards, a venting line was bubbled in water to ensure no nitrogen remained in the reactor.

The reactor was then inserted into the furnace and then programmed using a parrcom temperature controller communication software ver.1.0.0.9 (Parr Instrument Company, Moline, IL) according to temperature and residence time requirements. After reaching the targeted condition, the reactor was rapidly cooled to below 350°C by blowing cold air externally before being lifted and quickly quenched to a cold-water bath to reach ambient temperature. After

cooling down, the gas fraction was emptied through a needle valve connecting Tygon tubing and measured volumetrically using a water gasometer. The total volume of gas was measured with a ± 10% accuracy. Then, the reactor was demounted using a wrench, and the remaining reaction mixture was recovered according to a work-up procedure explained in section 3.3.7. In general, this study covers a subcritical water condition (< 374°C and < 22 MPa) and an SCW condition (> 374°C and > 22 MPa), with a residence time from 30 to 120 minutes and a feed concentration from 3 to 10 wt%.

### 3.3.7 Work-up Procedures for Reactor Content Recovery

Based on the work-out procedures described by Sato *et al.* (2006), Guan *et al.* (2008) and Sun *et al.* (2020), a new sequential procedure for reaction mixture recovery and tar extraction was developed in this study. In the mentioned studies, the author emptied the reactor and washed the reaction mixture with distilled water and filtration, resulting in an aqueous phase containing water-soluble tars and solid residuals. This method is sufficient for experiments with high biomass conversion and slight or no dissolved tars. Preliminary experiments showed that after washing with deionised water, a significant amount of tars remained dissolved in the solid char and others smeared on the inside walls of the reactor, requiring extraction by dissolving with organic solvent. In protocols developed in this study for tar recovery, distilled water, acetone, and n-hexane mixture was chosen because they are both non-toxic. Hexane dissolves non-polar compounds, and it has very low solubility in water (0.0095 g $L^{-1}$) while acetone dissolves the polar tars. Moreover, both organic solvents have low boiling points (acetone, 56°C and n-hexane, 69°C), hence they can be recovered without significant evaporation of sample.

Figure 20 is a sequential procedure for tar and char recovery; the numbers in brackets show the chronological order of the recovery process. First, the contents in the reactor are transferred into a clean beaker, and then the experiment setup is flashed three times by deionised water and then by n-hexane, which is then transferred into the same beaker. The setup is further flashed by acetone which is transferred into a different beaker. The obtained hexane phase is filtrated by vacuum filtration unit using a Whatman qualitative filter paper no. 1, and the filtrate is transferred to a separating funnel. Tarry compounds dissolved in the filtrate are extracted by the liquid-liquid extraction technique using n-hexane. During hexane extraction, polar tars emulsified into the filtrate phase and sticky to the walls of the separating funnel. The separating funnel is then washed with acetone to dissolve all tars, and the obtained solution is transferred to a conical flask. The acetone phase extracted from the experimental setup is filtrated through the same filter paper used for the hexane filtration, and more acetone is added to extract all tars

dissolved in the filter cake. The obtained acetone phase is poured into the conical flask containing the rinses from the funnel. After this step, a transparent aqueous layer is resulted, in addition to a tar-free char, a yellowish hexane phase and dark brown acetone phases are obtained. The dissolved water in hexane phase was dried by using anhydrous sodium sulphate. The acetone phase contains a high quantity of dissolved water and is recovered through a salting-out technique using anhydrous calcium chloride. The water-dry hexane and acetone phases are recovered in a rotary evaporator (Heidolph Instruments GmbH & Co. KG, Germany) at temperature 60°C, vacuum 870 mbar and 113 rpm for 10 minutes each phase. The char fraction is dried in the oven at 105°C for 4 hrs and cooled to room temperature in a desiccator. The tar and char fractions were gravimetrically weighed using a high precision analytical balance (Ohaus Explorer; accuracy ± 0.1 mg) and then characterised using Fourier-transform infrared spectroscopy (FTIR). Chemical characterisation of gas products is out of the scope of this study.

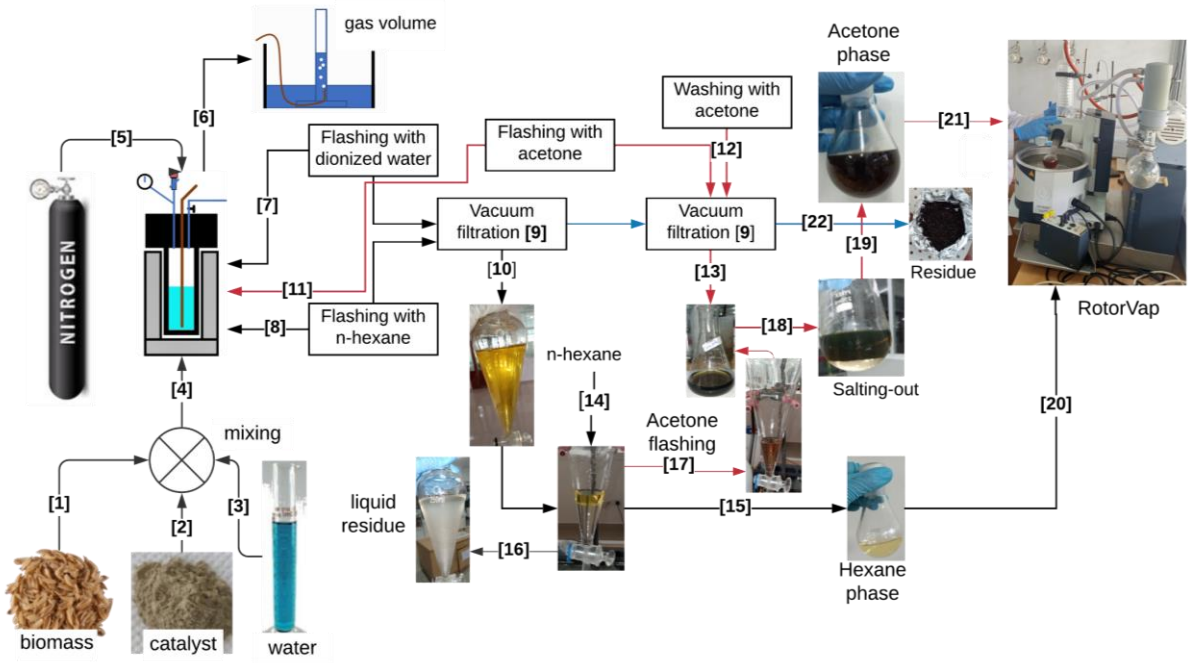


**Figure 20: Work-up sequence for the reaction mixture recovery**

### 3.3.8 Design of Experiments and Statistical Analysis

Response surface methodology is an empirical modelling method for establishing the interaction between numerous operating and response variables. It provides a systematic experimentation strategy for building and optimising an empirical model. In essence, RSM is a combination of mathematical and statistical approaches suitable for modelling and analysing problems in which the output is affected by input variables and their interactions (Fermoso *et al.*, 2010). A RSM

based on the I-optimality criterion was used to optimise three independent and four response variables in the current objective. Independent variables studied are reaction temperature (350-500°C), residence time (30-120 minutes) and feed concentration (3-10 wt%) while the observed responses were GE (%), char yield (wt%), gravimetric tar yield (mg/g biomass), and gas volume (mL/g biomass). The range of variables was chosen based on the data available in the literature (Borges *et al.*, 2019; Kumar & Reddy, 2019; H. Su *et al.*, 2020; Wang *et al.*, 2020). Table 1 shows the coded values for the levels of the studied variables. I-optimality RSM comprises of ten model points (run-1, 2, 4, 8, 9, 11, 16, 17, 18, and 20), five replicate points (run-6, 7, 13, 15, and 19), and five lack-of-fit points (run-3, 5, 10, 12 and 14), implying that 20 experimental runs were required as shown in Table 10. The RSM involves five steps: Firstly, the development of statistically designed experiments, followed by generating an empirical model, statistical analysis of the model, numerical optimisation by using desirability function and finally, model confirmation.

**Table 1: Levels of studied variable in subcritical and supercritical water gasification**

| Factor | Name | Units | Type | Min | Max | Coded Low | Coded High |
|---|---|---|---|---|---|---|---|
| $X_1$ | Temperature | °C | Continuous | 350 | 500 | -1 ↔ 350 | +1 ↔ 500.00 |
| $X_2$ | Resid. time | min | Continuous | 30 | 120 | -1 ↔ 30 | +1 ↔ 120.00 |
| $X_3$ | Feed conc. | wt% | Continuous | 3 | 10 | -1 ↔ 3 | +1 ↔ 10.00 |

The experimental run was randomised to diminish the error and effect of uncontrolled factors (Behera *et al.*, 2018). The observed responses were used to generate an empirical model, which conforms to the experimental variables using a quadratic Equation 9.

Experimental results from the 20 runs were used to determine the regression coefficient of the second-order polynomial models using Design-Expert Version 12.0.3 software (Stat-Ease, Inc., Minneapolis, USA). The coefficient of R-squared established the accuracy of the fitted model, and the significant model terms were assessed by the probability value (*P*-value) at a 95% confidence level. The contour and the 3D surface plots were developed to show the interaction of two independent variables while holding the third variable at the central value. The geometry of the surface plots generated provides valuable information about the behaviour of the system on the variation of the processing parameter within the design space. The SCW gasification conditions were numerically optimised using a desirability function of Design-Expert software for the minimisation of tar yield. Using the models created during analysis, the best-operating conditions that meet the defined goals were searched within the design space. Finally, one solution among the recommended solutions was selected for the model validation, whereby

three replicates of experimental runs were conducted, and results were compared with the predicted values.

### 3.3.9 Tar and Char Characterization

The Fourier Transform Infrared (FTIR) spectroscopy (Bruker Optic GmbH, alpha model, Laser class 1) was performed for the identification of distinct functional groups present in tar and char formed under different gasification conditions. The FTIR was evaluated in mid-infrared region which covers the spectrum range of 500–4000 $cm^{-1}$ at a resolution of 2 $cm^{-1}$. The spectral data were utilised to classify the sample compounds by correlating the fingerprints of the samples with those available in the database. Furthermore, the functional groups and structural properties of a chemical allowed to deduce the various structure types.

## 3.4 Catalytic Supercritical Water Gasification

The catalyst combinations used in this work were uncalcined dolomite [$(CaMg)CO_3$], and limestone ($CaCO_3$), calcined dolomite (CaMg)O and calcined limestone (CaO); and iron dopped calcined dolomite and limestone. During optimization of catalytic SCW gasification, the operating conditions for tar yield minimisation conditions obtained in section 3.3 were used. Before iron impregnation, preliminary experiments were conducted using 10% by weight uncalcined and calcined dolomite and limestone to determine its effects on gasification yield.

### 3.4.1 Catalyst Preparation

The starting materials were natural dolomite and limestone. A raw dolomite and limestone sample was grounded in a ball mill and sieved to pass 250 μm sieve to ensure homogeneity. Approximately 20 g of each sample was oven-dried at 105$^{o}$C for 2 hrs then cooled in the desiccator and stored in a dry glass bottle for further analysis. Another 50 g of grounded raw dolomite and limestone was calcined in a muffle furnace at 900$^{o}$C for 4 hrs at a heating rate of 3$^{o}$C/minutes to enhance its textural characteristics, surface areas, and its basicity (Di Felice *et al.*, 2011). A portion of 20 g of each calcined sample was stored in a dry glass bottle for further analysis. An iron (III) ammonium citrate salt was used as a metal precursor. The iron impregnation procedures were adopted from Di Felice *et al.* (2011) and described in detail in this section. Salt precursor equivalent to 10 wt% and 20 wt% of iron to the substrate was weighed to the nearest 0.1 mg in a 250 mL beaker and dissolved by deionized water. A beaker with a mixture was lined with foil paper and stirred by a magnetic stirrer for 4 hrs before adding a substrate. Then the required weight of calcined dolomite or limestone was added and stirred

further for 4 hrs to obtain a homogeneous mixture. The mixture was placed in the oven at 105$^{o}$C for 4 hrs to evaporate off the water, and the solid recovered dried at 120$^{o}$C for 6 hrs. The solid residual was grounded in a mortar and sieved to obtain particles ranging between 80 and 300 μm. The material was then thermally treated in the air at 900$^{o}$C for 6 hrs at a heating rate of 3$^{o}$C/minutes, then cooled in a desiccator and stored in glass bottles for further analysis. Since the impregnation-calcination processes can significantly affect the distribution of catalyst particle size (Huang *et al.*, 2012), catalyst samples were prepared under the same conditions. The samples were labelled as X%Fe/limestone or X%Fe/dolomite catalysts, where X represents the weight per cent of the iron and limestone and dolomite represent the calcined materials.

### 3.4.2 Catalyst Characterization

The natural, calcined and Fe doped limestone and dolomite crystal structural analysis was carried out using an XPERT-PRO X-ray diffractometer (XRD) (PANalytical BV, Netherlands) with reflection geometry at 2θ values (5 – 90°) and a step size of 0.05°, in conjunction with a Cu Kα radiation source (λ= 0.15418 nm) at 50 kV and 30 mA. The powder diffraction cards from JCPDS were used to assign the diffraction peak. The morphology and elemental composition of the catalyst were analysed by a Zeiss Ultra Plus 55 field emission scanning electron microscope (FE-SEM). The catalyst powder was placed to a SEM stub (layered with carbon tape). The stub was then coated with gold in a sputter coater for five minutes to give high reflectivity during the scanning process. Before SEM analysis, the samples were dried in an oven at 40°C. The SEM instrument was powered at 1.0 kV and equipped with an energy-dispersive X-ray spectrometer. For the transmission electron microscopes (TEM) analysis, the samples were ground in a mortar before being put on a Cu grid covered with a perforated carbon membrane before scanning. The catalysts' specific surface area and total pore volume were measured at 77 K by a nitrogen absorption apparatus (TriStar II 3020 device) run at a relative pressure (*P/Po*) ranging from 0.01 to 1.0.

### 3.4.3 Reactivity Tests and Product Analysis

In each experiment, the grounded RH sample and required amount of catalyst were mixed well with deionised water according to feed concentration requirement before being loaded into the reactor. The experimental runs for catalytic SCW gasification were conducted using RSM based on I-optimality criteria.

**Table 2: Levels of the studied factor in catalytic supercritical water gasification**

| Factor | Units | Type | Levels | Coded low | Coded high |
|---|---|---|---|---|---|
| Catalyst loading | % | Discrete | 3 | -1 ↔ 5 | 1 ↔ 20 |
| Fe-content | % | Discrete | 3 | -1 ↔ 0 | 1 ↔ 20 |
| Catalyst type | | Nominal | 2 | Limestone | Dolomite |

A three-level experiment was chosen to ovoid too many preparations for catalysts, as shown in Table 2. The observed responses were GE (%), char yield (wt%), gravimetric tar yield (mg/g), and gas volume (mL/g biomass). The I-optimality RSM for this experiment comprised nine model points, four replicate points, and four lack-of-fit points, implying that 17 experimental runs were required. Other procedures and analyses were conducted, as shown in section 3.3.7.

# CHAPTER FOUR

# RESULTS AND DISCUSSION

## 4.1 Physical Properties of Rice Husk

### 4.1.1 Moisture Content

The moisture content results are presented in Table 3. The moisture content value for the studied variety of RH ranges between 6.3% and 6.9%. These values are very close to the value of 6.37% and 7.2% reported in the literature (Kazawadi *et al.*, 2014; Tsai *et al.*, 2007). The slight difference in moisture content for the rice husk variety studied could be ascribed by variation in postharvest handling such as drying and storage. The moisture content of biomass significantly affects its quality as a fuel source. The higher moisture content lowers the heat value, which decreases the system conversion efficiency as a significant amount of energy is required during conversion to vaporise fuel moisture. For the combustion process, a dry fuel material is thus favoured, whereas a maximum fuel moisture between 20-30 %db is desirable for classical gasification (McKendry, 2002). On the other hand, no condition for the moisture content is needed for SCW gasification, so the studied RH sample is suitable for classical and SCW gasification processes.

**Table 3: Moisture content of as received rice husks from different regions**

| Rice husk | Moisture content[a] (%) |
|---|---|
| Shinyanga | 6.3 ±0.12 |
| Morogoro | 6.9 ±0.12 |
| Dodoma | 6.7 ±0.18 |
| Arusha | 6.3 ±0.16 |
| Iringa | 6.9 ±0.09 |

[a] Average of three replicates

### 4.1.2 Bulk Density and Particle Size Distribution

Table 4 shows the bulk density of as-received RH varieties from different regions of Tanzania. The average bulk density ranged between 125 kg/m$^3$ and 194 kg/m$^3$ whereby the sample from Arusha recorded the least density and Shinyanga the highest. The bulk densities of samples from Arusha, Morogoro, Dodoma and Iringa are within the ranges reported in the literature. Kumar *et al.* (2013) reported the range of bulk densities between 96 – 160 kg/m$^3$, and Muthadhi and

Kothandaraman (2007) reported 96 kg/m$^3$ and 160kg/m$^3$ from the studied varieties. However, the sample from Shinyanga deviated from published values. The variation of bulk densities is primarily influenced by the properties of rice kernel and postharvest operations such as differences in dehulling machine setup and moisture content. A sieving analysis was performed at different sieve sizes to study the particle size distribution's influence on the bulk density of the RH. The ANOVA test shows a significant difference in the mean bulk density of the studied RH varieties, $p$<0.001 and $F$= 323.65 at a 95% confidence level. The low bulk density of the RH reported from the study may cause challenges in downdraft or updraft gasification since it can reduce the residence time in the reactor and result in lower conversion efficiency (Olupot *et al.*, 2016). Therefore, densification by pelletising or briquetting the rice husks will increase the bulk density to 550-700 kg/m$^{3,}$ which is the recommended range for best gasification performance (Mansaray & Ghaly, 1997).

**Table 4: Bulk density of as received rice husks from different regions**

| **Rice husk variety** | **Bulk density[a] (kg/m$^3$)** |
|---|---|
| Arusha | 125±1.5 |
| Shinyanga | 194.1±2.3 |
| Morogoro | 138.9 ±0.7 |
| Dodoma | 149.3±1.1 |
| Iringa | 157.1±1.3 |
| *P-value* | <0.001 |
| *F-value* | 323.65 |

[a] Average of three replicates

Sieve analysis Fig. 21 shows that the RH variety from Shinyanga had the highest amount of finer particles (particle passing 0.75 mm mesh size), about 16.5%, while a sample from Morogoro had the least amount, about 9.7%. The particles passing the 0.75 mm mesh size are considered biomass dust that may cause sintering and block air and gas passages in the downdraft reactor. It is generally preferred for efficient gasification to use a uniform feedstock, particularly particle size and size distribution. In particular, too large particles are known to cause secondary reactions to occur within particles, leading to low conversion and higher formation of char and tars. On the other hand, too small particles may not be retained long enough in the reaction zone in downdraft gasification for complete conversion (Mansaray & Ghaly, 1997).

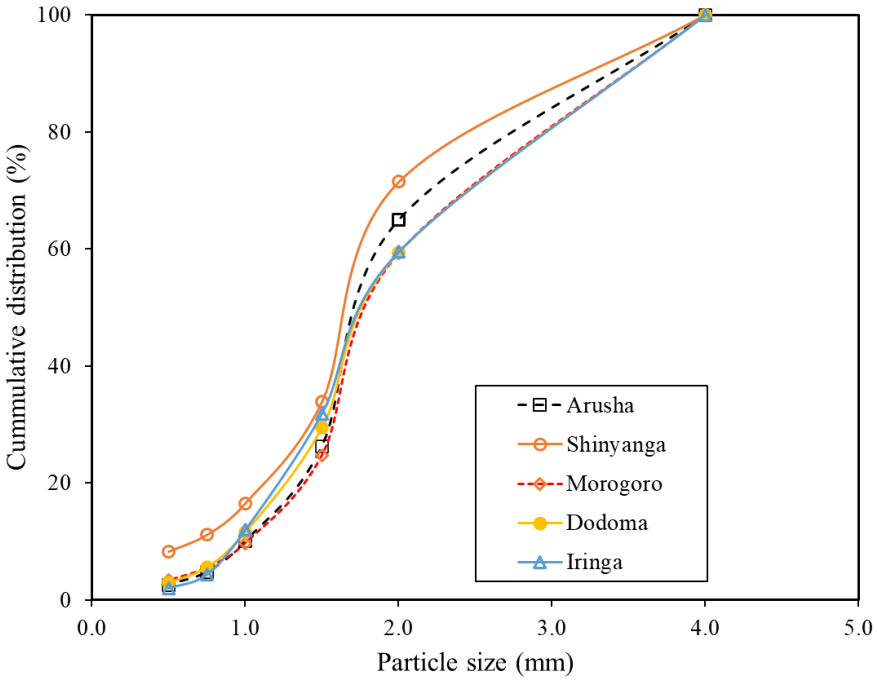


**Figure 21: Particle size distribution of varieties of rice husks**

Figure 22 depicts a measure of bulk density versus the percentage of coarse particles in the samples. It can be shown that the coarser particles there are, the lower the bulk density is, and vice versa. The linear fit trend line has an R-squared of 0.8618, indicating that the course particle data and bulk density data are well aligned.


**Plate 1: Visualization of particles sizes for different sieve sizes**

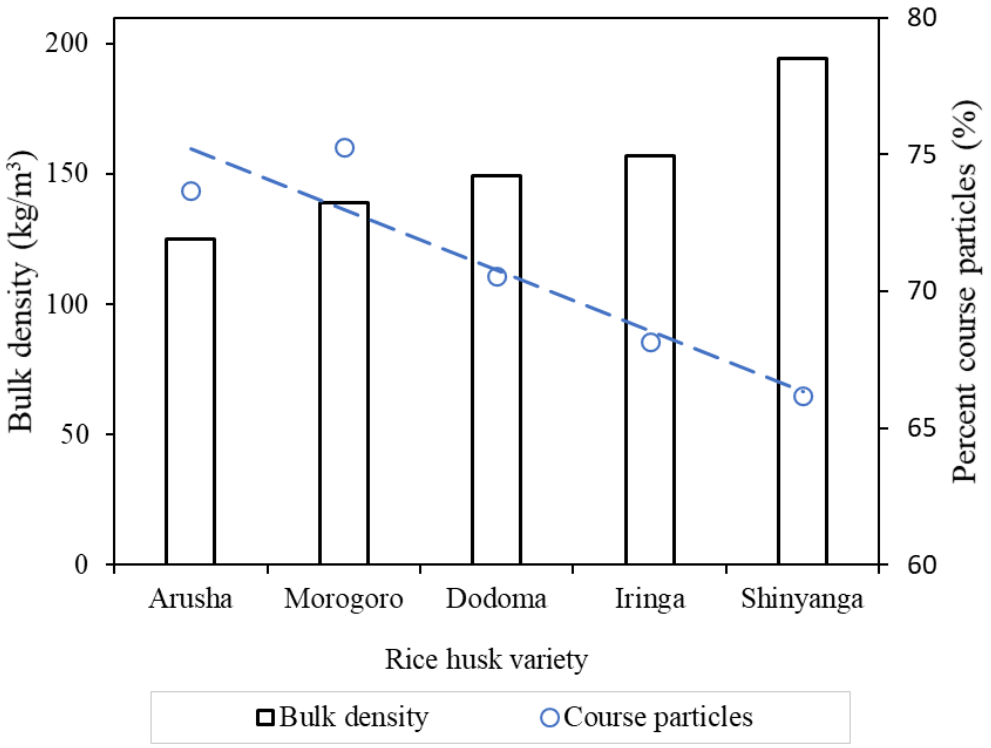


**Figure 22: Comparison of bulk density and coarse particles (particles retained up to 0.75 mm sieve) of different rice husk varieties**


**Plate 1: Visualization of different particles size at different sieve sizes: (a) d>2 mm (b) 1.5<d<2 mm (c) 1<d<1.5 mm (d) 0.75<d<1 mm (e) 0.5<d< 0.75 mm and (f) pan**

## 4.2 Chemical Properties of Rice Husk

### 4.2.1 Proximate Analyses

The proximate analysis classifies the fuel in terms of its volatile matter (VM), ash and fixed carbon (FC) (by-difference) contents, mainly reported on per cent dry basis. During testing, the

volatile materials are driven off at a high temperature (950$^{o}$C). Table 5 reports the proximate analyses for each variety of RH samples collected from five different regions in Tanzania. The ANOVA analysis revealed a significant difference in the proximate analysis value of the RH samples at a 5% confidence level since $p<0.05$. The RH varieties' volatile matter ranged between 56.85%db and 62.8%db of the least and highest been the Iringa and Arusha sample, respectively. The reported values are close to the range of 58.8%db to 66.4%db reported by Olupot *et al.* (2016). Said *et al.* (2014) and Kazawadi *et al.* (2014) reported the volatile matter of 56.20%db for the sample collected from Morogoro (3.44 less) and 59.6%db for a sample collected from Dodoma (1.53 higher), respectively. The variation of characteristics of the samples sourced from the same region could be due to differences in the rice paddy, soil, differences in handling protocols from farming to pre-and post-processing, and characterisation procedures such as sample preparation and equipment used. The relatively high volatile matter on the RH samples makes it more readily for devolatilization with fewer residuals, thanks to pyrolysis and gasification technology. On the other hand, high volatile matter feedstock needs less heat for thermochemical reactions; therefore, it is possible to gasify the rice husks at relatively low temperatures than other biomass types (Olupot *et al.,* 2016).

**Table 5: Individual proximate analyses of five varieties of rice husk with corresponding results of ANOVA test at a 5% confidence level**

| RH variety | Vm(%db)[a] | Ash(%db)[a] | FC(%db)[a] |
|---|---|---|---|
| Arusha | 62.80 ± 1.5 | 22.2 ± 0.3 | 15.00 ±1.5 |
| Shinyanga | 61.56 ± 0.9 | 26.8 ± 0.3 | 11.64 ± 0.9 |
| Morogoro | 59.64 ± 1.4 | 25.0 ± 0.2 | 15.36 ± 1.4 |
| Dodoma | 58.07 ± 0.2 | 22.4 ± 0.3 | 19.53± 0.2 |
| Iringa | 56.85 ± 0.2 | 27.3 ± 0.1 | 15.85 ± 0.2 |
| p-*value* | 0.001 | <0.001 | 0.004 |
| F-*value* | 5.91 | 109.97 | 7.832 |

[a]Average of three replicates

The five RH samples' fixed carbon ranged between 11.64%db and 19.53%db, which is relatively close to the range between 14.8%db to 17.8%db reported by Olupot *et al.* (2016). Moreover, Kazawadi *et al.* (2014), Mhilu (2014) and Said *et al.* (2014) reported the values of fixed carbon of 17.29%db, 14.60%db and 12.5%db, respectively, which are within the range found in this study. The correlation between FC and VM reported in Table 5 are somewhat deviated from the fact explained by Graboski and Bain (1979) that the higher the volatile matter content, the lower the fixed carbon. A similar case where some varieties with high volatile matter registered high

fixed carbon and vice versa were reported by Olupot *et al.* (2016). The presence of air in the samples could influence this anomaly, which significantly affects the proximate analysis test results. The higher fixed carbon in the sample is preferred for a gasifier to operate at high efficiency since the FC produces char required for the tar's thermal crack during the gasification process (Tilman *et al.*, 2006).

The ash content of biomass plays a significant role in the gasification product and is the potential candidate for forming an undesired fused deposit on reactor surface and disposal problems. Ash content of the biomass is determined by the combustion of its volatile matter and fixed carbon fractions. Therefore, they could not represent the original ash due to the presence of some mineral matter. The ash content obtained from this study ranged between 22.2%db and 27.3%db. The ash content of samples from Arusha, Morogoro and Dodoma conforms to the range of 14.28%db to 24.46%db and 15.9%db to 25.6%db reported by Mansaray and Ghaly (1997) and Olupot *et al.* (2016). The sample from Shinyanga and Iringa exhibited higher ash content of 26.8%db and 27.3%db, respectively. These findings were within the range of 22%db to 29%db reported by Muthadhi and Kothandaraman (2007). The high ash content of RH samples reported in this study makes them prone to slugging in updraft or downdraft gasifiers if the gasification temperature is not well controlled. Slugging behaviour is highly dependent on the ash melting temperature, which is influenced by the presence of trace elements (Mansaray & Ghaly, 1997). Slugging can lead to excessive tar formation and complete blockage of the reactor. Mansaray and Ghaly (1997) studied ash fusibility of different RH samples and recommended gasifier operation below 1300$^{o}$C to avoid slugging problems.

### 4.2.2 Ultimate Analyses

The ultimate analyses classify the fuels in terms of their weight fraction of elemental carbon, hydrogen, oxygen, nitrogen and sulphur. The major elemental constituents of RH are oxygen, carbon, and hydrogen. In some biomass varieties, low concentrations of nitrogen, sulphur and chloride can also be found. In evaluating the heat value and the material's suitability as fuel, the major elements are essential. The carbon and hydrogen content accounts for the hydrocarbon that can devolatilise during thermal degradation, while oxygen content lowers the fuel's energy content (Said *et al.*, 2014). Other elements, such as sulphur and chlorine, provide information on the production of unwanted products concerning environmental pollution problems during the thermochemical conversion process (Ghaly & Al-Taweel, 1990). The elemental composition of five varieties of RH samples is presented in Table 6.

**Table 6: Individual ultimate analyses of five varieties of rice husk with corresponding results of ANOVA test at a 5% confidence level**

| RH variety | Elemental composition[a] | | | | |
|---|---|---|---|---|---|
| | C(%db) | H(%db) | O(%db) | N(%db) | C/N |
| Arusha | 34.40±0.2 | 5.10±0.1 | 35.56±0.1 | 1.77±0.1 | 19.43±0.8 |
| Shinyanga | 29.97±0.6 | 4.56±0.1 | 37.19±0.4 | 1.50±0.1 | 19.87±0.5 |
| Morogoro | 34.06±0.7 | 4.85±0.1 | 35.28±0.8 | 1.21±0.0 | 28.37±0.2 |
| Dodoma | 32.95±0.1 | 4.50±0.1 | 38.35±0.1 | 1.29±0.0 | 25.50±0.0 |
| Iringa | 30.49±0.1 | 4.20±0.2 | 37.26±0.2 | 1.12±0.0 | 28.33±0.1 |
| p-*value* | <0.001 | 0.001 | 0.001 | <0.001 | <0.001 |
| F-*value* | 24.08 | 10.41 | 12.99 | 22.8 | 87.63 |

[a]Average of three replicates

The carbon content in the different RH varieties studied was found between 29.97%db and 34.40%db. These values agree with the range of 29.98 to 34.45%db reported by Olupot *et al.* (2016). On the other hand, Kazawadi *et al.* (2014), Mhilu (2014) and Said *et al.* (2014) reported higher values of carbon content for the samples collected from Dodoma (38%db), Morogoro (49%db) and Mbeya (45%db), respectively. The variation could be due to the rice paddies pre- and post-processing, sampling location, and analysis protocol. Hydrogen content for the studied RH variety ranged between 4.20%db and 5.20%db, within the range of 4.46 to 5.59%db and 3.9%db reported by Olupot *et al.* (2016) and Paethanom and Yoshikawa (2012), respectively. The Dodoma sample yielded hydrogen content close to 4.50%db (0.35 less) reported by Kazawadi *et al.* (2014) for the sample collected from the same region. The measured value for oxygen content in the five varieties of rice husks ranged between 35.28%db and 38.35%db. The oxygen content conforms to the range of 31%db to 37%db and 31.5%db to 35.2%db reported by Muthadhi *et al.* (2007) and Mansaray and Ghaly (1997), respectively.

Nitrogen and sulphur contents are considered unwanted content as far as thermochemical conversion is concerned. The nitrogen content of the five rice husks sample varieties studied ranged between 1.12%db and 1.77%db. In comparison to literature, Boot-Handford *et al.* (2018) reported the nitrogen content of RH as a range between 0.4%db and 0.8%db, Makwana *et al.* (2015) reported 4.3%db while Gaur and Reed (1995) reported 2.17%db. The range of the nitrogen content found in this study conforms to the reported range in the literature. The presence of low nitrogen content in rice husks adds an advantage to its utilisation in the thermochemical conversion: First, the risk of NOx formation is minimal, and since the gasification temperature is generally below 900$^{o}$C, NOx formation reaction is further hampered (Olupot *et al.,* 2016). The sulphur content for all RH varieties studied was exceptional low

below the detection limit. A similar observation was reported by Khonde and Chaurasia (2016). Olupot *et al.* (2016) found sulphur fraction to a range between 0.005%df and 0.014%db, while Maiti *et al.* (2006) and Mhilu (2014) reported 0.07%db and 0.02%db, respectively. The low content of sulphur offers a more desirable environmentally friendly fuel alternative since the reaction leading to the emission of $SO_2$ may not be expected.

Carbon to nitrogen ratio (C/N) is an important parameter as far as thermochemical conversion, or composting is concerned. The C/N of the RH variety studied ranged between 19:1 and 28:1as shown in Table 6. In comparison to literature, Gaur and Reed (1995) reported a C/N ratio of 18:1, Khonde and Chaurasia (2016) and Kazawadi *et al.* (2014) both reported C/N 56:1, while Olupot *et al.* (2016) reported a range between 54:1 and 87:1. The variation of the C/N ratio could be due to the difference in soil properties from the sampling locations. The C/N is an essential parameter influencing the digestion of feedstock in the composting process. Carbon provides energy for the bacteria, while nitrogen offers nutrients that enhance reproduction by the bacteria. There is, literally, no exact C/N ratio requirement for thermochemical conversion given in the literature. The C/N for all studied samples were considerably within the desired range of 20-35:1 for biogas production through anaerobic digestion (Matin *et al.,* 2018). These findings entail that the RH varieties from Tanzania are the potential feedstock for thermochemical conversion through gasification and biogas production. However, feedstock for anaerobic digestion must attain moisture content between 80%wb to 90%wb and a lower lignin fraction. A high lignin fraction of RH could hamper the decomposition by the micro-organism, and therefore pre-treatment is required (Matin *et al.,* 2018).

### 4.2.3 Biochemical Analyses

The biochemical analysis was performed on the ground and oven-dried RH samples to determine the composition of extractives, cellulose, hemicellulose and lignin. The results of the biochemical analysis conducted on five RH varieties are presented in Fig. 23. The extractive content for both RH varieties varied between 10.93%db and 18.03%db. The extractives fraction of RH varieties from Iringa is 10.93%db and from Dodoma is 12.68%db, which agrees with the 10.77%db and 12.66%db for the RH varieties reported by Abu-Bakar and Titiloye (2013) and Pinto *et al.* (2017), respectively. Sample from Morogoro, Shinyanga and Arusha exhibited higher extractive quantity ranging between 14.02%db and 18.03%db, which was significantly different from the rest of the samples. This value is lower or comparable to 18.4%db and 18.59%d for the RH reported by Wannapeera *et al.* (2008) and Guo *et al.* (2011), respectively.

The hemicellulose content varied between 17.02%db and 21.01%db. These values are close/or within the range of 11.39%db and 19.97%db reported by Olupot *et al.* (2016) for Uganda's RH. However, the measured hemicellulose was lower than 24.8%db reported by Chabi *et al.* (2018). The cellulose content ranged between 34.42%db and 38.52%db, within the range of 31.03%db to 36.54%db and 31.31 to 49.94%db reported by Olupot *et al.* (2016) and Menya *et al.* (2018), respectively. The composition of lignin varied between 16.34%db and 17.51%db. These results compare well with the lignin content range of 10.0%db and 18.3%db reported by Menya *et al.* (2018). However, these values are higher than the range of 10.58%db and 13.47%db reported by Olupot *et al.* (2016) for the RH varieties from Uganda. These rice husks have a high potential for thermochemical conversion processes because of the low lignin content and significantly high cellulose content. In general, the higher the content of lignin in biomass, the more resistant it becomes to hydrolysation (Zhao, 2013). Besides, cellulose and hemicellulose constituents are mainly made of carbohydrates which are less thermally stable than the polyaromatic hydrocarbons and complex organic compounds present in lignin (Menya *et al.,* 2018). As a result, cellulose and hemicellulose decompose quickly during pyrolysis, resulting in a higher gasification yield (Muley *et al.,* 2016). Pyrolysis is an important gasification route through which biomass is primarily converted into valuable intermediate products such as bio-oil, permanent gas and biochar (Bakari *et al.,* 2020).

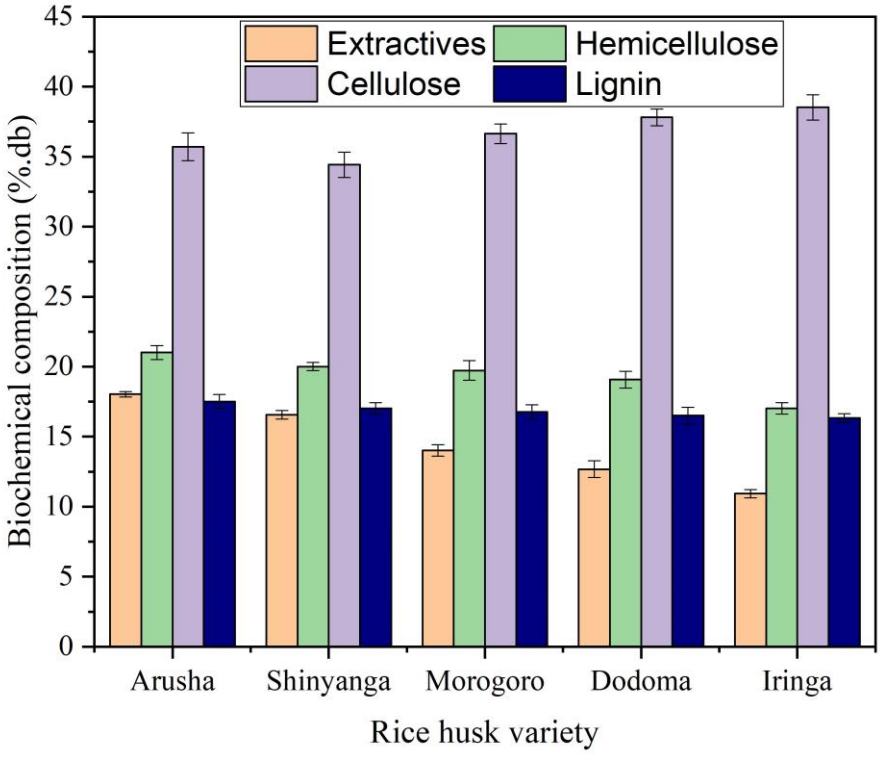


**Figure 23: Biochemical composition of varieties of rice husk**

The coefficient correlation between geographical parameters such as latitude, longitude, and altitude and the lignocellulosic constituents of rice husk varieties was computed and presented in Table 7 (geographical parameters for the five regions are presented in Appendix 2). The results showed that as latitude increased, cellulose content increased, but extractives, lignin, and hemicellulose content decreased. A robust correlation between lignocellulosic composition and latitude was observed. There is a negative correlation between latitude and extractives (-0.947), hemicellulose (-0.837), and lignin (-0.893), while a positive correlation exists between latitude and cellulose (0.88). There is a significant positive correlation between cellulose and longitude (0.406) and altitude (0.114) and a negative correlation between hemicellulose and altitude (-0.293). In addition, no correlation was found between lignin and longitude (0.038) and altitude (0.051), extractives and longitude (-0.120) and altitude (-0.001), and hemicellulose and longitude (0.094).

**Table 7: Coefficient correlation analysis between lignocellulosic composition and geographical factors**

| Composition | Latitude | Longitude | Altitude |
|---|---|---|---|
| Extractives | -0.9475 | -0.1207 | -0.0018 |
| Hemicellulose | -0.8378 | 0.0945 | -0.2938 |
| Cellulose | 0.8704 | 0.4061 | 0.1142 |
| Lignin | -0.8927 | 0.0381 | 0.0514 |

Further linear analysis was computed and presented in Fig. 24-26. The results demonstrated that regions with high latitude influenced high cellulose while negatively influencing the amount of extractives, hemicellulose, and lignin. The $R^2$ values were 0.5767 for cellulose, 0.7722 for hemicellulose, 0.7942 for lignin, and 0.8497 for extractives, showing that the linear fitting was credible, and the high credibility shows the correlation between lignocellulosic composition and latitude (Fig. 24). This finding was consistent with the findings of Xu *et al.* (2020) correlation analysis of miscanthus biomass. No linear correlation is observed between longitude, altitude, and lignocellulosic composition, as seen in Fig. 25 and 26. The correlation between lignocellulosic composition and region latitude could be related to cell wall metabolism and soluble sugar content differences between plants (Papini-Terzi *et al.*, 2009). Low temperature, in particular, increases the concentration of soluble sugar in plants, which protects the stability of cell membranes. As a result, under cold weather conditions, the plant increases its soluble sugar content, thereby stimulating the production of related lignocelluloses (Papini-Terzi *et al.*, 2009; Vicentini *et al.*, 2009).

Furthermore, variations in latitude cause significant variations in weather variables such as light time, temperature, and rainfall, all of which have a considerable impact on the flowering and maturity stages of the rice plant. For example, as latitude increases, light time increases, leading to shorter flowering time (Xu *et al.*, 2020). This means that variations in the length of the growing period could considerably impact the lignocellulosic composition of the rice husk type. Nevertheless, changes in rice kernels could play a significant role in this heterogeneity. It is important to note that these findings must be interpreted in light of some limitations. The first constraint is a lack of sufficient samples of rice husks for statistical quantification. The second limitation is a lack of weather data such as rainfall, light intensity, temperature, and information about kernel type, length of growing period and soil qualities was unavailable.

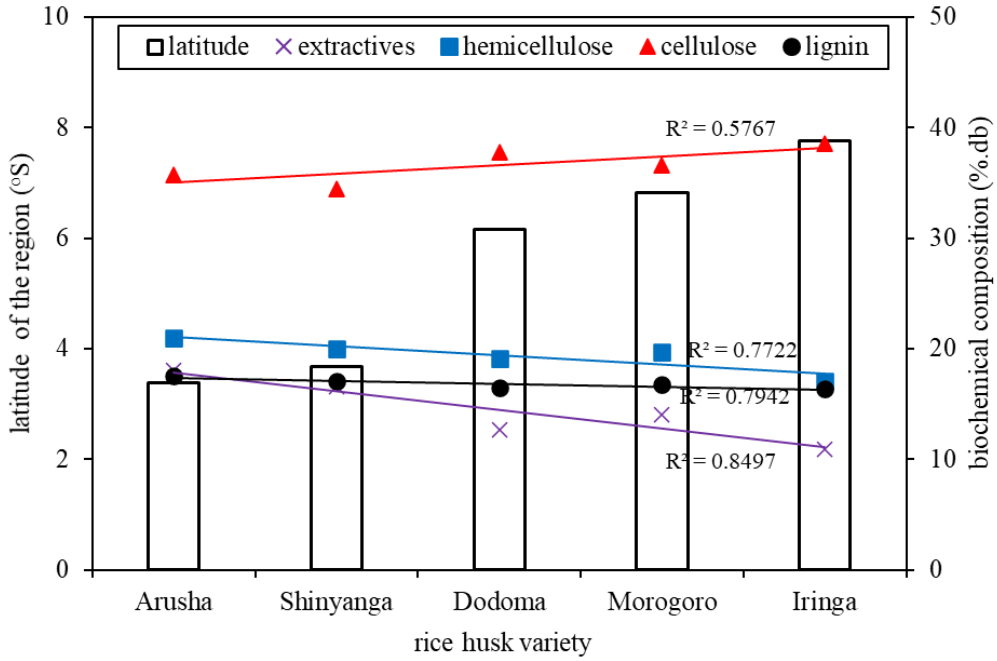


**Figure 24: Linear analysis of latitude of the region and lignocellulosic composition**

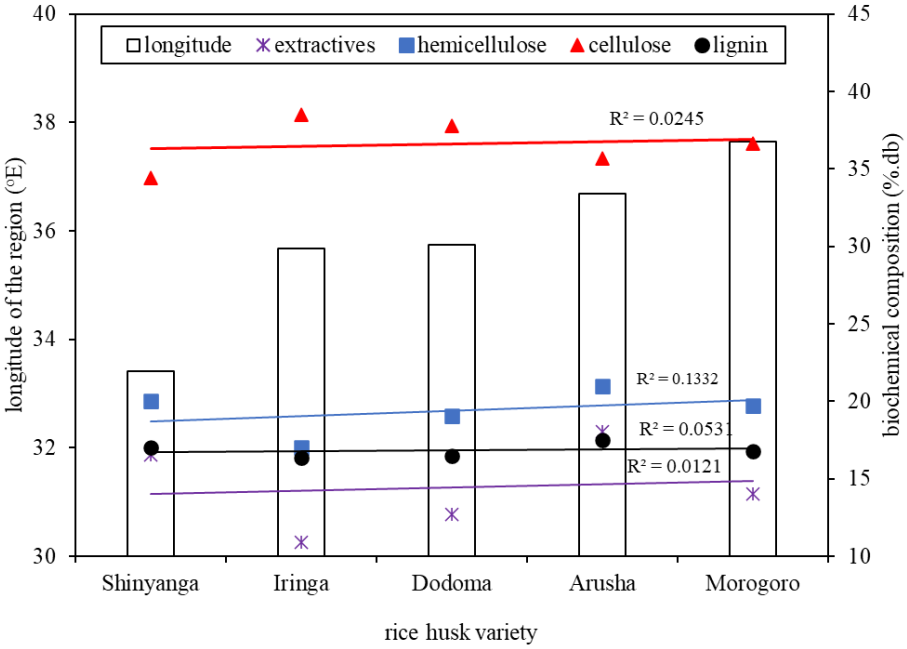


**Figure 25: Linear analysis of longitude of the region and lignocellulosic composition**

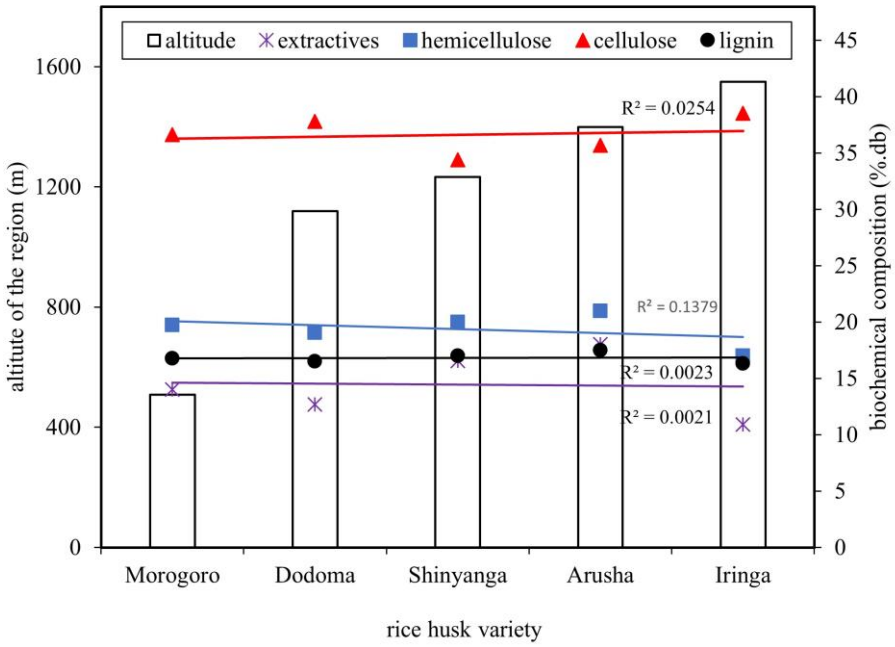


**Figure 26: Linear analysis of altitude of the region and lignocellulosic composition**

### 4.2.4 Rice Husk Ash Characterisation

Ash is a significant percentage of the solid by-product produced during biomass gasification. Understanding the variations in the chemical composition of biomass ash is of utmost importance for developing waste-to-energy conversion strategies and by-products utilisations. The ash composition analysis was performed on the ash obtained from grounded RH samples.

The results of the EDX analysis on the five RH varieties are presented in Fig. 27. The weight fraction of sodium (Na), magnesium (Mg), aluminium (Al), silica (Si), potassium (K), sulphur (S), chlorine (Cl), calcium (Ca), titanium (Ti), iron (Fe), manganese (Mn), molybdenum (Mo), and indium (In) is reported. The primary inorganic elements found in the rice husk ash samples were Si, K, Ca, P, Mg, Al and Fe. A small fraction of Na, Ti, Mn, Mo and In were also detected. The mineral components in rice husk ashes from different varieties varied greatly. Silicon is the main fraction of rice husk ash, and it varies between 86.6 and 90.9 wt%. The Iringa sample was found to contain the least concentration of silica while that of Morogoro contains the highest. Potassium fraction significantly varied with the variety of rice husk, and it ranges between 4.6 and 7.3 wt%. The sample from Morogoro contains the least amount of potassium, while that of Dodoma contains the highest amount. Traces of molybdenum was only found in a sample from Iringa, while indium was detected only in a sample from Iringa region. It was evident that the content of inorganic minerals varies significantly with the variety of rice husks, which could be explained by differences in soil qualities and climatic conditions, resulting in crop-specific mineral uptake differences.

The composition of inorganics in terms of decreasing content of the selected top five elements can be ranked as follows: Dodoma (Si > K > Ca > Al > P), Arusha (Si > K > Ca > Fe > P), Iringa (Si > K > Ca > Mg > P), Morogoro (Si > K > Ca > P > Fe), and Shinyanga (Si > K > Ca > Cl > In). Knowing interactions among minerals in the biomass is necessary since the detrimental effects of some minerals are dependent on the presence of others. The high content of K and Ca is undesirable for biomass combustion for energy purposes since they quickly react with other elements such as Si to create alkali with very low melting temperatures (about 700$^{o}$C). Biomass ashes with a larger K concentration may have a larger slag potential, whereas ashes with a lower K and higher Ca concentration may have more manageable slagging, fouling, and corrosion issues (Monti *et al.*, 2008; Zając *et al.*, 2018). On the other hand, at elevated temperatures, some volatile elements such as Cl may react to form a sticky deposit in the presence of K and Si (Miles *et al.*, 1996); again, high Si to K ratio is known to reduce slagging (Baxter *et al.*, 1998; Reumerman & Van den Berg, 2002). In the present study, both samples found a high concentration of K and Si/K and a significant concentration of Cl. These findings suggest that the rice husk variety investigated is better suited for SCW gasification than traditional downdraft gasification to avoid the risk of slugging and fouling problems. Furthermore, the presence of significant concentrations of K, Ca and Fe, as well as low amounts of potentially toxic elements such as arsenic and lead (which were below the detection limit),

suggests that rice husk ash residual could be utilised as a fertiliser in agriculture (Zając *et al.*, 2018). High Si composition suggests its industrial utilization (Antonkiewicz, 2009).

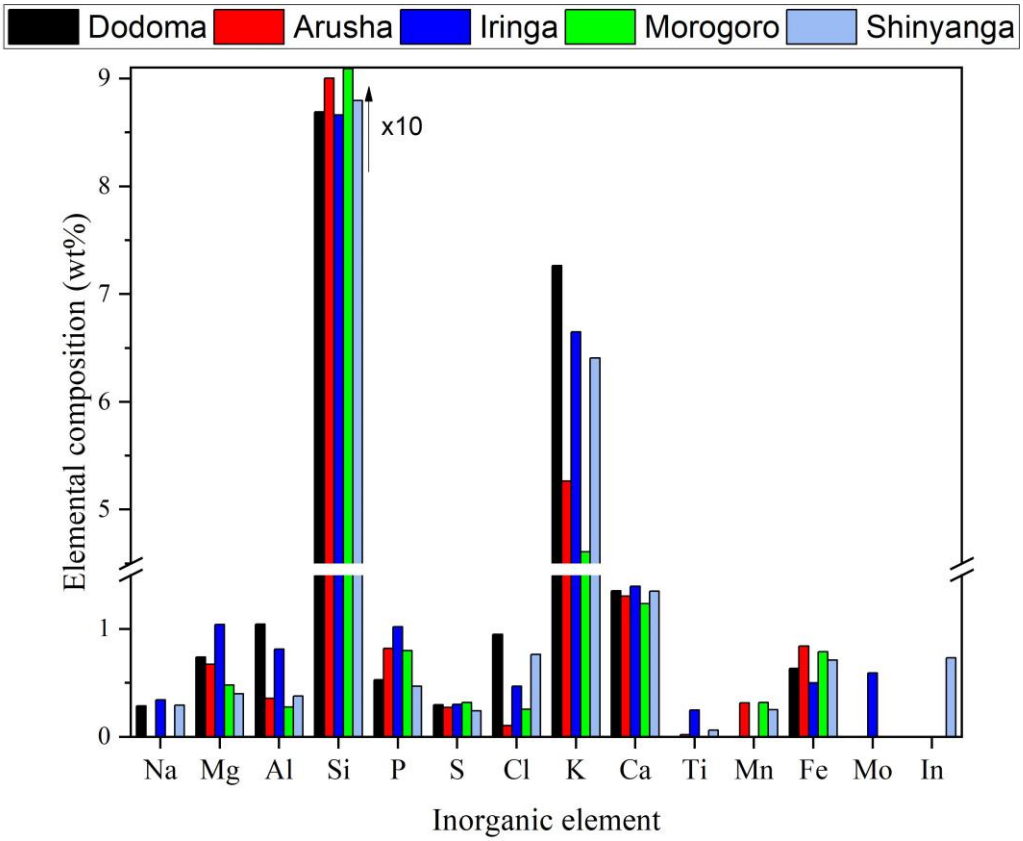


**Figure 27: The composition of inorganic elements presented in different rice husk variety determined via EDX analysis**

### 4.2.5 Calorimetric Analysis

The average HHV for the five different RH varieties ranged between 12.66 MJ/kg and 13.36 MJ/kg, while lower heating value based on calculation (Equation 26) ranged between 12.00 MJ/kg and 12.79 MJ/kg. One-way ANOVA revealed a significant difference in the heating value of varieties of rice husks at the 5% confidence level since $p<0.05$, as shown in Table 8. The obtained HHV values were within the range of 12.5 to14.6 MJ/kg and 12.8 to 14.5 MJ/kg reported by Sun *et al.* (2009) and Olupot *et al.* (2016), respectively. Said *et al.* (2014) reported the HHV value of 13.24 MJ/kg for the sample collected from Morogoro, close to the (0.34 higher) value of the sample from the same region reported in this study. Sheng and Azevedo (2005) developed a correlation based on ultimate analysis (Equation 25) to calculate the HHV to validate the value obtained by bomb calorimetry. The empirical HHV varied between 12.33 MJ/kg and 14.13 MJ/kg (Fig. 28). The HHV results from the experimental agreed well with the

value from empirical correlation with average error ranging between 2.4% and 7.1%. This error value is within 90% prediction accuracy of the correlation, as described by the author.

**Table 8: The Heating value of rice husks from different regions of Tanzania**

| Rice husk variety | High heating value[a] (MJ/kg) | Lower heating value (MJ/kg) |
|---|---|---|
| Arusha | 13.36±0.06 | 12.79 |
| Shinyanga | 12.81±0.06 | 12.26 |
| Morogoro | 12.86±0.12 | 12.21 |
| Dodoma | 13.04±0.08 | 12.42 |
| Iringa | 12.63±0.11 | 12.00 |
| p-*value* | <0.001 | - |
| F-*value* | 13.46 | - |

[a] Average of three replicates

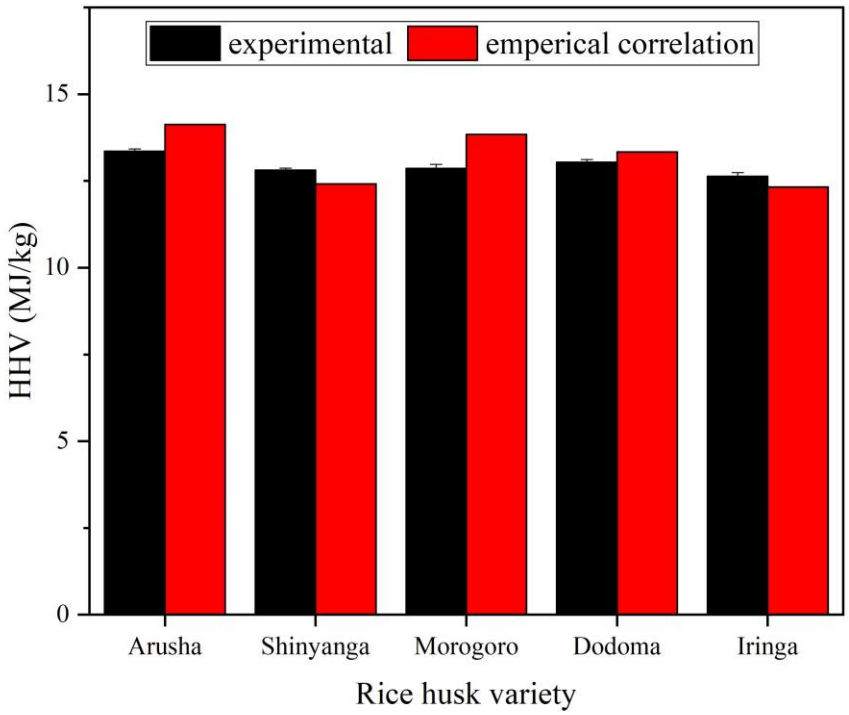


**Figure 28: Comparison of HHV from experimental and empirical correlation**

The HHV of different varieties of rice husk was correlated with geographical factors and chemical compositions. The coefficient correlation between geographical factors and the HHV of rice husk varieties showed a strong negative correlation with latitude (-0.6492), positive correlation with longitude (0.3241), and no correlation with altitude (0.0417). The results of linear correlation demonstrated no credible linear fitting between HHV and latitude ($R^2$ = 0.2616), longitude ($R^2$ = 0.1899) and altitude ($R^2$ = 0.0266) as shown in Fig. 29. In this study,

no clear variation in HHV with different geographical factors was found, which is consistent with Yan *et al.* (2018) analysis of variation in the calorific values of different plant organs.

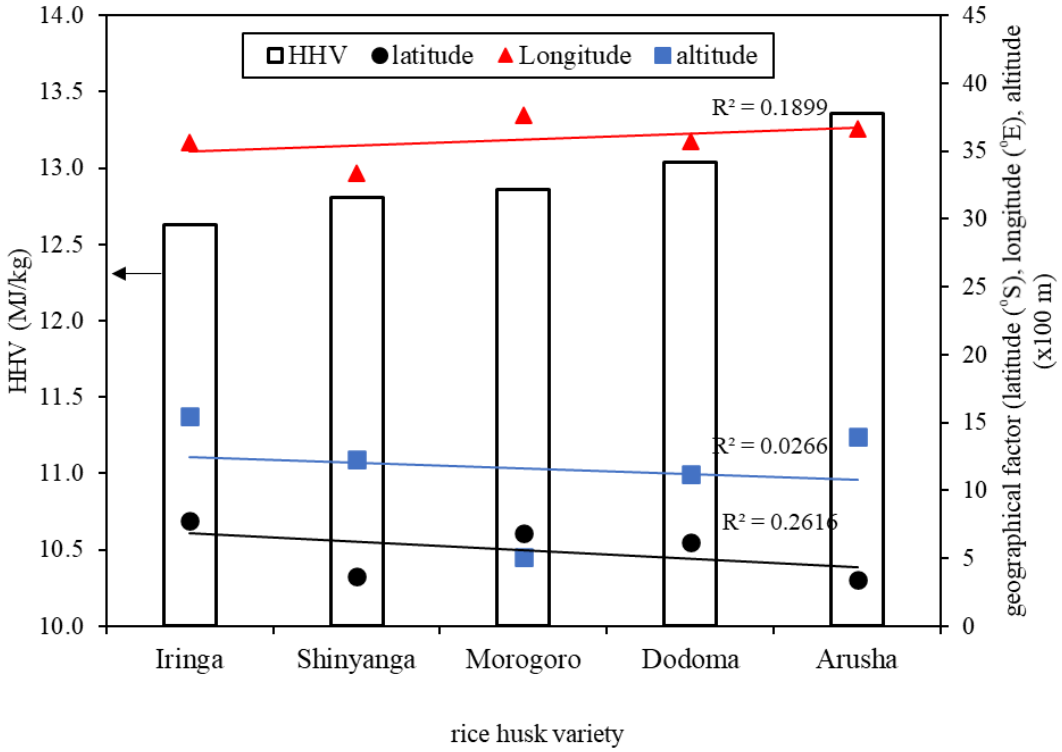


**Figure 29: Linear analysis of geographical factors of the regions and HHV**

Figure 30 depicts a qualitative relationship between HHV and the ash content, elemental carbon, oxygen, and holocellulose composition of various rice husks. There is a strong trend that HHV decreases with high ash content in biomass, which was also observed by Mansaray and Ghaly (1997), and Sheng and Azevedo (2005). The HHV and ash content have a significant correlation ($R^2$ = 0.9352). The correlation between HHV and holocellulose composition ($R^2$ = 0.5035), elemental carbon ($R^2$ = 0.7213), and oxygen ($R^2$ = 0.5883), on the other hand, shows a clear pattern, with the HHV value increasing with holocellulose composition, elemental carbon, and oxygen. The carbon content of biomass fuel contributes to increasing the HHV due to the release of $CO_2$ after combustion. A trend for increasing HHV with the increase of oxygen composition is observed in this study which contradicts the findings reported by Demirbas (2007). Since oxygen is not commonly thought to be a reactive element, higher oxygen content can indicate a low HHV value. Sheng and Azevedo (2005) found no correlation between oxygen content and HHV while developing a correlation for estimating HHV from proximate, ultimate and chemical analysis data. In contrast, only a trend exists between HHV and elemental hydrogen ($R^2$ = 0.3048), volatile matter ($R^2$ = 0.297), and fixed carbon ($R^2$ = 0.1219). A low R-squared indicates a slightly correlation between HHV, hydrogen, volatile matter, and fixed carbon. Higher HHV with high hydrogen content is in line with common sense that higher hydrogen content means

the higher energy content of biomass. A similar observation is published elsewhere ( Demirbas, 2007; Sheng & Azevedo, 2005). The HHV values of the RH variety studied are nearly half those of standard coal, indicating its potential as an alternative fuel feedstock for combustion and subsequent heat and electricity generation through gasification.

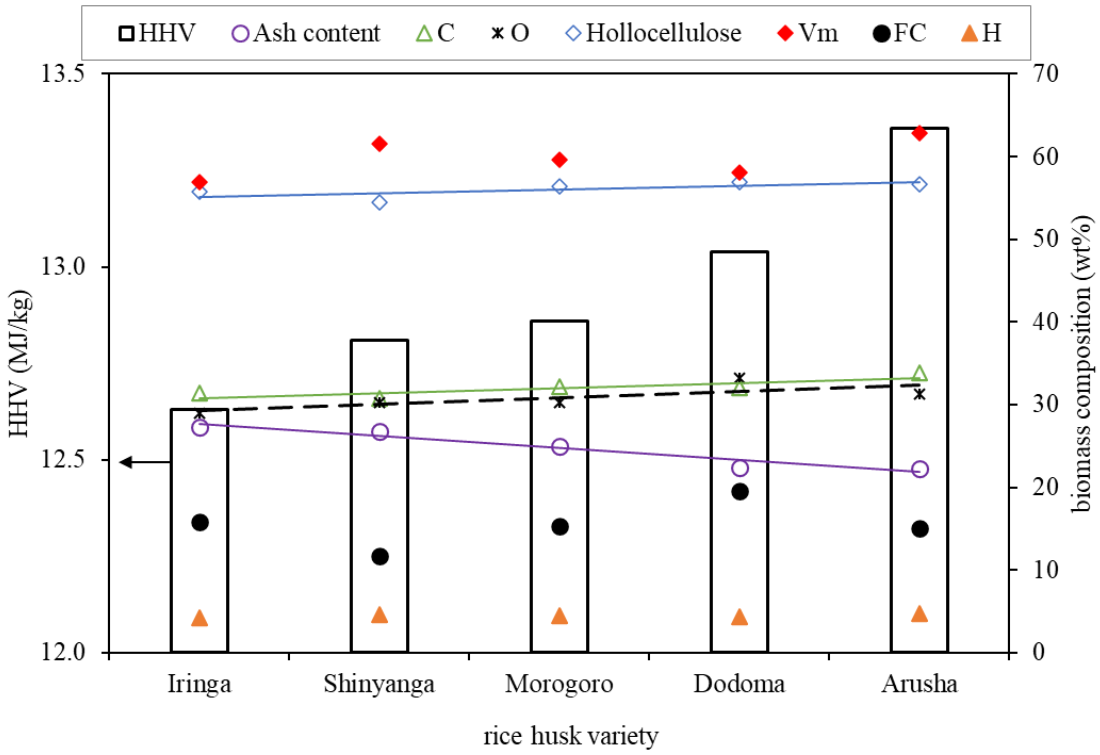


**Figure 30: Correlation of HHV and different biomass composition for varieties of rice husk**

### 4.2.6 XRD Analyses

The XRD measurements of unburnt RH powder were performed using Olympus Terra XRD/XRF portable device (Co Kα, λ = 1.5406 Å) at a 2θ = 5 to 55 and scanning step of 0.05. Figure 31 shows the X-ray diffractogram pattern of a variety of RH powder. The featureless pattern and lack of significant peaks in this diffractogram show that the RH contained silica, which was entirely amorphous to XRD. The occurrence of a diffuse maximum at around 2θ = 26° confirms the presence of $SiO_2$ compound (Hamdan *et al.*, 1997; Yusof *et al.*, 2010). It is important to note that not every RH powder has amorphic features; for example, Lee *et al.* (2013) discovered that the silica ($SiO_2$) found in unburnt Malaysia RH powder was predominantly crystalline. Amorphous silica is a highly reactive silicon source, though not all silica which is amorphous to XRD is equally suitable (Hamdan *et al.*, 1997). Therefore, the examined variety of RH could be employed as a low-cost substitute for silica in various industrial applications, including the manufacture of zeolites. Nevertheless, the reactivity of

silica is primarily reliant on the method of preparation and extraction from RH, which requires independent research.

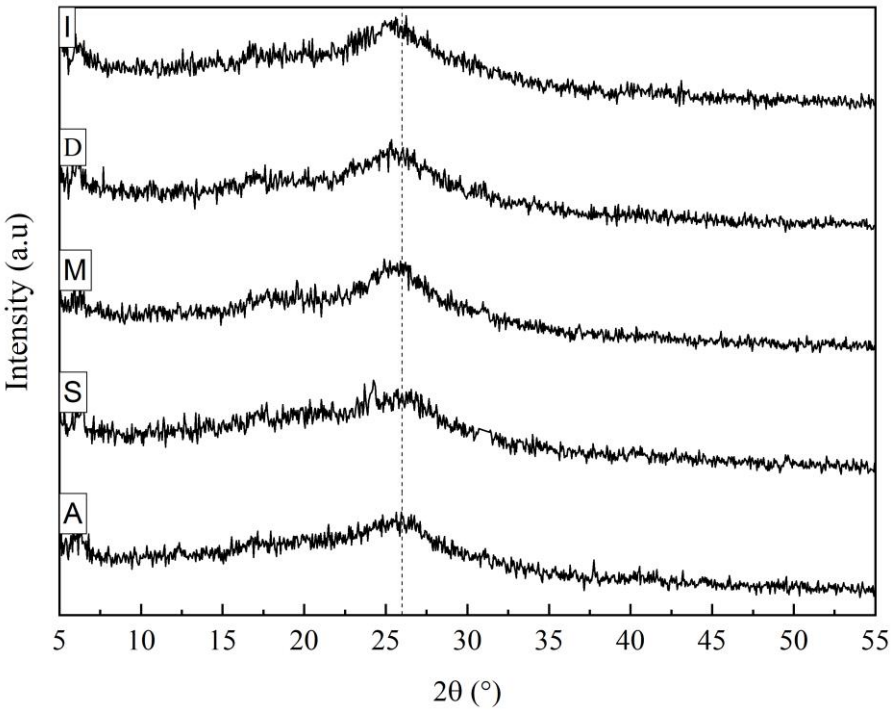


**Figure 31: X-ray diffractogram of a variety of rice husks. Arusha (A), Shinyanga (S), Morogoro (M), Dodoma (D), and Iringa (I)**

### 4.3 Optimization of Super Critical Water Gasification of Rice husk

The RH sample from the Dodoma region was randomly chosen as the starting feedstock for developing an optimization model to avoid running too many experiments. Following that, other gasification reactions for different rice husks were carried out based on the optimum condition found.

#### 4.3.1 Model Fit and Statistical Analysis

Table 10 shows the predicted and experimentally measured responses for the 20 runs according to the Design-Expert software formulated experiments. The GE ranged from 48.96% to 64.45% on dry basis feedstock, and the maximum value was obtained from the 9$^{th}$ run, under the condition of $X_1$ = 406°C, $X_2$ = 120 minutes and $X_3$ = 3.0 wt%. On the other hand, char and gravimetric tar yield assumed values from 24.96 to 39.42 wt% and 31.13 to 185.47 mg/g-biomass, respectively. The lowest gravimetric tar yield was observed from the 14$^{th}$ run under the experimental condition of $X_1$ = 500°C, $X_2$ = 70 minutes and $X_3$ = 7.8 wt%. The gas volume

ranged from 88.37 to 428 mL/g biomass, and the highest value was obtained from the 5$^{th}$ run, under the experimental condition of $X_1$ = 500°C, $X_2$ = 120 minutes and $X_3$ = 3.0 wt%.

The obtained results were fitted to a second-order polynomial model, and the Design-Expert software suggested a quadratic model for both responses, as shown in Table 9. The final empirical models in terms of the coded variable (Equation 31-34) were derived after the reduction of trivial terms ($p > 0.1$) through the *p*-values backward model selection algorithm in the Design-Expert software. Nominal terms that were required to support a hierarchy of the model were reserved. Therefore, $X_1$, $X_2$, $X_3$, $X_1 X_2$, $X_1^2$, $X_2^2$ and $X_3^2$ are significant terms for the GE model, while the terms $X_1$, $X_2$, $X_3$, $X_1 X_2$, $X_2^2$ and $X_3^2$ are significant terms for the char yield model. On the other hand, the model terms $X_1$, $X_2$, $X_3$, $X_1 X_2$, $X_1^2$ and $X_3^2$ are significant model terms from gravimetric tar yield, while $X_1$, $X_2$, $X_3$, $X_1 X_3$, $X_1^2$ and $X_3^2$ are significant model terms for gas volume model.

**Table 9: Response transformation and model fitting summary**

| Response | Response range | Ratio* | Transformation | Fit summary |
|---|---|---|---|---|
| GE | 49.0 – 64.5 | 1.3 | none | Quadratic |
| Char yield | 25 – 39.4 | 1.5 | none | Quadratic |
| Gravimetric tar yield | 31.1 – 185.5 | 5.9 | none | Quadratic |
| Gas volume | 88.4 – 428.6 | 4.8 | none | Quadratic |

*Ratio of maximum to the minimum response (a ratio >10 suggests response transformation)

$$\text{GE (\%)} = 59.46 + 2.65X_1 + 0.7985X_2 - 2.21X_3 + 1.59X_1X_2 - 4.72{X_1}^2 - 0.8557{X_2}^2 + 2.36{X_3}^2 \quad (31)$$

$$\text{Char yield (wt\%)} = 35.25 + 2.93X_1 + 0.1607X_2 + 3.58X_3 - 1.53X_1X_3 + 1.12{X_2}^2 - 3.30{X_3}^2 \quad (32)$$

$$\text{Gravimetric tar yield (wt\%)} = 54.41 - 56.09X_1 - 9.11X_2 - 12.30X_3 + 5.74X_1X_2 + 41.0{X_1}^2 + 9.90{X_3}^2 \quad (33)$$

$$\text{Gas volume } \left(\frac{\text{mL}}{\text{g}}\text{biomass}\right) = 187.65 + 119.58X_1 + 13.24X_2 - 35.32X_3 - 30.30X_1X_3 + 19.21{X_1}^2 + 18.47{X_3}^2 \quad (34)$$

Equation (31) – (34) can be used to predict the GE, char yield, gravimetric tar yield, and gas volume, respectively. Generally, the negative sign signifies the antagonistic effect of the factors, and the positive sign indicates the synergistic effects of the factors. Examining the coefficients and the power of the polynomial model factors, it is clear that the temperature has the most substantial influence on SCW gasification, followed by the feed concentration and the residence time. In the range of experimental parameters, the results of the experiments show that the order

of severity of factors on the GE, char yield, gravimetric tar yield and gas volume follows a similar trend: Temperature > feedstock concentration > residence time, which is in good agreement with the rank reported by Lu *et al.* (2012). On the other hand, Chen *et al.* (2020) found a different trend (temperature > residence time > feedstock concentration) while experimenting on the gasification characteristics of food waste using SCW. This inconsistency may be influenced by the range of operating conditions, reactor type, reactor configurations, and the type of biomass studied (Chen *et al.*, 2020).

A test for the significance of the regression model and its coefficient, lack-of-fit and pure-error was performed to ensure that the derived polynomial model fits well with the experimental data. The significant factors are ranked based on the probability value (*p*-value) with a 95% confidence level. The analysis of variance (ANOVA) for the responses generated by equations 31 to 34 are shown in Table 11. A smaller *p*-value ($p < 0.05$) indicates that both models are significant. Non-significant lack-of-fit ($p>0.05$) for both derived models implies that the lack-of-fit is not substantial relative to pure error, and the models can accurately predict the variations. The quality of the fitted polynomial model can be determined by R-squared, which represents the proportion of the variability of the data accounted for in the statistical model. It is more appropriate also to use Adj-$R^2$, which penalises the statistic $R^2$ if unnecessary terms are added in the model (Fermoso *et al.*, 2010). In practise, $R^2$ should be at least 0.75, and values above 0.90 are deemed very good (Gunst, 1996; Hamada & Wu, 2000). In this study, the $R^2$, adjusted $R^2$ and predicted $R^2$-value for all responses are close to 1 (>0.9), indicating the accuracy of the predicted polynomial model (Table 12). The predicted $R^2$ is in reasonable agreement with adjusted $R^2$ for both responses (the difference is less than 0.2), demonstrating a high correlation between the experimental and the predicted values. Moreover, it implies that the proposed regression models provide an acceptable explanation of the interaction between independent variables and responses. Adequate precision measures the signal to noise ratio, and a ratio greater than four is desirable. In this study, the ratio between 26.54 to 56.65 is obtained, indicating an adequate signal, and it also suggests that the models have a robust signal to be used for optimisation. The coefficient of variation (CV) indicates the degree of precision with which the experiments are compared (Gangadharan *et al.*, 2008). In this case, a low coefficient of variation (CV) for both regression models (< 8.05%) indicates that model reproducibility is satisfactory (Table 12).

The normal probability plots of the residual and experimental versus predicted values were used to ascertain the validity of the predicted models. The residuals are the difference between the

actual and the predicted values. The plots for the normal probability and the externally studentised residuals and the predicted versus actual values for both responses are presented in Fig. 32 and 33. Figures 32a to 32e reveals that the residuals are generally distributed along the line of best fit, implying that errors are distributed normally with no abnormality in the models. Observation of Fig. 33a to 33e suggests that the predicted values are in good agreement with the experimental ones within the design space.

**Table 10: Experimental variables and products distribution of sub- and supercritical water gasification of rice husk using I-optimality design**

| Run No | Variables | | | Response variables | | | | | | | |
|---|---|---|---|---|---|---|---|---|---|---|---|
| | $X_1$ | $X_2$ | $X_3$ | GE (%) | | Char yield (wt%) | | Gravimetric tar yield (mg/g) | | Gas volume (mL/g) | |
| | (°C) | (min.) | (w%) | Exp. | Pred. | Exp. | Pred. | Exp. | Pred. | Exp. | Pred. |
| 1 | 500 | 30 | 10 | 57.6 | 57.5 | 38.3 | 37.9 | 40.5 | 40.3 | 273.5 | 266.1 |
| 2 | 353 | 80 | 6 | 53.7 | 53.0 | 31.8 | 31.9 | 145.4 | 146.5 | 88.4 | 92.3 |
| 3 | 418 | 120 | 8 | 57.6 | 58.5 | 38.1 | 37.2 | 43.5 | 47.5 | 186.9 | 179.3 |
| 4 | 500 | 120 | 7 | 56.5 | 57.3 | 39.4 | 39.8 | 40.7 | 33.4 | 334.8 | 324.0 |
| 5 | 500 | 120 | 3 | 60.8 | 60.3 | 34.3 | 34.1 | 49.6 | 58.2 | 428.6 | 423.8 |
| 6 | 433 | 32 | 6 | 58.0 | 58.4 | 36.9 | 36.0 | 50.1 | 58.7 | 188.8 | 191.1 |
| 7 | 353 | 80 | 6 | 52.2 | 53.0 | 32.3 | 31.9 | 154.1 | 146.5 | 89.5 | 92.3 |
| 8 | 433 | 32 | 6 | 59.0 | 58.4 | 35.2 | 36.0 | 58.0 | 58.7 | 186.5 | 191.1 |
| 9 | 406 | 120 | 3 | 64.5 | 63.4 | 27.8 | 28.5 | 77.4 | 82.7 | 206.1 | 218.4 |
| 10 | 418 | 57 | 3 | 61.9 | 63.4 | 28.4 | 28.0 | 96.5 | 86.5 | 235.0 | 221.4 |
| 11 | 350 | 30 | 3 | 56.5 | 56.6 | 25.0 | 24.9 | 185.5 | 188.6 | 94.7 | 97.5 |
| 12 | 452 | 91 | 5 | 61.4 | 60.9 | 33.2 | 34.9 | 53.3 | 42.8 | 264.3 | 258.1 |
| 13 | 433 | 80 | 10 | 59.3 | 60.0 | 36.1 | 35.8 | 45.8 | 45.7 | 179.4 | 181.3 |
| 14 | 500 | 70 | 8 | 57.7 | 57.4 | 39.2 | 38.5 | 31.1 | 36.4 | 283.8 | 302.6 |
| 15 | 433 | 32 | 6 | 58.6 | 58.4 | 35.6 | 36.0 | 58.4 | 58.7 | 186.5 | 191.1 |
| 16 | 500 | 63 | 3 | 59.8 | 60.1 | 33.5 | 32.9 | 66.6 | 62.4 | 402.1 | 407.1 |

| Run No | Variables | | | Response variables | | | | | | | |
|---|---|---|---|---|---|---|---|---|---|---|---|
| | $X_1$ | $X_2$ | $X_3$ | GE (%) | | Char yield (wt%) | | Gravimetric tar yield (mg/g) | | Gas volume (mL/g) | |
| | (°C) | (min.) | (w%) | Exp. | Pred. | Exp. | Pred. | Exp. | Pred. | Exp. | Pred. |
| 17 | 433 | 80 | 10 | 61.0 | 60.0 | 34.5 | 35.8 | 44.9 | 45.7 | 179.4 | 181.3 |
| 18 | 350 | 120 | 10 | 50.5 | 50.6 | 36.0 | 35.4 | 135.1 | 134.2 | 104.2 | 114.0 |
| 19 | 353 | 80 | 6 | 53.3 | 53.0 | 32.5 | 31.9 | 141.6 | 146.5 | 105.1 | 92.3 |
| 20 | 350 | 30 | 10 | 49.0 | 49.0 | 34.5 | 35.1 | 165.7 | 164.0 | 95.2 | 87.5 |

Where: $X_1$ is the temperature, $X_2$ is the residence time, $X_3$ is the feed concentration, *Exp.* is the experimental value, and *Pred.* is the predicted value

**Table 11: Analysis of variance for the response surface reduced quadratic model**

| | GE (%) | | | Char yield (wt%) | | | Gravimetric tar yield (mg/g) | | | Gas volume (mL/g) | | |
|---|---|---|---|---|---|---|---|---|---|---|---|---|
| | **SS** | **F** | ***p*** | **SS** | **F** | ***p*** | **SS** | **F** | ***p*** | **SS** | **F** | ***p*** |
| Model | 293.86 | 56.83 | <0.0001 | 264.49 | 54.44 | <0.0001 | 47328.87 | 171.62 | <0.0001 | 193494.69 | 296.71 | <0.0001 |
| $X_1$ | 76.14 | 103.08 | <0.0001 | 93.02 | 114.88 | <0.0001 | 34178.85 | 743.63 | <0.0001 | 154830.46 | 1424.55 | <0.0001 |
| $X_2$ | 6.46 | 8.74 | 0.0120 | 0.26 | 0.32 | 0.5793 | 914.04 | 19.89 | 0.0006 | 1779.96 | 16.38 | 0.0014 |
| $X_3$ | 50.26 | 68.05 | <0.0001 | 132.38 | 163.49 | <0.0001 | 1421.32 | 30.92 | <0.0001 | 12879.64 | 118.50 | <0.0001 |
| $X_1 X_2$ | | | | | | | 180.53 | 3.93 | 0.0690 | | | |
| $X_1 X_3$ | 14.00 | 18.95 | 0.0009 | 13.02 | 16.07 | 0.0015 | | | | 5078.40 | 46.72 | <0.0001 |
| $X_1^2$ | 96.99 | 131.31 | <0.0001 | | | | 7117.23 | 154.85 | <0.0001 | 1604.43 | 14.76 | 0.0020 |
| $X_2^2$ | 3.09 | 4.18 | 0.064 | 5.30 | 6.55 | 0.0238 | | | | | | |
| $X_3^2$ | 22.30 | 30.19 | 0.0001 | 44.34 | 54.76 | <0.0001 | 417.66 | 9.09 | 0.0100 | 1401.04 | 12.89 | 0.0033 |
| Residual | 8.86 | | | 10.53 | | | 597.51 | | | 1412.94 | | |
| Lack of Fit | 5.76 | 1.33 | 0.3903 | 7.19 | 1.35 | 0.3874 | 470.98 | 2.33 | 0.1837 | 1233.31 | 4.29 | 0.0627 |
| Pure Error | 3.10 | | | 3.34 | | | 126.52 | | | 179.62 | | |

| | GE (%) | | | Char yield (wt%) | | | Gravimetric tar yield (mg/g) | | | Gas volume (mL/g) | | |
|---|---|---|---|---|---|---|---|---|---|---|---|---|
| | **SS** | **F** | ***p*** | **SS** | **F** | ***p*** | **SS** | **F** | ***p*** | **SS** | **F** | ***p*** |
| | 302.7 | | | 275.0 | | | 47926.3 | | | 194907.6 | | |
| Cor Total | 3 | | | 2 | | | 8 | | | 3 | | |

**Table 12: Model fit statistics for the gasification yield**

| Parameters | GE (%) | Char yield (wt%) | Gravimetric tar yield (mg/g) | Gas volume (mL/g) |
|---|---|---|---|---|
| $R^2$ | 0.9707 | 0.9617 | 0.9875 | 0.9928 |
| Adj $R^2$ | 0.9536 | 0.9441 | 0.9818 | 0.9894 |
| Pred $R^2$ | 0.9248 | 0.9172 | 0.9714 | 0.9814 |
| Adeq. precision | 26.543 | 27.981 | 38.675 | 54.525 |
| Std. Dev. | 0.859 | 0.900 | 6.78 | 10.430 |
| Mean | 57.45 | 34.13 | 84.19 | 205.64 |
| C.V. % | 1.50 | 2.64 | 8.05 | 5.07 |
| PRESS | 22.76 | 22.77 | 1371.88 | 3633.15 |

Where *CV* is the coefficient of variance

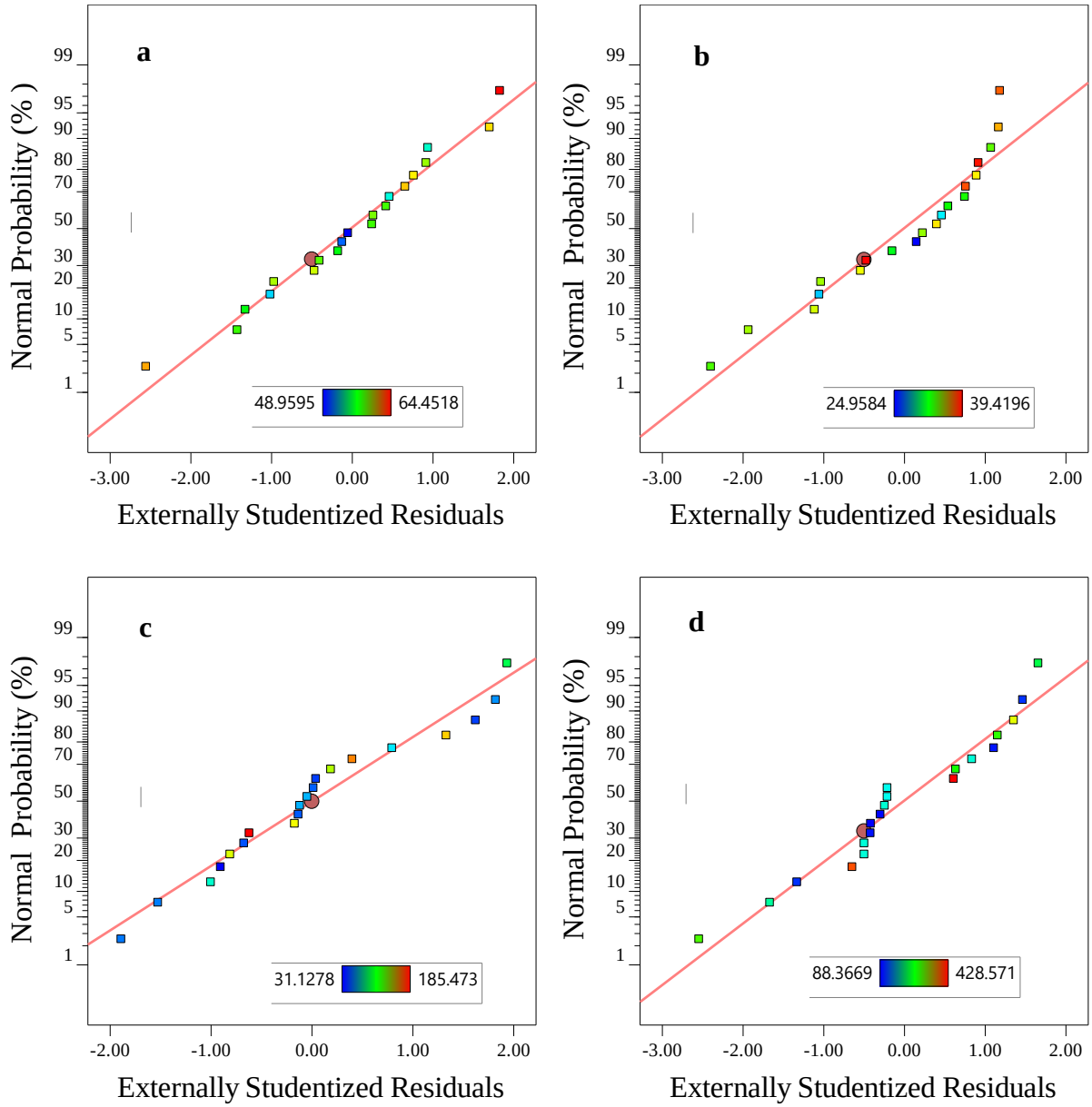


**Figure 32:** **Studentised residuals and normal percentage probability plot for (a) GE, % (b) char yield, wt% (c) gravimetric tar yield, mg/g-biomass and (d) gas volume, mL/g-biomass**

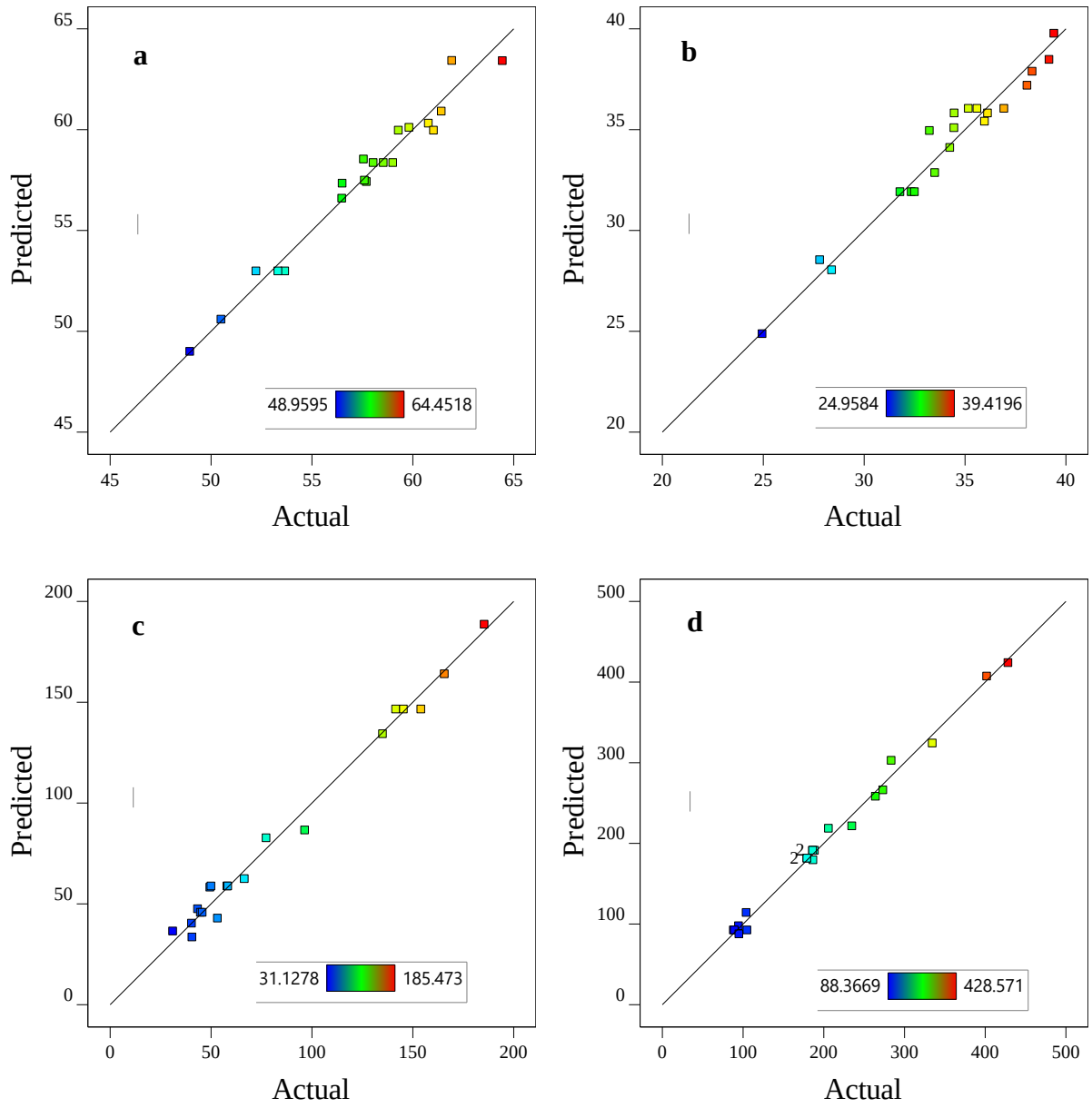


**Figure 33: Comparisons of predicted and experimental values of SCW gasification for (a) GE, % (b) char yield, wt% (c) gravimetric tar yield, mg/g-biomass and (d) gas volume, mL/g-biomass**

### (i) Influence of Gasification Parameters on Gasification Efficiency

Gasification efficiency is defined as the percentage of the total mass of gas product per total mass of the feed (GE = (the total mass of gas (g)/the mass of dry feedstock (g)) x 100%) (Chen *et al.*, 2020). The total mass of the gas product is obtained by differences (total mass of gas = mass of RH feed - total mass of tar - total mass of char). The perturbation plot is used in examining the impact of individual effects of temperature, residence time and feed concentration in SCW gasification yield. The plots help compare all the parameters at a particular point in the design space by shifting one factor while others remain constant.

Generally, the perturbation curve is plotted by picking a reference point and adjusting the operational range of each variable involved. Thereafter the reference point is adjusted at the centre of each factor, and the responses are plotted against the deviation from the reference point. A steeper or curvature slope in the response accentuates the level of the sensitiveness of the response to that parameter. A relatively flat line signifies that the response is insensitive to change in that particular factor (Hossain *et al.*, 2017). The perturbation plots for GE yield (Fig. 34) show that temperature and feed concentration have curvature slopes while the residence time has a gradual slope. These observations imply that the GE is sensitive to the changes of both temperature, feed concentration and residence time, the latter having a slight influence.

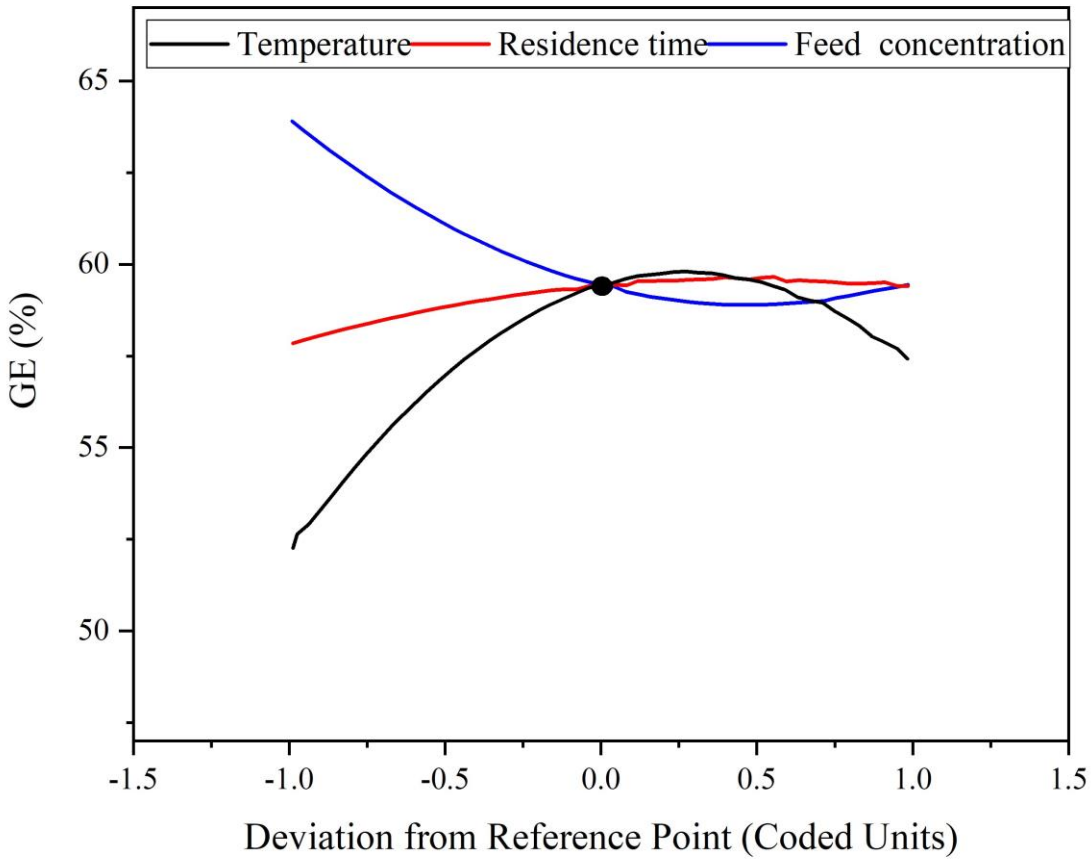


**Figure 34: Perturbation plot showing the interaction of factors on GE (process variables is found in Table 10)**

Figure 35 shows the contour and 3D surface plots for different interaction factors on GE. A contour and three-dimensional (3D) response surface plot provides the best way to visualise the interactions of the independent and dependent variables and facilitates the optimal condition for response yield. Figures 35a and 35b show that GE increases with an increase in temperature and residence time at a constant feed concentration of 6.5 wt%. The maximum GE of 60% was attained at a residence time of 95 minutes, and a temperature of 446°C, any further increase of

these two factors resulted in a steady reduction of GE. Deniz *et al.* (2015) reported a similar observation, but the maximum GE obtained (48%) was lower than that recorded in this study. The decrease of GE at higher temperature and residence time may be attributed to coke or carbon formation as a by-product of reforming reactions. Coke and carbon formation reactions are discussed in detail in section (iv).

The GE increases sharply with the rise in temperature from 350 to 446°C due to rapid devolatilization of feedstock but shows a more gradual increase with an increase in residence time due to a slow char gasification reaction (Wang *et al.,* 2020). Temperature is the most crucial parameter in the SCW gasification of biomass; higher temperature maximizes GE and increases the overall gas volume. As temperature increases beyond the critical point, water density decreases; thus, resulting in a lower ionic product favouring the shift of ionic mechanism to free radical mechanism. The latter enhances biomass decomposition and favours the reaction forming a gaseous product (Reddy *et al.,* 2014). Promdej and Matsumura (2011) investigated the subcritical, and SCW gasification of glucose model compounds at a temperature range of 300 to 460°C and a feed concentration of 1.5 wt%. The study revealed that subcritical water gasification reaction was dominated by ionic mechanisms, indicating low GE due to the insignificant amount of energy for endothermic reaction of breakdown of complex biomass molecules. The observed decrease in GE in this study at a temperature beyond 446°C could be attributed to coke and carbon formation. This finding is consistent with other existing literature (Hantoko *et al.,* 2019; Su *et al.,* 2020). The interaction between biomass concentration and other independent variables (temperature and residence time) Fig. 35c to 35e shows a similar trend whereby the maximum GE of approximately 64.15% was observed at the lowest biomass concentration of 3.0 wt%.

Notably, the effect of interaction between feed concentration and temperature on GE portrayed hyperbolic paraboloid-like shape. The GE under the condition of biomass concentration of 6.2 wt% and 9.3 wt% at a constant temperature of 450°C and residence time 75 minutes were similar, near 60%. Also, the same GE of 58% was observed under the following condition: The 407°C and 492°C and a constant biomass concentration of 7.4% and a residence time of 75 minutes (Fig. 35c and 35d). This trend may be influenced by the change of the two competing SCW reaction mechanisms, which are mass transfer and pyrolysis of the feedstock (Chen *et al.,* 2020). When the biomass concentration is 3 wt%, the mass transfer between biomass particles and water could be the dominating step in determining the overall reaction rate. When the feed concentration is increased, the mass transfer rate is suppressed, leading to a reduction of the GE.

The threshold at which the mass transfer rate starts to change is when the feed concentration exceeds 8 wt%. When the temperature reaches 450°C, and the feed concentration increases from 5.5 wt% to 10 wt%, the transition between the mass transfer mechanism and the pyrolysis of the feedstock occurs, the latter becomes the rate-determining step at a feed concentration of 10 wt%. This leads to a similar GE with different reaction mechanisms for the feed concentration of 5.5 wt% and 10 wt%. These findings are in good agreement with that reported in the literature (Chen *et al.,* 2020; Su *et al.,* 2015).

This study observed only a slight interaction of residence time with other independent variables in the overall GE. The GE varied slightly from 58.2 to 60% when the residence time increases from 30 to 95 minutes at 446°C (Fig. 3 (a, b)). Moreover, GE is significantly affected by the change in residence time for feed concentration below 5 wt% (Fig. 35e and 35f). At a feed concentration of 3 wt%, GE increases from 62.2 wt% to 64.2 wt% when the residence time changes from 30 to 118 minutes and then it begins to decrease, implying that a more extended residence will have a negligible impact on the change of GE. Similarly, as reported in other studies, Wang *et al.* (2020) noted a sharp increase of GE at residence time below 10 minutes and only slight variation beyond 15 minutes while studying the gasification mechanism of biomass in SCW. The impact of residence time was found to be more pronounced at low temperatures (<425°C) than at higher temperatures (Su *et al.,* 2020). In another study, Susanti *et al.* (2012) found no significant impact of residence time on the total GE in SCW gasification of glucose at 740°C. Reddy *et al.* (2014) showed that GE increases with residence time, usually in early-stage to a "certain time", and afterwards, no significant change resulted. This "certain time" is a function of many operating factors, including feedstock properties, feed concentration, reactor type and reaction temperature (Chen *et al.,* 2020). Under the condition of this study (constant feed concentration of 6.5 wt% and temperature 446°C), the "certain time" was found to be 95 minutes. This means that a residence time of 95 minutes was sufficient to some extent to yield higher GE during SCW gasification of RH at the condition of feed concentration 6.5 wt% and 446°C. Yet, in another study, Su *et al.* (2020) reported the "certain time" of 75 minutes at 480°C and feed concentration of 5 wt% during SCW gasification of unsorted food waste under the conditions of temperature between 420 to 480°C, feed concentration of 5 to 15 wt% and residence time 30 to 75 minutes.

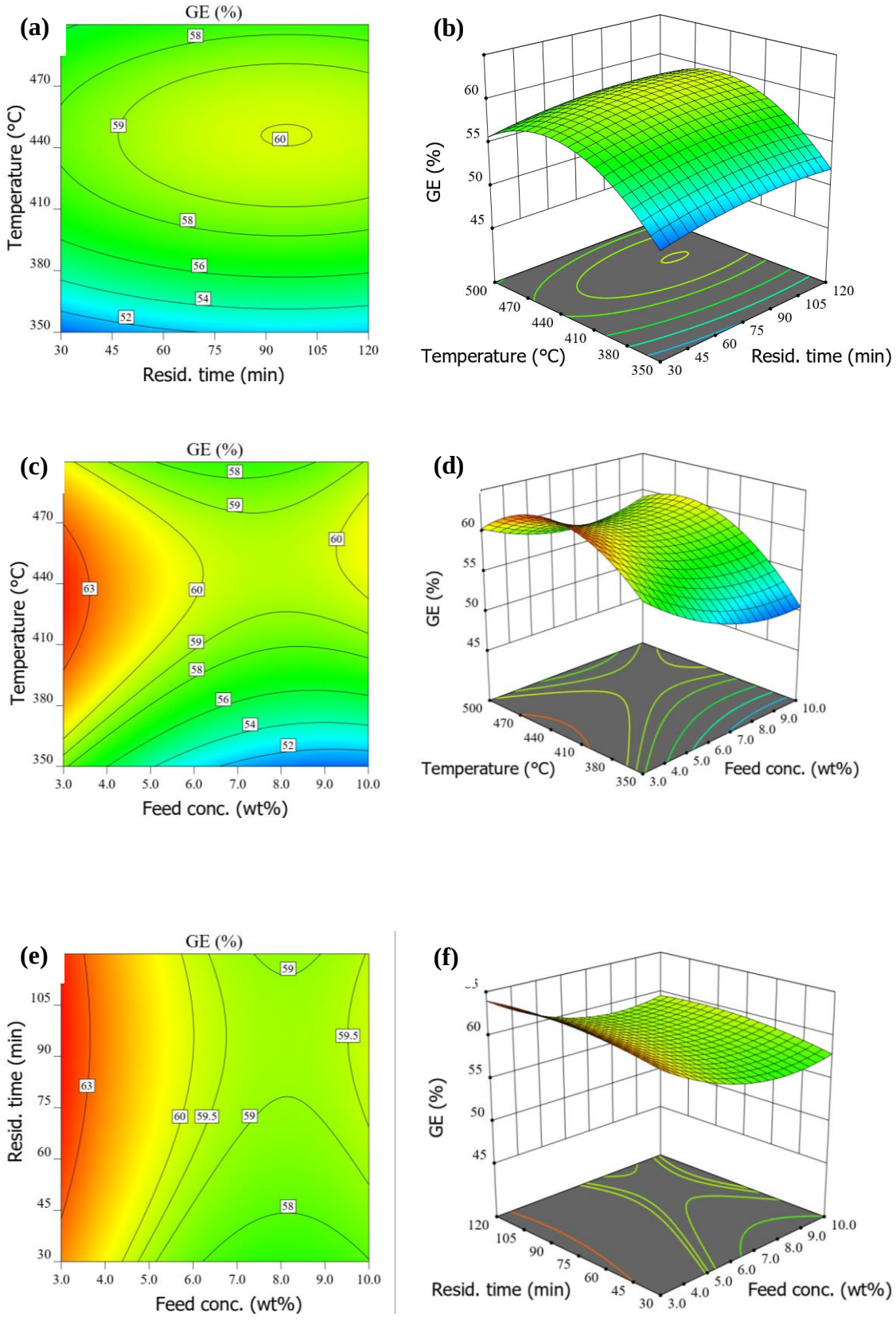


**Figure 35: Contour and 3D response surface plots representing different interactive effects of parameters on gasification efficiency: Temperature, residence time and feed concentration 6.5 wt% (a, b); temperature, feed concentration and residence time 66 minutes (c, d); and residence time, feed concentration and temperature 425°C (e, f)**

### (ii) Influence of Gasification Parameters on Gas yield

The perturbation plot of gas volume in Fig. 36 demonstrates that the temperature has a steeper slope, followed by feed concentration and then residence time. This implies that the gas volume is significantly sensitive to the temperature change and is moderately affected by feed concentration and residence time.

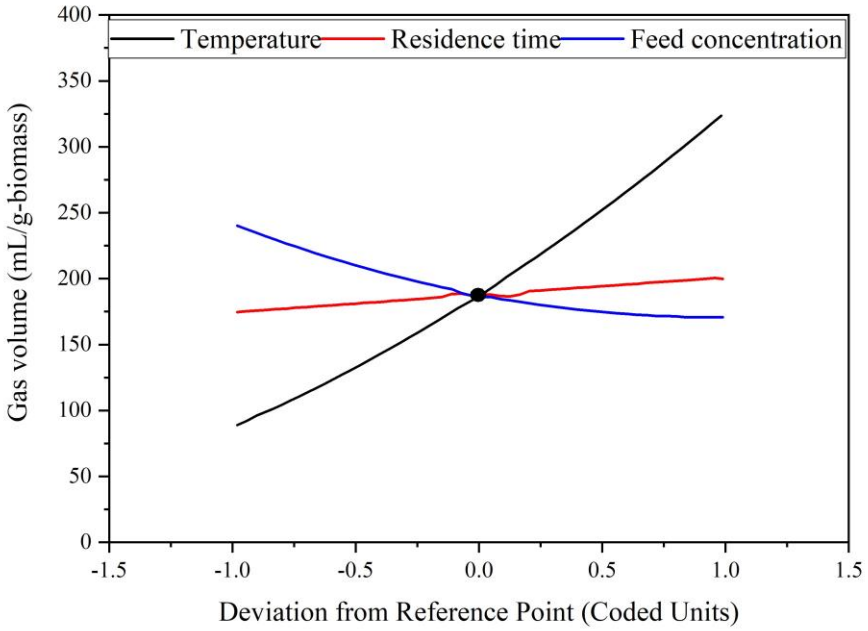


**Figure 36: Perturbation plot showing the interaction of factors on gas volume (process variables of Table 10)**

Figure 37a shows that a gas volume of 75 mL/g is obtained at a temperature of 350°C, a residence time of 30 minutes and a feed concentration of 6.5 wt%, and it rapidly increases to 313 mL/g when the temperature increases to 500°C. When the residence time increases from 30 to 120 minutes, the gas volume slightly increases from 313 to 339 mL/g. The increase in gas volume could be explained by the continuous breakdown of tar to form permanent gases. No significant interaction between residence time and feed concentration ($P$ = 0.7287) is observed, as shown in Fig. 37e and 37f.

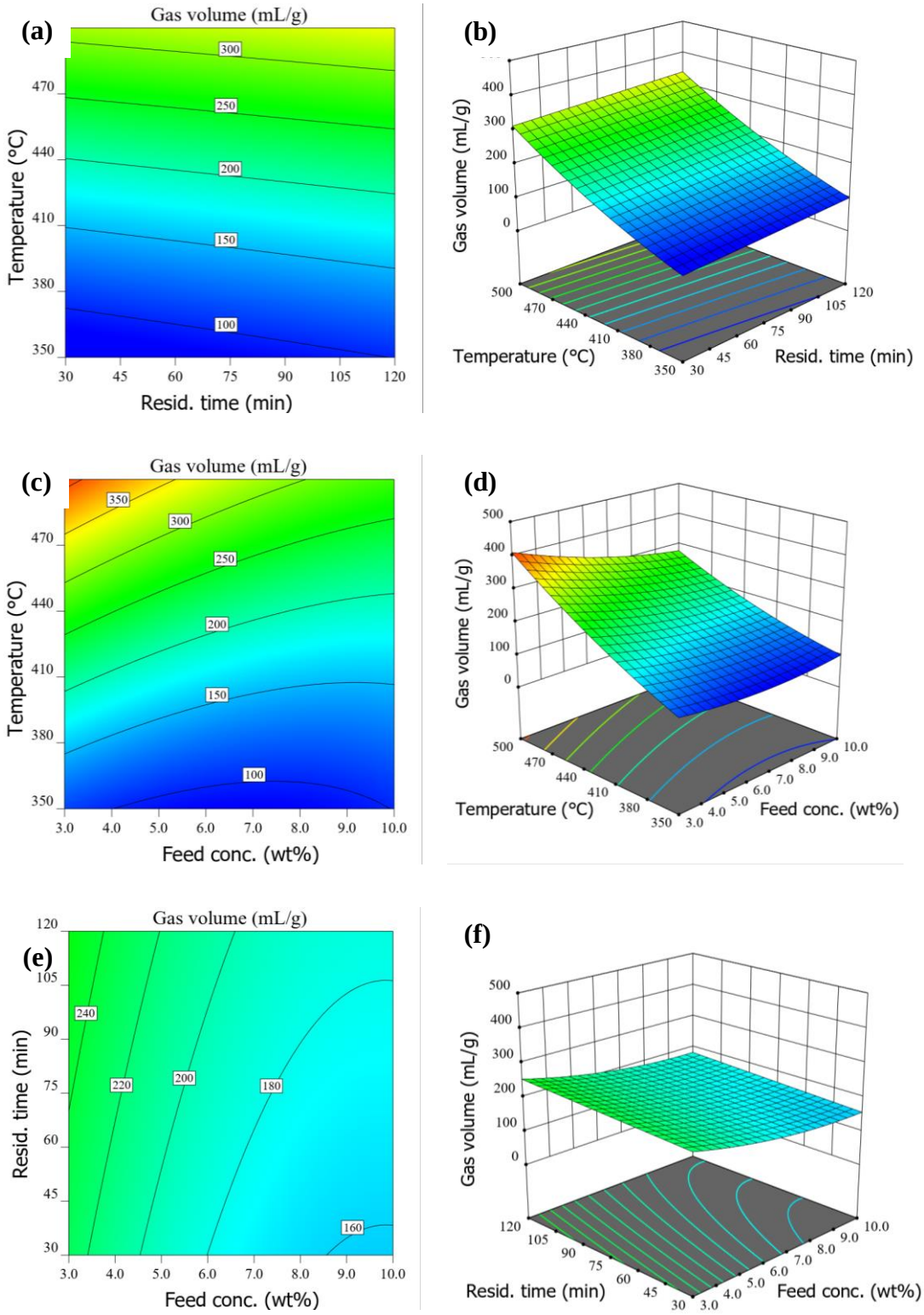


**Figure 37: Contour and 3D response surface plots representing different interactive effects of parameters on gas volume: Temperature and residence time, feed concentration 6.5 wt% (a, b); temperature and feed concentration, residence time 66 minutes (c, d) and residence and feed concentration, temperature 425°C (e, f)**

The results demonstrate a good agreement with the experimental data reported in the literature (Adar *et al.*, 2020; Su *et al.*, 2020). A close look at Fig. 37c and 37d shows that the maximum

gas volume of 410 mL/g could be obtained at 500°C and a feed concentration of 3.0 wt% while it sharply decreases to 279.3 mL/g when the feed concentration is increased to 10 wt%. At 350°C and a feed concentration of 3 wt%, a gas volume of 111 mL/g is archived, and it slightly decreases to 100 mL/g when the feed concentration rises to 10 wt%. This implies that temperature and feed concentration influence the gas volume, particularly at the higher reaction temperature. Higher feed concentration has an antagonistic effect on gas yield during the SCW gasification process. The volume of gas decreased abruptly with an increase in feed concentration inhibited presumably by the decomposition reactions of the biomass. Promdej and Matsumura (2011) reported a significant decrease in the gas yield by increasing glucose concentration from 1 to 17 wt%. The increase in feed concentration leads to a low fraction of water, thus impeding the reactions such as water-gas-shift reaction, backward methanation, and steam reforming (Equation 1-4), all of which utilise water as one of the reactants (Chen *et al.*, 2020; Wang *et al.*, 2020).

To illustrate the reaction behaviour inside the reactor, a representative of pressure and temperature for experiment run-4 (500°C and 120 minutes residence time) and run-12 (452°C and 90 minutes residence time) is presented in Fig. 38. In all experimental runs, the reactor was progressively heated from ambient temperature to a destination temperature at an average heating rate of 4°C/minutes and maintained for the required residence time. During the residence time, the temperature remained constant while the pressure slowly increased due to progressive partial gasification of the tar to form permanent gas. The maximum pressure reached in each experiment depends strongly on the feed concentration, reaction temperature and residence time, as observed by Müller and Vogel (2012). The average maximum pressure for the conditions studied ranged between 16.8 to 17.8 MPa for subcritical conditions and between 22.5 to 27 MPa for the supercritical conditions. Interestingly, a substantial rise in gas volume with the increase in temperature and residence time was observed, while GE increased up to a certain temperature and residence time and then it began to decrease. This phenomenon can be explained by the change in the gas composition with the increase in temperature and residence time. A continuous decomposition of $CH_4$, $CO_2$, $H_2O$ and $C_nH_{2n}$ into lighter gases and carbon (Equation 35-39) may increase the gas volume continuously while observing the drop in GE. The GE in the current study is determined by the converted gas per total mass of the feed and the converted gas is obtained by subtracting the mass of tar and char from the total feed. Wang *et al.* (2021) reported a decrease in the fraction of $CO_2$ and CO as the reaction time increased from 60 s to 1200 s; and significantly increased $H_2$ was also observed during the study of SCW gasification of depolymerization slag. It is also stated that $CH_4$ is the dominant product at lower

gasification temperature (<420°C), and there is a competitive process between the formation of $CH_4$ and $H_2$ when the temperature rises to near 500°C. The $H_2$ becomes the main product when the temperature is elevated to above 600°C while $CH_4$ decreases dramatically (Lu *et al.*, 2007). This is apparent when looking at the perturbation curve of the maximum reaction pressure against reaction temperature and residence time (Fig. 39). The fact that the maximum pressure rises with an increase in temperature and residence time suggests a steady rise in the volume of the gas generated.

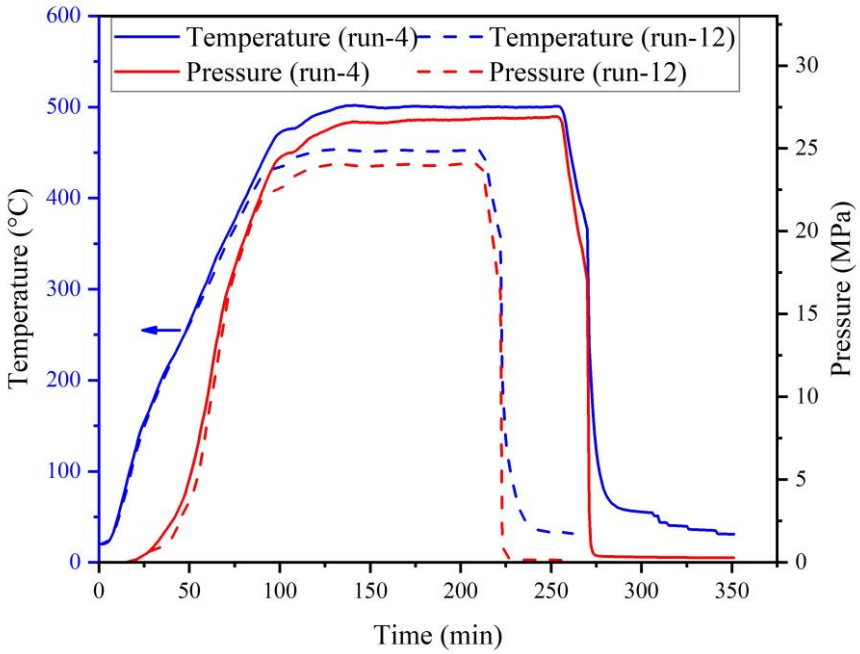


**Figure 38: Reaction temperature and pressure versus time for the representative runs number 4 and 12**

$$C_xH_yO_z \longrightarrow coke \quad (35)$$

$$CH_4 \leftrightarrow C + 2H_2 \ \Delta H_{298K} = 74.87 \text{ kj/mol} \quad (36)$$

$$2CO \leftrightarrow C + CO_2 \ \Delta H_{298K} = -272.45 \text{ kj/mol} \quad (37)$$

$$CO + H_2 \leftrightarrow C + H_2O \ \Delta H_{298K} = -131.29 \text{ kj/mol} \quad (38)$$

$$CO_2 + 2H_2 \leftrightarrow C + 2H_2O \ \Delta H_{298K} = -90.14 \text{kj/mol} \quad (39)$$

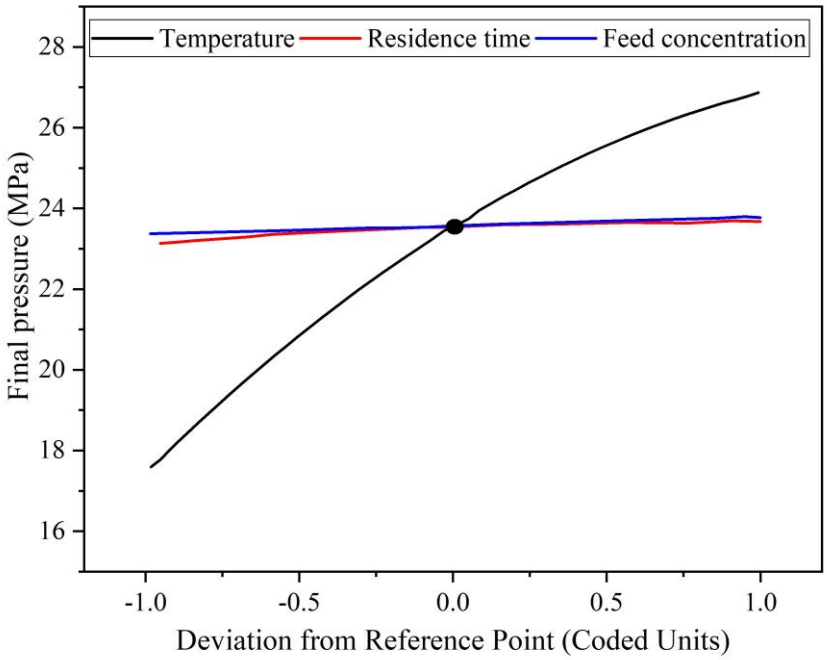


**Figure 39: Perturbation plot showing the effect of variation of temperature, residence time and feed concentration on maximum reaction pressure**

### (iii) Influence of Gasification Parameters on Tar Yield

Tar yield or gravimetric tar content is another aspect of the SCW gasification process affected by the operating conditions (temperature, feed concentration and residence time). Tar is the dark brown viscous oil obtained after solvent extraction by hexane and acetone. Gravimetric tar yield, in this context, is defined as grams of tar per grams of RH feed on a dry basis. The weight of tar includes those water-soluble and water-insoluble organic compounds.

After the filtration of the reaction mixture before hexane extraction, the liquid effluent remained displays colours that varied from golden yellow to almost clear liquid depending on the operating temperature. At lower temperature and short residence time (350°C and 30 minutes), a golden yellow liquid residual was observed which changes to almost a clear liquid at high temperature and long residence time (500°C and 120 minutes), implying that a higher temperature leads to more feed conversion. Moreover, the yellowish colour of the effluent means it contains water-soluble compounds. This observation is consistent with other studies reported in the literature (Basu & Mettanant, 2009; Yan *et al.*, 2020). Yan *et al.* (2020) studied the SCW gasification effluent from food waste and observed that at the subcritical condition, the liquid residual contained a high concentration of chemical oxygen demand (COD) and total organic carbon (TOC), which exhibited a yellowish tinge. This suggests that when the temperature increases from 350°C to 500°C, the COD and TOC are largely converted to gas or

water-insoluble organic products, making the liquid residue clear, similar to that reported by Borges *et al.* (2019). In the current study, it is observed that, after hexane extraction of the filtrate, the liquid residual changed from yellowish to brownish or clear colour depending on the operating temperature; this implies that most of the water-soluble compounds were extracted by hexane (steps 10, 14, 15 and 16 in Fig. 20). Figure 40 shows a perturbation plot of gravimetric tar yield with a curvature slope for temperature and a linear slope for residence time and feed concentration. As a result, temperature fluctuations significantly affect gravimetric tar yield, while feed concentration and residence time have only a slight impact.

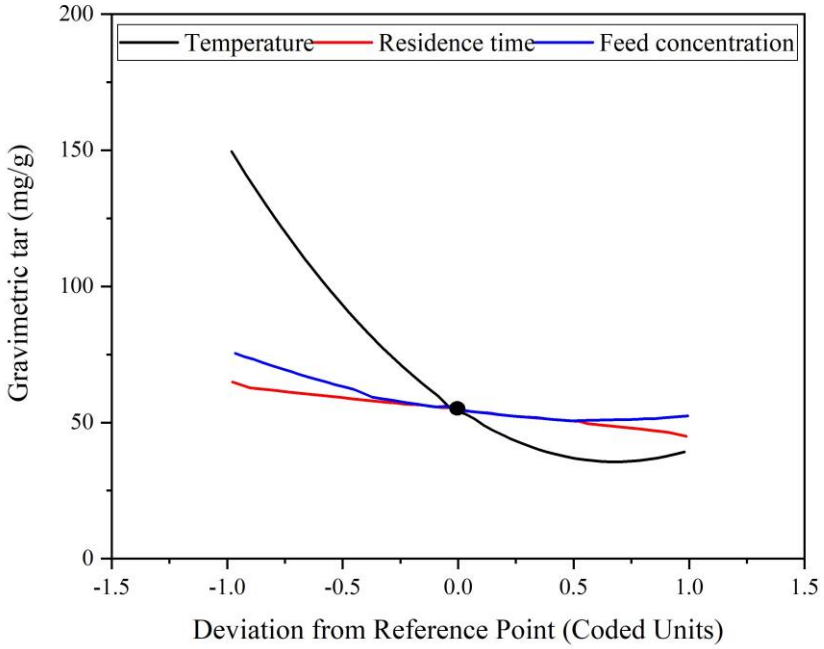


**Figure 40: Perturbation plot showing the effect of variation of temperature, residence time and feed concentration on gravimetric tar**

Contour and 3D surface plots for different interactions of factors in gravimetric tar yield are shown in Fig. 41. Figure 41a and 41b illustrate the interaction of temperature and residence time on gravimetric tar yield. The highest gravimetric tar yield of 166.35 mg/g-biomass is achieved at 350°C and a residence time of 30 minutes at a constant feed concentration of 6.5 wt%, while the lowest tar yield of 29.83 mg/g-biomass is achieved at 471°C and a residence time of 120 minutes. Temperature rise has the most substantial impact on the overall tar yield, which could be explained by the continuous conversion of tar compounds to form gas or coke. Furthermore, a longer residence time allows for more tar decomposition to form gas, which improves feedstock conversion in SCW. Tar characterisation is presented in Section (iii).

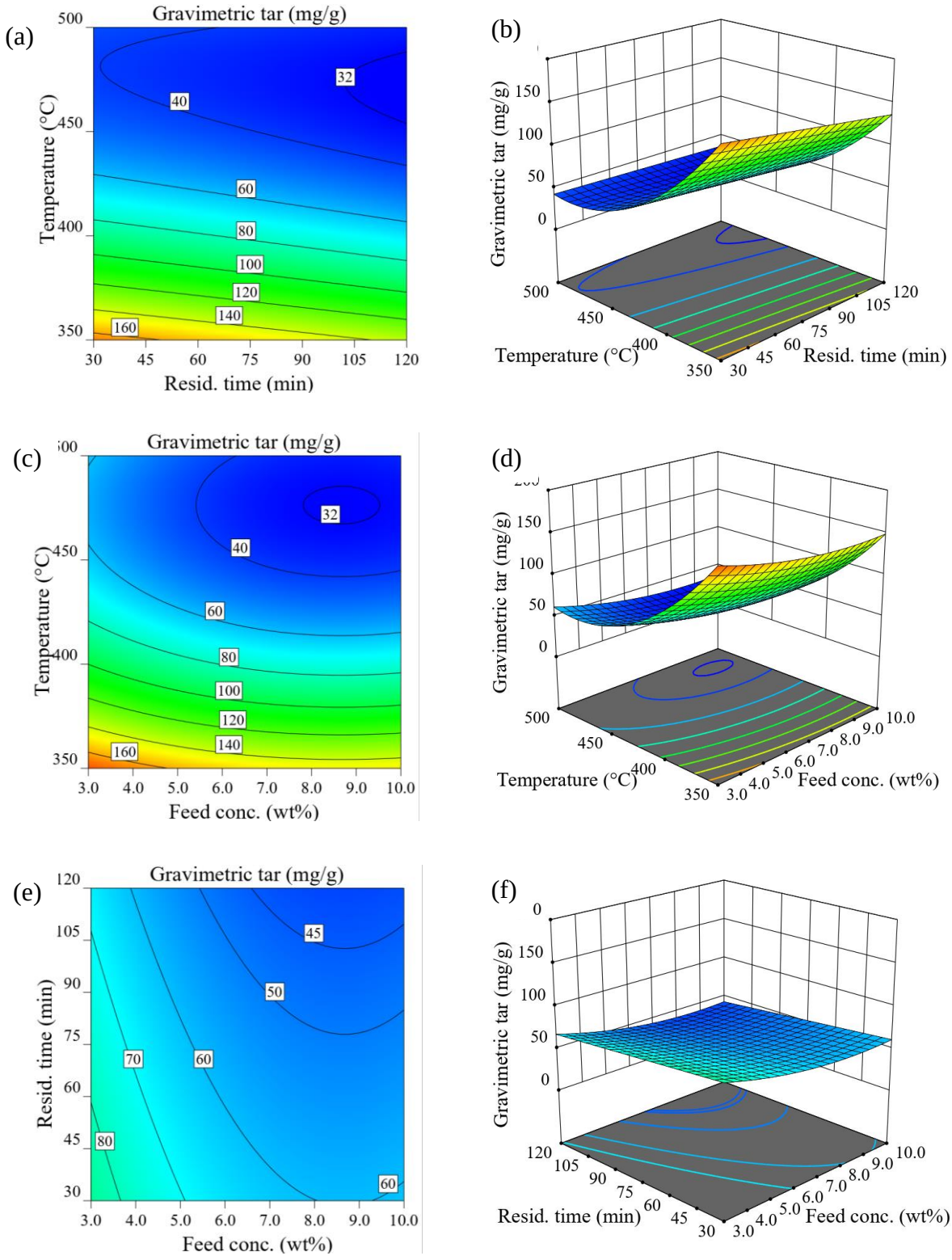


**Figure 41:** **Contour and 3D response surface plots representing different interactive effects of parameters on gravimetric tar yield: Temperature and residence time, feed concentration 6.5 wt% (a, b); temperature and feed concentration, residence time 66 minutes (c, d); residence and feed concentration, temperature 425°C (e, f)**

### (iv) Influence of Gasification Parameters on Char Yield

Char is one of the undesirable products in the SCW gasification of biomass; it, in fact, causes a reduction of the GE. In this study, char yield is defined as the total weight of any solid leftover after the reaction, including ashes, unreacted carbon and coke formed during the reaction, per weight (gram) of feed. The char yield perturbation plots (Fig. 42) show that the residence time and feed concentration curves have a curvature slope, while the temperature curve has a linear slope. The char yield is more susceptible to changes in feed concentration and temperature than it is to residence time, as seen in Fig. 42.

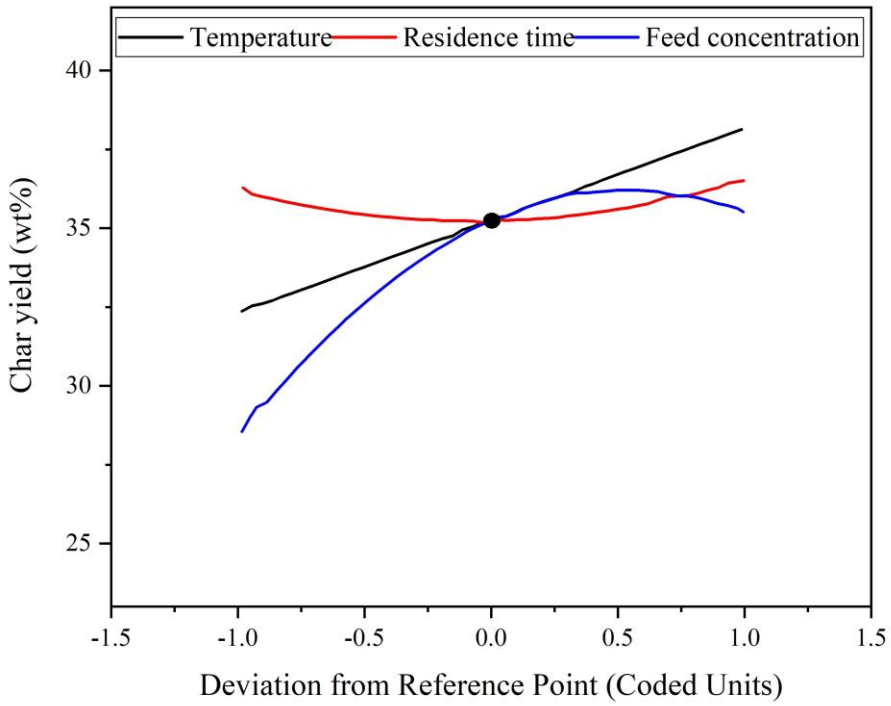


**Figure 42: Perturbation plot showing the effect of variation of temperature, residence time and feed concentration on gravimetric tar**

Contour and 3D surface plots for different interaction of factors in char yield are shown in Fig. 43. It is seen that the variation of temperature strongly influences the char yield, followed by feed concentration and residence time.

Figure 43a and 43b show that at a constant feed concentration of 6.5 wt%, the lowest char yield of 33.1 wt% is obtained at 350°C and a residence time of 75 minutes, while the highest char yield of 39.4 wt% is obtained at 500°C and a residence time of 120 minutes. At temperature 500°C, residence time 30 minutes, and biomass concentration 3 wt%, a char yield of 33.8 wt% is obtained, which is within the range of 33-34 wt% reported by Tsai *et al.* (2007) for the

pyrolysis of Taiwanese RH at 500°C and residence time of 8 minutes. When the residence time is increased to 120 minutes, the char yield rises slightly to 34.1 wt%, implying that as the temperature rises, the char yield rises significantly, but only marginally as the residence time rises. This is most likely due to the hydrocarbons cracking mechanism, which promotes the formation of coke or carbon at higher reaction temperatures. This study's findings are consistent with those of Susanti *et al.* (2010), who studied the gasification of an isooctane model compound in SCW gasification. Susanti *et al.* (2010) observed significantly more coke when the gasification was conducted higher than when it was performed at a lower temperature. It is hypothesized that SCW gasification of biomass occurs via a complicated pathway, one of which is the decomposition of biomass to form intermediate products, which are then broken down into gases, char and liquid via a different mechanism.

Furthermore, the intermediates produced underwent decomposition reactions during gas release to produce new intermediate molecules (Ferreira-Pinto *et al.,* 2019). Carbon-containing substances may be formed as a result of polymerisation and condensation of water-soluble compounds. Simultaneously, the water-insoluble fraction is pyrolyzed to form blackened biomass solid that resembles the original biomass. According to Chuntanapum and Matsumura (2010), the intermediate molecules responsible for the gas yield are low-molecular-weight acids, aldehydes, and ketones, while the ring compounds are responsible for the polymerisation reactions that result in char particles. Minowa *et al.* (1998) investigated the decomposition of cellulose in hot compressed water and suggested that cellulose first decomposes to form soluble compounds and oils. The soluble compounds decompose to form permanent gases as the reaction temperature increases, while the oil decomposes to form char and gas. These findings are consistent with the findings of this research, which show a low char and high tar yield at lower temperatures and a high char and low tar yield at higher temperatures. It is evident that at higher temperatures, tars decompose to form gas and char particles. In SCW gasification, a complex chemical reaction occurs, including biomass reforming, pyrolysis, methanation reactions and water-gas-shift (WGS), responsible for gas formation. However, other reactions such as polymerisation of intermediate products to form coke (Equation 35), methane cracking (Equation 36), Boudouard coking (CO disproportionation) (Equation 37), CO hydrogenation (Equation 38) and $CO_2$ hydrogenation (Equation 39) can compete with the primary reaction to form coke and carbon (Pettersson & Westerholm, 2001; Snoeck *et al.,* 2002).

The feed concentration significantly affects the char yield (Fig. 43 (c, d, e and f)). As the feed concentration increases, the total char yield significantly rises. The deficiency of water at high

feed concentration may be one of the reasons for the high char yield due to inhibition of gasification reactions. Moreover, high char yield could be influenced by the absence of catalyst, which plays an important role to inhibit the char formation from oil conversion. The use of catalysts is one of the efficient ways to improve gasification degree. It can accelerate gasification reactions that lead to an increase in gas yield and minimise char formation (Wang *et al.*, 2021). Gasification reactions in SCW gasification are more effective when feed concentration is less than 10 wt% (Ferreira-Pinto *et al.*, 2019). Table 13 shows the residual char characterization for a randomly chosen experimental runs. The char residual is rich in carbon, ranging from 30.5 to 42.04%db, and HHV ranging from 10.60 to 13.29 MJ/kg. It is worth noting that the HHV is calculated using the empirical correlation (Equation 40) established by Yin (2011), and its value is similar to that of the original biomass.

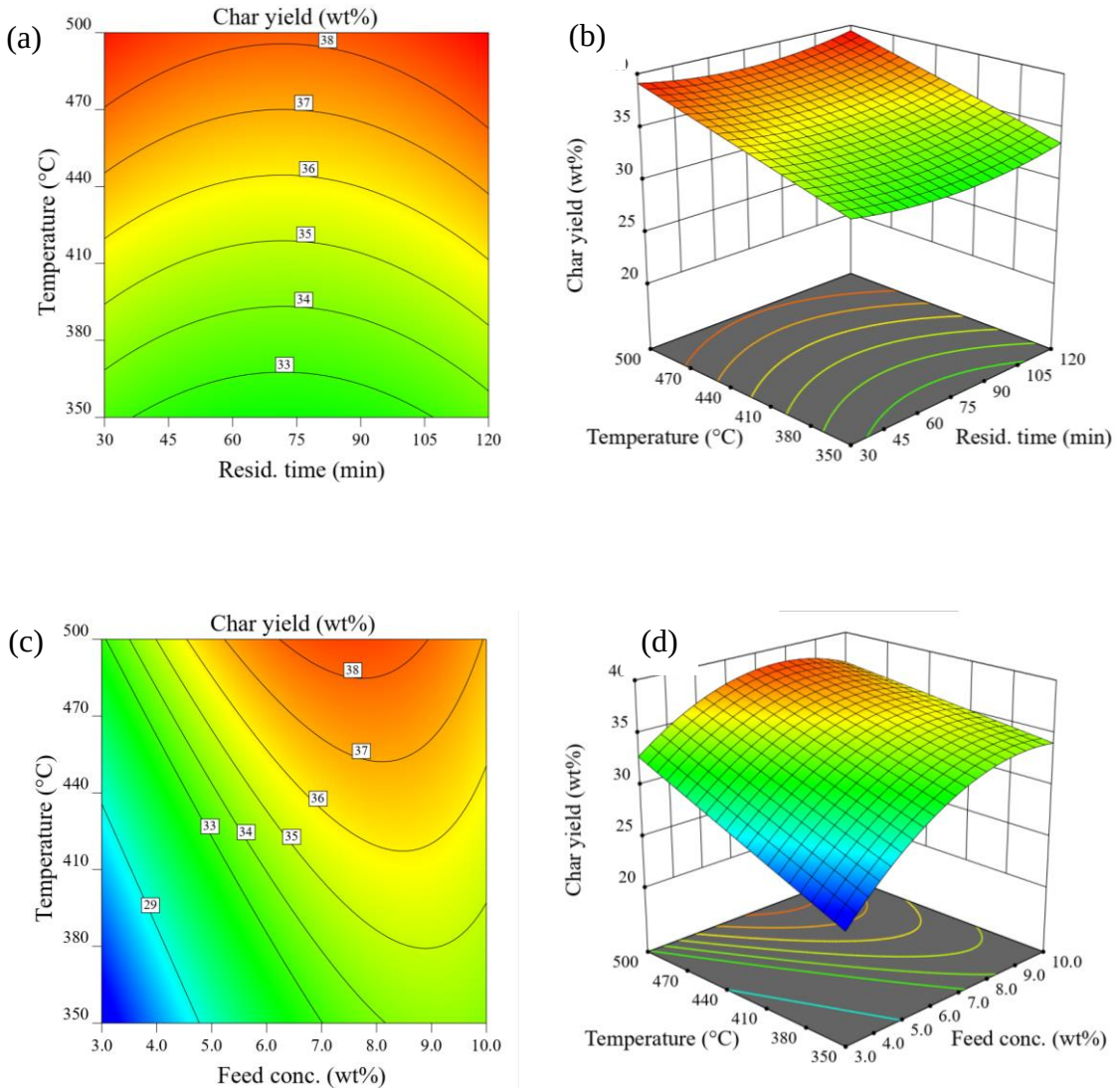

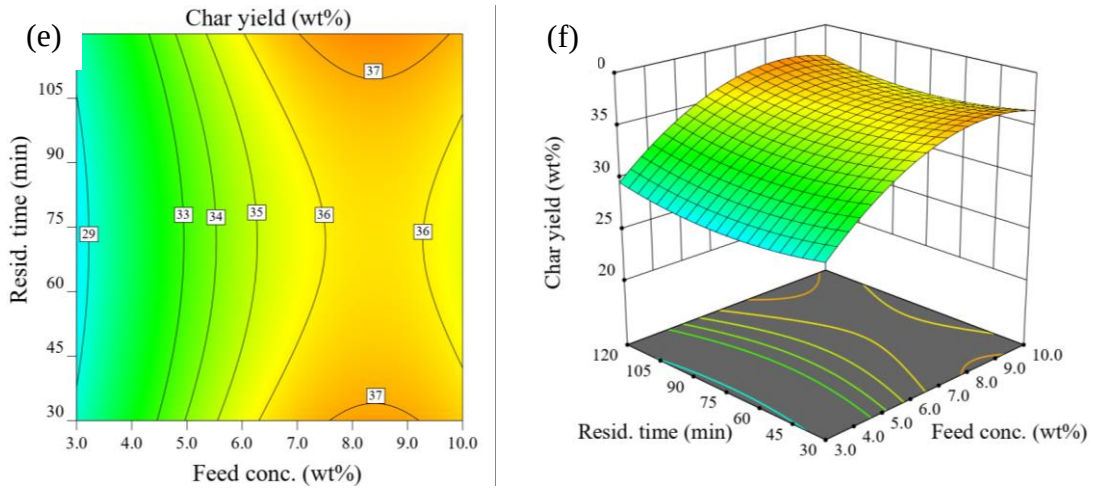


**Figure 43: Contour and 3D response surface plots representing different interactive effects of parameters on char yield: Temperature and residence time, feed concentration 6.5 wt% (a, b), temperature and feed concentration, residence time 66 minutes (c, d) and residence and feed concentration, temperature 425°C (e, f)**

$$HHV = 0.2949C + 0.825H \quad (40)$$

**Table 13: Characterization of char residual in different experimental runs**

| Experiment No. | Char yield (wt%) | Organic composition | | HHV (MJ/kg) |
|---|---|---|---|---|
| | | C (%db) | H (%db) | |
| Run 4 | 39.42 | 42.03 | 1.09 | 13.29 |
| Run 5 | 34.26 | 37.51 | 1.10 | 11.97 |
| Run 9 | 27.81 | 32.20 | 1.44 | 10.68 |
| Run 11 | 24.96 | 30.5 | 1.95 | 10.60 |
| Run 18 | 35.98 | 37.74 | 2.61 | 13.282 |

Figure 44 represents the FTIR spectra of RHC after gasification at varied gasification conditions (representative runs no 4, 5, 9, 11 and 18). In general, all four samples have similar spectra peaks at positions 1577, 1049, 787 and 454 $cm^{-1}$, except for run 4 and 5 char samples, which shows a unique peak at 618 $cm^{-1}$. The presence of C=C and C=O stretching in aromatic carbons of the sample is responsible for the peak at 1577 $cm^{-1}$ (Huff & Lee, 2016). As the temperature rises, the peaks become weaker, suggesting increasing volatile matter conversion or alteration of the aromatic carbon content of the sample. The firm, intense and broad signal detected at 1049 $cm^{-1}$ corresponds to the Si-O-Si asymmetric vibration due to the stronger ionic character of the Si-O group (Yusof *et al.*, 2010). This spectrum also contains bands at 787 and 454 $cm^{-1}$, which correlate to the symmetric stretching of $SiO_4$ tetrahedra and the Si–O bending band vibrations, respectively. Alternatively, the peak at 787 $cm^{-1}$ has been ascribed to aromatic C-H stretching in biochar samples. The peak becomes stronger as the temperature rises, confirming

increasing char production with rising temperatures. Moreover, there was also an increase in peak intensity at 787 $cm^{-1}$ for sample from run five compared to run four, indicating an increase in C–H stretching (Wang & Griffiths, 1985), potentially due to conversion from aromatic C=C ring structures impacted by feed concentration reduction. The existence of bands 619 cm-1 on samples from runs 4 and 5 is identical to tridymite (crystalline phase), which demonstrates the presence of the cristobalite phase (Willis *et al.*, 1987).

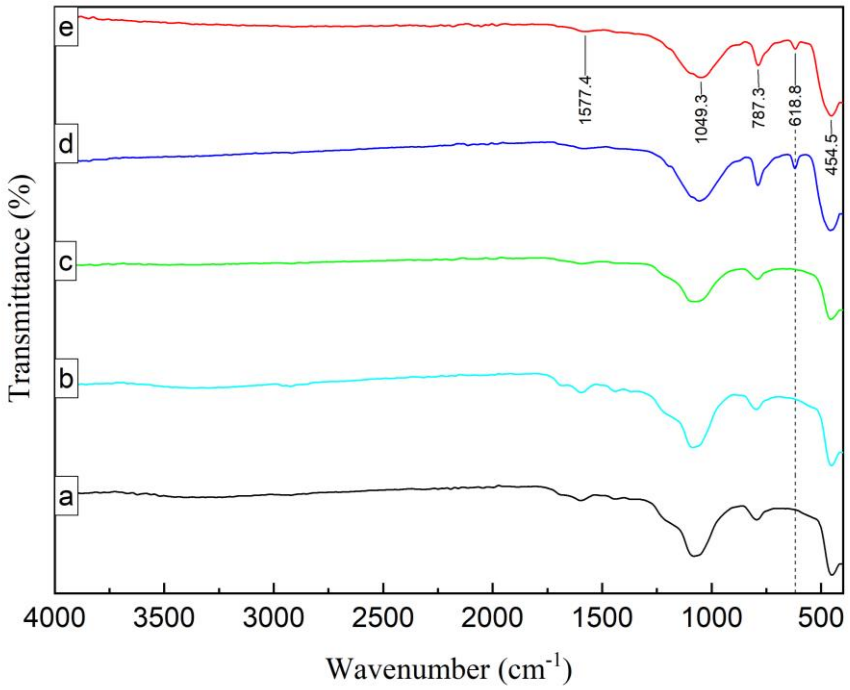


**Figure 44: Fourier transform infrared spectroscopy (FT-IR) of selected char samples (a) run 11, (b) run 18, (c) run 9, (d) run 5 and (e) run 4**

Based on these observations, the silica phase observed in RHC samples from runs 9, 11 and 18 was utterly amorphous, while that of runs 4 and 5 was partially crystalline cristobalite (Yusof *et al.*, 2010). This observation is consistent with the XRD results of RH samples (Fig. 31), which show that the RH contains amorphous silica. Therefore, the char residual can be used directly or after further processing as a fuel (Siddiqui *et al.*, 2018), the catalyst for thermochemical cracking of tars (Nanda *et al.*, 2016), adsorbent (Kizito *et al.*, 2015), soil conditioner (Haefele *et al.*, 2011), activated carbon precursor (Mohan *et al.*, 2014), and high quality silica for different industrial applications such as zeolite synthesis (Ahmed & Adam, 2009; Lee *et al.*, 2013).

### 4.3.2 Optimisation of the Responses and Validation of the Model

In this objective, a RSM using the I-optimality criterion was employed to establish the optimum operation parameters for SCW gasification of RH. The numerical optimisation was carried out

by using the Design-Expert software to analyse the preliminary experimental results. In general, the SCW gasification of lower biomass concentration consumes extra heat energy to raise the temperature of the water, while the high biomass concentration suffers from system plugging (Reddy *et al.*, 2014). Hence, high feed concentration is used to attain high-energy efficiency (Samiee-Zafarghandi *et al.*, 2018). High temperature and long reaction time of gasification favour high gas yield; however, these conditions also contribute to higher energy consumption, not to mention increased complexity in vessel design and cost in construction materials. As a result, it is hoped that by optimizing the SCW gasification process here, the optimum condition for high GE will be achieved. In addition to GE, other products, including char yield, gravimetric tar yield and gas volume, were considered as independent responses in SCW gasification of RH. Figure 45 shows the optimum conditions for each independent response that meet the required goals. As expected, the selected gasification condition for RH, at a feed concentration of 3 wt%, a maximum temperature of 500°C and a duration of 120 minutes, leads to the highest gas volume of 423.8 mL/g biomass. Moreover, the optimum condition for minimum tar yield of 29.98 mg/g-biomass could be archived at 492°C, 120 minutes and 9.5 wt% feed concentration. The desirability value near one show that the optimisation criteria are well satisfied with imposed constraints.

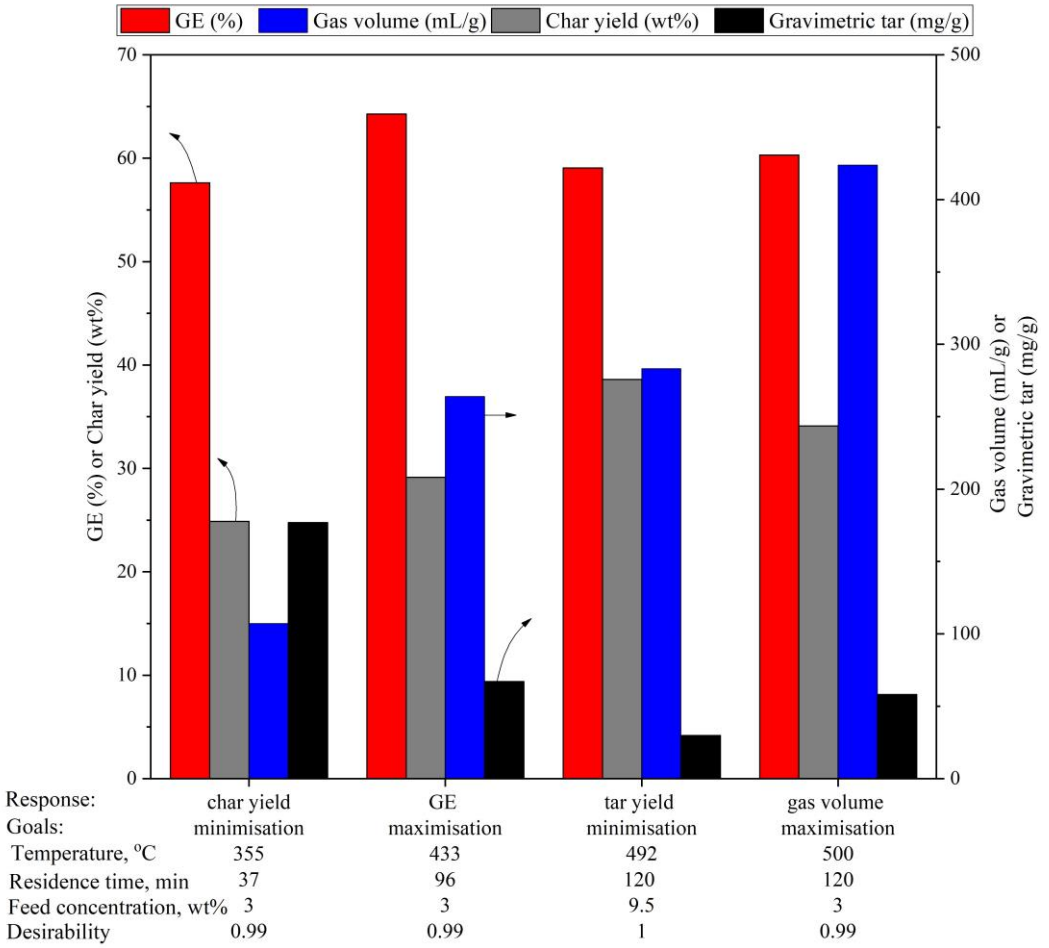


**Figure 45: Predicted response values and their corresponding optimum operating conditions for various optimisation goals**

With multiple dependence factors, the optimum condition where all factors simultaneously meet the desirable condition for optimum tar yield could be envisaged graphically by superimposing the contours of the response in an overlay plot. The overlaying of contour plots (Fig. 46) constructed by combining three independent factors allows searching visually for a compromised region while satisfying different response requirements. A two-sided confidence interval of 95% was used to obtain high and low prediction intervals. The prediction interval of the response is considered as the acceptable response range within the optimum space. With this interval, the ranges can predicted for individual observations rather than the mean value. The intervals used to construct the overlay plots in Fig. 46 were adopted to generate the outcomes, as shown in Table 14. The overlay plots show the intervals for predicting the optimum tar yield and other responses over the set range of the independent variables. The yellow shaded region defines the acceptable factor settings, while the grey shaded shows the unacceptable operating condition.

**Table 14: The criteria used for constructing overlay plots**

| Response | 95% PI low | Predicted value | 95% PI high |
|---|---|---|---|
| GE (%) | 57.3 | 59.07 | 60.83 |
| Char yield (wt%) | 36.80 | 38.62 | 40.43 |
| Gravimetric tar yield (mg/g) | 16.38 | 29.78 | 43.14 |
| Gas volume (mL/g biomass) | 262.42 | 283.15 | 303.88 |

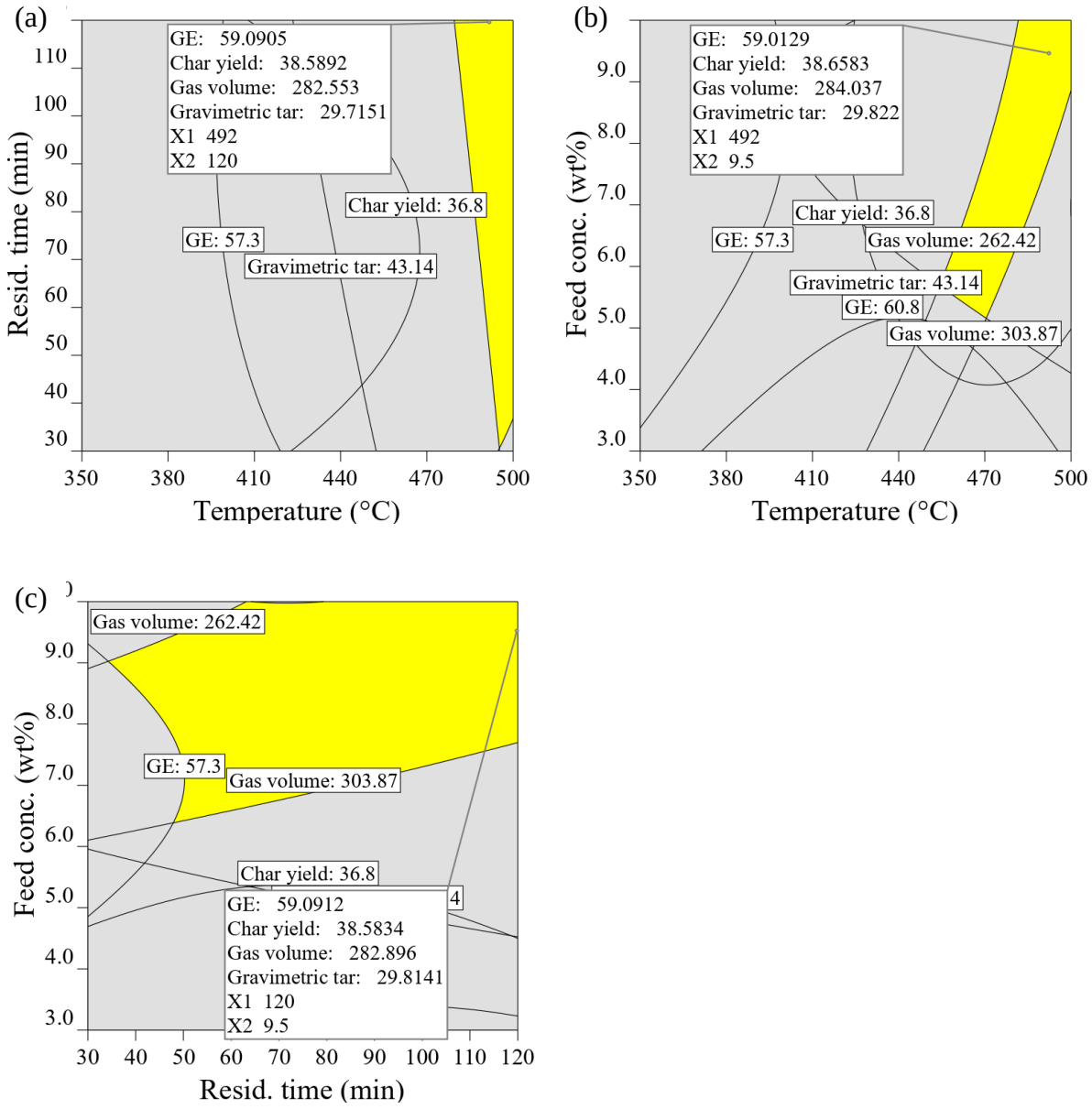


**Figure 46: Overlay plot showing the best compromise region for optimal tar yield as a function of (a) temperature and residence time at feed concentration 9.5 wt%, (b)Temperature and feed concentration and residence time 120 minutes and (c) residence time and feed concentration at temperature 492°C**

The validity of the predicted models was assessed by running three replicates of confirmation experiments at the optimum operating condition for the minimisation of tar yield. Table 15 shows the Residual Standard Error (RSE) results using Equation 41; here, the RSE value of less than 6.5% implies an excellent agreement of experimental values with the model predicted results (Gratuito *et al.,* 2008).

$$RSE\ (\%) = 100\ X\ \frac{|(Exp.value - pred.value)|}{pred.value} \quad (41)$$

**Table 15: Predicted and experimental values at optimum conditions for the minimisation of tar yield (492°C, 120 minutes, 9.5 wt%)**

| Responses | Predicted value | Experimental value* | RSE (%) |
|---|---|---|---|
| GE (%) | 59.07 | 59.59 ± 0.4 | 0.8 |
| Char yield (wt%) | 38.62 | 37.46 ± 0.38 | 3.0 |
| Gravimetric tar (mg/g) | 29.76 | 29.76 ± 0.13 | 6.5 |
| Gas volume (mL/g biomass) | 283.15 | 286.20 ± 2.14 | 1.0 |

*is the average of triplicate runs

### (i) Effect of Particle Size on Gasification Yield

The size of biomass particles is an important design factor in the gasification process, as the smaller the particle size, the more energy is required to prepare the feed. Only a few studies have looked into the impact of biomass particle size on SCW gasification (Basu *et al.,* 2009; Okolie *et al.,* 2019). Figure 47 depicts the results of a study involving four different sizes of biomass particles during SCW gasification. Particle sizes 1>dp>750 microns have the highest GE (61.5%), while full grain has the lowest (56.2%). The char yield ranged from 35.2 to 40.39 wt%, with the highest being for particle sizes of dp<180 microns and the lowest for particle sizes of 1>dp>750 microns. The gravimetric tar yield ranged slightly from 29.50 mg/g-biomass to 34.38 mg/g-biomass, with the lowest being 350>dp>250 microns and the highest being dp180 microns. On the other hand, the gas volume ranged marginally between 276.98 and 297.69 mL/g-biomass, with the lowest value for particle size dp180 microns and the highest value for particle size 1>dp>750 microns. Gasification yields do not appear to show any clear trend across the range of particle sizes studied. Contrary to expectations, small particles have a larger surface area per unit mass, which improves heat accessibility and penetration, thus increasing the conversion efficiency. Septien *et al.* (2012) assessed the effects of particle sizes ranging from 0.35 mm to 0.80 mm on biomass pyrolysis and found that particle size did not affect the

pyrolysis product. A similar observation was made by Basu *et al.* (2009). Zhang *et al.* (2009) investigated the thermochemical liquefaction of grassland perennials with particle sizes ranging from 0.5 to 2 mm. It was found that particle size did not affect product yield at 350$^{o}$C; however, under SCW conditions, particle size reduction resulted in a decrease in solid yield. A related observation can be made in this study when comparing char yield for full-grain and ground samples (1>d>750 microns). However, it is worth mentioning that when the sample is ground to a particle size smaller than 750 microns, the char yield marginally increases. The fact that biomass particle size differences have no significant effect on product yield can be explained in light of mass transfer effect. It is possible that the mass transfer resistance between different particles during SCW gasification is insignificant, and thus its impact on product yield is uncertain.

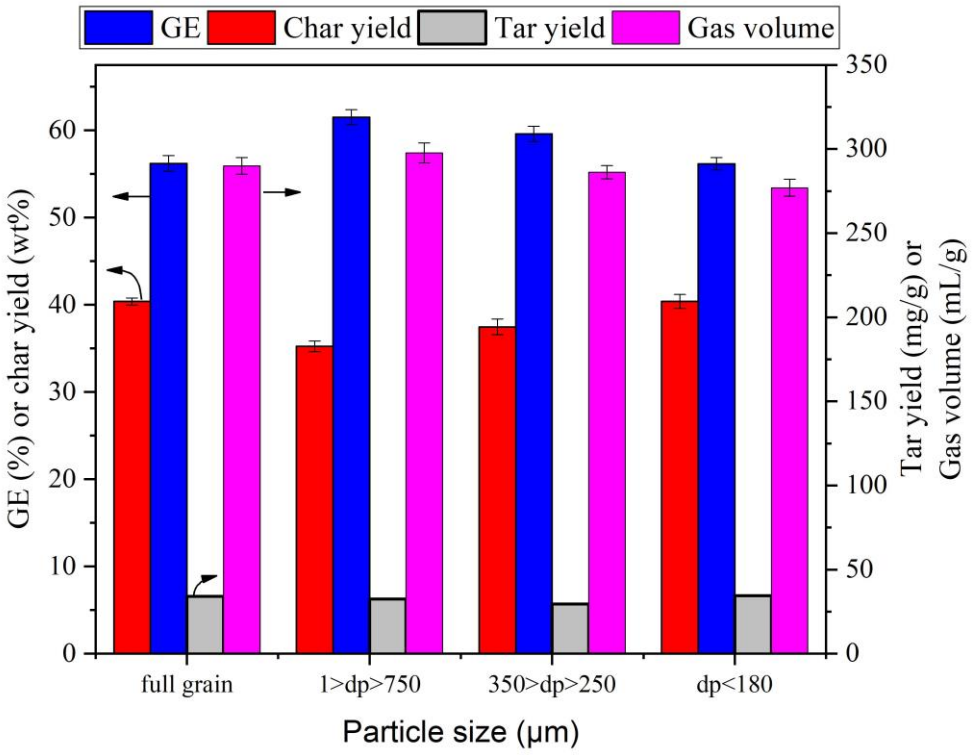


**Figure 47: Effect of biomass particle size on different gasification products (Rice husk Dodoma variety, reaction temperature 492$^{o}$C, residence time 120 minutes and feed concentration 9.5 wt%)**

**(ii) Supercritical Water Gasification of Rice Husk Varieties**

The GE for the RH variety studied ranged from 59.34 % to 62.74 %, with the Iringa sample having the lowest GE and the Arusha sample having the highest. There is a credible linear correlation between the GE and the volatile matter ($R^2$ = 0.9945), hemicellulose ($R^2$ = 0.9120),

and lignin ($R^2$ = 0.9560) all seem to have a positive effect on GE. There is also a clear trend between GE and cellulose composition ($R^2$ = 0.7595), with the sample with the highest cellulose composition having the lowest GE (Fig. 48). Basu *et al.* (2009) published a similar finding that GE decreases as cellulose concentration increases. This claim can be clarified by considering the energy consumption of biomass model components during pyrolysis, as explained by Yang *et al.* (2007). The author published the findings on hemicellulose, cellulose, and lignin pyrolysis characteristics and discovered that cellulose energy consumption differed from hemicellulose and lignin at low temperatures (<500$^o$C) the former's pyrolysis was endothermic, while the latter's is exothermic. These findings ascribe why biomass with a higher cellulose content has lower GE than that contains lower cellulose composition.

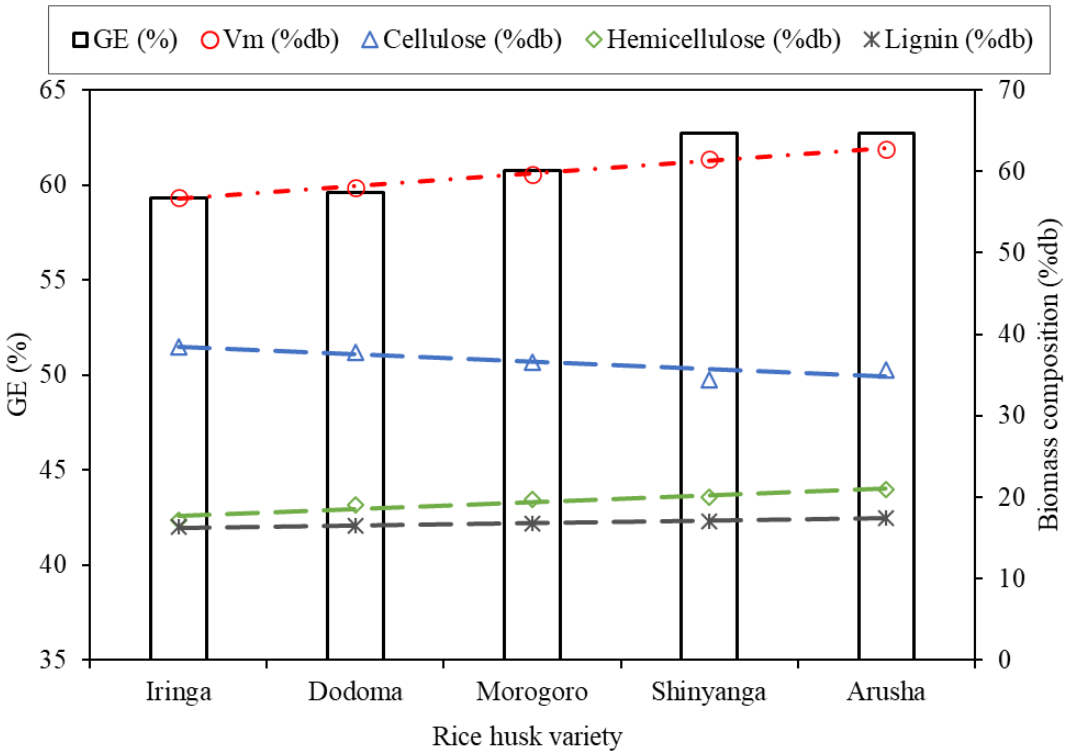


**Figure 48: The effect of different biomass compositions on the GE of SCW gasification of rice husk varieties**

The gas volume generated by SCW gasification of RH varieties ranged from 278.5 mL/ g-biomass to 305.3 mL/g-biomass (Fig. 49). As expected, the order of ranking of gas volume from low to high is like that of GE. The gas volume has a good correlation with volatile content ($R^2$ = 0.9945), hemicellulose ($R^2$ = 0.9120), extractives ($R^2$ = 0.9908), and lignin ($R^2$ = 0.9560), all of which have a positive impact on gas volume. On the other hand, there is a clear trend between gas volume and biomass cellulose content ($R^2$ = 0.7598), the biomass with high cellulose

composition producing the least amount of gas. However, it has been reported that cellulose contributes more to $H_2$ yield than lignin and hemicellulose (Okolie *et al.*, 2019). Yoshida and Matsumura (2001) investigated the gasification of three biomass components and discovered that the hydrogen yield from these components could be ranked as cellulose > hemicellulose > lignin. Unfortunately, since this study only looked at the total amount of gas, it was not easy to affirm this hypothesis.

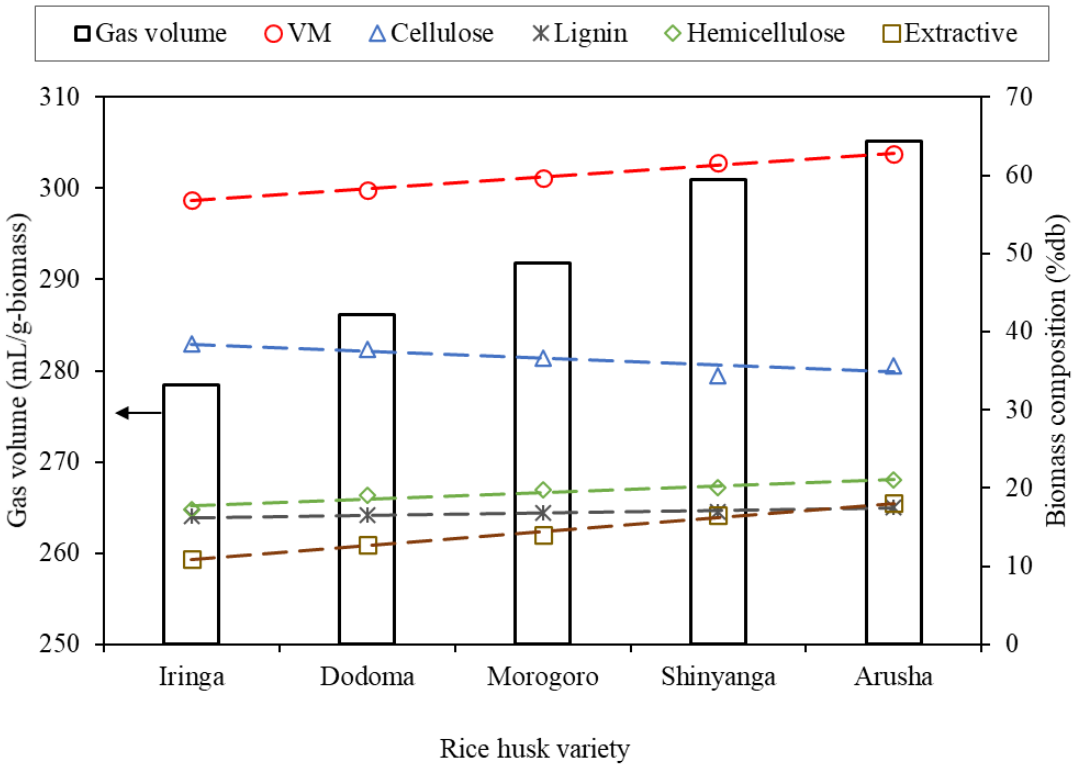


**Figure 49: The effect of different biomass compositions on the gas volume of SCW gasification of rice husk varieties**

The influence of the volatile fraction on gas volume is evident in the gasification studies reported by Ji-lu (2007) and Guo *et al.* (2011). Ji-lu (2007) reported a gas yield of 26 wt% by mass for the rice with 64.30%db volatile matter, while Guo *et al.* (2011) reported a slightly lower gas yield of 24 wt% by mass for the RH containing 60.98%db volatile matter. The effect of extractives on gasification products is usually ignored during biomass gasification because their fraction is typically less than 10% (Ranzi *et al.*, 2008; Wang & Li, 2008); however, the extractive content in this study ranges between 10.93%db and 18.09%db, so their influence cannot be ignored. In the current study, there is a strong correlation between gas volume and extractive content of biomass ($R^2$ = 0.9908). Extractives component is critical in thermochemical conversion in which it decomposes to form permanent gases at temperatures just above 300°C (Matsumura *et al.*, 2005). As a result, biomass with a higher extractive fraction

is more likely to produce more gas volume. Figure 49 shows that the Arusha sample with the highest extractives content of 18.08%db produced the most volume of gas.

The gravimetric tar yield for the RH varieties studied ranged from 24.3 to 31.6 mg/g-biomass, with the Arusha sample producing the lowest tar yield and the Iringa sample having the highest (Fig. 50). Gravimetric tar yield correlates with the extractives content ($R^2$ = 0.9908), volatile content ($R^2$ = 0.9945), lignin ($R^2$ = 0.9560), hemicellulose ($R^2$ = 0.9120), and cellulose ($R^2$ = 0.7598). The cellulose composition has a synergistic effect on tar yield, while the content of volatile matter, hemicellulose, lignin, and extractives fractions has a negative impact, with the biomass with the lowest content of the latter producing more tars. Yang *et al.* (2007) found almost no organic liquid from lignin pyrolysis while studying the pyrolysis behaviours of the three components of biomass (lignin, cellulose, and hemicellulose), suggesting that more gas is generated for the biomass with a higher lignin fraction, as seen in Fig. 49.

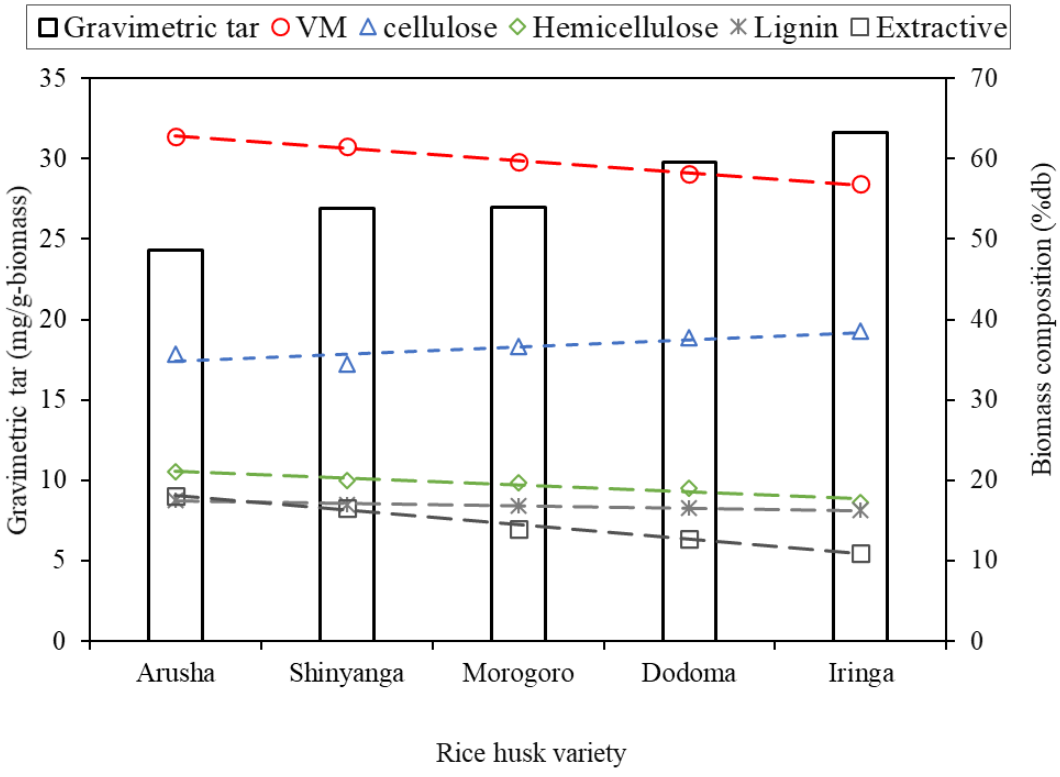


**Figure 50: The effect of different biomass compositions on the gravimetric tar yield of SCW gasification of rice husk varieties**

The char yield for the RH varieties studied ranged from 34.60 wt% to 38.60 wt%, the Shinyanga sample yielding the least and the Dodoma sample yielding the most (Fig. 51). The amount of cellulose and fixed carbon in the biomass has a significant impact on the char yield. Cellulose decomposition likely leads to a secondary char formation reaction, resulting in a high char yield

for biomass with higher cellulose composition. The decomposition pathway of cellulose was previously reported by Minowa *et al.* (1995) and Minowa *et al.* (1998). Around 250$^{o}$C, cellulose decomposes rapidly to produce water-soluble products (including sugars and non-sugar materials), gas, oil, and char. Char production continued at temperatures above 300$^{o}$C, even though no cellulose was left in the reactor, and sugars and oil decomposed. Finally, char is primarily obtained from a yield of 60% on a carbon basis, with 10% gas and 15% non-sugar water-soluble products. According to Wang *et al.* (1996), the decomposition of hydroxyacetaldehyde, another product of cellulose decomposition, occurs through cracking to form smaller molecules and self-condensation reactions to form many higher molecular weight species, with the formation of char and tar being a key aspect, as the trend observed in Fig. 50 and 51. Williams and Onwudili (2006) studied the subcritical and supercritical gasification of cellulose, starch and glucose and found that cellulose produces higher char content compared to starch and glucose. Ji-lu (2007) found that RH with fixed carbon 9.2 wt% had a char content of 21 wt%, while Guo *et al.* (2011) found that RH with fixed carbon 14.4 wt% had a slightly higher char content of 28 wt%. The char yield is also found to increase with a decrease in biomass lignin fraction ($R^2$ = 0.5581), contrary to the assumption that secondary char is originated from lignin decomposition due to its high aromatic content, as well as its complex polymer structure as reported elsewhere (Menya *et al.*, 2018; Yang *et al.*, 2007). Branca *et al.* (2006) published a paper that made a similar assertion to this one. In contrast to assumptions that ash fraction contributes to char yield, this experimental study found no linear correlation between char yield and ash content ($R^2$ = 0.0601).

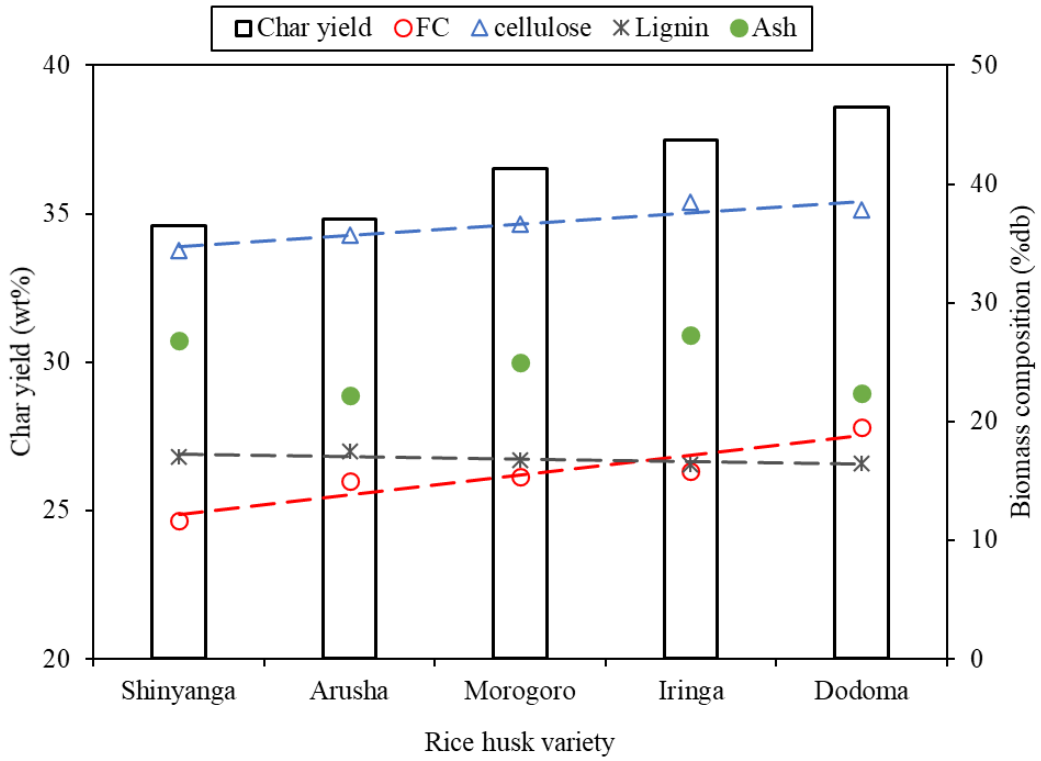


**Figure 51: The effect of different biomass compositions on the char yield of SCW gasification of rice husk varieties**

In addition to proximate, ultimate, and biochemical correlation, the concentrations of certain trace elements in the ash were also correlated with gasification yields. Because of the high variability of inorganic elements in RH ash, distinct catalytic effects of these elements during gasification are expected, which may influence the variation of gasification yields between variety of RH. The coefficient correlation between different inorganic minerals and gasification yield was computed using Pearson's correlation and presented in Table 16. Several significant correlations have been identified between various inorganic elements and gasification yields. Gasification efficiency was found to be positively correlated to Mn (0.82) > Fe (0.77) > Si (0.52) and negatively correlated to Al (-0.77) and S (-0.69). Equally, gas volume was positively correlated with Fe (0.87) > Mn (0.83) > Si (0.60), and negatively with Al (-0.72) > Mg (-0.71) > S (-0.65) > Ti (-0.59) > Na (-0.57). Gravimetric tar yield was positively correlated with Al (0.79) > Na (0.78) > K (0.68) > Mg (0.68) > Ti (0.65) > Ca (0.64) > Cl (0.53) and negatively with Fe (-0.96) > Mn (-0.91) > Si (-0.79). Again, char yield was positively correlated with Al (0.85) > S (0.70) > Mg (0.60) > K (0.51) and negatively with Mn (-0.82) > Fe (-0.66) > Si (-0.52).

**Table 16: Coefficient correlation between inorganic minerals and gasification yield**

| Yield | Si | K | Ca | Cl | Fe | P | Mg | Al | Na | Mn | S | Ti |
|---|---|---|---|---|---|---|---|---|---|---|---|---|
| GE | 0.52 | -0.44 | -0.32 | -0.33 | 0.77 | -0.34 | -0.69 | -0.77 | -0.45 | 0.82 | -0.74 | -0.41 |
| Gas vol. | 0.60 | -0.47 | -0.43 | -0.33 | 0.87 | -0.39 | -0.71 | -0.72 | -0.57 | 0.83 | -0.65 | -0.59 |
| Tar yield | -0.79 | 0.68 | 0.64 | 0.53 | -0.96 | 0.22 | 0.68 | 0.79 | 0.78 | -0.91 | 0.40 | 0.65 |
| Char | -0.52 | 0.51 | 0.28 | 0.44 | -0.66 | 0.14 | 0.60 | 0.85 | 0.41 | -0.82 | 0.70 | 0.19 |

**Table 17: R-squared for linear fitting between inorganic minerals and gasification yield**

| Yield | Si | K | Ca | Cl | Fe | P | Mg | Al | Na | Mn | S | Ti |
|---|---|---|---|---|---|---|---|---|---|---|---|---|
| GE | 0.4214 | 0.2824 | 0.2264 | 0.1707 | 0.8039 | 0.102 | 0.4585 | 0.5491 | 0.4005 | 0.7239 | 0.3438 | 0.3501 |
| Gas vol. | 0.4214 | 0.2824 | 0.2264 | 0.5491 | 0.8039 | 0.102 | 0.4585 | 0.5491 | 0.4005 | 0.7239 | 0.3438 | 0.3501 |
| Tar yield | 0.4214 | 0.2824 | 0.2264 | 0.1707 | 0.8039 | 0.102 | 0.4585 | 0.5491 | 0.3501 | 0.7239 | 0.3438 | 0.3501 |
| Char | 0.2057 | 0.206 | 0.0617 | 0.1112 | 0.3426 | 0.0484 | 0.4366 | 0.7087 | 0.0934 | 0.6219 | 0.5271 | 0.024 |

The linear fitting results between organic minerals and gasification yield are depicted in Fig. 52 to 55, and the relative $R^2$ are displayed in Table 17. The results show that different organic minerals in rice husk ash contributed to the variation of gasification behaviour. There is a high credibility of linear fitting between Fe and GE, gas volume, and gravimetric tar yield, with $R^2$ = 0.8039. High iron content influenced gas volume, char gasification and tar cracking which could be explained by increased water-gas shift reactions. Manganese shows a similar correlation to that of Fe, a credible linear fitting was observed between Mn and char yield ($R^2$ = 0.6219), and between Mn and GE, gas volume and tar yield, both with $R^2$ = 0.7239. A clear linear relationship between Cl and gas volume ($R^2$ = 0.5491) shows that high Cl content contributed to low gas volume. It is possible that Cl reacted with K and Si to form a sticky deposit which resulted to low gas volume and high char and tar yield as confirmed by coefficient correlation of 0.44 and 0.53 for char and tar yield, respectively. A similar finding is published elsewhere (Boot-Handford *et al.*, 2018; Miles *et al.*, 1996). Moreover, the presence of Al, S, Mg and Na is more likely to cause inhibition of char gasification and tar cracking, resulting in low GE and gas volume for the varieties with high concentrations of these elements.

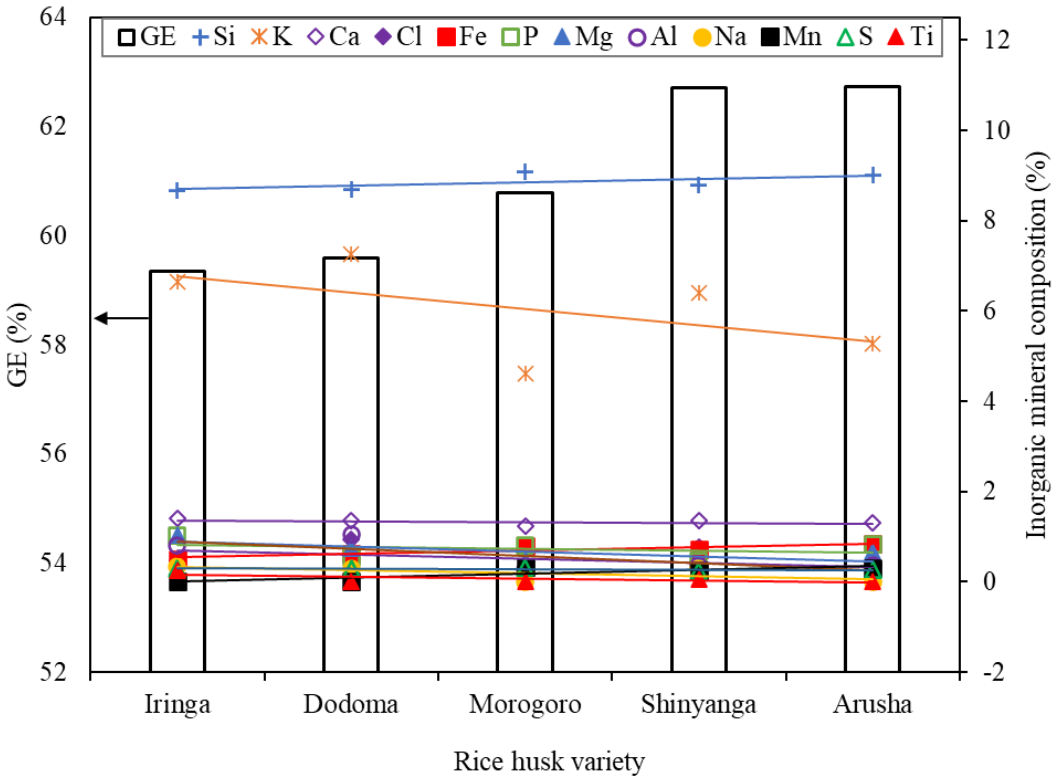


**Figure 52: Linear fitting curves between gasification efficiency and different inorganic elements (remark: + = Si x10)**

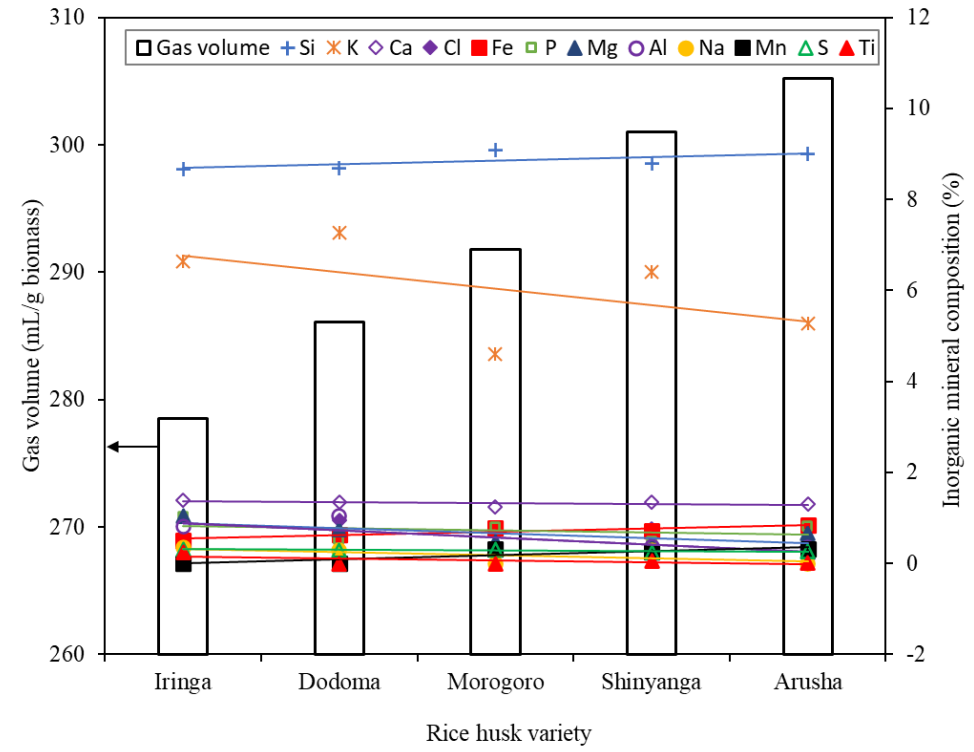


**Figure 53: Linear fitting curves between gas volume and different inorganic elements (remark: + = Si x10)**

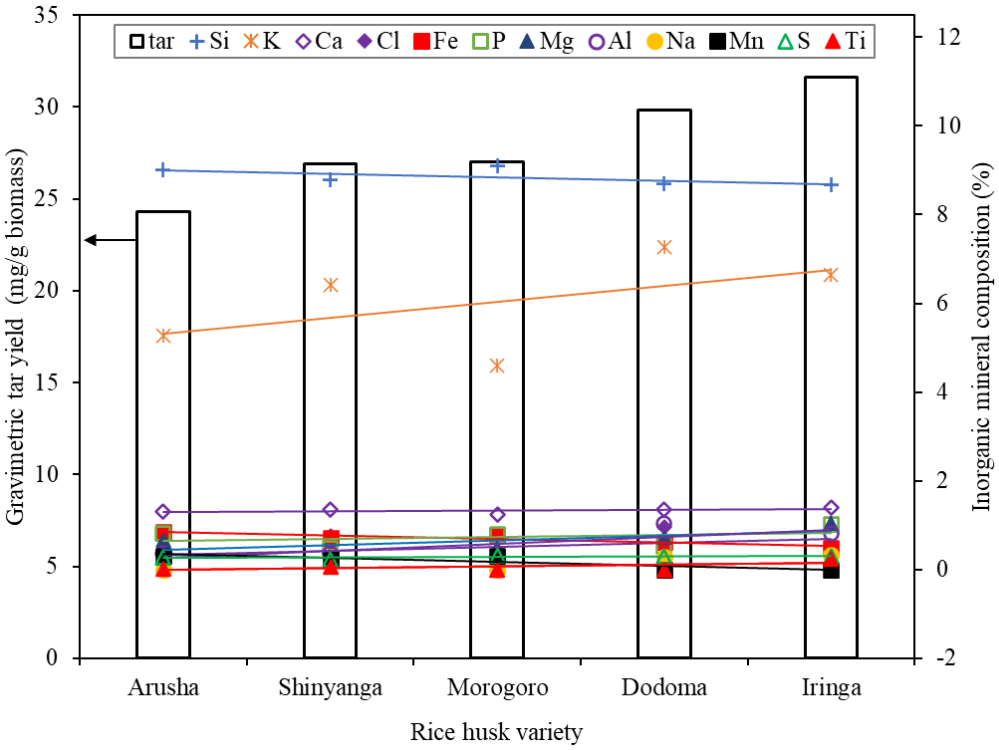


**Figure 54: Linear fitting curves between gravimetric tar and different inorganic elements (remark: + = Si x10)**

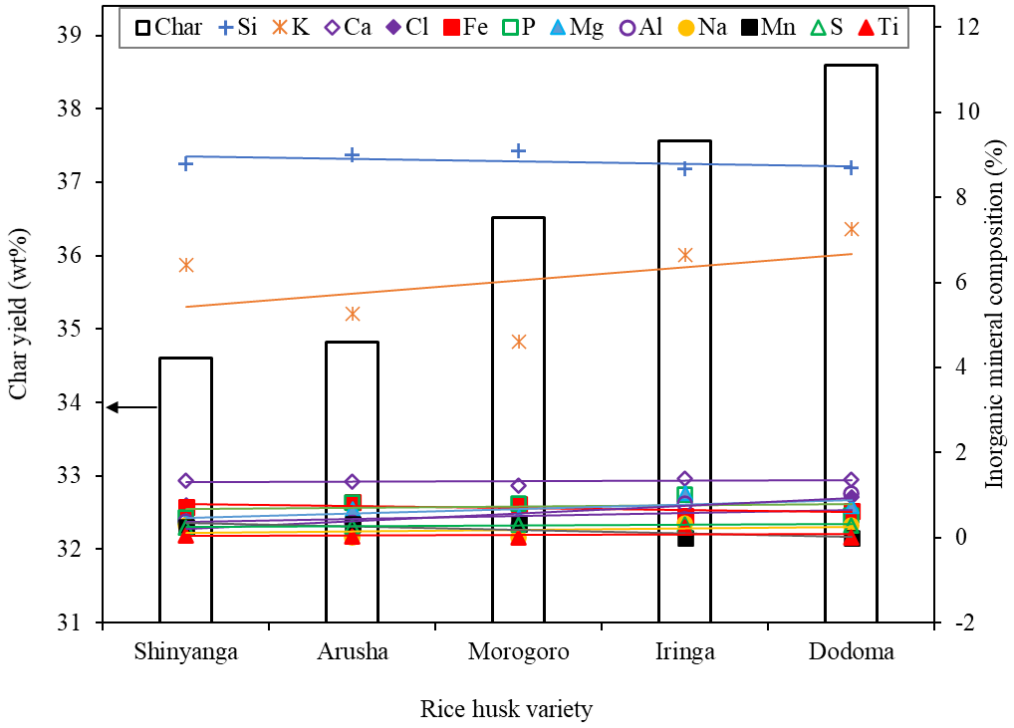


**Figure 55: Linear fitting curves between char yield and different inorganic elements (remark: + = Si x10)**

## 4.4 Catalyst Characterizations

### 4.4.1 Phase Characterization

The crystalline phases observed in the samples and the structural changes during calcination and Fe doping of limestone and dolomite are presented in Fig. 56 and 57, respectively. According to the XRD patterns in Fig. 56a, uncalcined limestone is mainly composed of calcite ($CaCO_3$) (JCPDS 47-1743) and coesite ($SiO_2$) (JCPDS 01-083-1832). On the other hand, the calcined limestone (Fig. 56b) is mainly constituted of portlandite ($Ca(OH)_2$) (JCPDS 01-084-1268), coesite and hematite ($Fe_2O_3$) (JCPDS 13-0534). According to this analysis, $CaCO_3$ in a raw limestone transformed to CaO phases when calcined at 900$^o$C according to Equation 42. The surface hydration by atmospheric water vapour occurs according to Equation 43, which transforms the CaO phases to $Ca(OH)_2$. The XRD peaks for the 10%Fe-doped and 20%Fe-doped limestone catalysts are characterized in Fig. 56c and 56e, respectively. The principal phases found for 10-20%Fe-doped catalyst are $Ca_2Fe_2O_5$ (srebrodolskite) (JCPDS 03-0804), hematite ($Fe_2O_3$) and $Ca(OH)_2$. The $Ca_2Fe_2O_5$ phase was formed due to the *in situ* solid-state reactions of Ca and Fe precursors during calcination at 900°C. The presence of free iron oxides in both the calcined and the Fe-doped limestone catalysts suggests that the catalyst is suitable for promoting the water-gas-shift reaction.

$$CaCO_3 \longrightarrow CaO + CO_2 \quad (42)$$

$$CaO + H_2O \longleftrightarrow Ca(OH)_2 \quad (43)$$

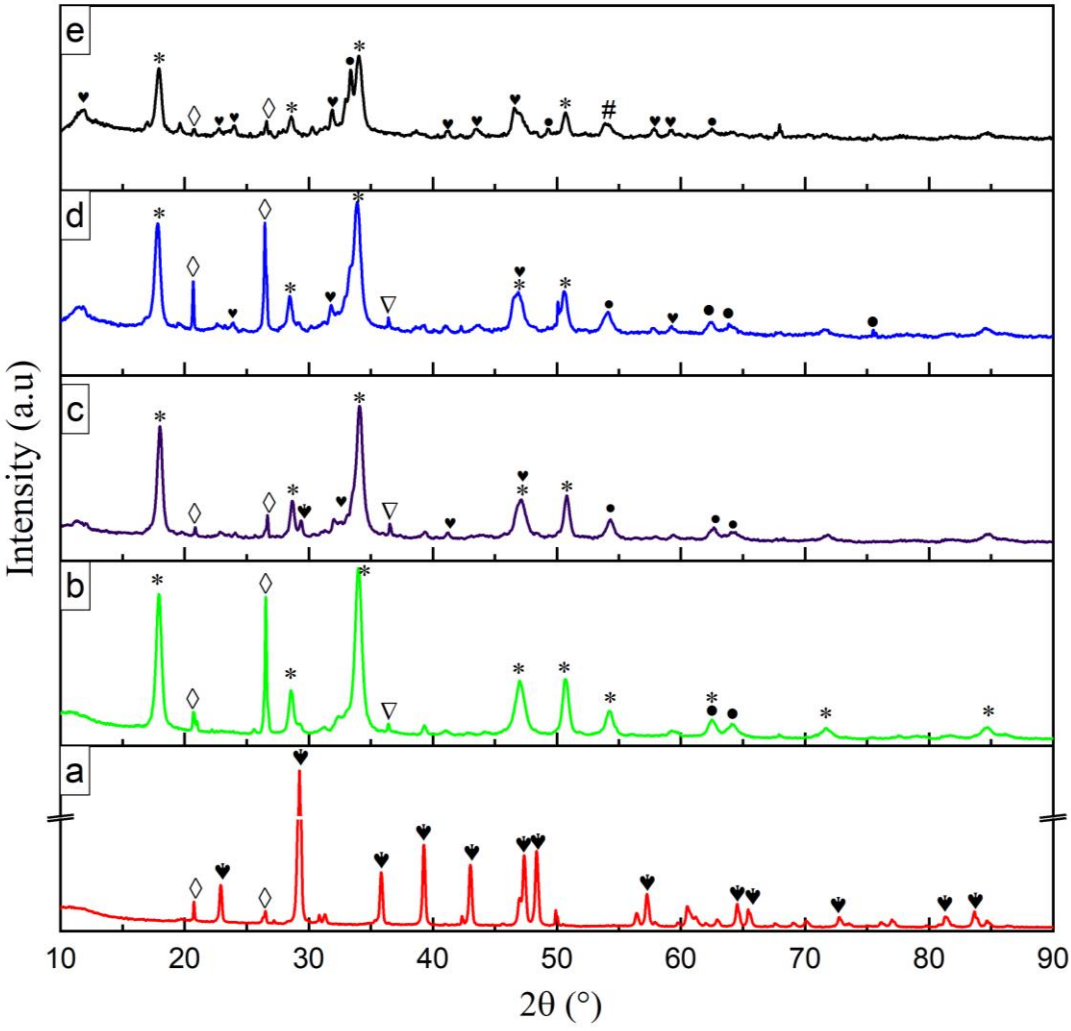


**Figure 56: XRD spectra of limestone-based catalyst**

Where (a) natural (b) calcined at 900 ºC (c) 5%Fe-doped (d) 10%Fe-doped (e) 20%Fe-doped, with the peaks of$CaCO_3$(♥), $Ca(OH)_2$ (∗), $Fe_2O_3$ (•), $SiO_2$ (◊), $Ca_2FeO_5$ (♥), $Fe_3O_4$ (#), and $Fe_2O_4Si$ (∇).

The XRD patterns for natural dolomites reveal that practically the majority of the peaks correspond to those of $CaMg(CO_3)_2$ (JCPDS-036-0426), but there are additional peaks for calcite ($CaCO_3$) (JCPDS-05-0586), quartz ($SiO_2$) (JCPDS-46-1045) and $TiO_2$ (JCPDS 46-1237). Other research works (Gunasekaran & Anbalagan, 2007; Mohammed *et al.*, 2013) found comparable XRD peaks to the examined dolomite, demonstrating that the dolomite from Tanzania has nearly the same properties as other dolomites. The XRD pattern for calcined dolomites, on the other hand, differs significantly from that of natural dolomites. New dominant

peaks which belong to $Ca(OH)_2$ (JCPDS 4-0733) and $Mg(OH)_2$ (JCPDS 7-0239) were observed. It is evident that during calcination, the dolomite sample decomposes to CaO and MgO according to Equation 44, then it contacts moisture in the atmosphere during the XRD analysis and transforms to $Ca(OH)_2$ and $Mg(OH)_2$ according to Equation 43 and 45, respectively. It has been reported that the transition of CaO to $Ca(OH)_2$ occurs very rapidly (Demirbas, 2007).

$$CaMg(CO_3)_2 \longrightarrow CaO + MgO + CO_2 \quad (44)$$

$$MgO + H_2O \longleftrightarrow Mg(OH)_2 \quad (45)$$

Diffraction patterns in Fig. 57c and 57d show the characterisation of phases obtained for 10%Fe-dolomite and 20%Fe-dolomite, respectively. The principal phases found for 10-20%Fe-doped catalyst are $Ca_2Fe_2O_4$ (srebrodolskite) (JCPDS 47-1744), $SiO_2$ (JCPDS 38-0651), MgO identified as periclase (JCPDS 45-0946) and $Ca(OH)_2$ (portlandite) (JCPDS 4-0733). Interestingly, only one peak for $MgFe_2O_4$ (magnesioferrite) (JCPDS 036-0398) is identified for 10%Fe-doped catalyst, whereas no such peaks are detected on the 20%Fe-doped catalyst, indicating a weak interaction between iron-magnesium oxide and robust interaction with calcium oxide. As has been previously reported by Di Felice *et al.* (2011), free iron oxides were not found in either case. As the Fe content increased, the strength of the $CaO/Ca(OH)_2$ peak reduced, indicating that $Ca_2Fe_2O_5$ had distributed across the surface of the $CaO/Ca(OH)_2$ support and gradually became the primary phase of the catalyst.

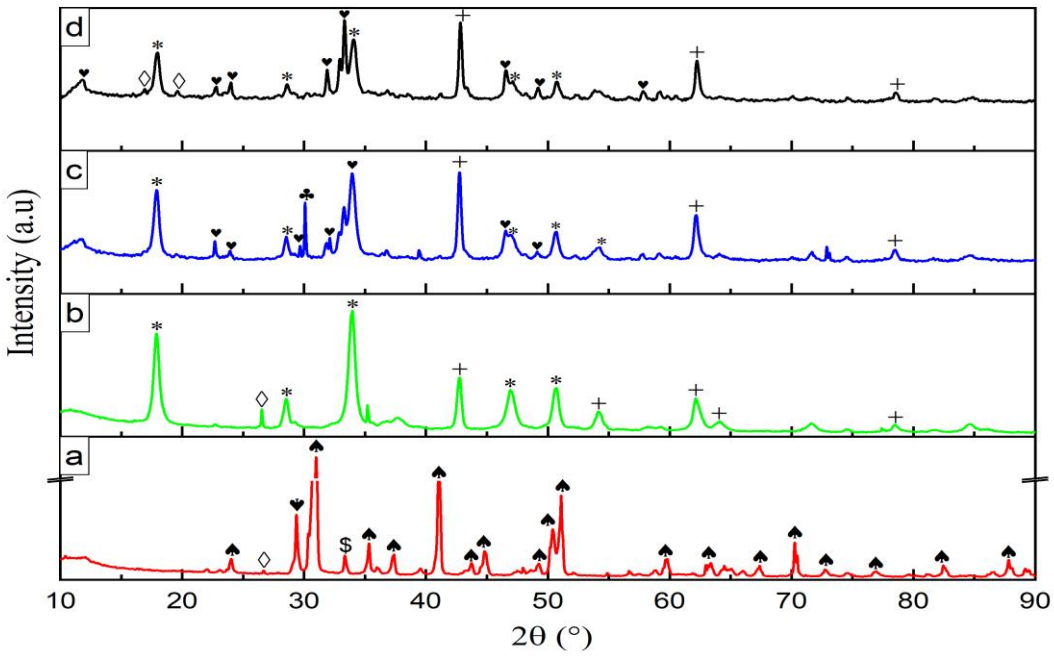


**Figure 57: XRD spectra of dolomite-based catalyst**

Where (a) natural (b) calcined 900 ºC (c) 10%Fe-doped (d) 20%Fe-doped, with the peaks of $CaMg(CO_3)_2$ (♠), $CaCO_3$(♥), $CaO/Ca(OH)_2$ (*), $MgO/Mg(OH)_2$ (+), $SiO_2$ (◊), $MgFe_2O_4$ (♣), $Ca_2Fe_2O_5$ (♥), and $TiO_2$ ($).

Figures 58 and 59 present calculated Scherrer's crystallite size based on the XRD analysis. The calculated crystallite size of $CaMg(CO_3)_2$ (natural dolomite) and $CaCO_3$ (natural limestone) ranged between 28.6 - 77.1 nm and 30.4 - 49.3 nm, respectively. The main phases for the calcined dolomite is $CaO/Ca(OH)_2$ and $MgO/Mg(OH)_2$ with crystallite size ranging between 16.8 – 23.9 nm and 15 – 24.9 nm, respectively. The reported crystallite size for the $CaO/Ca(OH)_2$ is below 28 – 42 nm reported for the Aqliliriana *et al.* (2015), which could be attributed to the milling process as observed by Sánchez-Jiménez *et al.* (2016). On the other hand, the main crystalline phases for the calcined limestone is $CaO/Ca(OH)_2$ and $Fe_2O_3$ with crystallite size between 13.8-29.1 nm and 12.8 – 15.5 nm, respectively. When 10% iron is added in both calcined dolomite and limestone, a new phase of $Ca_2Fe_2O_5$ with crystallite size ranged between 42.1 – 57.9 nm for dolomite-based and 15.2 – 27.8 nm for limestone-based catalyst are formed. In general, as more iron is added to the calcined dolomite or limestone, the produced catalysts show a slight decrease in $Ca_2Fe_2O_5$ crystallite size, whereas there is no apparent trend for $Fe_2O_3$ crystallite size.

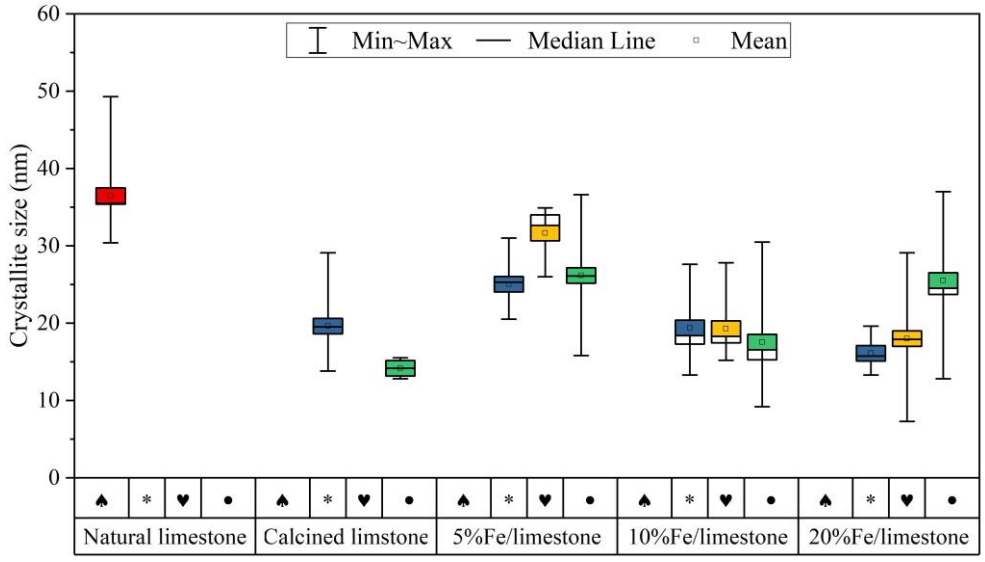


**Figure 58: Crystallite size for selected active phases of limestone-based catalysts**

Where $CaCO_3$ (♠), $CaO/Ca(OH)_2$ (*), $Ca_2Fe_2O_5$ (♥), and $Fe_2O_3$ (•).

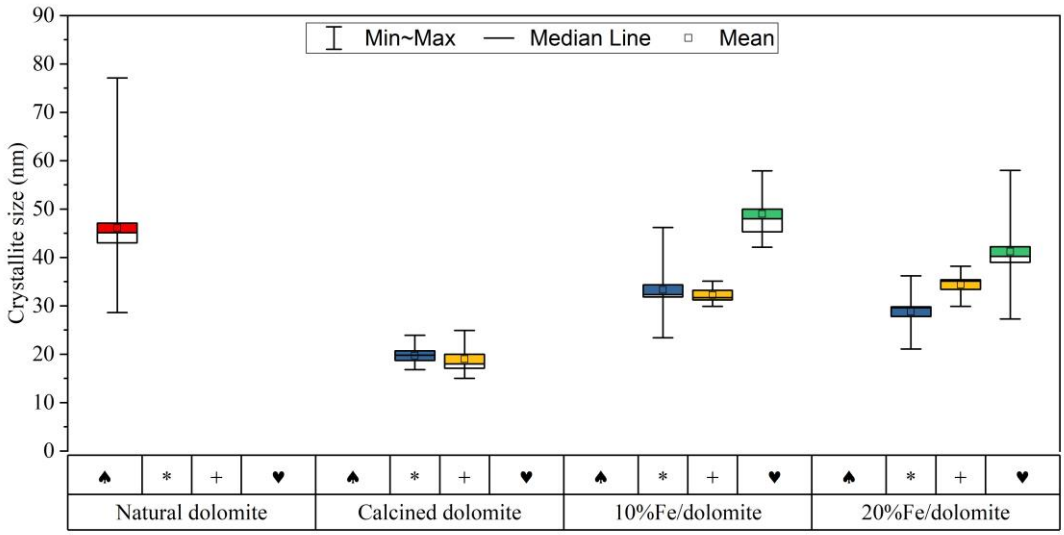


**Figure 59: Crystallite size for selected active phases of dolomite-based catalysts**

Where $CaMg(CO_3)_2$ (♠), $CaO/Ca(OH)_2$ (*), $MgO/Mg(OH)_2$ (+), and $Ca_2Fe_2O_5$ (♥).

### 4.4.2 Morphology of the Catalysts

Figure 60 and Fig. 61 shows the high magnification (1 µm scale bar) SEM micrographs of natural (unmodified) and modified catalysts prepare from limestone and dolomite, respectively. According to the figures, the morphology of calcined samples differs markedly from uncalcined and Fe doped samples. The SEM micrographs of the natural limestone show a clear structure of a mixture of tiny and large rhombohedral-like plates with surface roughness and fracture, indicating the existence of bulky calcite phases as confirmed by XRD analyses (Fig. 56a). The SEM image of calcined limestone displays clumps of globular crystals indicating the structural transformation (Fig. 60 a and b). On the other hand, the SEM morphology of natural dolomite exhibits a rough and unstructured surface with low-porosity grains, whereas the surface of the calcined sample displays clusters of tidy and porous grains, confirming thermal decomposition (Fig. 61a and b). When Fe was added to the calcined dolomite and limestone, the micrograph revealed a transformation in surface morphology with the formation of coarse crystals, indicating a favourable interaction between Fe and the phases of dolomite and limestone. As more Fe is added to calcined dolomite, the crystals agglomerate into larger ones, as seen in 10 wt% and 20 wt% Fe-loading (Fig. 61c and d).

Consequently, as the concentration of Fe on the catalyst increases, so does the particle size, resulting in a decrease in porosity. Interestingly, SEM micrographs of limestone with varying iron loading reveal a mixture of rod-shaped and sphere-like particles (Fig. 60c and d). In the case of a dolomite-based catalyst, only a sphere-like shape is observed. The formation of free

iron oxide phases on the limestone surface could ascribe this behaviour, whereas no such phases were seen on the dolomite surface, as shown by XRD patterns in Fig. 56 and 57.

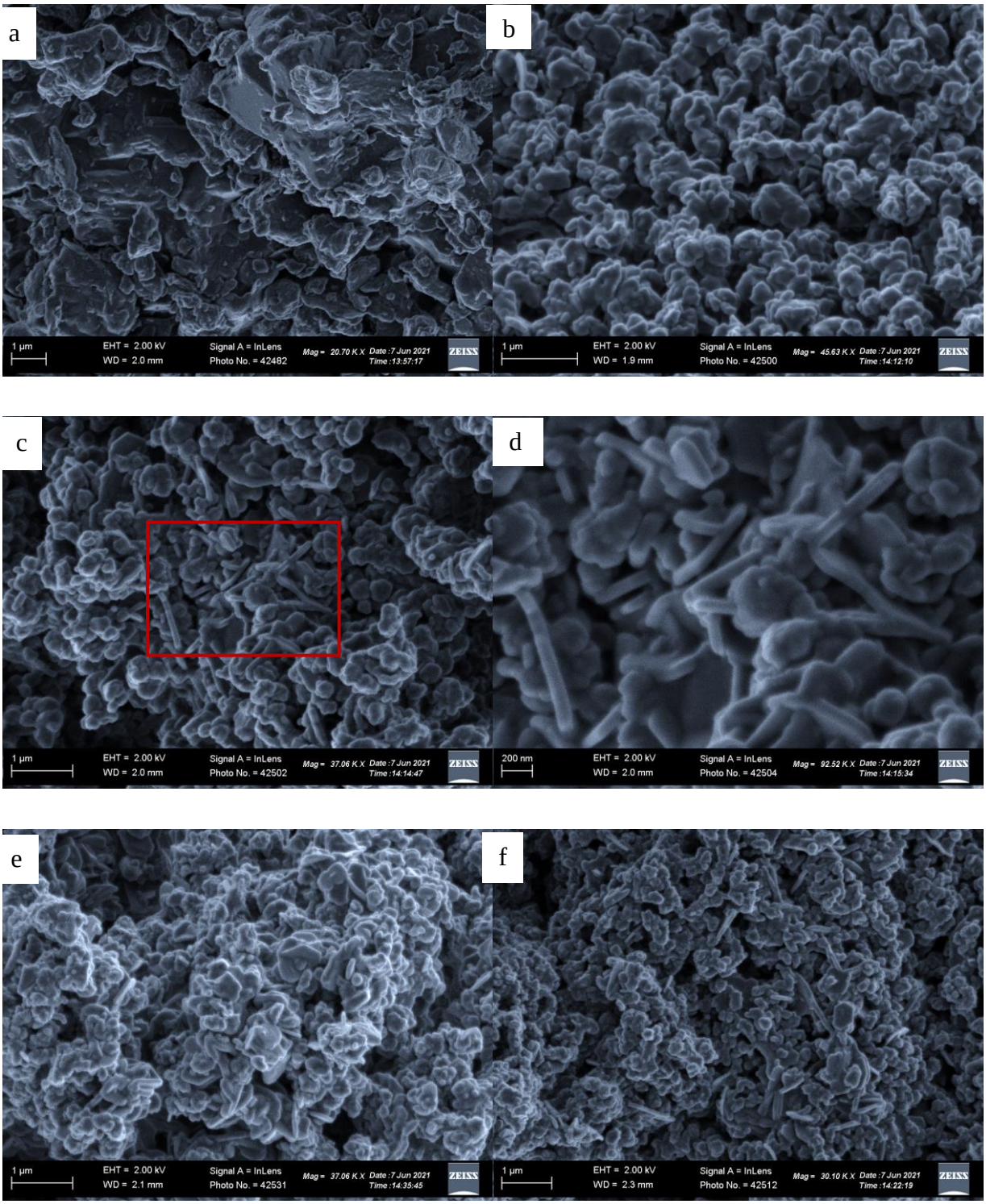


**Figure 60: SEM microphotograph of limestone (a) natural (b) calcined at 900ºC (c) 5%Fe-doped (d) insert of cropped section in c (e) 10%Fe-doped (f) 20%Fe-doped**

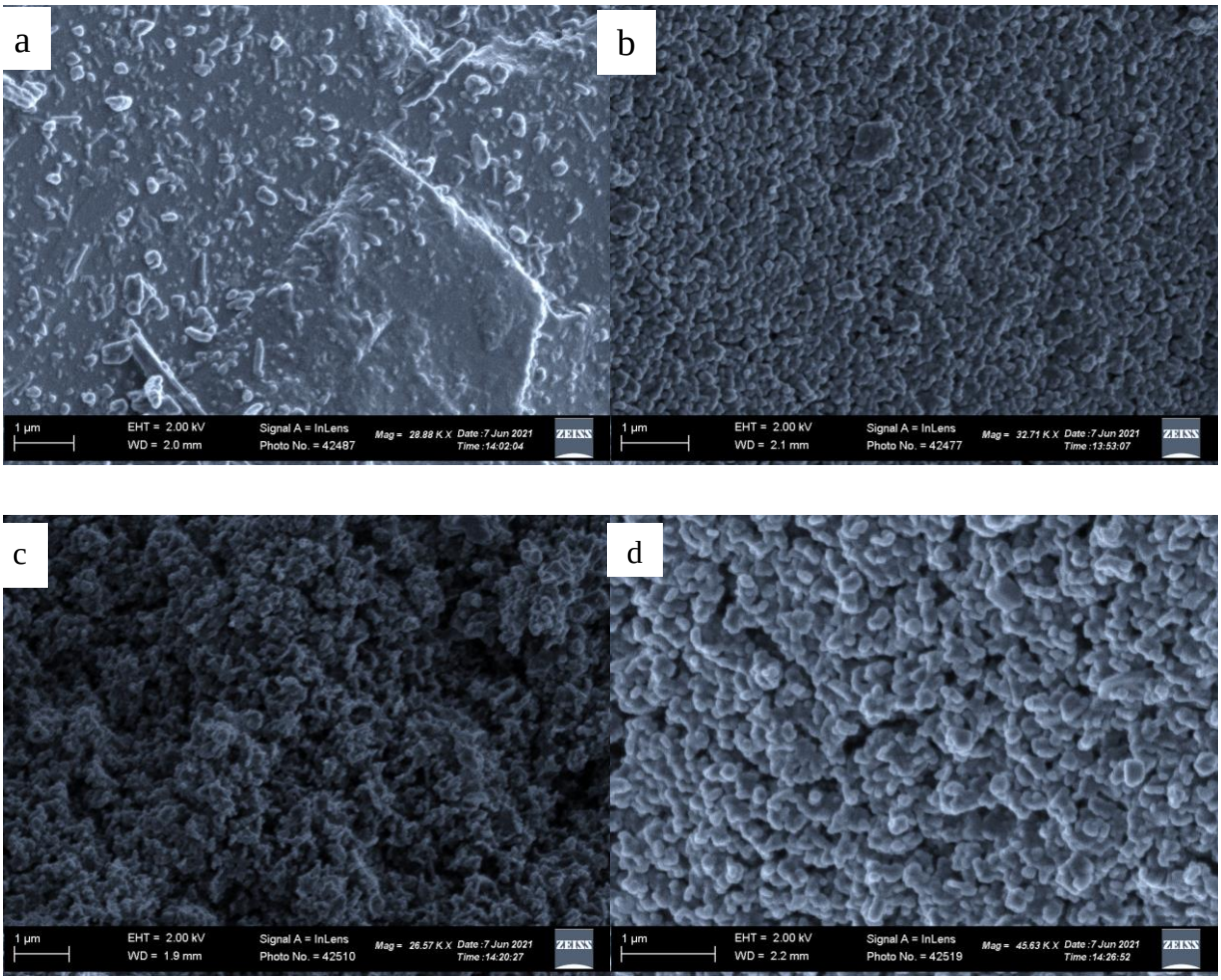


**Figure 61: SEM microphotograph of dolomite (a) natural form (b) calcined at 900ºC (c) 10%Fe-doped (d) 20%Fe-doped**

Figure 2 shows TEM images of the selected, manufactured catalysts before use in gasification reaction studies. The dark areas in Fig. 62 (b, c and d) are iron particles, whereas the grey areas in Fig. 62a is calcium. The scale bars in both images are 200 nm in length. The results suggest that iron tends to develop irregular clumps, but it also shows some dispersion as nanoparticles with particle sizes less than 60 nm in the catalyst matrix, as proven by XRD. When comparing Fig. 62a (calcined limestone before iron impregnation) and Fig. 62 (b and c) (after impregnation with 5% and 10% Fe, respectively), it is evident that there is good interaction between catalytic support and iron precursor. Another finding is that the particle distribution in 5%Fe/limestone and 10%Fe/dolomite catalysts was very comparable.

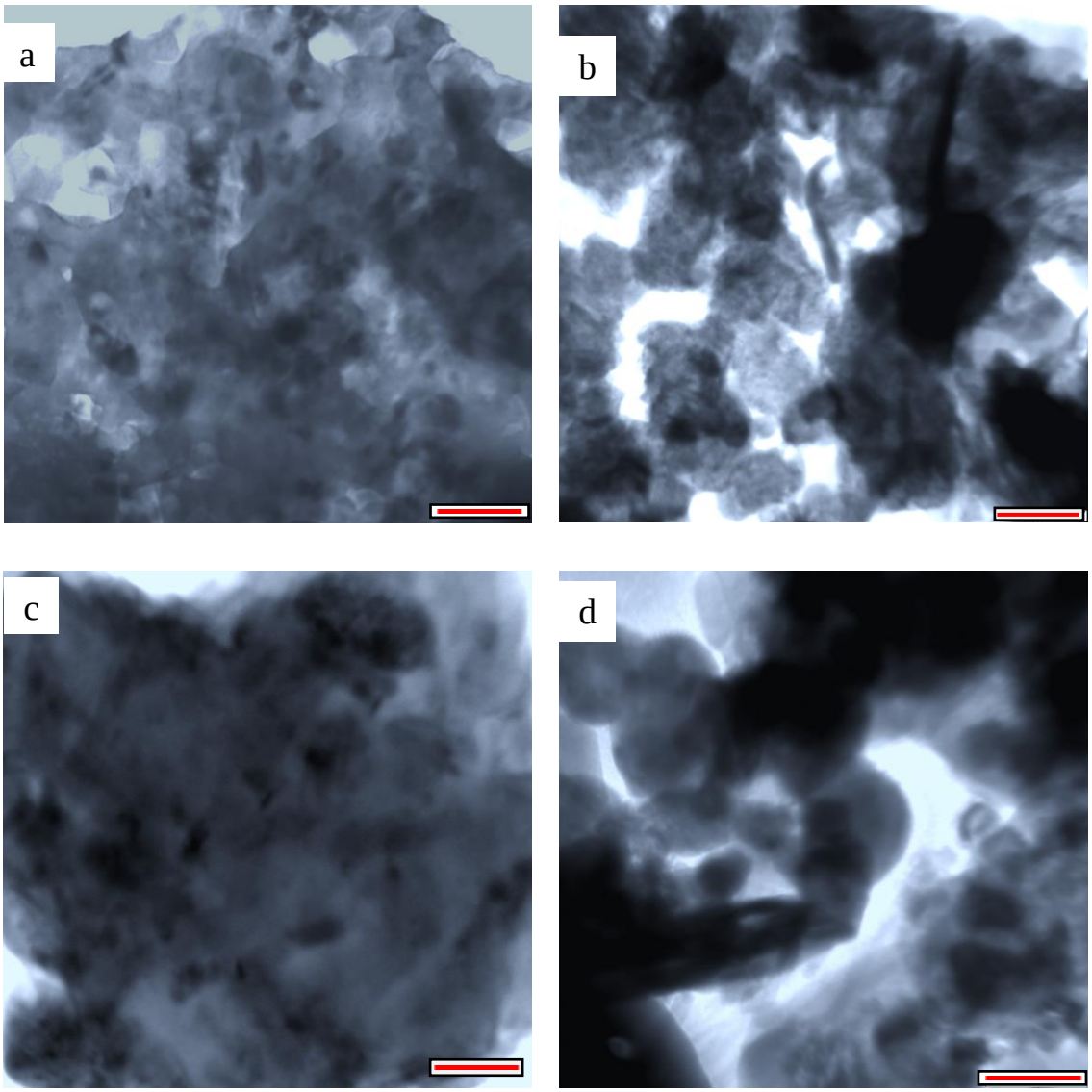


**Figure 62: TEM image of the selected fabricated catalysts. (a) calcined limestone; (b) 5%Fe/limestone; (c)10%Fe/limestone; (d) 10%Fe/dolomite**

### 4.4.3 Surface Area and Pore Volume Analysis

The nitrogen adsorption/desorption isotherms, BET surface area, and the BJH pore volume of various limestone and dolomite-based catalysts are shown in Fig. 63 and Fig. 64. The adsorbed volume increased from 5 $cm^3/g$ to 29.2 $cm^3/g$ when comparing natural and calcined limestone (Fig. 63a), increasing from 1.5 $cm^3/g$ to 29 $cm^3/g$ (Fig. 63b) when comparing between natural and calcined dolomite. Increased nitrogen adsorption can be explained by enhanced specific surface area and pore volume caused by sample decomposition to form metal oxides and $CO_2$. The BET surface area of the calcined dolomite is slightly higher compared to calcined limestone (Fig. 64), which can be explained by the higher content of CaO and MgO and lower content of

impurities (quartz) in dolomite than in limestone (Fig. 56 and Fig. 57). As previously reported by Mohammed *et al.* (2013), quartz combines with CaO to forms slag during high-temperature treatment, resulting in low pore volume and surface area. In this study, the calcined limestone attained a BET surface area of 7.5 $m^2$/g, nearly half reported by Ngamcharussrivichai *et al.* (2011) at the calcination temperature of 800ºC, which was 13.8 $m^2$/g. On the other hand, the BET surface area of 10.5 $m^2$/g is obtained for the calcined dolomite which is slightly higher than 8.8 $m^2$/g for the Shanxi dolomite reported by Yu *et al.* (2009) and slightly less than 12 $m^2$/g for Mallaga dolomite reported by Pérez *et al.* (1997). The variation of surface area and porosity could be influenced by the system used for the calcination as well as the operating temperature. Besides, high temperatures and long thermal treatment duration during the calcination cause particle sintering and a loss in both BET surface areas and porosity (Silcox *et al.*, 1989; Stanmore & Gilot, 2005). Nonetheless, in this study, the BET surface area is not an essential factor to consider because the catalyst surface area has no known influence on SCW gasification.

When iron is added, the nitrogen adsorption decreases, indicating a decrease in surface area and pore volume. Because of the small number of pores in the calcined material, samples doped with varying iron concentrations did not demonstrate significant changes in the volume of nitrogen adsorbed or the BET surface area. A similar observation was reported by Huang *et al.* (2012). In general, the surface area analysis found no significant trend in BET surface area, pore-volume, or average pore diameter for catalysts doped with varying iron content. According to the IUPAC classification of adsorption isotherms, natural dolomite exhibited type III isotherm (curve overlap with the adsorption-desorption), whereas other samples exhibit a type IV adsorption isotherm which is a typical characteristic of mesoporous and macroporous materials (Al-Othman, 2012; Ávila *et al.*, 2012; Gregg *et al.*, 1967; Shen & Yoshikawa, 2014; Webb & Orr, 1997). A type IV adsorption isotherm is characterised by surface coverage of mesoporous walls proceeded by pore-filling coupled with distinct hysteresis loops. At *p/po* values below 0.4, the adsorption-desorption isotherm shape is similar to that of the type III isotherm, but at p/po value above 0.4, pore condensation occurs, signifying the porous structure of the catalysts. Similarly, at higher relative pressure ranges (*p/po* >0.4), all samples, except for natural dolomite, exhibit hysteresis loops (zoom image), which could be induced by capillary condensation in the mesoporous architectures of the catalysts. The hysteresis behaviour of both samples can be characterised as type H3 (Sing, 1985). As per the IUPAC, comparable hysteresis is exhibited in particle aggregates having pore-shaped cracks (Fakher & Imqam, 2019; Sing *et al.*, 1999). Figure 63 (a and b) show no abrupt nitrogen uptake at the lower relative pressure for the samples indicating that the materials contain a small number of micropores.

The pore size distributions of the catalyst samples obtained using the BJH method are presented in Fig. 63(c and d). The pore size distribution of all samples except for the uncalcined dolomite is relatively homogeneous and concentrated below 10 nm, with abscissa peaks value distributed at approximately 1.5 nm, 2.5 nm, 3.8 nm, 5.8 nm and 7 nm. The pore diameter of less than 10 nm confirms the presence of micropores and mesopores, as corroborated by Al-Othman (2012). Figure 63c shows that as the iron content increases, the differential volume decreases, which is a possible pore-clogging. On the other hand, Fig. 63d shows that the differential volume increases with the addition of 10% iron and then decreases with more iron, suggesting a good interaction between iron and CaO at lower iron content that caused the material to develop more pores at lower iron content.

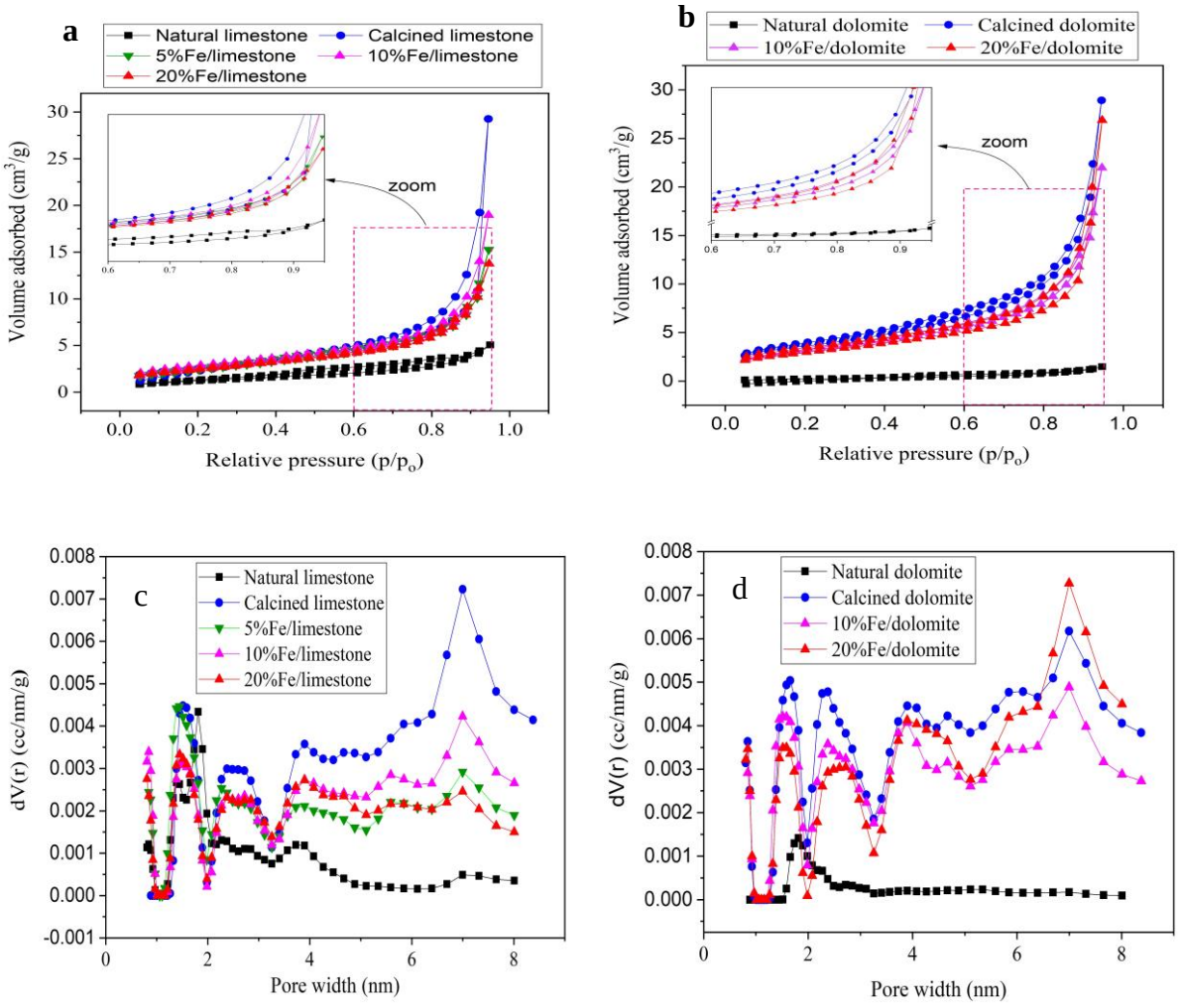


**Figure 63: Nitrogen adsorption/desorption isotherms of limestone-based catalyst (a), dolomite-based catalyst (b); pore size distribution computed by BJH method using a desorption isotherm of limestone-based catalyst (c) and dolomite-based catalyst (d)**

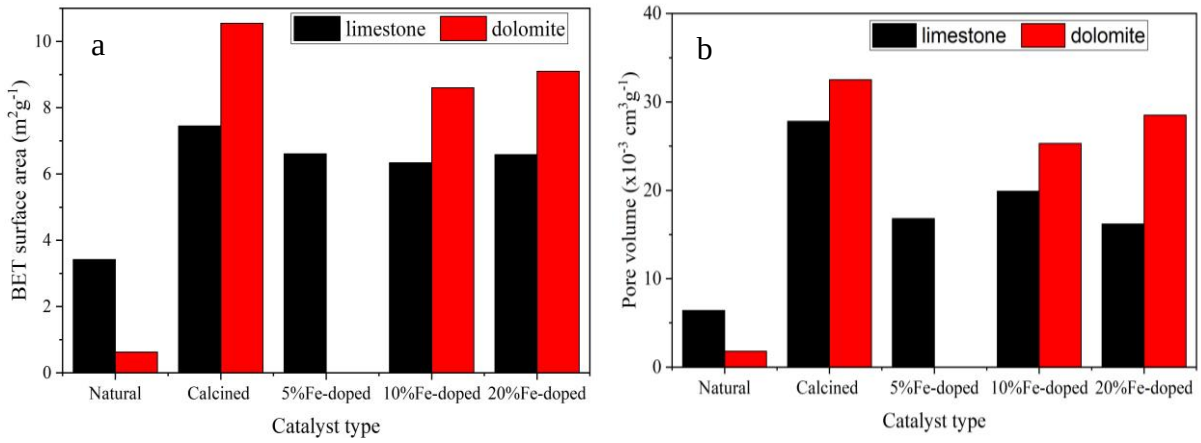


**Figure 64: Comparison of BET surface area (a) and pore volume (b)**

## 4.5 Optimization of Catalytic Supercritical Water Gasification

The addition of catalysts in SCW gasification is one of the efficient ways to improve gasification degree and hydrogen yield. Based on the results of the previous objective, SCW gasification conditions for this set of experiments were temperature 492°C, 120 minutes residence time, and 9.5 wt% biomass concentration. The influence of dolomite and limestone enhanced with Fe catalysts on the product yield of SCW gasification of rice husks was studied using different catalyst loadings (5-20 wt%) and Fe-content (0-20 wt%).

### 4.5.1 Model Fit and Statistical Analysis for Catalytic Supercritical Water Gasification

Table 19 shows the results from the predicted and experimentally measured responses for the 17 experimental runs according to the Design-Expert software. The GE ranged from 62.07% to 68.47% (dry basis). The maximum GE was observed from the 12$^{th}$ run, under the condition of $X_1$ = 20%, $X_2$ = 10% minutes and $X_3$ = limestone. On the other hand, char and gravimetric tar yields varied from 25.43 to 33.67 wt%, and 42.6 to 61.1 mg/g biomass, respectively. The lowest gravimetric tar yield was observed from the 8$^{th}$ run under the experimental condition of $X_1$ = 5%, $X_2$ = 20% and $X_3$ = dolomite. The gas volume ranged between 344.2 to 431.8 mL/g biomass, and the highest value was obtained from the 9$^{th}$ run, under the experimental condition of $X_1$ = 20%, $X_2$ = 20% and $X_3$ = dolomite.

The results obtained were fitted to a second-order polynomial model. The Design-Expert software suggested quadratic models for GE, char yield and gas volume, and 2-factor interactions for gravimetric tar, as shown in Table 18. The final empirical models in terms of the coded variable (Equation 46-49) were derived after the reduction of trivial terms ($p > 0.1$)

through the *p*-values backward model selection algorithm in the Design-Expert software. However, some of the insignificant terms were reserved for promoting the hierarchy of the model.

**Table 18: Response transformation and model fitting summary**

| Response | Response range | Ratio* | Transformation | Fit summary |
|---|---|---|---|---|
| GE (%) | 62.1– 68.5 | 1.1 | none | Quadratic |
| Char yield (wt%) | 25.4 – 33.7 | 1.3 | none | Quadratic |
| Gravimetric tar (mg/g) | 42.6 – 61.1 | 1.4 | none | 2FI** |
| Gas volume (mL/g) | 344.2 – 431.8 | 1.3 | none | Quadratic |

*Means ratio of maximum to the minimum response (a ratio >10 suggests response transformation) and ** 2FI means 2-factor interactions

$$\text{GE (\%)} = 68.02 + 1.23X_1 - 0.78X_2 - 0.80X_3 + 0.59X_2X_3 - 1.51{X_1}^2 - 2.0{X_2}^2 \quad (46)$$

$$\text{Char yield (wt\%)} = 26.81 - 1.80X_1 + 0.62X_2 + 0.80X_3 - 0.50X_2X_3 + 1.27{X_1}^2 + 2.26{X_2}^2 \quad (47)$$

$$\text{Gravimetric tar yield } (mg/g) = 52.84 + 5.80X_1 + 0.75X_2 - 0.809X_3 + 3.09X_1X_2 \quad (48)$$

$$\text{Gas volume } \left(\frac{\text{mL}}{\text{g}}\right) = 390.97 + 28.63X_1 + 10.94X_2 + 3.77X_3 - 6.20X_1X_3 + 9.86{X_2}^2 \quad (49)$$

The polynomial Equations 46 – 49 can be used to precisely predict the GE, char, gravimetric tar, and gas volume of SCW gasification of RH, respectively. Generally, the negative sign signifies the antagonistic effect of the factors, and the positive sign indicates the synergistic effects of the factors. Examining the coefficients and the power of the polynomial model factors, the catalyst loading has the most substantial influence on SCW gasification of RH, followed by the Fe-content and finally, the catalyst type. The effect of factors on the GE, char yield and gravimetric tar follows a similar trend: Catalyst loading > catalyst type > Fe-content. On the other hand, the pattern of gas volume factors follows a different order: Catalyst loading> Fe-content > catalyst type.

To ensure that the derived polynomial model matches well with the experimental results, a test for the significance of the regression model and its coefficient, lack-of-fit and pure-error is performed. Essential variables are ranked based on the probability value (*p*-value) with a confidence level of 95%. The outcome of the analysis of variance (ANOVA) for the responses

provided by Equations 46 to 49 is tabulated in Table 20. A lower *p*-value ($p < 0.05$) means that both models are significant, whereas a non-significant lack-of-fit ($p>0.05$) for both models suggests that the lack-of-fit is not significant in contrast with pure error, and the models can predict variations correctly.

The R-squared is used to determine the consistency of the fitted polynomial model, representing the proportion of the uncertainty of the data compensated for by the mathematical model. Therefore, it is more suitable to use Adj-$R^2$, which penalises the static R-squared if unnecessary terms are added to the model (Fermoso *et al.*, 2010). The $R^2$, adjusted $R^2$ and predicted $R^2$-value for both models are close to 1 (>0.9), suggesting the precision of the predicted polynomial model (Table 21). The difference between predicted R-squared and adjusted R-squared is less than 0.2, suggesting a strong correlation between actual and predicted data. It also means that the proposed regression models offer an adequate description of the relationship between responses and factors.

Adequate precision measures the signal to noise ratio by comparing the range of the predicted values at the design points to the average prediction error. A ratio higher than four suggests adequate model discrimination (Dritsa *et al.*, 2009). In this study, the ratio of 15.63 and 21.92 is obtained, suggesting an adequate signal, and it also means that the models provide a robust signal to navigate the design space. The coefficient of variation (CV) indicates the degree of precision with which the repeated experiments are compared (Gangadharan *et al.*, 2008). Generally, a CV <5% is considered acceptable (Campbell *et al.*, 2010). In this study, a CV of < 3.55% is obtained for both regression models, suggesting that model reproducibility is satisfactory (Table 21).

The normal probability plots of the residual and experimental versus predicted values are used to ascertain the predicted models' validity. The normal probability plot measure whether the data set is approximately normally distributed or not (Chambers *et al.*, 1983). The data are plotted against a theoretical normal distribution so that the points should form an approximate straight line. Deviation from this straight line implies a divergence from normality. The plots for the normal probability and the externally studentised residuals and the predicted versus actual values for both responses are presented in Fig. 65 and 66. Visually, the normal probability plots display a linear pattern that is verified by a slight deviation of points from the straight line. The fact that the data in the lower and upper ends of the plot does not deviate substantially from the best fit lines means that there are no significant outliers and that the errors are distributed normally without any abnormality in the models (Fig. 65). Figure 66 is a scatter plot of the

results of the experimental values against the predicted values of the RSM at a 95% confidence interval. The value of determination of coefficient (R-squared) of >0.9 (Table 21) for both plots means that the predicted values correspond well to the experimental ones within the design region. In addition, the established models can give a practically good estimation of the responses.

**Table 19: Experimental variables and products distribution of catalytic supercritical water gasification of rice husk using I-optimality design**

| Run No | Variables | | | Response variables | | | | | | | |
|---|---|---|---|---|---|---|---|---|---|---|---|
| | $X_1$ (%) | $X_2$ (%) | $X_3$ (-) | GE (%) | | Char yield (wt%) | | Gravimetric tar (mg/g biomass) | | Gas volume (mL/g biomass) | |
| | | | | Exp. | Pred. | Exp. | Pred. | Exp. | Pred. | Exp. | Pred. |
| 1 | 5 | 10 | Dolomite | 64.2 | 64.5 | 31.2 | 30.7 | 45.9 | 46.2 | 364.5 | 372.3 |
| 2 | 10 | 10 | Dolomite | 66.1 | 66.7 | 28.8 | 28.3 | 51.0 | 50.3 | 388.0 | 388.0 |
| 3 | 20 | 10 | Limestone | 68.0 | 68.5 | 26.1 | 25.5 | 59.2 | 59.5 | 427.1 | 422.0 |
| 4 | 5 | 0 | Dolomite | 62.6 | 62.7 | 32.6 | 32.8 | 48.2 | 48.6 | 375.5 | 371.2 |
| 5 | 5 | 0 | Limestone | 64.8 | 65.5 | 30.3 | 30.2 | 49.0 | 50.2 | 344.2 | 351.3 |
| 6 | 5 | 10 | Limestone | 66.5 | 66.1 | 28.9 | 29.1 | 46.0 | 47.9 | 353.6 | 352.4 |
| 7 | 10 | 10 | Dolomite | 67.1 | 66.7 | 27.8 | 28.3 | 50.9 | 50.3 | 388.8 | 388.0 |
| 8 | 5 | 20 | Dolomite | 62.1 | 62.3 | 33.7 | 33.1 | 42.6 | 43.9 | 391.1 | 393.1 |
| 9 | 20 | 20 | Dolomite | 64.9 | 64.7 | 29.0 | 29.5 | 61.1 | 61.7 | 431.8 | 438.0 |
| 10 | 20 | 0 | Limestone | 68.4 | 67.9 | 26.1 | 26.6 | 54.9 | 55.6 | 419.3 | 421.0 |
| 11 | 10 | 20 | Limestone | 64.1 | 64.9 | 30.7 | 30.0 | 52.4 | 51.7 | 409.9 | 397.6 |
| 12 | 20 | 10 | Limestone | 68.5 | 68.5 | 25.4 | 25.5 | 61.0 | 59.5 | 415.1 | 422.0 |
| 13 | 20 | 0 | Dolomite | 65.1 | 65.1 | 29.6 | 29.2 | 52.6 | 54.0 | 419.3 | 416.1 |
| 14 | 10 | 10 | Dolomite | 67.3 | 66.7 | 27.4 | 28.3 | 53.1 | 50.3 | 395.8 | 388.0 |
| 15 | 10 | 20 | Limestone | 65.1 | 64.9 | 30.1 | 30.0 | 48.7 | 51.7 | 394.2 | 397.6 |
| 16 | 10 | 0 | Limestone | 68.0 | 67.7 | 28.0 | 27.8 | 54.2 | 52.1 | 377.0 | 375.7 |
| 17 | 5 | 20 | Limestone | 63.6 | 62.7 | 31.6 | 32.5 | 48.1 | 45.5 | 372.3 | 373.2 |

Where: $X_1$ is catalyst loading, $X_2$ is the Fe content, $X_3$ is the catalyst type (limestone = -1 and dolomite = 1), *Exp.* is the experimental value, and *Pred.* is the predicted value

**Table 20: Analysis of variance for the response surface predicted model**

| | GE (%) | | | Char yield (wt%) | | | Gravimetric tar (mg/g biomass) | | | Gas volume (mL/g biomass) | | |
|---|---|---|---|---|---|---|---|---|---|---|---|---|
| | **SS** | **F** | ***p*** | **SS** | **F** | ***p*** | **SS** | **F** | ***p*** | **SS** | **F** | ***p*** |
| Model | 61.75 | 26.55 | <0.0001 | 82.16 | 32.54 | <0.0001 | 402.44 | 29.38 | <0.0001 | 10115.82 | 45.68 | <0.0001 |
| $X_1$ | 15.89 | 40.99 | <0.0001 | 34.26 | 81.43 | <0.0001 | 356.09 | 103.99 | <0.0001 | 18768.52 | 197.97 | <0.0001 |
| $X_2$ | 5.74 | 14.81 | 0.0032 | 3.59 | 8.53 | 0.0153 | 5.19 | 1.52 | 0.2417 | 1162.25 | 26.24 | 0.0003 |
| $X_3$ | 10.51 | 27.10 | 0.0004 | 10.40 | 24.72 | 0.0006 | 10.88 | 3.18 | 0.1000 | 224.82 | 5.08 | 0.0457 |
| $X_1X_2$ | | | | | | | 62.87 | 18.36 | 0.0011 | | | |
| $X_1X_3$ | | | | | | | | | | 364.70 | 8.23 | 0.0178 |
| $X_2X_3$ | 3.25 | 8.37 | 0.0160 | 2.33 | 5.54 | 0.0404 | | | | | | |
| $X_1^2$ | 6.81 | 17.58 | 0.0019 | 4.81 | 11.43 | 0.0070 | | | | | | |
| $X_2^2$ | 15.62 | 40.30 | <0.0001 | 20.01 | 47.55 | <0.0001 | | | | 343.42 | 7.75 | 0.0178 |
| Residual | 3.88 | | | 4.21 | | | 41.09 | | | 487.21 | | |
| Lack of Fit | 2.40 | 1.09 | 0.4899 | 2.72 | 1.22 | 0.4434 | 29.78 | 1.32 | 0.4202 | 255.16 | 0.6283 | 0.7228 |
| Pure Error | 1.47 | | | 1.49 | | | 11.31 | | | 232.05 | | |
| Cor Total | 65.62 | | | 86.36 | | | 443.53 | | | 10603.03 | | |

**Table 21: Model fit statistics for the gasification yield**

| | GE (%) | Char yield (wt%) | Gravimetric tar (mg/g biomass) | Gas volume (mL/g) |
|---|---|---|---|---|
| $R^2$ | 0.9409 | 0.9513 | 0.9074 | 0.9540 |
| Adj $R^2$ | 0.9055 | 0.9220 | 0.8765 | 0.9332 |
| Pred $R^2$ | 0.8453 | 0.8589 | 0.8169 | 0.8899 |
| Adeq. Precision | 15.638 | 18.203 | 17.726 | 21.924 |
| Std. Dev. | 0.6226 | 0.6487 | 1.85 | 6.66 |
| Mean | 65.66 | 29.25 | 51.70 | 392.20 |
| C.V. % | 0.9481 | 2.22 | 3.58 | 1.70 |
| PRESS | 10.15 | 12.18 | 81.20 | 1167.41 |

Where *CV* is the coefficient of variance

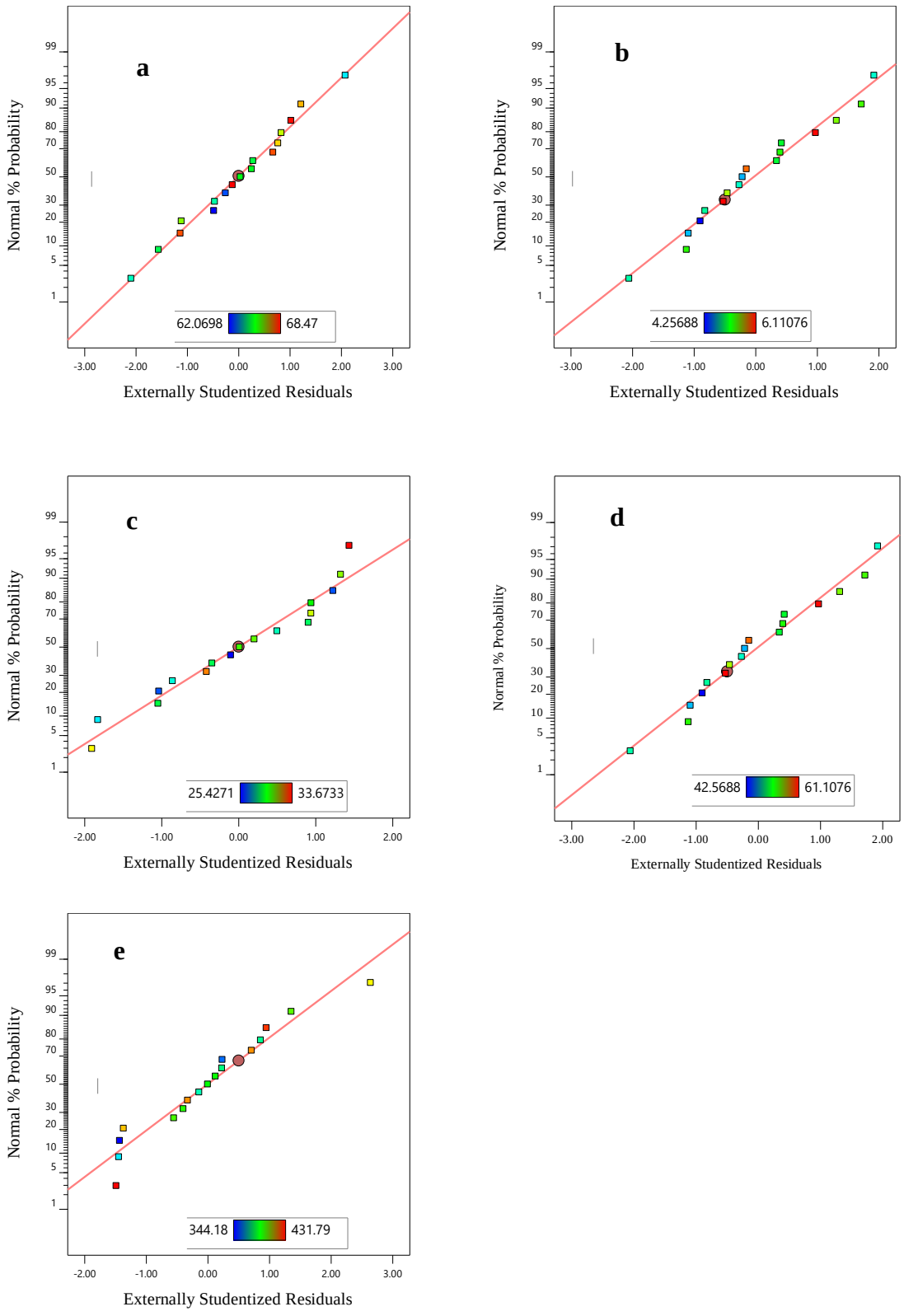


**Figure 65: Studentised residuals and normal percentage probability plot for (a) GE, % (b) tar yield, wt% (c) char yield, wt% (d) gravimetric tar, mg/g biomass and (e) gas volume, mL/g biomass**

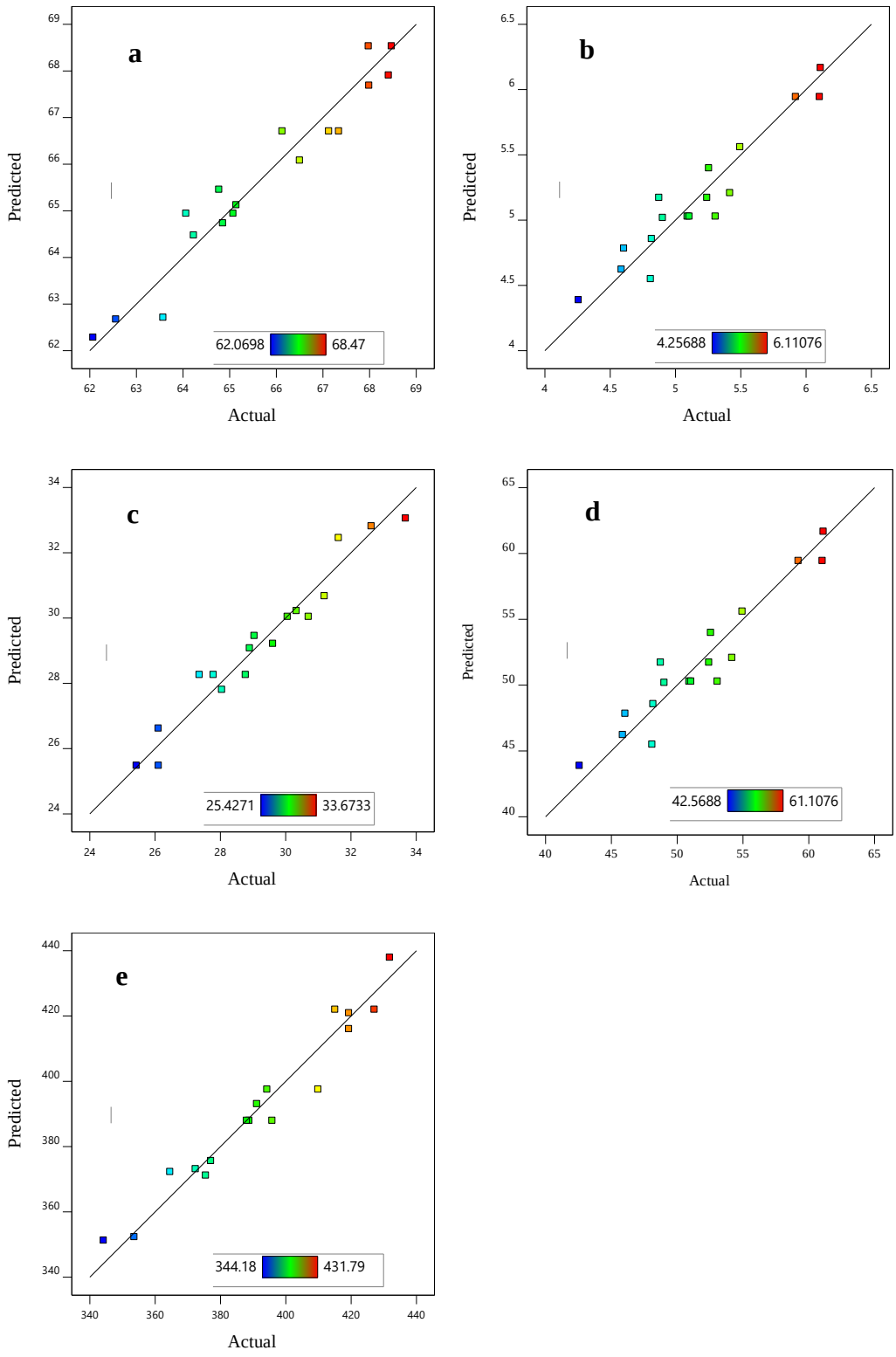


**Figure 66: Comparisons of predicted and experimental values of catalytic SCW gasification for: (a) GE, % (b) tar yield, wt% (c) char yield, wt% (d) gravimetric tar, mg/g biomass and (e) gas volume, mL/g-biomass**

### (i) Influence of Catalyst Parameters on Gasification Efficiency

The GE was observed using 10% uncalcined and calcined dolomite and limestone, and the results were compared to the results of a non-catalytic SCW gasification. When uncalcined limestone or dolomite was added, the GE increased by 12.2% and 12.6%, respectively. Figure 65 shows that when the calcined catalyst is added, the GE marginally increases by 1.0% for calcined limestones and decreases by 3.0% for calcined dolomite compared to uncalcined ones. It is possible that calcined dolomite promoted reaction leading to tar formation as described in section (iii). The order of catalytic effect on GE of SCW gasification using 10% catalyst loading is as follows: Calcined limestone ≈ uncalcined (dolomite ≈ limestone) > calcined dolomite > non-catalytic.

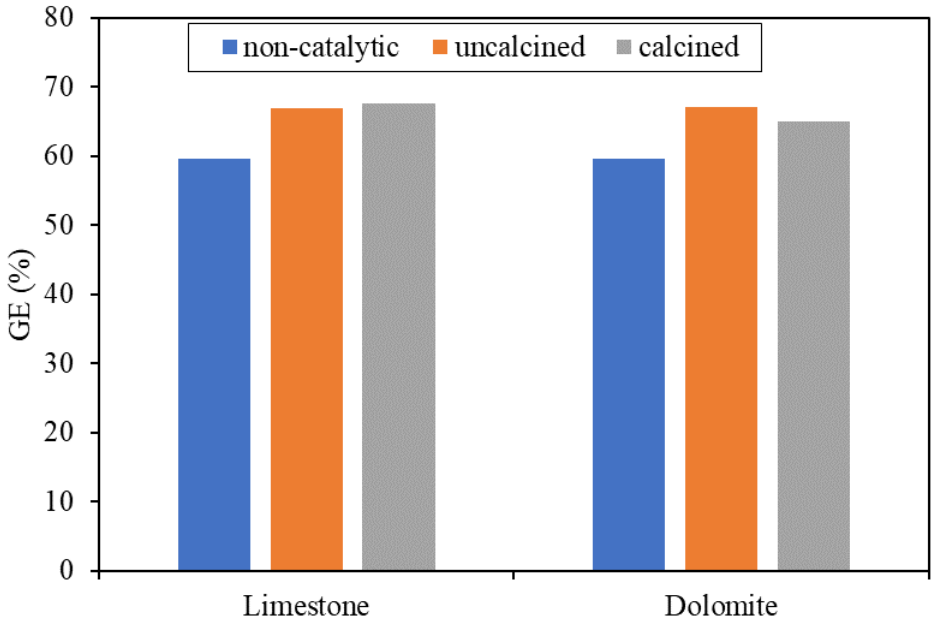


**Figure 67: Gasification efficiency obtained from rice husk gasification with and without catalyst (catalyst loading 10 wt% and operating condition 492ºC, residence time 120 minutes and feed concentration 9.5 wt%)**

The interactions of catalyst-loading and Fe-content on the GE are studied, and responses are presented by perturbation, contour, and 3D surface plots. The perturbation plots were used in examining the impact of individual effects of catalyst loading and Fe-content in gasification yield. The plots help compare all the parameters at a particular point in the design space by shifting one factor while others remain constant. The perturbation plots for GE yield (Fig. 68) demonstrate that the relationship between Fe-content and catalyst loading has an inverted C-like shape. These observations imply that the GE is sensitive to the changes of both parameters. The perturbation plot for limestone-based catalyst (Fig. 68a) shows that both Fe-content and catalyst loading have steeper slopes than the perturbation curves for dolomite-based catalyst

(Fig. 68b). This implies that GE varies with the variation of both catalyst loading and Fe-content, the latter having a slight influence on GE with more pronounced in dolomite-based compared to limestone-based catalyst.

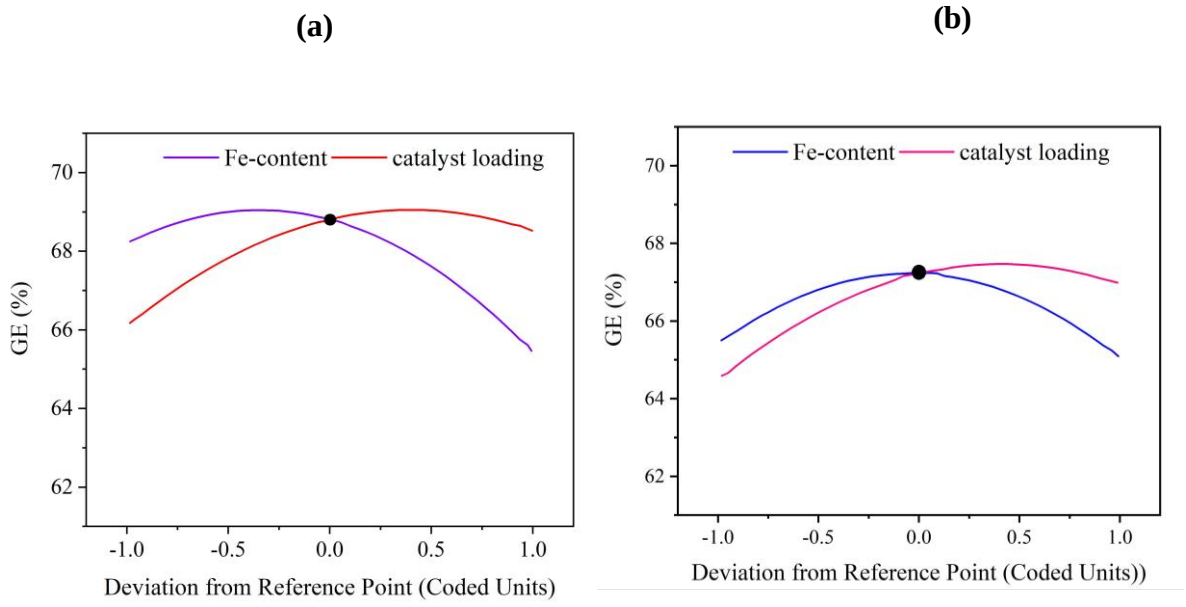


**Figure 68: Perturbation plot showing the interaction of factors on GE on catalytic SCW gasification of rice husk with; (a) limestone-based catalyst and (b) dolomite-based catalyst**

Observation in Fig. 69a to 69b shows that the GE is enhanced by 9.9% and 5.2% from 59.59% for non-catalytic SCW gasification to 65.5% and 62.7% for catalytic gasification reaction using 5 wt% of calcined limestone and dolomite, respectively. The GE increased further with catalyst loading and reached a maximum value of 68.4% and 65.7% using catalyst loading of 15% and calcined limestone and dolomite. The addition of Fe increased the GE slightly, reaching a maximum value of 69.3% and 67.3% using 7%Fe/limestone and 7%Fe/dolomite, respectively. Any further addition of the two variables led to a decrease in GE. The increase in GE is attributed to an enhancement in char gasification induced by MgO, CaO, $Ca_2Fe_2O_5$, and free iron oxide catalyst, resulting in more gas products. On the other hand, the decrease in GE due to increased iron content could be attributed to increased tar and char yield, as described in sections (iii) and (iv). It is worth mentioning that an appropriate balance of CaO, $Ca_2Fe_2O_5$, and free iron oxide phases on the catalyst is critical for improving GE. As more iron is added, $Ca_2Fe_2O_3$ spreads across the entire catalyst surface, reducing the proportion of CaO active sites involved in the gasification reaction and lowering the GE.

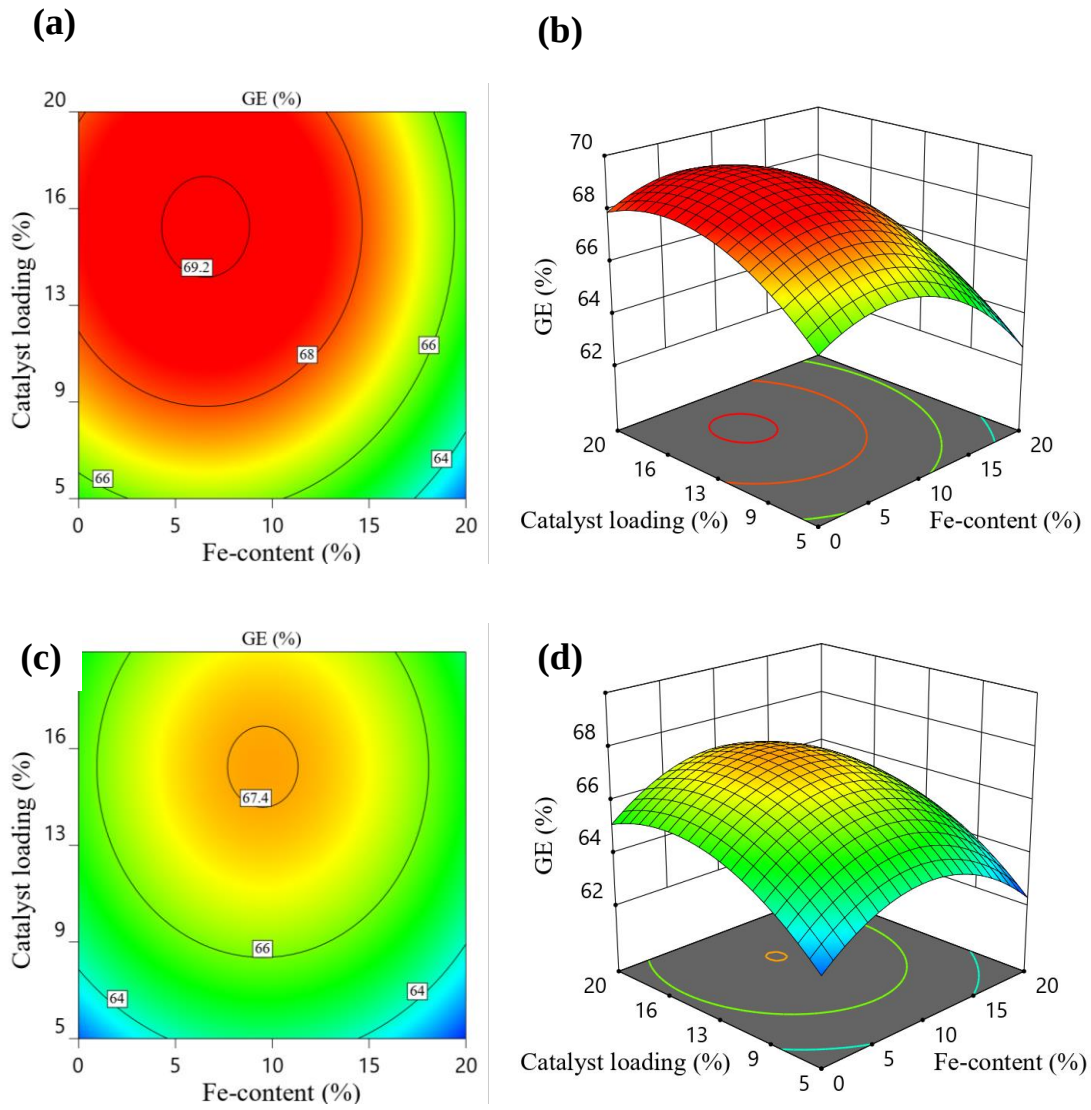


**Figure 69: Contour and 3D response surface plots representing different interactive effects of catalyst loading and Fe-content on gasification efficiency, (a, b) limestone-based catalyst and (c, d) dolomite-based catalyst**

### (ii) Influence of Catalyst Parameters on Gas Yield

Initially, gas volume was observed with the addition of either 10% uncalcined limestone or dolomite catalyst and with 10% calcined-dolomite or limestone (Fig. 70). Gas volume increased by 17.02% when 10 wt% of uncalcined limestone was added and by 11.55% when 10 wt% uncalcined dolomite was added. When Madenoğlu *et al.* (2012) studied SCW gasification of tobacco stalks at 600°C with 10 wt% dolomite, they found a 14.3% increase in gas volume, higher than reported in this study. This situation can be explained by differences in biomass composition, operating condition and composition of dolomite used. Orío *et al.* (1997) observed the increase of the lower heating value of the gas by 15% and the $H_2$ content rise by 4%, while the content of CO, $CH_4$ and $CO_2$ remained unchanged. When 10% calcined-limestone or

dolomite is added, the gas volume increases from 286.1 mL/g-biomass for non-catalytic gasification to 373.12 mL/g-biomass and 399.71 mL/g-biomass, respectively (Fig. 70). The formation of a complex of CaO-MgO during calcination of dolomite, a mixed oxide acid-base type catalyst with active polar sites, could explain why calcined-dolomite produces more gas than calcined-limestone. During SCW gasification of biomass, these active sites can absorb hydrocarbons and break C–C and C–H bonds to produce gas and liquid products in small molecular sizes (Jin *et al.,* 2014). Compared to non-catalytic and uncalcined limestone and dolomite, calcined limestone and dolomite demonstrate strong gas yield potential during SCW gasification. The order of catalytic effect on gas yield of SCW gasification of RH using 10% catalyst follows the trend: calcined (dolomite > limestone) > uncalcined (limestone > dolomite) > non-catalytic.

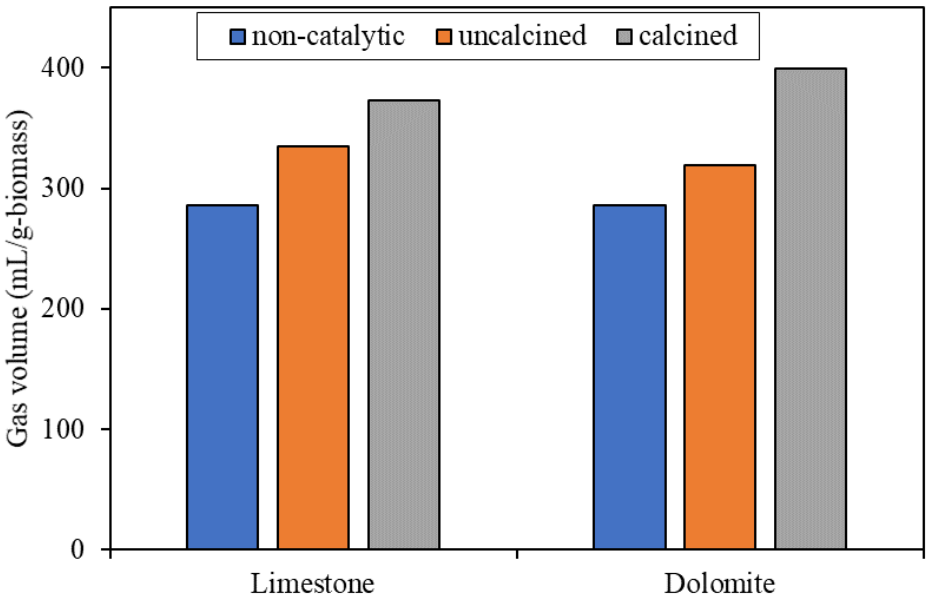


**Figure 70: Gas volume obtained from rice husk gasification with and without catalyst (catalyst loading 10 wt% and operating condition 492°C, residence time 120 minutes and feed concentration 9.5 wt%)**

The interaction of the catalyst loading and Fe-content on the gas volume is shown by perturbation, contour, and 3D surface plots in Fig. 71 and 72. Figures 71a and 71b show that gas volume is proportional to catalyst loading, with the curve for calcined-limestone based catalysts having a steeper slope than calcined-dolomite based catalysts. This means that, in comparison to iron content, catalyst loading is more sensitive to gas formation. On the other hand, iron content has a steeper slope at higher content than lower ones for both calcined-limestone and dolomite-based catalysts, indicating that the amount of iron in the catalyst significantly impacts gas formation reactions.

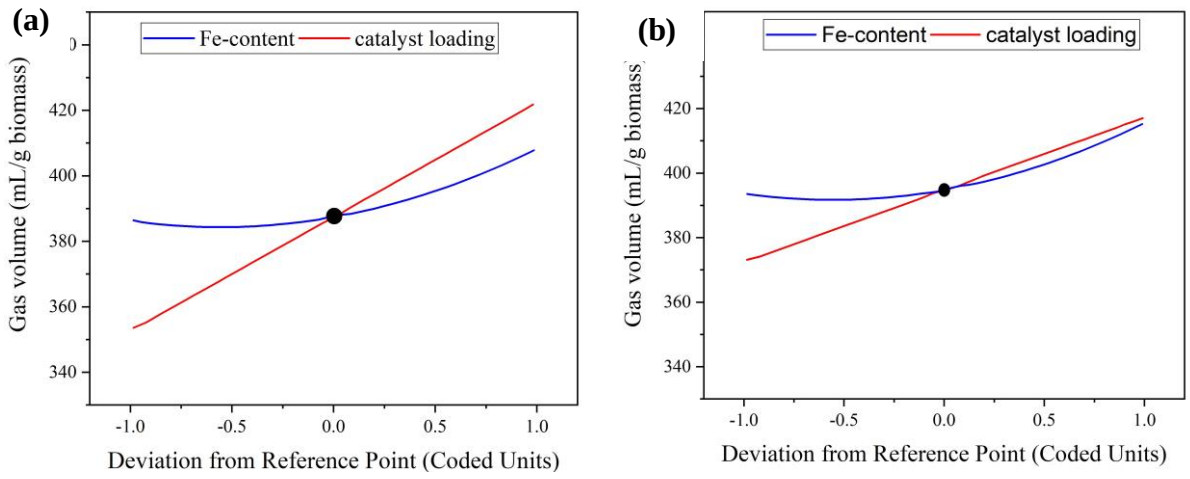


**Figure 71: Perturbation plot showing the effect of factors on gas volume in catalytic SCW gasification of rice husk with; (a) limestone-based catalyst and (b) dolomite-based catalyst**

Figure 72 (a-d) shows the effects of catalytic SCW gasification on gas volume as a contour and 3D surface plots. The gas volume rose sharply by 22.7% and 29.7% from 286.2 mL/g-biomass to reach 351.3 mL/g-biomass and 371.2 mL/g-biomass the addition of 5% calcined limestone or dolomite, respectively. The result is higher than the 10-20% obtained by Orío *et al.* (1997) while investigating the activity of various calcined dolomites for hot gas cleaning.

On the addition of Fe, the gas volume rose sharply in comparison to the non-catalytic configuration. The highest gas volume of 442.8 mL/g-biomass (57.7% increase) and 438 mL/g biomass (53% increase) was reached with the addition of 20% of 20%Fe/limestone or 20%Fe/dolomite catalyst, respectively.

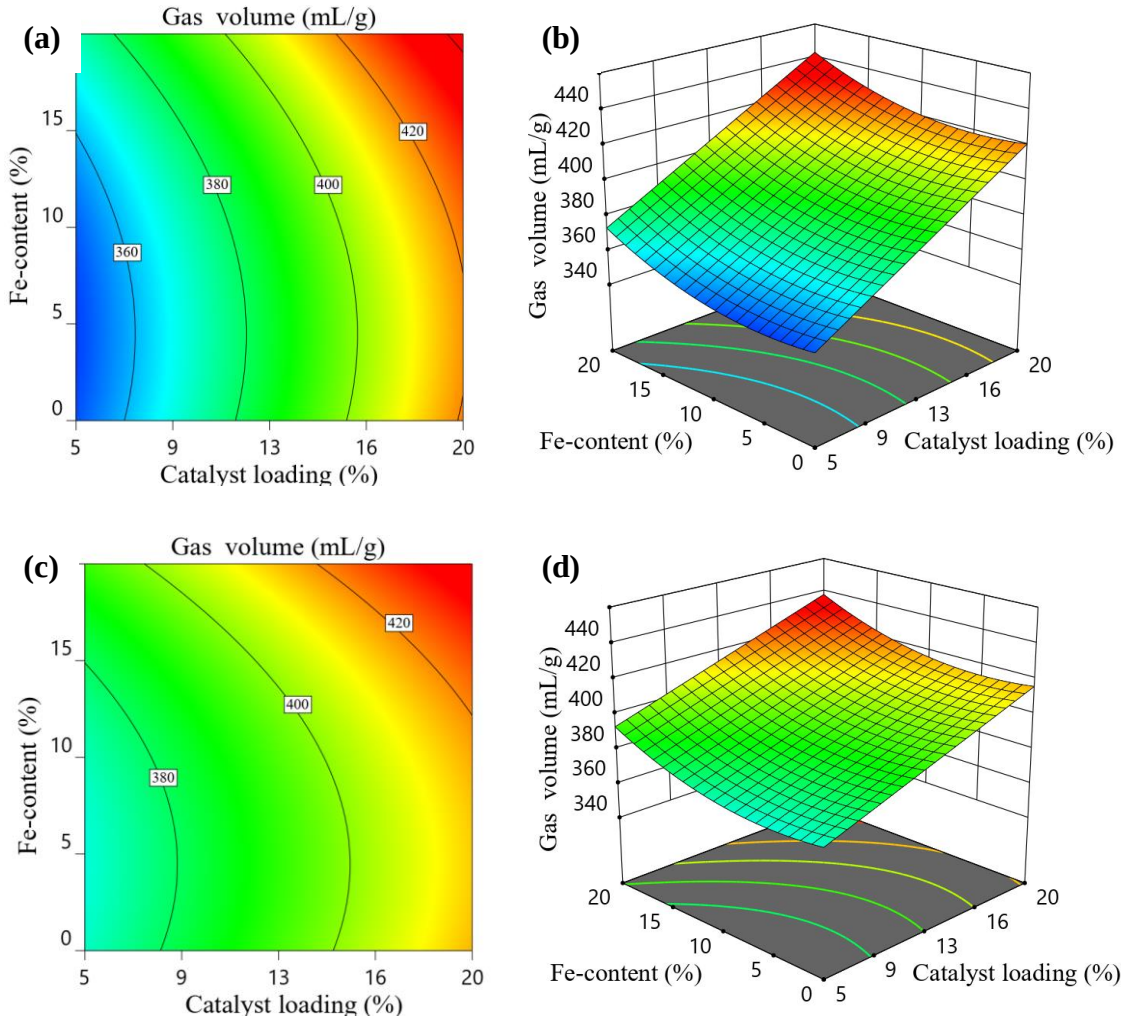


**Figure 72: Contour and 3D response surface plots representing different interactive effects of catalyst loading and Fe-content on gas yield: limestone-based catalyst (a, b) and dolomite-based catalyst (c, d)**

The reaction pressure versus the time curves of selected representative experimental runs could also demonstrate an increased gas volume (Fig. 73). The experiments with a high volume of gas represented a high final pressure throughout the entire experimental cycle. The temperate remained constant during the residence, although the pressure was increasing steadily due to incremental partial gasification of the reaction mixture to form permanent gas. Each experiment's maximum pressure is highly dependent on the catalyst charge and the Fe content.

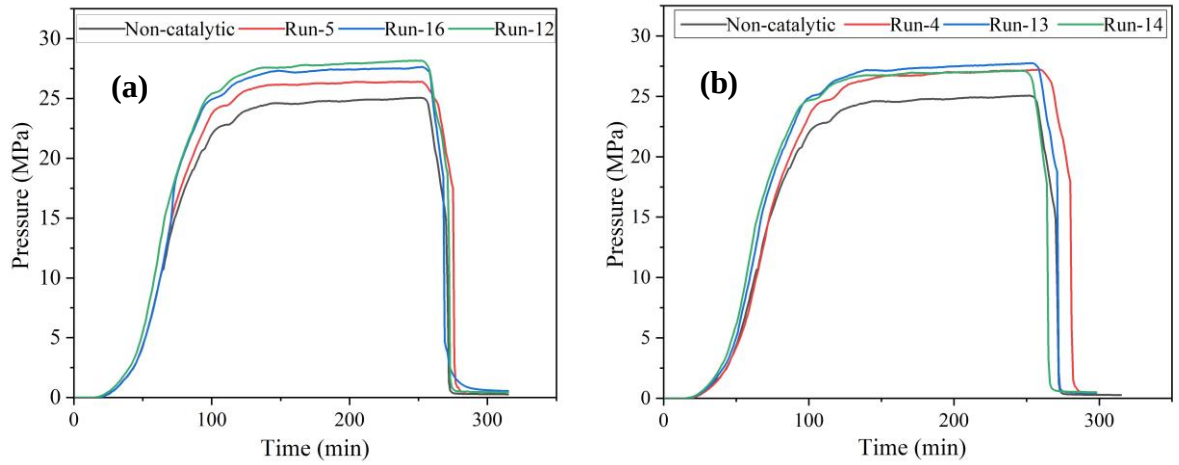


**Figure 73: Reaction pressure versus time for the representative runs of SCW gasification of rice husk with feed concentrations 9.5 wt% using; (a) limestone-based catalyst and (b) dolomite-based catalyst. The reactor was heated gradually from ambient temperature to 492°C at 4°C/minutes and held for 120 minutes**

The perturbation plots for maximum pressure (Fig. 74) demonstrate that the catalyst loading curve has a steeper slope than the Fe-content curve.

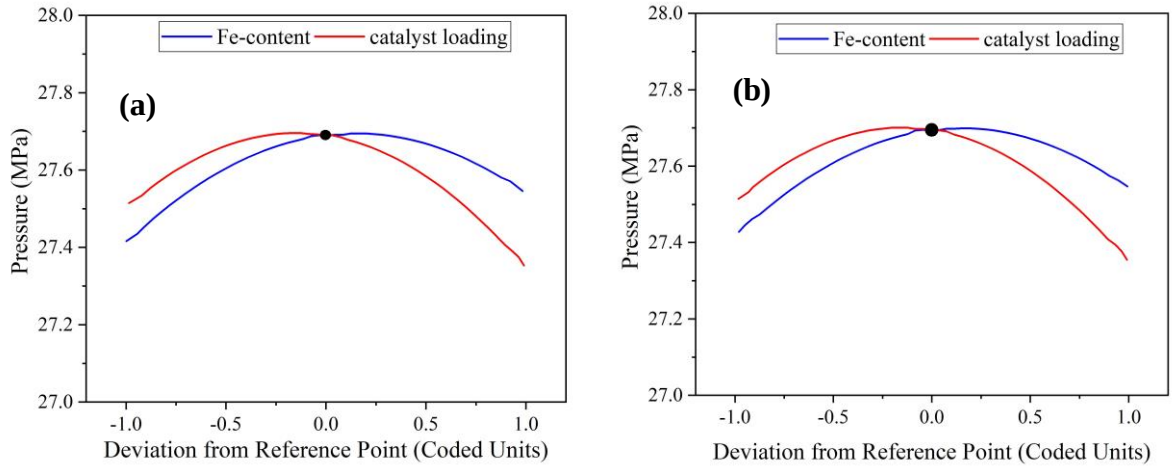


**Figure 74: Perturbation plot showing the effect of factors on maximum reaction pressure on catalytic SCW gasification of rice husk with; (a) limestone-based catalyst and (b) dolomite-based catalyst**

This is evident that the volume of gas is more responsive to the change in the loading of the catalyst compared to Fe content. The maximum pressure for both limestone and dolomite-based catalyst ranged between 27-28.2 MPa, marginally higher than 26.2 MPa for non-catalytic reactions. Pressure has recorded a less significant impact on catalytic SCW gasification (Hu *et al.*, 2020; Osada *et al.*, 2006). Therefore, this study did not consider the influence of pressure changes in gasification products.

### (iii) Influence of Catalyst Parameters on Tar Yield

Gravimetric tar yield was at first investigated by adding either 10% uncalcined or calcined dolomite or limestone and comparing the results to non-catalytic findings (Fig. 75). When 10% uncalcined limestone is added, the gravimetric tar yield increases by 18.45% compared to the non-catalytic yield, whereas it remains nearly constant when 10% uncalcined dolomite is added. This finding can be explained by comparing the BET surface area and pore volume of natural dolomite and limestone (Fig. 64a and b); the latter is considerably higher, implying that the limestone catalyst absorbs significantly more tar than dolomite. On the other hand, when 10% calcined limestone or dolomite was added, the gravimetric tar increased by 89.09% and 65.45%, respectively. The increase in BET surface area and pore volume for the calcined catalyst is responsible for the rise in tar production. However, it should be observed that the calcined dolomite has a greater BET surface area and pore volume than the calcined limestone, but the tar yield is much higher for the former. This implies that the presence of CaO and MgO on the calcined dolomite promoted tar cracking processes. Probably, tar produced during steam reforming is instantly absorbed by the catalyst matrix, but it is either not converted to permanent gases or the active CaO sites are rapidly deactivated, as previously documented by Florin and Harris (2008). Matsuoka *et al.* (2006) also reported a similar phenomenon while studying steam reforming of woody biomass using iron oxide impregnated porous alumina. Another postulate is that calcined limestone or dolomite enhanced the cracking of higher tars compounds to lighter tar compounds, as Boot-Handford *et al.* (2018) observed. The order of catalytic effect of dolomite and limestone on gravimetric tar cracking of SCW gasification of RH is as follows: non-catalytic ≈ uncalcined dolomite > calcined dolomite > uncalcined limestone > calcined limestone.

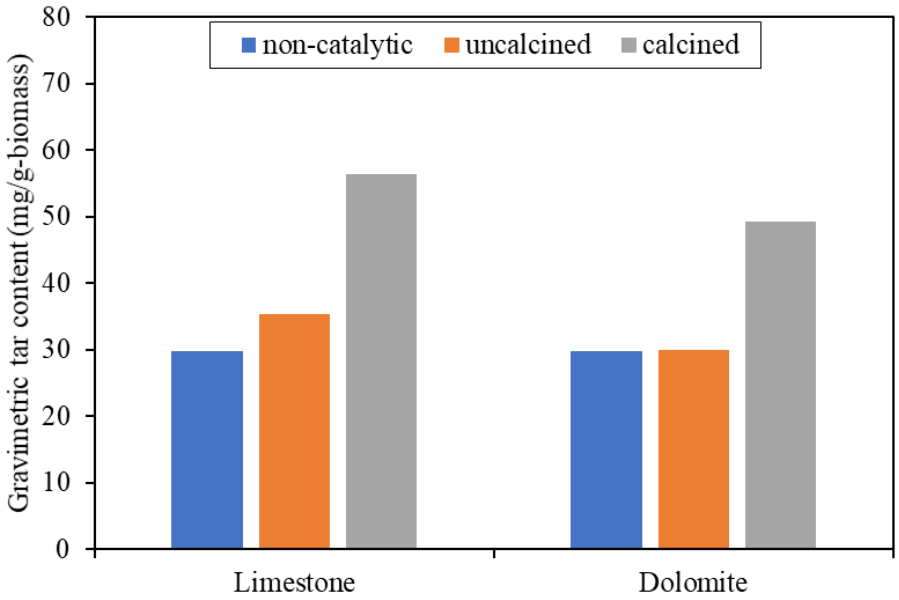


**Figure 75: Gravimetric tar content obtained from rice husk gasification with and without catalyst (catalyst loading 10 wt% and operating condition 492ºC, residence time 120 minutes and feed concentration 9.5 wt%)**

Figures 76 and 77 present the interaction between Fe-content and catalyst loading on gravimetric tar yield, respectively. The perturbation plots for gravimetric tar yield (Fig. 76) show a linear relationship for both Fe-content and catalyst loading. In comparison to Fe-content curves, the catalyst loading curve has steeper slopes. These findings suggest that gravimetric tar is more sensitive to the changes of catalyst loading than Fe-content. Figure 77(a-d) present the contour and 3D surface plot for the interaction of catalyst loading and Fe-content on gravimetric tar yield. The gravimetric tar yield rose from 29.8 mg/g biomass for non-catalytic SCW gasification to 50.2 mg/g-biomass and 48.6 mg/g-biomass in addition to 5% calcined limestone and dolomite, respectively. The gravimetric tar rises sharply to 63.3 mg/g-biomass (112.4%) and 61.7 mg/g-biomass (107.0%) after the adding 20% Fe/limestone and 20% Fe/dolomite, respectively. Interestingly, it can be observed that the tar yield decreases with increasing iron content and sharply increases with increasing catalyst loading. However, the pattern reversed above 10 wt% catalyst loading when the tar yield increases with increasing iron content and catalyst loading. This could be attributed to other factors such as the interaction of catalyst surface area, pore-volume, pore structure, active phases, and reaction mechanisms, which requires further investigation. Wang *et al.* (2021) reported a similar observation while researching SCW gasification of depolymerizing slag with various forms of catalysis. It was discovered that the organic liquid produced by catalytic gasification is greater than that produced by non-catalytic gasification at the same reaction time. Furthermore, phenols, furans, benzene series, organic acids, and ketones compounds were the most common components found in tar.

It can be explained that under the gasification conditions of 492°C, 120 minutes of residence time, and a feed concentration of 9.5 wt% with the addition of limestone- or dolomite-based catalysts can promote the degradation of RH biomass to produce more tar and gas.

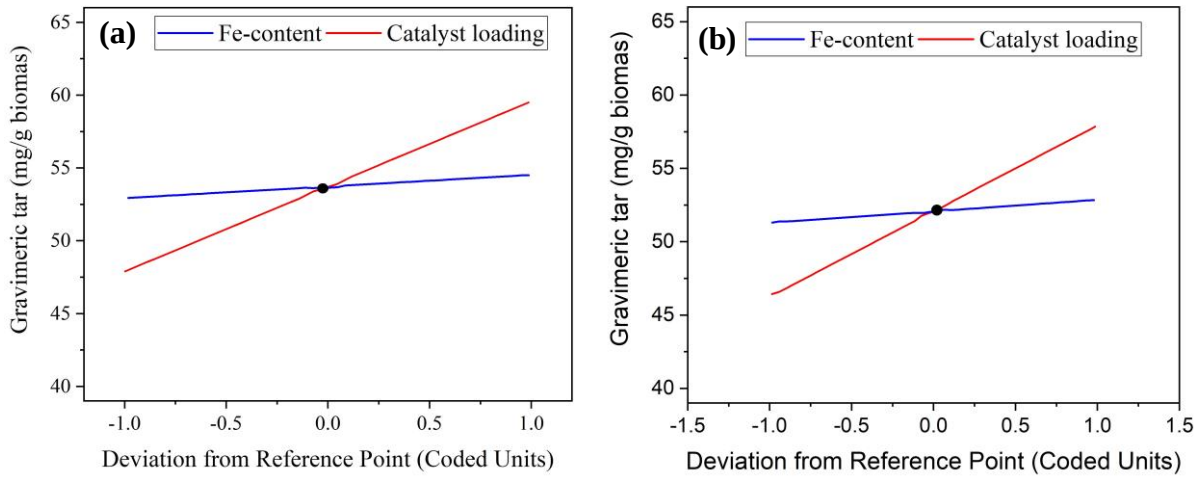


**Figure 76: Perturbation plot showing the effect of factors on gravimetric tar yield in catalytic SCW gasification of rice husk with; (a) limestone-based catalyst and (b) dolomite-based catalyst**

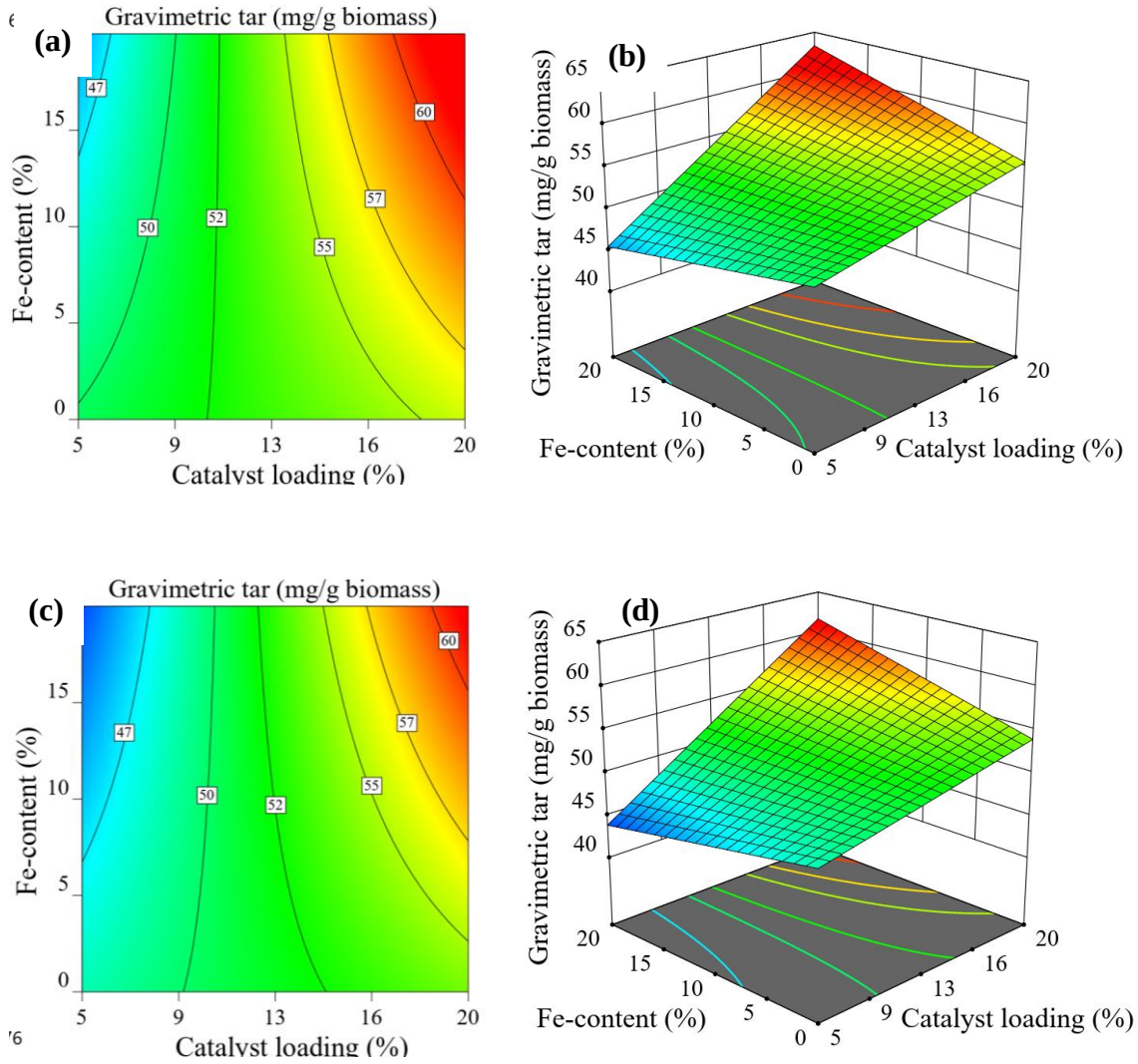


**Figure 77: Contour and 3D response surface plots representing different interactive effects of catalyst loading and Fe-content on gravimetric tar yield: limestone-based catalyst (a, b) and dolomite-based catalyst (c, d)**

Figure 78 presents FTIR spectra of tar obtained at optimal SCW gasification conditions and catalytic SCW gasification of RH biomass. It is evident that the two spectra have only slight differences, suggesting a strong resemblance in their organic structures. A strong absorption was observed at 3360 and 3318 $cm^{-1}$ which correspond to -OH stretching vibrations, 3047 $cm^{-1}$ (aromatic C-H stretching) which is observed only in catalytic tar product. The presence of alkanes is identified by C-H scissoring, and bending vibrations range between 1457–53 cm, confirming benzene derivatives in the tar product (Gaurh & Pramanik, 2018). The spectra bands 2922, 1451-1450 $cm^{-1}$ conforms to the asymmetric stretching vibration of aliphatic methylene group C-H structure, 2860, 2853 and 1370 $cm^{-1}$ confirm symmetric vibration of aliphatic methyl group C-H, while bands frequency 1600-1508 $cm^{-1}$ confirm aromatic C=C and aromatic ring stretch. The band frequency 1205-1206 $cm^{-1}$ refers to the vibration of the aromatic C-O band, and 1030-750 $cm^{-1}$ is the vibrations of aromatic rings. Therefore, it can be summarized that the

tar produced in both catalytic and noncatalytic SCW gasification consists of a complex mixture of aliphatic, aromatic, and heterocyclic organics, as well as aromatic-aliphatic hydrocarbons. A similar finding is reported elsewhere (Ariunaa *et al.*, 2018; Jin *et al.*, 2016; Wang *et al.*, 2013).

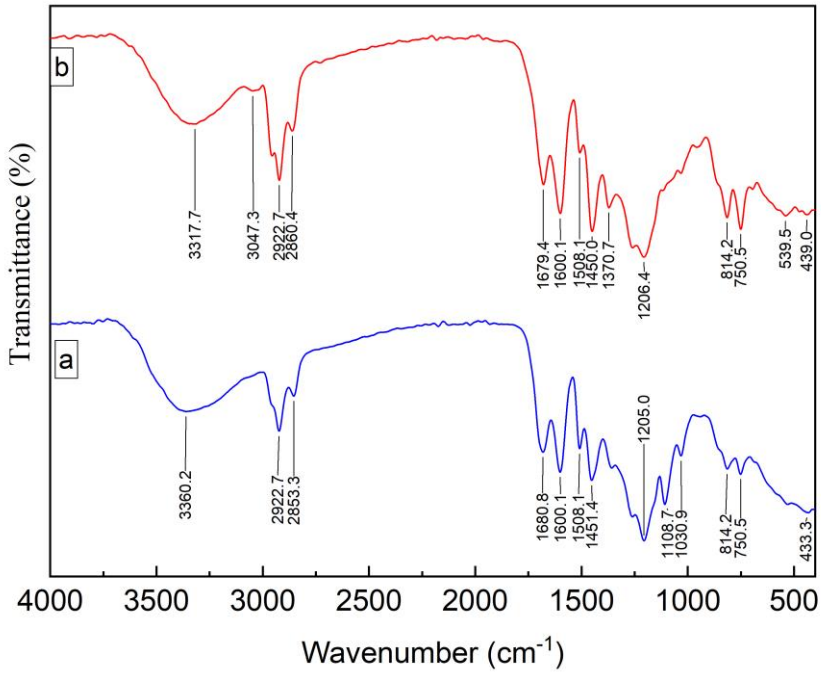


**Figure 78: Comparison of FT-IR spectrometry of tar obtained at; (a) optimized condition for non-catalytic SCW gasification (492ºC, 9.5 wt%, 120 minutes), (b) optimized condition for catalytic gasification (15% catalyst loading, 5%Fe/limestone)**

The properties of tar were compared to the data published in the literature for the properties of commercial unleaded gasoline (Uguru-Okorie *et al.*, 2018) and diesel (Coronado *et al.*, 2017). The spectrum comparison in Table 22 highlights and identifies the significant structural differences between produced gasification tar and commercial gasoline and diesel. It is evident that tar products and commercial gasoline and diesel exhibit identical behaviour, as seen by differing peak intensities. Compared to FT-IR peaks of gasification tar, the difference displayed includes: no peaks identified for gasoline and diesel between 3360-3317 cm-1 caused by the removal of -OH group via hydrodeoxygenation, the peak for alkanes at 2924 $cm^{-1}$ became stronger, while peaks at 731-722 are relatively minor for gasoline and diesel due to increased content of alkanes and low aromatic groups, no visible peaks at fingerprint region at 1600 $cm^{-1}$ suggesting an absence of C–O bonds. These results show good correlations between biomass tar and commercial biodiesel and gasoline, indicating that tars can be used directly as combustion fuels. However, its use in other applications could be limited due to its high viscosity and variability in other properties (Guo *et al.*, 2011). Therefore, tars need further

characterization and treatment to produce high-grade liquid fuel that can be used as an alternative to fossils fuel. Biomass tar has the advantage of being renewable, clean and pollution-free. It is reported that biomass-derived liquid fuel contains almost no metals and contains low levels of harmful elements such as sulfur and nitrogen (Wang *et al.*, 2021).

**Table 22: Comparisons of the function groups of gasification tar, commercial biodiesel, and gasoline**

| Tar product | | Commercial fuel (cm-1) | | Type of vibration |
|---|---|---|---|---|
| **Noncatalytic ($cm^{-1}$)** | **Catalytic ($cm^{-1}$)** | **Gasoline ($cm^{-1}$)** | **Diesel ($cm^{-1}$)** | |
| 3360 | 3317 | | - | -OH stretching vibration confirms the presence of hydroxyl compounds such as alcohol |
| - | 3047 | 3026 | - | aromatic C-H stretching |
| 2922 -2853 | 2922-2860 | 2957-2866 | 2954-2854 | C-H stretching vibration of $CH_3$, $CH_2$ and CH groups, confirming the presence of alkanes |
| 1680-1508 | 1670-1508 | - | - | C=C stretching vibration, presence of alkenes/fingerprint region. It confirms the presence of olefinic compounds such as vinyl and vinylidene |
| 1451 | 1450 | 1458 | 1457 | flexion or deformation experienced by the C–H, suggesting aromatic ring stretching |
| - | 1370 | 1375 | 1377 | flexion or deformation experienced by the C–H bond and the existence of C=C bonds |
| 1205 | 1206 | - | - | The vibration of the C-O band |
| 1030 | - | - | - | C-H bending vibration, presence of alkenes |
| 814 | 814 | 881 | 805 | Certification of the presence of vinylidene function group |
| 750 | 750 | 731 | 722 | C-H bending vibration, presence of phenyl ring substitutional band, confirming mono or ortho substitutional of the benzene ring |

### (iv) Influence of Catalyst Parameters on Char Yield

A preliminary evaluation of the activity of calcined and uncalcined dolomite and limestone was conducted to investigate the effect of the catalyst on char yield. The experiment was carried out by incorporating 10% calcined or uncalcined dolomite and limestone, as shown in Fig. 79. When 10% uncalcined limestone or dolomite is added, char yield declines by 23.04 % and 22.39 %, respectively, compared to non-catalytic. The addition of 10% calcined limestone or dolomite reduces char yield by 29.0 % and 22.0 %, respectively, compared to non-catalytic. Interestingly, calcined dolomite produced a somewhat larger char yield than uncalcined dolomite, showing that the latter is more resistant to coke deposits. The activity order for char yield of SCW gasification of RH with 10% uncalcined and calcined catalyst is as follows: calcined limestone > calcined dolomite ≈ uncalcined (limestone ≈ dolomite) > non-catalytic.

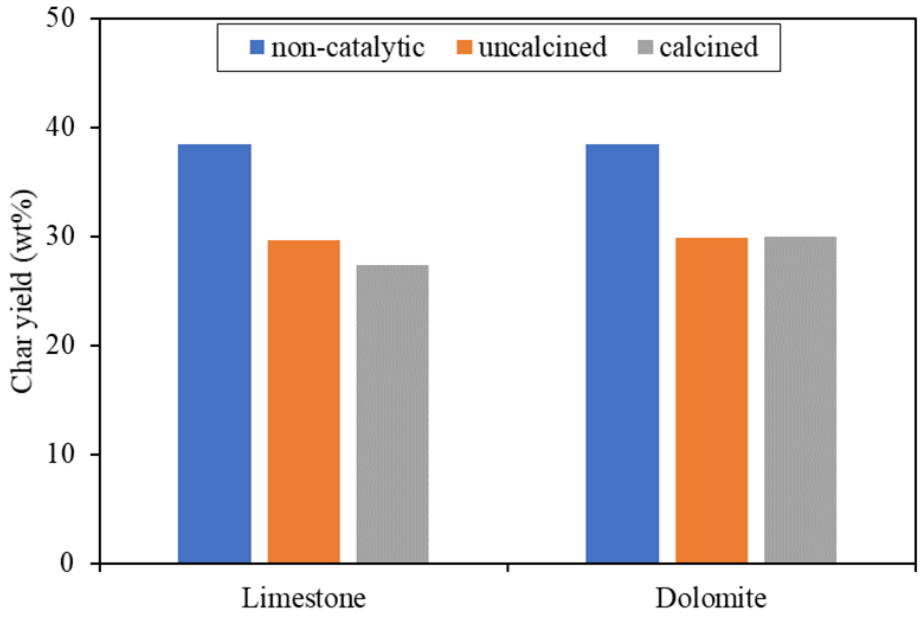


**Figure 79: Char yield obtained from rice husk gasification with and without catalyst (catalyst loading 10 wt% and operating condition 492°C, residence time 120 minutes and feed concentration 9.5 wt%)**

The interaction between Fe-content and catalyst loading on char yield is shown in Fig. 80 and 81. The perturbation plots for char yield (Fig. 80) exhibit a curvature shape for both Fe-content and catalyst loading changes. Compared to catalyst loading curves, the Fe-content curve has steeper slopes, suggesting that char yield is more sensitive to Fe content changes than catalyst loading. The char yield decreases rapidly as the catalyst loading is increased, whereas when the Fe-content is increased, the char yield decreases to a certain point before sharply rising.

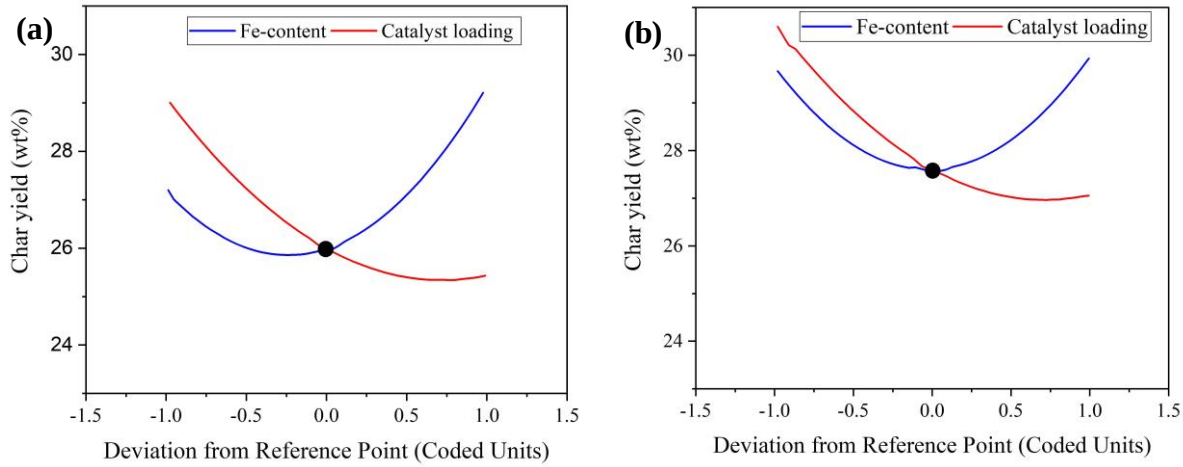


**Figure 80: Perturbation plot showing the effect of factors on char yield in catalytic SCW gasification of rice husk with; (a) limestone-based catalyst and (b) dolomite-based catalyst**

The contour and 3D surface plots for the interaction of catalyst loading and Fe-content on char yield are shown in Fig. 81(a-d). With the addition of 5% calcined limestone or dolomite, the char yield drops from 38.62 wt% for non-catalytic gasification to 30.2 wt% and 32.8 wt%, respectively. On the other hand, the addition of 18% of 7.3%Fe/limestone or 9.7%Fe/dolomite catalyst yields 25 wt% and 26.9 wt% of char, respectively. More catalyst loading resulted in a negligible decrease in char yield, whereas more Fe-content led to a significant increase in the char product. The results show that when biomass is gasified in the presence of CaO and MgO (calcined samples), the char yield significantly decreases compared to the process without catalyst. Moreover, the active sites generated by the addition of iron slightly promoted char gasification, demonstrating that $Ca_2Fe_2O_5$ and $Fe_2O_3$ sites also improve biomass gasification by producing more condensable tars and less char residue. Char yield increases when more iron is added, notably when 20% iron is added, indicating that $Ca_2Fe_2O_5$ is less active in char gasification under the conditions examined and a synergistic effect between Fe and CaO/MgO in the catalyst exists and needs to be optimised to improve gasification.

Furthermore, char gasification is slightly higher for the limestone-based catalyst than the dolomite-based catalyst due to the formation of free iron oxides on the surface of the iron-doped limestone catalyst, as confirmed by XRD. In fact presence of iron oxide has been reported to improve the catalytic activity of calcined limestone and dolomite in SCW gasification. Furthermore, the reduction in char caused by the addition of catalysts suggests that the catalysts are resistant to carbon deposition during gasification. It was found that catalysts containing a smaller amount of iron (< 10%) are more catalytic active for char gasification than the amount

>10%. According to Di Felice *et al.* (2011), lower metal content causes lower kinetic limitations and $CO_2$ sorption capacity decay than higher metal content. This suggests that a lower amount of iron content favours forward Boudouard reaction while a higher content favour backwards Boudouard reaction (Equation 50) due to equilibrium shift as ascribed in Le Chatelier's principle. It can also be concluded that kinetic limitations are less significant in Fe/limestone interactions than in Fe/dolomite interactions, as evidenced by the char yield, with the latter having a higher char content. This conclusion is in line with previous research (Di Felice *et al.*, 2011).

$$CO_2 + C \longleftrightarrow 2CO \tag{50}$$

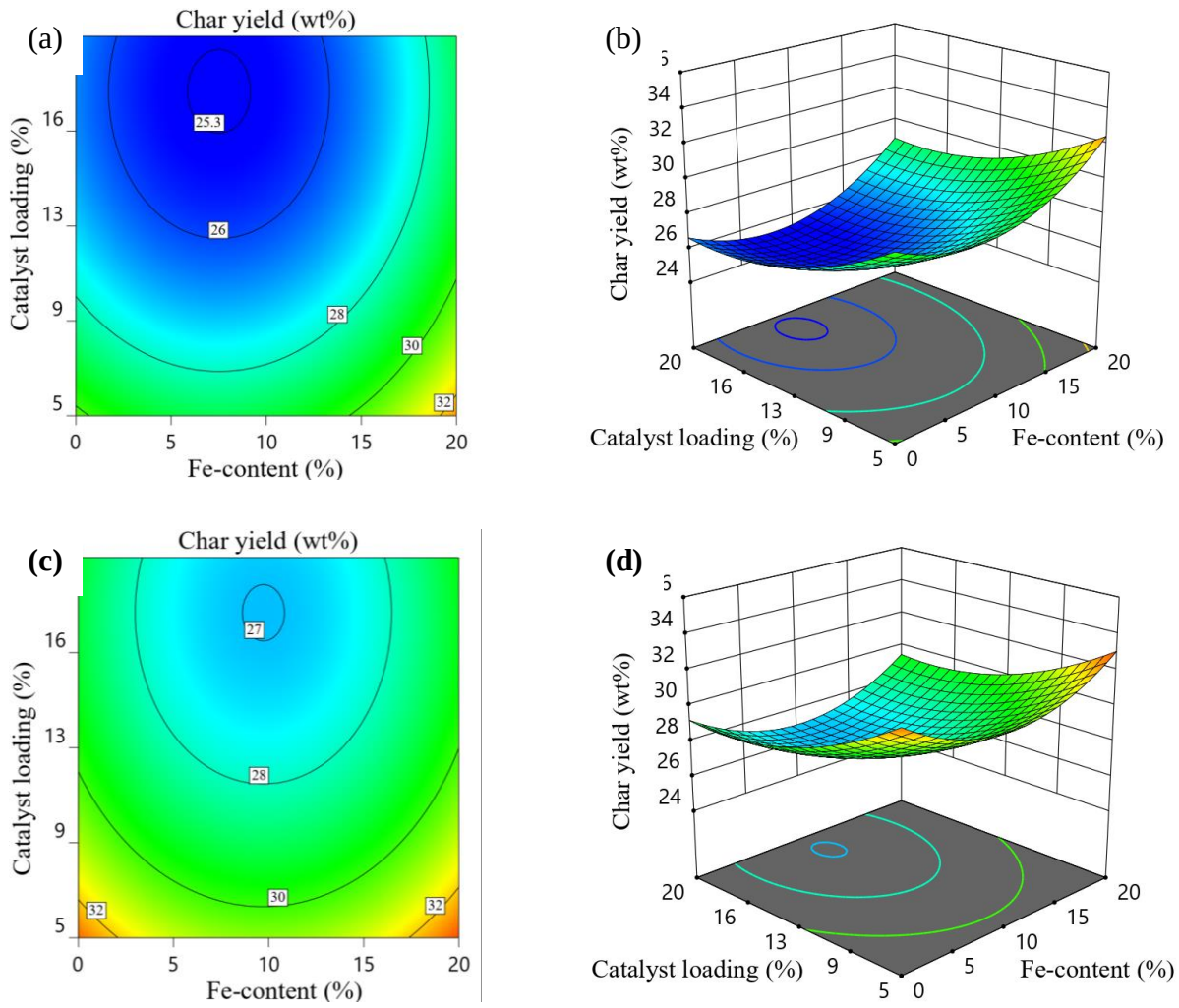


**Figure 81: Contour and 3D response surface plots representing different interactive effects of catalyst loading and Fe-content on char yield: Limestone-based catalyst (a, b) and dolomite-based catalyst (c, d)**

### 4.5.2 Optimization of the Responses and Validation of the Model

Gasification outputs including GE, gas volume, gravimetric tar yield and char yield were considered independent responses during optimisation of catalytic SCW gasification of RH biomass. Figure 82 shows the optimum conditions for each independent variable in terms of meeting the output goals. The optimum GE of 69.5%, equivalent to a 17.7% rise over the non-catalytic condition, is obtained for the catalyst loading of 15% using 5%Fe/limestone catalysts. These findings corroborate Di Felice *et al.* (2011)'s results from studying the catalytic activity of iron-doped alkaline earth metal for model biomass gasification. The reactivity order 5%Fe > 1%Fe > 10% Fe ≈20%Fe has been reported. The gasification condition using 5% catalyst loading and 10.6%Fe/limestone catalyst results in a 60.0% increase in gravimetric tar yield from 29.8 mg/g for non-catalytic compared to 47.7 mg/g of catalytic. On the other hand, 20% catalyst loading, and 20%Fe/limestone catalyst resulted in the highest gas volume of 442 mL/g-biomass (56.1% increase) compared to the non-catalytic condition. Both responses have a desirability value near one, indicating that the constraints well fulfil the optimisation requirements.

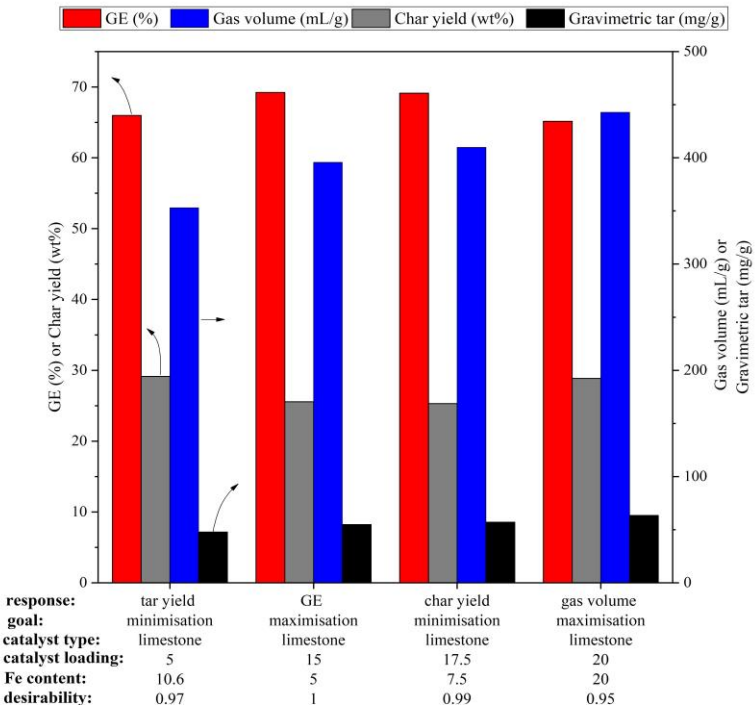


**Figure 82: Predicted responses values for catalytic SCW gasification at different optimisation goals (operating conditions: temperature 492°C, residence time 120 minutes and feed concentration 9.5 wt%)**

The optimisation of catalytic SCW gasification in this study is aimed to realize the optimum condition for high GE. With multiple dependency factors, the optimal condition for maximising GE, where all factors meet the desired conditions simultaneously, could be visualized

graphically by superimposing the response contours in an overlay plot (Fig. 83). Table 23 shows the two-sided prediction intervals used to build the overlay plot. The acceptable factor settings that meet optimisation requirements are defined by the yellow shaded region, while the grey shaded region shows the unacceptable operating conditions.

**Table 23: The criteria for constructing overlay plots**

| Response | 95% PI low | Predicted value | 95% PI high |
|---|---|---|---|
| GE (%) | 67.98 | 69.24 | 70.51 |
| Char yield (wt%) | 24.24 | 25.56 | 26.88 |
| Gravimetric tar (mg/g) biomass | 51.44 | 57.50 | 57.94 |
| Gas volume (mL/g biomass) | 383.64 | 395.88 | 408.0 |

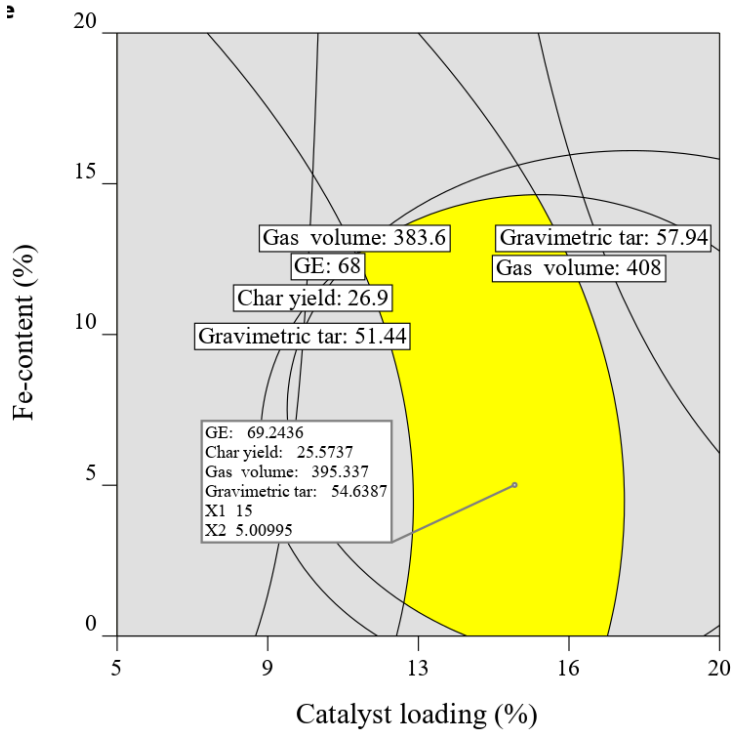


**Figure 83: Overlay plot showing the best compromise region for optimal GE as a function of catalyst loading and Fe-content**

Three replicates of confirmation experiments at the optimum operating conditions for GE maximisation were used to test the validity of the projected models. Furthermore, multiple confirmation runs were carried out under a variety of conditions that were chosen at random. Tables 24 and 25 show Residual Standard Error (RSE) results obtained using Equation 41 for GE maximisation proposed by the Design-Expert software and randomly selected conditions. The RSE value of less than 6.8% indicates excellent agreement between experimental and model-predicted results (Gratuito *et al.*, 2008).

**Table 24: Predicted and experimental values at optimum conditions for the catalytic optimisation of GE (15% catalyst loading and 5%Fe/limestone catalyst)**

| Responses | Predicted value | Experimental value* | RSE (%) |
|---|---|---|---|
| GE (%) | 69.25 | 69.57 ± 0.6 | 0.4 |
| Char yield (wt%) | 25.56 | 24.68± 0.6 | 3.4 |
| Gravimetric tar (mg/g biomass) | 54.70 | 57.50± 1.8 | 5.1 |
| Gas volume (mL/g) | 395.81 | 402.8 ± 6.6 | 1.7 |

**Table 25: Model confirmation at randomly selected catalyst condition**

| Responses | Catalyst loading (%) | Catalyst type | Pred. value | Exp. value* | RSE (%) |
|---|---|---|---|---|---|
| GE (%) | 10 | 0%Fe/dolomite | 64.83 | 65.05 | 0.3 |
| | 5 | 5%Fe/limestone | 66.27 | 67.16 | 1.34 |
| | 10 | 20%Fe/dolomite | 64.87 | 66.03 | 1.8 |
| Char yield (wt%) | 10 | 0%Fe/dolomite | 30.49 | 30.01 | 1.5 |
| | 5 | 5%Fe/limestone | 29.08 | 27.74 | 4.6 |
| | 10 | 20%Fe/dolomite | 30.14 | 29.17 | 3.2 |
| Gravimetric tar (mg/g-biomass) | 10 | 0%Fe/dolomite | 50.38 | 49.34 | 1.9 |
| | 5 | 5%Fe/limestone | 49.01 | 50.90 | 3.8 |
| | 10 | 20%Fe/dolomite | 51.4 | 47.90 | 6.8 |
| Gas volume (mL/g- biomass) | 10 | 0%Fe/dolomite | 386.18 | 399.72 | 3.5 |
| | 5 | 5%Fe/limestone | 349.36 | 358.26 | 2.5 |
| | 10 | 20%Fe/dolomite | 396.4 | 400.1 | 0.9 |

### (i) Effect of Catalyst Under Different SCW Gasification Optimization Goals

Catalytic SCW gasification using optimized catalyst conditions (catalyst loadings of 15% and 5%Fe/limestone catalyst, Section 4.5.2) was carried out to tests the activity of the catalyst under various SCW gasification optimization conditions (Fig. 45). The effect of the catalyst on product yield is highly dependent on the operating conditions, as shown in Fig. 84. When compared to other conditions, catalytic gasification using the conditions for GE maximisation resulted in the lowest gas volume increase (27.7%), a moderate increase in GE (28.37%), and the highest char conversion (65.87%). Catalytic SCW gasification under gas volume maximisation conditions resulted in mild char conversion (53.87%) and gas volume increase (32.15%), and the highest GE increase (33.83%). Surprisingly, the conditions for tar yield minimisation resulted in a two-

fold increase in tar yield (92.99%), whereas the conditions for gas volume maximisation resulted in a substantial decrease in tar yield (22.07%). Nonetheless, the condition of tar yield minimization contributed to a significant increase in gas volume. It is worth noting that the maximum gas volume (560.05 mL/g) is observed for the condition of gas volume maximisation, which also recorded the highest increases in GE (33.83%) (Fig. 85). The decrease in tars and substantial rise in gas volume can be explained by the fact that iron oxide effectively targets tar cracking and water-gas shifting reactions (Uddin *et al.*, 2008). Under all conditions tested, the manufactured catalyst is exceptionally active in char gasification, and the condensable tars are probably absorbed in the catalyst matrix before being broken down to generate permanent gas. Furthermore, it is discovered that tar reactions are strongly favoured at higher temperatures. Based on these findings, it is evident that the 5% Fe/limestone catalyst is active for tar conversion at higher temperatures, longer residence times, and lower feed concentrations.

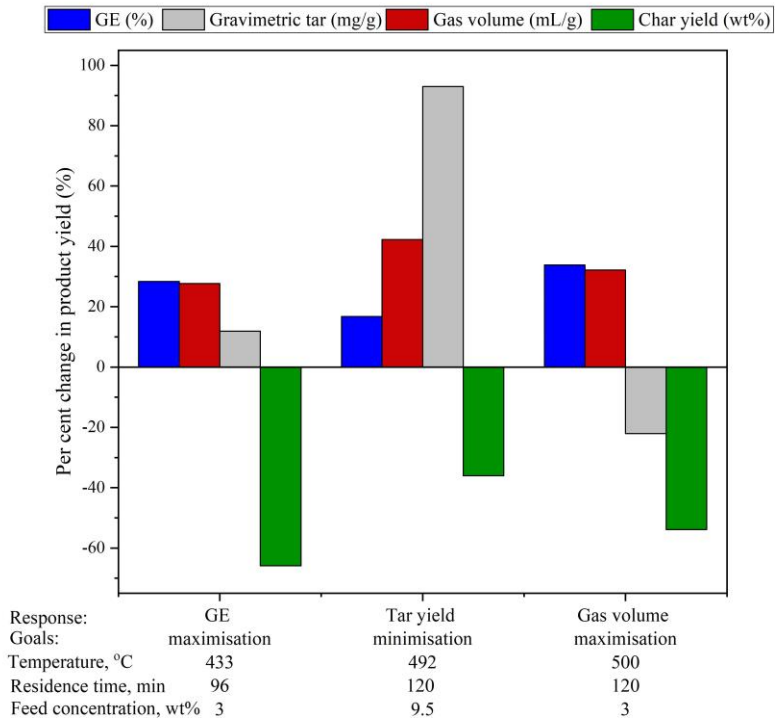


**Figure 84: Effect of addition of catalyst on per cent change in product yield under various SCW gasification optimisation goals**

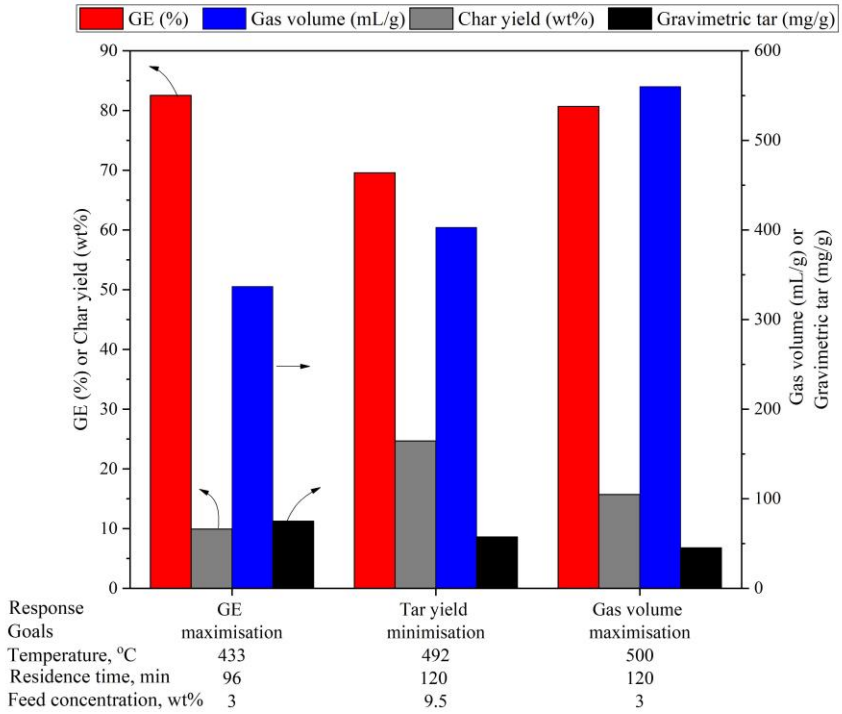


**Figure 85: Effect of addition of catalyst on different SCW gasification optimisation conditions (catalyst used; 15% catalyst loading, 5%Fe-limestone)**

### (ii) Catalytic SCW Gasification of a Variety of Rice Husks

Table 26 compares non-catalytic and catalytic gasification results, whereas Fig. 86 represents the variation in product output for various rice husk varieties.

**Table 26: Comparisons between catalytic and non-catalytic SCW gasification of varieties of rice**

| RH | GE (%) | | Char yield (wt%) | | Gravimetric tar (mg/g biomass) | | Gas volume (mL/g) | |
|---|---|---|---|---|---|---|---|---|
| | Non. | Cat. | Non. | Cat. | Non. | Cat. | Non. | Cat. |
| Iringa | 59.34 | 69.32 | 37.50 | 24.85 | 31.6 | 58.3 | 278.5 | 401.8 |
| Morogoro | 60.78 | 71.39 | 36.52 | 22.45 | 27.0 | 61.6 | 291.8 | 411.5 |
| Shinyanga | 62.71 | 73.78 | 34.60 | 20.41 | 26.9 | 58.1 | 301.0 | 427.3 |
| Arusha | 62.74 | 73.58 | 34.82 | 20.14 | 24.3 | 62.8 | 305.2 | 426.0 |
| Dodoma | 59.59 | 69.57 | 38.60 | 24.68 | 29.8 | 57.5 | 286.1 | 402.8 |

Where: *Non.* means noncatalytic and *Cat.* means catalytic gasification

Figure 86 shows that the increase in GE in SCW gasification of RH varieties with the addition of 15 wt% of 5%Fe/limestone catalyst ranged slightly from 16.7% to 17.7%, with the Dodoma sample having the lowest increase and the Shinyanga sample having the highest. There is a substantial difference in char conversion between the Iringa and Arusha samples, with the Iringa

sample having the slightest change (33.7%) and the Arusha sample having the highest variation (42.1%). On the other hand, the Arusha sample had the most significant increase in tar output (158.4%), nearly double that of the Iringa sample (84.5%). Except for the Iringa sample, which indicated nearly 3.4% greater than the average of the others, there is no notable variance in gas volume change for all samples. As described in section (ii), the existence of diverse inorganic element compositions could account for the variance in gasification yield for different varieties of rice husks. Furthermore, the interaction of the inorganic elements with the fabricated catalyst may result in either synergetic or unsynergetic gasification reactions. It should be noted that the interaction of the elements with the added catalyst necessitates further investigation.

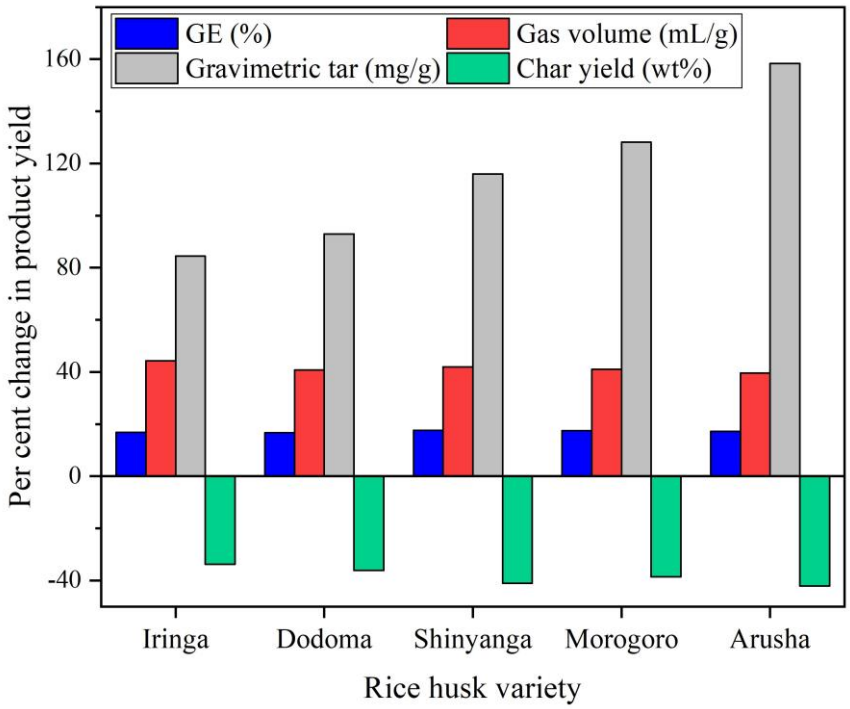


**Figure 86: Variations of product yields between catalytic and non-catalytic SCW gasification of variety of rice husks (operating conditions: temperature 492ºC, residence time 120 minutes, feed concentration 9.5 wt%, catalyst loading 15 wt%, and catalyst type 5%Fe/limestone)**

# CHAPTER FIVE

# CONCLUSION AND RECOMMENDATIONS

## 5.1 Conclusion

In this work, RH biomass has been characterised and utilized as a feedstock for hydrothermal (subcritical and SCW) gasification to produce gas and liquid fuel, a green fuel that can be used as an alternative to detrimental fossil fuels. The effects of the operating parameters, namely reaction temperature (350 to 500°C), residence time (30 to 120 minutes), and feed concentration (3 to 10 wt%) on subcritical and SCW gasification of RH, were experimentally studied using response surface methodology. The gasification yields were enhanced by using a locally available and simple prepared catalyst using an alkaline earth catalyst promoted using iron. The Fe/alkaline-earth catalysts were fabricated via facile impregnation of iron oxide on calcined dolomite and limestone. The interaction between iron content (0-20%Fe content) and catalyst loading (5-20%) and the inter-relationship between catalyst properties on gasification yields was investigated and reported. The changes in gasification yields, including GE, gas volume, gravimetric tar yield, and char yield, were optimised using Design-Expert software. Based on the findings, the following conclusions were reached:

(i) The moisture content of both rice husk varieties varied slightly between 6.3 and 6.9 %, which can be related to changes in postharvest activities such as drying and storage. The low moisture level of both samples suggests that they are suitable for thermochemical conversion without incurring the cost of drying.

(ii) Rice husk has a high volatile fraction (56.85 – 62.8 % db), a high heating value (12.66 – 13.36 MJ/kg), and a low nitrogen and sulphur content (1.12 – 1.77 % db) (below detection limit). Due to its high volatile matter and heating value, rice husk may be processed to high energy fuel using less heat via thermochemical reaction, while its low nitrogen and sulphur content adds an advantage to its use due to the minimal risk of pollutant gas generation, such as NOx.

(iii) Response surface methodology involving the I-optimality design for was used for optimisation of SCW gasification operating conditions. Quadratic models were proposed for both responses, and the predicted values by the models were in excellent agreement with the experimental values. The reaction temperature is the most influential factor affecting SCW gasification, followed by feed concentration and residence time.

(iv) The GE increased with the rise of temperature and residence time at a constant feed concentration to a “certain time”, and after that, it started to decrease. The highest GE of 64.2% could be archived under 433°C, residence time 96 minutes and a feed concentration 3 wt%, while the minimum tar yield of 29.8 wt% is obtained for the condition of 492°C, residence time 120 minutes and a feed concentration of 9.5 wt%.

(v) Char yield increased with the rise of reaction temperature and feed concentration, being caused by unwanted char/coke formation as a competing reaction to the main SCW gasification reactions. Therefore, the utilisation of in-situ solid catalyst to enhance char gasification and accelerate the gasification reactions in general by suppressing the unwanted reaction pathways leading to char formation is desirable.

(vi) The rice husk sample from Arusha yielded a high GE (62.74%), a high gas volume (305.3 mL/g), and a lower gravimetric tar (24.3 mg/g) compared to other varieties due to higher volatile matter, hemicellulose, lignin, and low cellulose content. Char gasification was much lower for the Dodoma sample due to high cellulose, fixed carbon, potassium, and chlorine which favour char formation reactions.

(vii) A fresh and calcined limestone and dolomite were primarily used as catalysts to improve gasification yields. A phase characterisation reveals that the reactive site of the fresh dolomite is predominantly $CaMg(CO_3)_2$, that of natural limestone is calcite ($CaCO_3$), while for the calcined limestone and dolomite is CaO and (CaMg)O, respectively. These reactive sites are responsible for the breakage of C-C and C-H bonds of large hydrocarbon molecules to produce gas and liquid products in small molecule sizes.

(viii) Calcined dolomite and limestone were impregnated with Fe, and a new reactive site, calcium ferrite ($Ca_2Fe_2O_5$), was formed on the catalyst's surface. When the Fe content was increased from 5% to 20%, calcium ferrite replaced the CaO phases and dominated almost the entire surface of the catalyst. Calcium ferrite and CaO are active sites promoting char gasification and tar compounds cleavage to produce more gas under optimization conditions.

(ix) A weak phase of $MgFe_2O_4$ is formed for the 10% Fe/dolomite, whereas for 20% Fe/dolomite, only $Mg(OH)_2$ peaks are observed, showing a weak interaction between iron-magnesium oxide and a strong interaction between iron-calcium oxide.

(x) Free iron oxides peaks were not formed in either case of dolomite impregnated catalyst, while such peaks were observed on the surface of Fe/limestone catalyst suggesting good catalytic properties for water-gas shift reaction.

(xi) Response surface methodology was used to optimise catalytic SCW gasification of rice husk and a quadratic model for GE, char yield, and gas yield and a two-factor interaction model for gravimetric tar yield were proposed. The predicted values by models were very close to the experimental data, with a residual standard error of less than 6.8%. The catalyst loading was the most crucial factor affecting gasification yield followed by Fe content.

(xii) The fabricated catalyst promoted char gasification and tar formation under the tar yield minimisation conditions (492$^{o}$C, 120 minutes, and 9.5 wt% feed concentration). The condition for 15% catalyst loading and 5%Fe/limestone catalyst increased GE by 16%, gas volume by 42.2%, and tar yield by 93%, but char yield reduced by 36.1%. As gas volume was maximised (500$^{o}$C, 120 minutes, and 3 wt% feed concentration), GE increased by 33.8% and gas volume by 32.1%, while gravimetric tar and char production reduced by 22% and 54%, respectively, when compared to non-catalytic gasification.

(xiii) The fabricated 5%Fe/limestone catalyst is highly active on char gasification under all conditions examined, while it is only active on tar cracking at higher temperatures, longer residence times, and lower feed concentrations.

A promising strategy for enhancing SCW gasification was demonstrated in the current study using Fe impregnated alkaline-earth catalyst. The manufactured catalyst showed great potential for the combined production of liquid and gaseous fuels. The results revealed that the SCW gasification could provide an effective mechanism for transforming the energy content of RH into a substantial fuel product.

## 5.2 Recommendations

This study optimized the sub and SCW gasification of varieties of RH enhanced with Fe doped alkaline earth catalyst as the potential waste-to-energy recovery method. Based on the findings of this study, the following recommendations are made:

(i) Because of the limitations of the online syngas analyser, gas characterisation was not performed; consequently, future research should analyse the effect of operating conditions and the addition of catalysts on the change of syngas compositions.

(ii) The findings of this study show that a 5%Fe/limestone catalyst is more effective in char gasification and tar cracking at higher temperatures and lower feed concentrations; therefore, future work should focus on optimising this catalyst at higher temperatures, particularly >500$^{o}$C, 3 wt% feed concentration, and 120 minutes residence time.

(iii) The SCW gasification of rice husks has shown potential for concurrent production of liquid, gas, and solid fuels. Therefore, future work should consider optimising the tar and char product as the fuel potential by-product.

(iv) In this study techno economic analysis was not done to realise feasibility of the technology for electricity generation, therefore future work should consider energetic, energetic, and economic analysis of the process.

(v) Even though the solid residual (biochar) was only evaluated gravimetrically by ultimate and XRD analyses, the results show that RHC, after gasification, contains useful secondary products such as amorphous silica and minerals. Future research is recommended to investigate the use of RHC residual as a building material, fertiliser, and other industrial applications.

(vi) In this study, characterisation of the liquid effluent was not carried out to guarantee that it meets disposal standards; therefore, future works should address liquid effluent characterisation.

## REFERENCES


Abu-Bakar, M. S., & Titiloye, J. O. (2013). Catalytic pyrolysis of rice husk for bio-oil production. *Journal of Analytical and Applied Pyrolysis, 103,* 362-368. https://doi.org/10.1016/j.jaap.2012.09.005

Abu-El-Rub, Z., Bramer, E. A., & Brem, G. (2004). Review of catalysts for tar elimination in biomass gasification processes. *Industrial & Engineering Chemistry Research, 43*(22), 6911-6919. https://doi.org/10.1021/ie0498403

Adam, F., Appaturi, J. N., & Iqbal, A. (2012). The utilization of rice husk silica as a catalyst: Review and recent progress. *Catalysis Today, 190*(1), 2-14. https:// doi. org/ 10. 1016/ j. cattod.2012.04.056

Adar, E., Ince, M., & Bilgili, M. S. (2020). Supercritical water gasification of sewage sludge by continuous flow tubular reactor: A pilot scale study. *Chemical Engineering Journal, 391*, 123499. https://doi.org/10.1016/j.cej.2019.123499

Ahmed, A. E., & Adam, F. (2009). The benzylation of benzene using aluminium, gallium and iron incorporated silica from rice husk ash. *Microporous and Mesoporous Materials, 118*(1), 35-43. https://doi.org/10.1016/j.micromeso.2008.08.024

Ahmed, T., Xiu, S., Wang, L., & Shahbazi, A. (2018). Investigation of Ni/Fe/Mg zeolite-supported catalysts in steam reforming of tar using simulated-toluene as model compound. *Fuel, 211*, 566-571. https://doi.org/10.1016/j.fuel.2017.09.051

Al-Rahbi, A. S., & Williams, P. T. (2017). Hydrogen-rich syngas production and tar removal from biomass gasification using sacrificial tyre pyrolysis char. *Applied Energy, 190*, 501-509. https://doi.org/10.1016/j.apenergy.2016.12.099

Ali, A., Hira Z. M. Z., Haq, I., Phull, A. R., Ali, J. S., & Hussain, A. (2016). Synthesis, characterization, applications, and challenges of iron oxide nanoparticles. *Nanotechnology, Science and Applications, 9*, 49—67. https:// doi. org/ 10. 2147/ NSA. S99986

Al-Othman, Z. A. (2012). A Review: Fundamental Aspects of Silicate Mesoporous Materials. *Materials, 5*(12), 2874-2902. https://doi.org/10.3390/ma5122874

Alvarez, J., Lopez, G., Amutio, M., Bilbao, J., & Olazar, M. (2014). Upgrading the rice husk char obtained by flash pyrolysis for the production of amorphous silica and high quality activated carbon. *Bioresource Technology, 170*, 132-137. https:// doi. org/ 10. 1016/ j. biortech. 2014.07.073

Anikeev, V., & Fan, M. (2014). *Supercritical fluid technology for energy and environmental applications*. Elsevier, Amsterdam, the Netherlands. https://www.google.com

Antonkiewicz, J. (2009). Use incineration ash for binding heavy metals in soils. *Environmental Protection and Natural Resources, 41*, 398-405.

Aqliliriana, C., Ernee, N., & Irmawati, R. (2015). Preparation and characterization of modified calcium oxide from natural sources and their application in the transesterification of palm oil. *International Journal of Scientific and Technology Research, 4*(11), 168-175.

Arafat, H. M., Ganesan, P., Jewaratnam, J., & Chinna, K. (2017). Optimization of process parameters for microwave pyrolysis of oil palm fiber (OPF) for hydrogen and biochar production. *Energy Conversion and Management, 133*, 349-362. https:// doi. org/ 10. 1016/j. enconman.2016.10.046

Ariunaa, A., Otgonchuluun, D., Purevsuren, B., & Ya, D. (2018). *Property of upgraded solid and liquid products from Baganuur lignite by thermal reaction with solvent. Proceedings of the Mongolian Academy of Sciences*. https:// doi. org/ 10. 5564/ pmas. v58i4. 1048

Asadullah, M. (2014). Biomass gasification gas cleaning for downstream applications: A comparative critical review. *Renewable and Sustainable Energy Reviews, 40*, 118-132. https://doi.org/10.1016/j.rser.2014.07.132

Asami, K., & Ohtsuka, Y. (1993). Highly active iron catalysts from ferric chloride for the steam gasification of brown coal. *Industrial & Engineering Chemistry Research, 32*(8), 1631-1636. https://doi.org/10.1021/ie00020a014

ASTM. (2013). *Annual book of ASTM standard, American Society for Testing and Materials*. Philadelphia. https://www.google.com

ASTM. (2016). *Annual book of ASTM standard, American Society for Testing and Materials*. Philadelphia. https://www.google.com

Ávila, I., Crnkovic, P. M., Milioli, F. E., & Luo, K. H. (2012). Investigation of the pore blockage of a Brazilian dolomite during the sulfation reaction. *Applied Surface Science, 258*(8), 3532-3539. https://doi.org/10.1016/j.apsusc.2011.11.108

Azadi, P., Afif, E., Foroughi, H., Dai, T., Azadi, F., & Farnood, R. (2013). Catalytic reforming of activated sludge model compounds in supercritical water using nickel and ruthenium catalysts. *Applied Catalysis B: Environmental, 134-135*, 265-273. https:// doi. org/ 10. 1016/ j. apcatb.2013.01.022

Aznar, M. P., Caballero, M. A., Gil, J., Martín, J. A., & Corella, J. (1998). Commercial Steam Reforming Catalysts to Improve Biomass Gasification with Steam−Oxygen Mixtures: Catalytic Tar Removal. *Industrial & Engineering Chemistry Research, 37*(7), 2668-2680. https://doi.org/10.1021/ie9706727

Baerns, M. (2013). *Basic principles in applied catalysis*. Springer Science & Business Media, Berlin. https://www.google.com

Bai, B., Wang, W., & Jin, H. (2020). Experimental study on gasification performance of polypropylene (PP) plastics in supercritical water. *Energy, 191*, 116527. https:// doi. org/ 10. 1016/ j. energy.2019.116527

Bakari, R., Kivevele, T., Huang, X., & Jande, Y. A. C. (2020). Simulation and optimisation of the pyrolysis of rice husk: Preliminary assessment for gasification applications. *Journal of Analytical and Applied Pyrolysis*, 104891. https:// doi. org/ 10. 1016/ j. jaap. 2020. 104891

Baker, E., Brown, M., Elliott, D. C., & Mudge, L. (1988). Characterization and treatment of tars from biomass gasifiers. *AIChE 1988 Summer National Meeting*, 11-11. http:// www. osti. gov/energycitations/product.biblio.jsp?osti_id=5132941

Banerjee, R. (2006). Comparison of options for distributed generation in India. *Energy Policy, 34*(1), 101-111. https://doi.org/10.1016/j.enpol.2004.06.006

Barot, B. S., Parejiya, P. B., Patel, H. K., Gohel, M. C., & Shelat, P. K. (2012). Microemulsion-Based Gel of Terbinafine for the Treatment of Onychomycosis: Optimization of Formulation Using D-Optimal Design. *AAPS PharmSciTech, 13*(1), 184-192. https://doi.org/10.1208/s12249-011-9742-7

Baş, D., & Boyacı, İ. H. (2007). Modeling and optimization I: Usability of response surface methodology. *Journal of Food Engineering, 78*(3), 836-845. https:// doi. org/ 10. 1016/ j. jfoodeng. 2005.11.024

Basu, P., & Mettanant, V. (2009). Biomass Gasification in Supercritical Water: A Review. *International Journal of Chemical Reactor Engineering, 7*(1), 1542-6580. https:// doi. org/ 10. 2202/ 1542-6580.1919

Basu, P., Mettanant, V., & Leon, A. (2009). *Gasification of rice husk in supercritical water. In Proceedings of the 8th World Conference on Chemical Engineering*. Montreal, Canada. https://www.google.com

Baxter, L. L., Miles, T. R., Miles, T. R., Jenkins, B. M., Milne, T., Dayton, D., Bryers, R. W., & Oden, L. L. (1998). The behavior of inorganic material in biomass-fired power boilers: Field and laboratory experiences. *Fuel Processing Technology, 54*(1), 47-78. https:// doi. org/ 10.1016/S0378-3820(97)00060-X

Behera, S. K., Meena, H., Chakraborty, S., & Meikap, B. C. (2018). Application of response surface methodology (RSM) for optimization of leaching parameters for ash reduction from low-grade coal. *International Journal of Mining Science and Technology, 28*(4), 621-629. https://doi.org/10.1016/j.ijmst.2018.04.014

Benjamin, K. M., & Savage, P. E. (2004). Hydrothermal reactions of methylamine. *The Journal of Supercritical Fluids, 31*(3), 301-311. https://doi.org/10.1016/j.supflu.2003.12.009

Bezerra, M. A., Santelli, R. E., Oliveira, E. P., Villar, L. S., & Escaleira, L. A. (2008). Response surface methodology (RSM) as a tool for optimization in analytical chemistry. *Talanta, 76*(5), 965-977. https://doi.org/10.1016/j.talanta.2008.05.019

Blanchard, F., Reymond, J. P., Pommier, B., & Teichner, S. J. (1982). On the mechanism of the Fischer-Tropsch synthesis involving unreduced iron catalyst. *Journal of Molecular Catalysis, 17*(2), 171-181. https://doi.org/10.1016/0304-5102(82)85028-1

Boot-Handford, M. E., Virmond, E., Florin, N. H., Kandiyoti, R., & Fennell, P. S. (2018). Simple pyrolysis experiments for the preliminary assessment of biomass feedstocks and low-cost tar cracking catalysts for downdraft gasification applications. *Biomass and Bioenergy, 108*, 398-414. https://doi.org/10.1016/j.biombioe.2017.10.048

Borges, A. C. P., Onwudili, J. A., Andrade, H. M. C., Alves, C. T., Ingram, A., Vieira de Melo, S. A. B., & Torres, E. A. (2019). Catalytic supercritical water gasification of eucalyptus wood chips in a batch reactor. *Fuel, 255*, 115804. https:// doi. org/ 10. 1016/ j. fuel. 2019. 115804

Box, G. E. P., & Behnken, D. W. (1960). Some New Three Level Designs for the Study of Quantitative Variables. *Technometrics, 2*(4), 455-475. https:// doi. org/ 10. 1080/ 00401706.1960.10489912

Box, G. E. P., & Wilson, K. B. (1951). On the Experimental Attainment of Optimum Conditions. *Journal of the Royal Statistical Society: Series B, 13*, 1-45. https:// doi. org/ 10. 1007/ 978-1-4612-4380-9_23

Branca, C., Di Blasi, C., & Elefante, R. (2006). Devolatilization of Conventional Pyrolysis Oils Generated from Biomass and Cellulose. *Energy & Fuels, 20*(5), 2253-2261. https:// doi. org/ 10.1021/ef0601059

Bühler, W., Dinjus, E., Ederer, H. J., Kruse, A., & Mas, C. (2002). Ionic reactions and pyrolysis of glycerol as competing reaction pathways in near- and supercritical water. *The Journal of Supercritical Fluids, 22*(1), 37-53. https://doi.org/10.1016/S0896-8446(01)00105-X

Butt, J. B. (1990). Carbide phases on iron-based Fischer-Tropsch synthesis catalysts part I: Characterization studies. *Catalysis Letters, 7*(1), 61-81. https:// doi. org/ 10. 1007/ BF00764492

Byrd, A. J., Kumar, S., Kong, L., Ramsurn, H., & Gupta, R. B. (2011). Hydrogen production from catalytic gasification of switchgrass biocrude in supercritical water. *International Journal of Hydrogen Energy, 36*(5), 3426-3433. https:// doi. org/ 10. 1016/ j. ijhydene. 2010. 12.026

Cabuk, B., Duman, G., Yanik, J., & Olgun, H. (2019). Effect of fuel blend composition on hydrogen yield in co-gasification of coal and non-woody biomass. *International Journal of Hydrogen Energy*, 45(5), 3435-3443. https:// doi. org/ 10. 1016/j. ijhydene. 2019. 02.130

Campbell, M. J., Machin, D., & Walters, S. J. (2010). *Medical statistics: A textbook for the health sciences*. John Wiley & Sons. https://www.google.com

Cao, W., Guo, L., Yan, X., Zhang, D., & Yao, X. (2018). Assessment of sugarcane bagasse gasification in supercritical water for hydrogen production. *International Journal of Hydrogen Energy, 43*(30), 13711-13719. https:// doi. org/ 10. 1016/ j. ijhydene. 2017. 12. 013

Chabi, E., Lecomte, A., Adjovi, E. C., Dieye, A., & Merlin, A. (2018). Mix design method for plant aggregates concrete: Example of the rice husk. *Construction and Building Materials, 174*, 233-243. https://doi.org/10.1016/j.conbuildmat.2018.04.097

Chambers, J. M., Cleveland, W. S., Kleiner, B., & Tukey, P. A. (1983). *Graphical methods for data analysis.* Wadsworth & Brooks. Cole Statistics/Probability Series. https:// www. google. com

Chen, G., Andries, J., Luo, Z., & Spliethoff, H. (2003). Biomass pyrolysis/gasification for product gas production: The overall investigation of parametric effects. *Energy Conversion and Management, 44*(11), 1875-1884. https://doi.org/10.1016/S0196-8904(02)00188-7

Chen, J., Fan, Y., Zhao, X., Xu, W., Zhang, F., Liao, G., Leng, E., & Liu, S. (2020). Experimental investigation on gasification characteristic of food waste using supercritical water for combustible gas production: Exploring the way to complete gasification. *Fuel, 263*, 116735. https://doi.org/10.1016/j.fuel.2019.116735

Chesson, A. (1978). The maceration of linen flax under anaerobic conditions. *Journal of Applied Bacteriology, 45*(2), 219-230. https:// doi. org/ 10. 1111/j. 1365-2672. 1978. tb04217.x

Chuntanapum, A., & Matsumura, Y. (2010). Char Formation Mechanism in Supercritical Water Gasification Process: A Study of Model Compounds. *Industrial & Engineering Chemistry Research, 49*(9), 4055-4062. https://doi.org/10.1021/ie901346h

Coronado, M. A., Montero, G., García, C., Valdez, B., Ayala, R., & Pérez, A. (2017). Quality Assessment of Biodiesel Blends Proposed by the New Mexican Policy Framework. *Energies, 10*(5), 631. https://doi.org/10.3390/en10050631

Courson, C., Makaga, E., Petit, C., & Kiennemann, A. (2000). Development of Ni catalysts for gas production from biomass gasification. Reactivity in steam- and dry-reforming. *Catalysis Today, 63*(2), 427-437. https://doi.org/10.1016/S0920-5861(00)00488-0

Czitrom, V. (1999). One-Factor-at-a-Time versus Designed Experiments. *The American Statistician, 53*(2), 126-131. https://doi.org/10.1080/00031305.1999.10474445

D'Jesús, P., Boukis, N., Kraushaar-Czarnetzki, B., & Dinjus, E. (2006). Gasification of corn and clover grass in supercritical water. *Fuel, 85*(7), 1032-1038. https:// doi. org/ 10. 1016/ j.fuel.2005.10.022

David, E. (2015). Steam Reforming of Biomass Tar Using Iron-based Catalysts. *Chemical Engineering Transactions, 43*, 403-408. https://doi.org/10.3303/CET1543068

Demirbas, A. (2007). Biodiesel from sunflower oil in supercritical methanol with calcium oxide. *Energy Conversion and Management, 48*(3), 937-941. https:// doi. org/ 10. 1016/j. enconman.2006.08.004

Demirbas, A. (2007). Effects of Moisture and Hydrogen Content on the Heating Value of Fuels. *Energy Sources, Part A: Recovery, Utilization, and Environmental Effects, 29*(7), 649-655. https://doi.org/10.1080/009083190957801

Demirbas, A. (2009). Biorefineries: Current activities and future developments. *Energy Conversion and Management, 50*(11), 2782-2801. https:// doi. org/ 10. 1016/j. enconman. 2009. 06. 035

Deniz, I., Vardar-Sukan, F., Yüksel, M., Saglam, M., Ballice, L., & Yesil-Celiktas, O. (2015). Hydrogen production from marine biomass by hydrothermal gasification. *Energy Conversion and Management, 96*, 124-130. https:// doi. org/ 10. 1016/j. enconman. 2015.02.048

Devi, L., Ptasinski, K. J., & Janssen, F. J. (2003). A review of the primary measures for tar elimination in biomass gasification processes. *Biomass and Bioenergy, 24*(2), 125-140. https://doi.org/10.1016/S0961-9534(02)00102-2

Di Felice, L., Courson, C., Foscolo, P. U., & Kiennemann, A. (2011). Iron and nickel doped alkaline-earth catalysts for biomass gasification with simultaneous tar reformation and CO2 capture. *International Journal of Hydrogen Energy, 36*(9), 5296-5310. https:// doi. org/ 10.1016/j.ijhydene.2011.02.008

Dictor, R. A., & Bell, A. T. (1986). Fischer-Tropsch synthesis over reduced and unreduced iron oxide catalysts. *Journal of Catalysis, 97*(1), 121-136. https:// doi. org/ 10. 1016/ 0021-9517(86)90043-6

Dritsa, V., Rigas, F., Doulia, D., Avramides, E. J., & Hatzianestis, I. (2009). Optimization of Culture Conditions for the Biodegradation of Lindane by the Polypore Fungus Ganoderma australe. *Water, Air, and Soil Pollution, 204*(1), 19-27. https:// doi. org/ 10. 1007/ s11270-009-0022-z

Ehara, K., Saka, S., & Kawamoto, H. (2002). Characterization of the lignin-derived products from wood as treated in supercritical water. *Journal of Wood Science, 48*(4), 320-325. https://doi.org/10.1007/BF00831354

Elliott, D. C., Sealock, L. J., & Baker, E. G. (1993). Chemical processing in high-pressure aqueous environments: Development of catalysts for gasification. *Industrial & Engineering Chemistry Research, 32*(8), 1542-1548. https:// doi. org/ 10. 1021/ ie 00020 a002

Fakher, S., & Imqam, A. (2019). A review of carbon dioxide adsorption to unconventional shale rocks methodology, measurement, and calculation. *Applied Sciences, 2*(1), 1-14. https://doi.org/10.1007/s42452-019-1810-8

Fang, Z., Minowa, T., Smith, R. L., Ogi, T., & Koziński, J. A. (2004). Liquefaction and Gasification of Cellulose with $Na_2CO_3$ and Ni in Subcritical Water at 350°C. *Industrial & Engineering Chemistry Research, 43*(10), 2454-2463. https:// doi. org/ 10. 1021/ ie034146t

Fang, Z., Sato, T., Smith, R. L., Inomata, H., Arai, K., & Kozinski, J. A. (2008). Reaction chemistry and phase behavior of lignin in high-temperature and supercritical water. *Bioresource Technology, 99*(9), 3424-3430. https:// doi. org/ 10. 1016/j. biortech. 2007. 08. 008

Faria, J. (2021). *Production volume of rice in Tanzania from seasons 2010/11 to 2018/19*. Retrieved 08/03/2022 from https://www.statista.com/statistics/1168387/production-volume-of-rice-in-tanzania

Fermoso, J., Gil, M. V., Arias, B., Plaza, M. G., Pevida, C., Pis, J. J., & Rubiera, F. (2010). Application of response surface methodology to assess the combined effect of operating

variables on high-pressure coal gasification for $H_2$-rich gas production. *International Journal of Hydrogen Energy, 35*(3), 1191-1204. https:// doi. org/ 10. 1016/j. ijhydene. 2009. 11.046

Ferreira-Pinto, L., Silva Parizi, M. P., Carvalho de Araújo, P. C., Zanette, A. F., & Cardozo-Filho, L. (2019). Experimental basic factors in the production of $H_2$ via supercritical water gasification. *International Journal of Hydrogen Energy*, *44*(47), 25365-25383. https://doi.org/10.1016/j.ijhydene.2019.08.023

Florin, N. H., & Harris, A. T. (2008). Enhanced hydrogen production from biomass with in situ carbon dioxide capture using calcium oxide sorbents. *Chemical Engineering Science, 63*(2), 287-316. https://doi.org/10.1016/j.ces.2007.09.011

Galvis, H. M. T., Bitter, J. H., Khare, C. B., Ruitenbeek, M., Dugulan, A. I., & De Jong, K. P. (2012). Supported iron nanoparticles as catalysts for sustainable production of lower olefins. *Science*, *335*(6070), 835-838. https://doi.org/10.1126/science.1215614

Gangadharan, D., Sivaramakrishnan, S., Nampoothiri, K. M., Sukumaran, R. K., & Pandey, A. (2008). Response surface methodology for the optimization of alpha amylase production by Bacillus amyloliquefaciens. *Bioresource Technology, 99*(11), 4597-4602. https://doi.org/10.1016/j.biortech.2007.07.028

Gaur, S., & Reed, T. B. (1995). *An atlas of thermal data for biomass and other fuels*. https://www.google.com

Gaurh, P., & Pramanik, H. (2018). A novel approach of solid waste management via aromatization using multiphase catalytic pyrolysis of waste polyethylene. *Waste Management, 71*, 86-96. https://doi.org/10.1016/j.wasman.2017.10.053

Ghaly, A., & Al-Taweel, A. (1990). Physical and thermochemical properties of cereal straws. *Energy Sources*, *12*(2), 131-145. https://doi.org/10.1080/00908319008960195

Graboski, M., & Bain, R. (1979). *Properties of biomass relevant to gasification.* Solar Energy Research Institute, New Jersey https://www.google.com

Gratuito, M. K. B., Panyathanmaporn, T., Chumnanklang, R. A., Sirinuntawittaya, N., & Dutta, A. (2008). Production of activated carbon from coconut shell: Optimization using

response surface methodology. *Bioresource Technology*, *99*(11), 4887-4895. https://doi.org/10.1016/j.biortech.2007.09.042

Gregg, S. J., Sing, K. S. W., & Salzberg, H. W. (1967). Adsorption Surface Area and Porosity. *Journal of the Electrochemical Society*, *114*(11), 279C. https:// doi. org/ 10. 1149/ 1. 2426447

Guan, G., Kaewpanha, M., Hao, X., & Abudula, A. (2016). Catalytic steam reforming of biomass tar: Prospects and challenges. *Renewable and Sustainable Energy Reviews*, *58*, 450-461. https://doi.org/10.1016/j.rser.2015.12.316

Guan, Y., Pei, A., & Guo, L. (2008). Hydrogen production by catalytic gasification of cellulose in supercritical water. *Frontiers of Chemical Engineering in China*, *2*(2), 176-180. https://doi.org/10.1007/s11705-008-0026-z

Gunasekaran, S., & Anbalagan, G. (2007). Thermal decomposition of natural dolomite. *Bulletin of Materials Science*, *30*(4), 339-344. https://doi.org/10.1007/s12034-007-0056-z

Gunst, R. F. (1996). Response Surface Methodology: Process and Product Optimization Using Designed Experiments. *Technometrics*, *38*(3), 284-286. https:// doi. org/ 10. 1080/ 00401706. 1996.10484509

Guo, F., Li, X., Liu, Y., Peng, K., Guo, C., & Rao, Z. (2018). Catalytic cracking of biomass pyrolysis tar over char-supported catalysts. *Energy Conversion and Management*, *167*, 81-90. https://doi.org/10.1016/j.enconman.2018.04.094

Guo, L. J., Lu, Y. J., Zhang, X. M., Ji, C. M., Guan, Y., & Pei, A. X. (2007). Hydrogen production by biomass gasification in supercritical water: A systematic experimental and analytical study. *Catalysis Today*, *129*(3), 275-286. https:// doi. org/ 10. 1016/j. cattod. 2007.05.027

Guo, S., Guo, L., Cao, C., Yin, J., Lu, Y., & Zhang, X. (2012). Hydrogen production from glycerol by supercritical water gasification in a continuous flow tubular reactor. *International Journal of Hydrogen Energy*, *37*(7), 5559-5568. https:// doi. org/ 10. 1016/j. ijhydene.2011.12.135

Guo, X., Wang, S., Wang, Q., Guo, Z., & Luo, Z. (2011). Properties of Bio-oil from Fast Pyrolysis of Rice Husk. *Chinese Journal of Chemical Engineering, 19*(1), 116-121. https://doi.org/10.1016/S1004-9541(09)60186-5

Guo, Y., Wang, S., Wang, Y., Zhang, J., Xu, D., & Gong, Y. (2012). Gasification of two and three-components mixture in supercritical water: Influence of NaOH and initial reactants of acetic acid and phenol. *International Journal of Hydrogen Energy, 37*(3), 2278-2286. https://doi.org/10.1016/j.ijhydene.2011.10.074

Guo, Y., Wang, S. Z., Xu, D. H., Gong, Y. M., Ma, H. H., & Tang, X. Y. (2010). Review of catalytic supercritical water gasification for hydrogen production from biomass. *Renewable and Sustainable Energy Reviews, 14*(1), 334-343. https:// doi. org/ 10. 1016/j. rser.2009.08.012

Gusta, E., Dalai, A. K., Uddin, M. A., & Sasaoka, E. (2009). Catalytic Decomposition of Biomass Tars with Dolomites. *Energy & Fuels, 23*(4), 2264-2272. https:// doi. org/ 10. 1021/ ef8009958

Haefele, S. M., Konboon, Y., Wongboon, W., Amarante, S., Maarifat, A. A., Pfeiffer, E. M., & Knoblauch, C. (2011). Effects and fate of biochar from rice residues in rice-based systems. *Field Crops Research, 121*(3), 430-440. https:// doi. org/ 10. 1016/j. fcr. 2011. 01. 014

Hamada, M., & Wu, C. F. (2000). *Experiments: Planning, Analysis and Parameter Design Optimization.* Wiley, New York. https://www.google.com

Hamdan, H., Muhid, M. N. M., Endud, S., Listiorini, E., & Ramli, Z. (1997). 29Si MAS NMR, XRD and FESEM studies of rice husk silica for the synthesis of zeolites. *Journal of Non-Crystalline Solids, 211*(1), 126-131. https:// doi. org/ 10. 1016/S0022-3093(96)00611-4

Hantoko, D., Kanchanatip, E., Yan, M., Weng, Z., Gao, Z., & Zhong, Y. (2019). Assessment of sewage sludge gasification in supercritical water for $H_2$-rich syngas production. *Process Safety and Environmental Protection, 131*, 63-72. https:// doi. org/ 10. 1016/j. psep. 2019.08.035

Hao, W., Björkman, E., Yun, Y., Lilliestråle, M., & Hedin, N. (2014). Iron oxide nanoparticles embedded in activated carbons prepared from hydrothermally treated waste biomass. *ChemSusChem, 7*(3), 875-882. https://doi.org/10.1002/cssc.201300912

Hayashi, S., Nomaguchi, K., Okusawa, T., Yokomizo, O., Ishagaki, Y., & Ishimaru, H. (1998). An energy balance study of a newly developed recycling system for waste plastics. *Papers of Ship Research Institute, 35,* 133-150.

Henrikson, J. T., Chen, Z., & Savage, P. E. (2003). Inhibition and Acceleration of Phenol Oxidation by Supercritical Water. *Industrial & Engineering Chemistry Research, 42*(25), 6303-6309. https://doi.org/10.1021/ie030020k

Hervy, M., Olcese, R., Bettahar, M. M., Mallet, M., Renard, A., Maldonado, L., Remy, D., Mauviel, G., & Dufour, A. (2019). Evolution of dolomite composition and reactivity during biomass gasification. *Applied Catalysis A: General, 572,* 97-106. https:// doi. org/ 10. 1016/j.apcata.2018.12.014

Holm, R., Jensen, I. H. M., & Sonnergaard, J. (2006). Optimization of Self-Microemulsifying Drug Delivery Systems Using a D-Optimal Design and the Desirability Function. *Drug Development and Industrial Pharmacy, 32*(9), 1025-1032. https:// doi. org/ 10.1080/03639040600559024

Hossain, M. Z., Chowdhury, M. B. I., Jhawar, A. K., & Charpentier, P. A. (2017). Supercritical water gasification of glucose using bimetallic aerogel Ru-Ni-$Al_2O_3$ catalyst for $H_2$ production. *Biomass and Bioenergy, 107,* 39-51. https:// doi. org/ 10. 1016/j. biombioe. 2017.09.010

Hosseini, S. E., Abdul, W. M., Jamil, M., Azli, A. A., & Misbah, M. F. (2015). A review on biomass-based hydrogen production for renewable energy supply. *International Journal of Energy Research, 39*(12), 1597-1615. https://doi.org/10.1002/er.3381

Hu, Y., Gong, M., Xing, X., Wang, H., Zeng, Y., & Xu, C. C. (2020). Supercritical water gasification of biomass model compounds: A review. *Renewable and Sustainable Energy Reviews, 118,* 109529. https://doi.org/10.1016/j.rser.2019.109529

Huang, B. S., Chen, H. Y., Chuang, K. H., Yang, R. X., & Wey, M. Y. (2012). Hydrogen production by biomass gasification in a fluidized-bed reactor promoted by an Fe/CaO catalyst. *International Journal of Hydrogen Energy, 37*(8), 6511-6518. https:// doi. org/ 10. 1016/j. ijhydene.2012.01.071

Huang, J., Lian, X., Wang, L., Zhu, C., Jin, H., & Wang, R. (2017). Hydrogen production from glucose by supercritical water gasification with Ni/Zr(Ce,Y)$O_2$-δ catalysts. *International*

*Journal of Hydrogen Energy*, *42*(7), 4613-4625. https:// doi. org/ 10. 1016/j. ijhydene.2016.10.012

Huang, J., Schmidt, K. G., & Bian, Z. (2011). Removal and conversion of tar in syngas from woody biomass gasification for power utilization using catalytic hydrocracking. *Energies*, *4*(8), 1163-1177. https://doi.org/10.3390/en4081163

Huang, J., Zhu, C., Lian, X., Feng, H., Sun, J., Wang, L., & Jin, H. (2019). Catalytic supercritical water gasification of glucose with in-situ generated nickel nanoparticles for hydrogen production. *International Journal of Hydrogen Energy*, *44*(38), 21020-21029. https:// doi. org/10.1016/j.ijhydene.2019.04.184

Huff, M. D., & Lee, J. W. (2016). Biochar-surface oxygenation with hydrogen peroxide. *Journal of Environmental Management*, *165*, 17-21. https:// doi. org/ 10. 1016/j. jenvman. 2015. 08.046

Ibtissem, H., Nawel, O., Hassen, M. A., & Elsa, W. (2019). *Supercritical water gasification of glycerol for Hydrogen production using response surface methodology. The 10th International Renewable Energy Congress*. https:// doi. org/ 10. 1109/ IREC. 2019. 8754520

Ji-lu, Z. (2007). Bio-oil from fast pyrolysis of rice husk: Yields and related properties and improvement of the pyrolysis system. *Journal of Analytical and Applied Pyrolysis*, *80*(1), 30-35. https://doi.org/10.1016/j.jaap.2006.12.030

Jin, H., Lu, Y., Guo, L., Zhang, X., & Pei, A. (2014). Hydrogen Production by Supercritical Water Gasification of Biomass with Homogeneous and Heterogeneous Catalyst. *Advances in Condensed Matter Physics, 2014*, 160565. https:// doi. org/ 10. 1155/ 2014/ 160565

Jin, W., Shen, D., Liu, Q., & Xiao, R. (2016). Evaluation of the co-pyrolysis of lignin with plastic polymers by TG-FTIR and Py-GC/MS. *Polymer Degradation and Stability, 133*, 65-74. https://doi.org/10.1016/j.polymdegradstab.2016.08.001

Johnsson, F., Kjärstad, J., & Rootzén, J. (2019). The threat to climate change mitigation posed by the abundance of fossil fuels. *Climate Policy, 19*(2), 258-274. https:// doi. org/ 10. 1080/ 14693062.2018. 1483885

Jones, B., & Goos, P. (2012). I-Optimal Versus D-Optimal Split-Plot Response Surface Designs. *Journal of Quality Technology, 44*(2), 85-101. https:// doi. org/ 10. 1080/ 00224065. 2012. 11917886

Jozwiak, W. K., Kaczmarek, E., Maniecki, T. P., Ignaczak, W., & Maniukiewicz, W. (2007). Reduction behavior of iron oxides in hydrogen and carbon monoxide atmospheres. *Applied Catalysis A: General, 326*(1), 17-27. https:// doi. org/ 10. 1016/j. apcata. 2007. 03. 021

Juan, J. C., Kartika, D. A., Wu, T. Y., & Hin, T. Y. Y. (2011). Biodiesel production from jatropha oil by catalytic and non-catalytic approaches: An overview. *Bioresource Technology, 102*(2), 452-460. https://doi.org/10.1016/j.biortech.2010.09.093

Jung, H., & Thomson, W. J. (1992). Dynamic X-ray diffraction study of an unsupported iron catalyst in Fischer-Tropsch synthesis. *Journal of Catalysis, 134*(2), 654-667. https://doi.org/10.1016/0021-9517(92)90350-Q

Kabyemela, B. M., Adschiri, T., Malaluan, R. M., & Arai, K. (1999). Glucose and Fructose Decomposition in Subcritical and Supercritical Water: Detailed Reaction Pathway, Mechanisms, and Kinetics. *Industrial & Engineering Chemistry Research, 38*(8), 2888-2895. https://doi.org/10.1021/ie9806390

Kang, K., Azargohar, R., Dalai, A. K., & Wang, H. (2015). Noncatalytic Gasification of Lignin in Supercritical Water Using a Batch Reactor for Hydrogen Production: An Experimental and Modeling Study. *Energy & Fuels, 29*(3), 1776-1784. https:// doi. org/ 10. 1021/ ef5027345

Kang, K., Azargohar, R., Dalai, A. K., & Wang, H. (2017). Hydrogen generation via supercritical water gasification of lignin using Ni-Co/Mg-Al catalysts. *International Journal of Energy Research, 41*(13), 1835-1846. https://doi.org/10.1002/er.3739

Karim, W., Kleibert, A., Hartfelder, U., Balan, A., Gobrecht, J., Van Bokhoven, J. A., & Ekinci, Y. (2016). Size-dependent redox behavior of iron observed by in-situ single nanoparticle spectro-microscopy on well-defined model systems. *Scientific Reports, 6*, 18818. https://doi.org/10.1038/srep18818

Kazawadi, D., John, G. R., & King'ondu, C. K. (2014). Experimental Investigation of Thermal Characteristics of Kiwira Coal Waste with Rice Husk Blends for Gasification. *Journal of Energy, 2014*, 562382. https://doi.org/10.1155/2014/562382

Khader, M. M., El-Anadouli, B. E., El-Nagar, E., & Ateya, B. G. (1991). Kinetics of the reduction of $Fe_2O_3$ with hydrogen. *Journal of Solid State Chemistry, 93*(2), 283-290. https://doi.org/10.1016/0022-4596(91)90302-X

Khatib, H. (2012). IEA World Energy Outlook 2011-A comment. *Energy Policy, 48*, 737-743. https://doi.org/10.1016/j.enpol.2012.06.007

Khonde, R., & Chaurasia, A. (2016). Rice husk gasification in a two-stage fixed-bed gasifier: Production of hydrogen rich syngas and kinetics. *International Journal of Hydrogen Energy, 41*(21), 8793-8802. https://doi.org/10.1016/j.ijhydene.2016.03.138

Khuri, A. I., & Mukhopadhyay, S. (2010). Response surface methodology. *Computational Statistics, 2*(2), 128-149. https://doi.org/10.1002/wics.73

Kirnbauer, F., Wilk, V., Kitzler, H., Kern, S., & Hofbauer, H. (2012). The positive effects of bed material coating on tar reduction in a dual fluidized bed gasifier. *Fuel, 95*, 553-562. https://doi.org/10.1016/j.fuel.2011.10.066

Kizito, S., Wu, S., Kipkemoi, K. W., Lei, M., Lu, Q., Bah, H., & Dong, R. (2015). Evaluation of slow pyrolyzed wood and rice husks biochar for adsorption of ammonium nitrogen from piggery manure anaerobic digestate slurry. *Science of the Total Environment, 505*, 102-112. https://doi.org/10.1016/j.scitotenv.2014.09.096

Kritzer, P. (2004). Corrosion in high-temperature and supercritical water and aqueous solutions: A review. *The Journal of Supercritical Fluids, 29*(1), 1-29. https:// doi. org/ 10. 1016/ S0896-8446(03)00031-7

Kritzer, P., & Dinjus, E. (2001). An assessment of supercritical water oxidation: Existing problems, possible solutions and new reactor concepts. *Chemical Engineering Journal, 83*(3), 207-214. https://doi.org/10.1016/S1385-8947(00)00255-2

Kruse, A. (2008). Supercritical water gasification. *Biofuels, Bioproducts and Biorefining, 2*(5), 415-437. https://doi.org/10.1002/bbb.93

Kruse, A., & Dinjus, E. (2007a). Hot compressed water as reaction medium and reactant: Degradation reactions. *The Journal of Supercritical Fluids, 41*(3), 361-379. https://doi.org/10.1016/j.supflu.2006.12.006

Kruse, A., & Dinjus, E. (2007b). Hot compressed water as reaction medium and reactant: Properties and synthesis reactions. *The Journal of Supercritical Fluids, 39*(3), 362-380. https://doi.org/10.1016/j.supflu.2006.03.016

Kruse, A., & Gawlik, A. (2003). Biomass Conversion in Water at 330−410°C and 30−50 MPa. Identification of Key Compounds for Indicating Different Chemical Reaction Pathways. *Industrial & Engineering Chemistry Research, 42*(2), 267-279. https:// doi. org/ 10. 1021/ ie0202773

Kruse, A., Krupka, A., Schwarzkopf, V., Gamard, C., & Henningsen, T. (2005). Influence of Proteins on the Hydrothermal Gasification and Liquefaction of Biomass: Comparison of Different Feedstocks. *Industrial & Engineering Chemistry Research, 44*(9), 3013-3020. https://doi.org/10.1021/ie049129y

Kruse, A., Meier, D., Rimbrecht, P., & Schacht, M. (2000). Gasification of Pyrocatechol in Supercritical Water in the Presence of Potassium Hydroxide. *Industrial & Engineering Chemistry Research, 39*(12), 4842-4848. https://doi.org/10.1021/ie0001570

Kumagai, S., Alvarez, J., Blanco, P. H., Wu, C., Yoshioka, T., Olazar, M., & Williams, P. T. (2015). Novel Ni–Mg–Al–Ca catalyst for enhanced hydrogen production for the pyrolysis–gasification of a biomass/plastic mixture. *Journal of Analytical and Applied Pyrolysis, 113,* 15-21. https://doi.org/10.1016/j.jaap.2014.09.012

Kumar, A., & Reddy, S. N. (2019). In Situ Sub- and Supercritical Water Gasification of Nano-Nickel ($Ni^{2+}$) Impregnated Biomass for $H_2$ Production. *Industrial & Engineering Chemistry Research, 58*(12), 4780-4793. 10.1021/acs.iecr.9b00425

Kumar, M., Olajire, O. A., & Kumar, A. (2018). A review on the current status of various hydrothermal technologies on biomass feedstock. *Renewable and Sustainable Energy Reviews, 81,* 1742-1770. https://doi.org/10.1016/j.rser.2017.05.270

Kumar, S., Sangwan, P., Dhankhar, R. M. V., & Bidra, S. (2013). Utilization of rice husk and their ash: A review. *Research Journal of Chemical and Environmental Sciences, 1*(5), 126-129.

Kutz, M. (2007). *Environmentally conscious materials and chemicals processing*.Wiley Online Library. https://www.google.com

Lee, I. G., Kim, M. S., & Ihm, S. K. (2002). Gasification of Glucose in Supercritical Water. *Industrial & Engineering Chemistry Research, 41*(5), 1182-1188. https:// doi. org/ 10. 1021/ ie010066i

Lee, T., Othman, R., & Yeoh, F.Y. (2013). Development of photoluminescent glass derived from rice husk. *Biomass and Bioenergy, 59*, 380-392. https:// doi. org/ 10. 1016/j. biombioe. 2013.08.028

Li, S., Savage, P. E., & Guo, L. (2018). Stability and activity maintenance of $Al_2O_3$- and carbon nanotube-supported Ni catalysts during continuous gasification of glycerol in supercritical water. *The Journal of Supercritical Fluids, 135*, 188-197. https:// doi. org/ 10. 1016/j. supflu.2017.12.006

Liu, H., Chen, T., Chang, D., Chen, D., Kong, D., Zou, X., & Frost, R. L. (2012). Effect of preparation method of palygorskite-supported Fe and Ni catalysts on catalytic cracking of biomass tar. *Chemical Engineering Journal, 188*, 108-112. https:// doi. org/ 10. 1016/j. cej. 2012. 01.109

Liu, L., Huang, Y., & Liu, C. (2016). Prediction of rice husk gasification on fluidized bed gasifier based on ASPEN Plus. *BioResources, 11*(1), 2744-2755.

Liu, L., Zhang, Z., Das, S., & Kawi, S. (2019). Reforming of tar from biomass gasification in a hybrid catalysis-plasma system: A review. *Applied Catalysis B: Environmental, 250*, 250-272. https://doi.org/10.1016/j.apcatb.2019.03.039

Lorente, E., Peña, J. A., & Herguido, J. (2011). Cycle behaviour of iron ores in the steam-iron process. *International Journal of Hydrogen Energy, 36*(12), 7043-7050. https:// doi. org/ 10. 1016/j.ijhydene.2011.03.069

Lu, Y., Guo, L., Zhang, X., & Ji, C. (2012). Hydrogen production by supercritical water gasification of biomass: Explore the way to maximum hydrogen yield and high carbon gasification efficiency. *International Journal of Hydrogen Energy, 37*(4), 3177-3185. https://doi.org/10.1016/j.ijhydene.2011.11.064

Lu, Y., Guo, L., Zhang, X., & Yan, Q. (2007). Thermodynamic modeling and analysis of biomass gasification for hydrogen production in supercritical water. *Chemical Engineering Journal, 131*(1), 233-244. https://doi.org/10.1016/j.cej.2006.11.016

Lu, Y. J., Guo, L. J., Ji, C. M., Zhang, X. M., Hao, X. H., & Yan, Q. H. (2006). Hydrogen production by biomass gasification in supercritical water: A parametric study. *International Journal of Hydrogen Energy, 31*(7), 822-831. https:// doi. org/ 10. 1016/j. ijhydene. 2005.08.011

Madenoğlu, T. G., Kurt, S., Sağlam, M., Yüksel, M., Gökkaya, D., & Ballice, L. (2012). Hydrogen production from some agricultural residues by catalytic subcritical and supercritical water gasification. *The Journal of Supercritical Fluids, 67*, 22-28. https://doi.org/10.1016/j.supflu.2012.02.031

Maheshwari, K. (2011). *Sustainable metal catalysis the paradigm of iron metal.* Department of Chemistry at the Institute of Chemical Technology, Mumbai. https:// www. google. com

Maiti, S., Dey, S., Purakayastha, S., & Ghosh, B. (2006). Physical and thermochemical characterization of rice husk char as a potential biomass energy source. *Bioresource Technology, 97*(16), 2065-2070. https://doi.org/10.1016/j.biortech.2005.10.005

Makwana, J. P., Joshi, A. K., Athawale, G., Singh, D., & Mohanty, P. (2015). Air gasification of rice husk in bubbling fluidized bed reactor with bed heating by conventional charcoal. *Bioresource Technology, 178*, 45-52. https:// doi. org/10. 1016/j. biortech. 2014. 09.111

Mansaray, K. G., & Ghaly, A. E. (1997). Physical and Thermochemical Properties of Rice Husk. *Energy Sources, 19*(9), 989-1004. https://doi.org/10.1080/00908319708908904

Matin, H. H. A., & Hadiyanto, H. J. J. (2018). Optimization of Biogas Production from Rice Husk Waste by Solid State Anaerobic Digestion Using Response Surface Methodology. *Journal of Environmental Science and Technology*, *11*(3), 147-156.

Matsumura, Y., Minowa, T., Potic, B., Kersten, S. R. A., Prins, W., Van Swaaij, W. P. M., Van De Beld, B., Elliott, D. C., Neuenschwander, G. G., Kruse, A., & Jerry, A. J., M. (2005). Biomass gasification in near- and super-critical water: Status and prospects. *Biomass and Bioenergy*, *29*(4), 269-292. https://doi.org/10.1016/j.biombioe.2005.04.006

Matsuoka, K., Shimbori, T., Kuramoto, K., Hatano, H., & Suzuki, Y. (2006). Steam reforming of woody biomass in a fluidized bed of iron oxide-impregnated porous alumina. *Energy & Fuels*, *20*(6), 2727-2731. https://doi.org/10.1021/ef060301f

Matsuoka, K., Shinbori, T., Kuramoto, K., Nanba, T., Morita, A., Hatano, H., & Suzuki, Y. (2006). Mechanism of woody biomass pyrolysis and gasification in a fluidized bed of porous alumina particles. *Energy & Fuels, 20*(3), 1315-1320. https:// doi. org/ 10. 1021/ ef0600210

McKendry, P. (2002). Energy production from biomass (part 2): Conversion technologies. *Bioresource Technology, 83*(1), 47-54. https://doi.org/10.1016/S0960-8524(01)00119-5

Meier, D., Ante, R., & Faix, O. (1992). Catalytic hydropyrolysis of lignin: Influence of reaction conditions on the formation and composition of liquid products. *Bioresource Technology, 40*(2), 171-177. https://doi.org/10.1016/0960-8524(92)90205-C

Menya, E., Olupot, P. W., Storz, H., Lubwama, M., & Kiros, Y. (2018). Characterization and alkaline pretreatment of rice husk varieties in Uganda for potential utilization as precursors in the production of activated carbon and other value-added products. *Waste Management, 81*, 104-116. https://doi.org/10.1016/j.wasman.2018.09.050

Mhilu, C. (2014). Analysis of energy characteristics of rice and coffee husks blends. *Chemical Engineering, 2014*, 1-6. https://doi.org/10.1155/2014/196103

Miccio, F., Picarelli, A., & Ruoppolo, G. (2016). Increasing tar and hydrocarbons conversion by catalysis in bubbling fluidized bed gasifiers. *Fuel Processing Technology, 141*, 31-37. https://doi.org/10.1016/j.fuproc.2015.06.007

Miccio, F., Piriou, B., Ruoppolo, G., & Chirone, R. (2009). Biomass gasification in a catalytic fluidized reactor with beds of different materials. *Chemical Engineering Journal, 154*(1-3), 369-374. https://doi.org/10.1016/j.cej.2009.04.002

Miles, T. R., Miles, T. R., Baxter, L. L., Bryers, R. W., Jenkins, B. M., & Oden, L. L. (1996). Boiler deposits from firing biomass fuels. *Biomass and Bioenergy, 10*(2), 125-138. https://doi.org/10.1016/0961-9534(95)00067-4

Minowa, T., Ogi, T., & Yokoyama, S. Y. (1995). Hydrogen production from wet cellulose by low temperature gasification using a reduced nickel catalyst. *Chemistry Letters, 24*(10), 937-938. https://doi.org/10.1246/cl.1995.937

Minowa, T., Zhen, F., & Ogi, T. (1998). Cellulose decomposition in hot-compressed water with alkali or nickel catalyst. *The Journal of Supercritical Fluids, 13*(1), 253-259. https://doi.org/10.1016/S0896-8446(98)00059-X

Mohamed, O. A., Masood, S. H., & Bhowmik, J. L. (2016). Optimization of fused deposition modeling process parameters for dimensional accuracy using I-optimality criterion. *Measurement, 81*, 174-196. https://doi.org/10.1016/j.measurement.2015.12.011

Mohammed, M. A. A., Salmiaton, A., Wan, A. W. A. K. G., Mohamad, A. M. S., & Taufiq-Yap, Y. H. (2013). Preparation and Characterization of Malaysian Dolomites as a Tar Cracking Catalyst in Biomass Gasification Process. *Journal of Energy, 2013*, 1-8. https://doi.org/10.1155/2013/791582

Mohan, D., Sarswat, A., Ok, Y. S., & Pittman, C. U. (2014). Organic and inorganic contaminants removal from water with biochar, a renewable, low cost and sustainable adsorbent: A critical review. *Bioresource Technology, 160*, 191-202. https:// doi. org/ 10. 1016/j. biortech. 2014. 01.120

Monti, A., Di Virgilio, N., & Venturi, G. (2008). Mineral composition and ash content of six major energy crops. *Biomass and Bioenergy, 32*(3), 216-223. https:// doi. org/ 10. 1016/j. biombioe. 2007.09.012

Muley, P. D., Henkel, C., Abdollahi, K. K., Marculescu, C., & Boldor, D. (2016). A critical comparison of pyrolysis of cellulose, lignin, and pine sawdust using an induction heating reactor. *Energy Conversion and Management, 117*, 273-280. https:// doi. org/ 10. 1016/j. enconman.2016.03.041

Müller, J. B., & Vogel, F. (2012). Tar and coke formation during hydrothermal processing of glycerol and glucose. Influence of temperature, residence time and feed concentration. *The Journal of Supercritical Fluids, 70*, 126-136. https:// doi. org/10. 1016/ j. supflu. 2012. 06.016

Munnik, P., De Jongh, P. E., & De Jong, K. P. (2015). Recent developments in the synthesis of supported catalysts. *Chemical Reviews, 115*(14), 6687-6718. https:// doi. org/ 10. 1021/ cr500486u

Muthadhi, A., Anitha, R., & Kothandaraman, S. (2007). Rice husk ash-Properties and its uses: A review. *Journal of the Institution of Engineers. India. Civil Engineering Division, 88*(5), 50-56.

Muthadhi, A., & Kothandaraman, S. (2007). Rice Husk Ash—Properties and its Uses: A Review Rice Husk Ash. *Journal of the Institution of Engineers. India. Civil Engineering Division, 88*, 101-104.

Nanda, S., Dalai, A. K., Berruti, F., & Kozinski, J. A. (2016). Biochar as an Exceptional Bioresource for Energy, Agronomy, Carbon Sequestration, Activated Carbon and Specialty Materials. *Waste and Biomass Valorization, 7*(2), 201-235. https:// doi. org/ 10. 1007/s12649-015-9459-z

Nanda, S., Dalai, A. K., & Kozinski, J. A. (2016). Supercritical water gasification of timothy grass as an energy crop in the presence of alkali carbonate and hydroxide catalysts. *Biomass and Bioenergy, 95*, 378-387. https://doi.org/10.1016/j.biombioe.2016.05.023

Nanda, S., Gong, M., Hunter, H. N., Dalai, A. K., Gökalp, I., & Kozinski, J. A. (2017). An assessment of pinecone gasification in subcritical, near-critical and supercritical water. *Fuel Processing Technology, 168*, 84-96. https://doi.org/10.1016/j.fuproc.2017.08.017

Nanda, S., Rana, R., Zheng, Y., Kozinski, J. A., & Dalai, A. K. (2017). Insights on pathways for hydrogen generation from ethanol. *Sustainable Energy & Fuels, 1*(6), 1232-1245. https://doi.org/10.1039/C7SE00212B

Nanda, S., Reddy, S. N., Hunter, H. N., Dalai, A. K., & Kozinski, J. A. (2015). Supercritical water gasification of fructose as a model compound for waste fruits and vegetables. *The Journal of Supercritical Fluids, 104*, 112-121. https:// doi. org/ 10. 1016/j. supflu. 2015. 05. 009

Ngamcharussrivichai, C., Meechan, W., Ketcong, A., Kangwansaichon, K., & Butnark, S. (2011). Preparation of heterogeneous catalysts from limestone for transesterification of vegetable oils—Effects of binder addition. *Journal of Industrial and Engineering Chemistry, 17*(3), 587-595. https://doi.org/10.1016/j.jiec.2011.05.001

Noichi, H., Uddin, A., & Sasaoka, E. (2010). Steam reforming of naphthalene as model biomass tar over iron-aluminum and iron-zirconium oxide catalyst catalysts. *Fuel Processing Technology, 91*(11), 1609-1616. https:// doi. org/ 10. 1016/j. fuproc. 2010. 06. 009

Nordgreen, T., Nemanova, V., Engvall, K., & Sjöström, K. (2012). Iron-based materials as tar depletion catalysts in biomass gasification: Dependency on oxygen potential. *Fuel, 95*, 71-78. https://doi.org/10.1016/j.fuel.2011.06.002

Ogunsola, O. M., & Berkowitz, N. (1995). Removal of heterocyclic S and N from oil precursors by supercritical water. *Fuel, 74*(10), 1485-1490. https:// doi. org/ 10. 1016/0016-2361(95)00099-Q

Ohtsuka, Y., & Asami, K. (1991). Steam gasification of low-rank coals with a chlorine-free iron catalyst from ferric chloride. *Industrial & Engineering Chemistry Research, 30*(8), 1921-1926. https://doi.org/10.1021/ie00056a038

Okolie, J. A., Epelle, E. I., Nanda, S., Castello, D., Dalai, A. K., & Kozinski, J. A. (2021). Modeling and process optimization of hydrothermal gasification for hydrogen production: A comprehensive review. *The Journal of Supercritical Fluids, 173*, 105199. https://doi.org/10.1016/j.supflu.2021.105199

Okolie, J. A., Rana, R., Nanda, S., Dalai, A. K., & Kozinski, J. A. (2019). Supercritical water gasification of biomass: A state-of-the-art review of process parameters, reaction mechanisms and catalysis. *Sustainable Energy & Fuels, 3*(3), 578-598. https:// doi. org/ 10. 1039/C8SE00565F

Okuda, K., Man, X., Umetsu, M., Takami, S., & Adschiri, T. (2004). Efficient conversion of lignin into single chemical species by solvothermal reaction in water–p-cresol solvent. *Journal of Physics: Condensed Matter, 16*(14), 1325-1330. https:// doi. org/ 10. 1088/ 0953-8984/16/14/045

Olupot, P., Candia, A., Menya, E., & Walozi, R. (2016). Characterization of rice husk varieties in Uganda for biofuels and their techno-economic feasibility in gasification. *Chemical Engineering Research and Design, 107*, 63-72. https:// doi. org/ 10. 1016/j. cherd. 2015. 11. 010

Onwudili, J. A., & Williams, P. T. (2009). Role of sodium hydroxide in the production of hydrogen gas from the hydrothermal gasification of biomass. *International Journal of Hydrogen Energy, 34*(14), 5645-5656. https://doi.org/10.1016/j.ijhydene.2009.05.082

Orío, A., Corella, J., & Narváez, I. (1997). Characterization and Activity of Different Dolomites for Hot Gas Cleaning in Biomass Gasification. In A. V. Bridgwater & D. G. B. Boocock (Eds.), *Developments in Thermochemical Biomass Conversion: Volume 1 / Volume 2* (pp. 1144-1157). Springer Netherlands, Dordrecht https:// doi. org/ 10. 1007/978 -94-009-1559-6_92

Osada, M., Sato, O., Watanabe, M., Arai, K., & Shirai, M. (2006). Water Density Effect on Lignin Gasification over Supported Noble Metal Catalysts in Supercritical Water. *Energy & Fuels, 20*(3), 930-935. https://doi.org/10.1021/ef050398q

Paethanom, A., & Yoshikawa, K. (2012). Influence of pyrolysis temperature on rice husk char characteristics and its tar adsorption capability. *Energies, 5*(12), 4941-4951. https://doi.org/10.3390/en5124941

Papini-Terzi, F. S., Rocha, F. R., Vêncio, R. Z. N., Felix, J. M., Branco, D. S., Waclawovsky, A. J., Del Bem, L. E. V., Lembke, C. G., Costa, M. D. L., Nishiyama, M. Y., Vicentini, R., Vincentz, M. G. A., Ulian, E. C., Menossi, M., & Souza, G. M. (2009). Sugarcane genes associated with sucrose content. *BMC Genomics, 10*(1), 120. https:// doi. org/ 10. 1186/ 1471-2164-10-120

Park, K. C., & Tomiyasu, H. (2003). Gasification reaction of organic compounds catalyzed by $RuO_2$ in supercritical water [10.1039/B211800A]. *Chemical Communications*(6), 694-695. https://doi.org/10.1039/B211800A

Peng, W., Wang, L., Mirzaee, M., Ahmadi, H., Esfahani, M., & Fremaux, S. (2017). Hydrogen and syngas production by catalytic biomass gasification. *Energy Conversion and Management, 135*, 270-273. https://doi.org/10.1016/j.enconman.2016.12.056

Penninger, J. M. L., Kersten, R. J. A., & Baur, H. C. L. (1999). Reactions of diphenylether in supercritical water-mechanism and kinetics. *The Journal of Supercritical Fluids, 16*(2), 119-132. https://doi.org/10.1016/S0896-8446(99)00024-8

Penninger, J. M. L., Kersten, R. J. A., & Baur, H. C. L. (2000). Hydrolysis of diphenylether in supercritical water: Effects of dissolved NaCl. *The Journal of Supercritical Fluids, 17*(3), 215-226. https://doi.org/10.1016/S0896-8446(00)00046-2

Pérez, P., Aznar, P. M., Caballero, M. A., Gil, J., Martín, J. A., & Corella, J. (1997). Hot Gas Cleaning and Upgrading with a Calcined Dolomite Located Downstream a Biomass Fluidized Bed Gasifier Operating with Steam−Oxygen Mixtures. *Energy & Fuels, 11*(6), 1194-1203. https://doi.org/10.1021/ef970046m

Pettersson, L. J., & Westerholm, R. (2001). State of the art of multi-fuel reformers for fuel cell vehicles: problem identification and research needs. *International Journal of Hydrogen Energy, 26*(3), 243-264. https://doi.org/10.1016/S0360-3199(00)00073-2

Pinto, F., Gominho, J., André, R. N., Gonçalves, D., Miranda, M., Varela, F., Neves, D., Santos, J. O., Lourenço, A., & Pereira, H. (2017). Effect of Rice Husk Torrefaction on Syngas Production and Quality. *Energy & Fuels, 31*(5), 5183-5192. https:// doi. org/ 10. 1021/acs. energyfuels.7b00259

Poliakoff, M., Darr, J., Ikehans, T., & Cabanas, A. (1999). *The synthesis of crystalline metal oxide particles in sub-and supercritical water mixtures. Proceedings of the 6th Meeting on Supercritical Fluids, Nottingham, England*. https://www.google.com

Promdej, C., & Matsumura, Y. (2011). Temperature Effect on Hydrothermal Decomposition of Glucose in Sub- And Supercritical Water. *Industrial & Engineering Chemistry Research, 50*(14), 8492-8497. https://doi.org/10.1021/ie200298c

Rabenau, A. (1985). The Role of Hydrothermal Synthesis in Preparative Chemistry. *Angewandte Chemie International Edition in English, 24*(12), 1026-1040. https:// doi. org/ 10.1002/anie.198510261

Ramadhani, B., Kivevele, T., Kihedu, J. H., & Jande, Y. A. C. (2020). Catalytic tar conversion and the prospective use of iron-based catalyst in the future development of biomass gasification: A review. *Biomass Conversion and Biorefinery*. https:// doi. org/ 10. 1007/ s13399-020-00814-x

Ramsurn, H., Kumar, S., & Gupta, R. B. (2011). Enhancement of Biochar Gasification in Alkali Hydrothermal Medium by Passivation of Inorganic Components Using $Ca(OH)_2$. *Energy & Fuels, 25*(5), 2389-2398. https://doi.org/10.1021/ef200438b

Ranade, S. S., & Thiagarajan, P. (2017). Selection of a design for response surface. *IOP Conference Series: Materials Science and Engineering, 263*, 022043. https:// doi. org/ 10. 1088/ 1757-899x/263/2/022043

Ranzi, E., Cuoci, A., Faravelli, T., Frassoldati, A., Migliavacca, G., Pierucci, S., & Sommariva, S. (2008). Chemical Kinetics of Biomass Pyrolysis. *Energy & Fuels, 22*(6), 4292-4300. https://doi.org/10.1021/ef800551t

Rapagnà, S., Gallucci, K., & Foscolo, P. U. (2018). Olivine, dolomite and ceramic filters in one vessel to produce clean gas from biomass. *Waste Management, 71*, 792-800. https://doi.org/10.1016/j.wasman.2017.07.038

Rapagnà, S., Jand, N., Kiennemann, A., & Foscolo, P. U. (2000). Steam-gasification of biomass in a fluidised-bed of olivine particles. *Biomass and Bioenergy, 19*(3), 187-197. https:// doi. org/10.1016/S0961-9534(00)00031-3

Rapagnà, S., Virginie, M., Gallucci, K., Courson, C., Di Marcello, M., Kiennemann, A., & Foscolo, P. U. (2011). Fe/olivine catalyst for biomass steam gasification: Preparation, characterization and testing at real process conditions. *Catalysis Today, 176*(1), 163-168. https://doi.org/10.1016/j.cattod.2010.11.098

Rauch, R., Pfeifer, C., Bosch, K., Hofbauer, H., Świerczyński, D., Courson, C., & Kiennemann, A. (2004). *Comparison of different olivines for biomass steam gasification. Proceedings of the Conference for Science in Thermal and Chemical Biomass Conversion, Victoria, Canada*. https://www.google.com

Reddy, S. N., Nanda, S., Dalai, A. K., & Kozinski, J. A. (2014). Supercritical water gasification of biomass for hydrogen production. *International Journal of Hydrogen Energy, 39*(13), 6912-6926. https://doi.org/10.1016/j.ijhydene.2014.02.125

Resende, F. L. P., & Savage, P. E. (2010). Effect of Metals on Supercritical Water Gasification of Cellulose and Lignin. *Industrial & Engineering Chemistry Research, 49*(6), 2694-2700. https://doi.org/10.1021/ie901928f

Reumerman, P., & Van den Berg, D. (2002). *Reduction of fouling, slagging and corrosion characteristics of miscantus for power & heat generation using biotechnology*. https://www.google.com

Rodriguez, C. C., & Kruse, A. (2018). Supercritical water gasification of biomass for hydrogen production: Review. *The Journal of Supercritical Fluids, 133*, 573-590. https:// doi. org/ 10. 1016/j.supflu.2017.09.019

Said, M., John, G., & Mhilu, C. (2014). Thermal characteristics and kinetics of rice husk for pyrolysis process. *International Journal of Renewable Energy Research, 4*(2), 1-4.

Saisu, M., Sato, T., Watanabe, M., Adschiri, T., & Arai, K. (2003). Conversion of Lignin with Supercritical Water−Phenol Mixtures. *Energy & Fuels, 17*(4), 922-928. https:// doi. org/ 10. 1021/ef0202844

Samiee-Zafarghandi, R., Karimi-Sabet, J., Abdoli, M. A., & Karbassi, A. (2018). Supercritical water gasification of microalga Chlorella PTCC 6010 for hydrogen production: Box-Behnken optimization and evaluating catalytic effect of $MnO_2/SiO_2$ and $NiO/SiO_2$. *Renewable Energy, 126*, 189-201. https://doi.org/10.1016/j.renene.2018.03.043

Sánchez-Jiménez, P. E., Valverde, J. M., Perejón, A., De la Calle, A., Medina, S., & Pérez-Maqueda, L. A. (2016). Influence of Ball Milling on CaO Crystal Growth During Limestone and Dolomite Calcination: Effect on $CO_2$ Capture at Calcium Looping Conditions. *Crystal Growth & Design, 16*(12), 7025-7036. https:// doi. org/ 10. 1021/ acs. cgd. 6b01228

Sansaniwal, S. K., Pal, K., Rosen, M. A., & Tyagi, S. K. (2017). Recent advances in the development of biomass gasification technology: A comprehensive review. *72*, 363-384. https://doi.org/10.1016/j.rser.2017.01.038

Sasaki, M., Adschiri, T., & Arai, K. (2004). Kinetics of cellulose conversion at 25 MPa in sub- and supercritical water. *American Institute of Chemical Engineers Journal, 50*(1), 192-202. https:// doi. org/ 10. 1002/ aic. 10018

Sato, T., Furusawa, T., Ishiyama, Y., Sugito, H., Miura, Y., Sato, M., Suzuki, N., & Itoh, N. (2006). Effect of Water Density on the Gasification of Lignin with Magnesium Oxide Supported Nickel Catalysts in Supercritical Water. *Industrial & Engineering Chemistry Research, 45*(2), 615-622. https://doi.org/10.1021/ie0510270

Sato, T., Osada, M., Watanabe, M., Shirai, M., & Arai, K. (2003). Gasification of Alkylphenols with Supported Noble Metal Catalysts in Supercritical Water. *Industrial & Engineering Chemistry Research, 42*(19), 4277-4282. https://doi.org/10.1021/ie030261s

Savage, P. E. (2009). A perspective on catalysis in sub- and supercritical water. *The Journal of Supercritical Fluids, 47*(3), 407-414. https://doi.org/10.1016/j.supflu.2008.09.007

Seçer, A., Şayan, E., Üzden, Ş. T., & Hasan, A. (2021). Evaluation of the Process Parameters on Subcritical Water Gasification of Sorghum by Response Surface Methodology. *Journal of the Turkish Chemical Society Section B: Chemical Engineering, 4*(1), 1-12.

Septien, S., Valin, S., Dupont, C., Peyrot, M., & Salvador, S. (2012). Effect of particle size and temperature on woody biomass fast pyrolysis at high temperature (1000–1400°C). *Fuel, 97*, 202-210. https://doi.org/10.1016/j.fuel.2012.01.049

Shahbaz, M., Inayat, A., Patrick, D. O., & Ammar, M. (2017). The influence of catalysts in biomass steam gasification and catalytic potential of coal bottom ash in biomass steam gasification: A review. *Renewable and Sustainable Energy Reviews, 73*, 468-476. https://doi.org/10.1016/j.rser.2017.01.153

Shaw, R., & Dahmen, N. (2000). Destruction of toxic organic materials using super-critical water oxidation: Current state of the technology. https:// doi. org/ https:// doi. org/ 10. 1007/ 978-94-011-3929-8_17

Shen, Y., & Yoshikawa, K. (2013). Recent progresses in catalytic tar elimination during biomass gasification or pyrolysis: A review. *Renewable and Sustainable Energy Reviews, 21*, 371-392. https://doi.org/10.1016/j.rser.2012.12.062

Shen, Y., & Yoshikawa, K. (2014). Tar Conversion and Vapor Upgrading via in Situ Catalysis Using Silica-Based Nickel Nanoparticles Embedded in Rice Husk Char for Biomass Pyrolysis/Gasification. *Industrial & Engineering Chemistry Research, 53*(27), 10929-10942. https://doi.org/10.1021/ie501843y

Shen, Y., Zhao, P., Shao, Q., Ma, D., Takahashi, F., & Yoshikawa, K. (2014). In-situ catalytic conversion of tar using rice husk char-supported nickel-iron catalysts for biomass pyrolysis/gasification. *Applied Catalysis B: Environmental, 152-153*, 140-151. https://doi.org/10.1016/j.apcatb.2014.01.032

Sheng, C., & Azevedo, J. L. T. (2005). Estimating the higher heating value of biomass fuels from basic analysis data. *Biomass and Bioenergy, 28*(5), 499-507. https:// doi. org/ 10. 1016/j. biombioe.2004.11.008

Sheth, P. N., & Babu, B. V. (2009). Experimental studies on producer gas generation from wood waste in a downdraft biomass gasifier. *Bioresource Technology, 100*(12), 3127-3133. https://doi.org/10.1016/j.biortech.2009.01.024

Shroff, M. D., Kalakkad, D. S., Coulter, K. E., Kohler, S. D., Harrington, M. S., Jackson, N. B., Sault, A. G., & Datye, A. K. (1995). Activation of precipitated iron Fischer-Tropsch synthesis catalysts. *Journal of Catalysis, 156*(2), 185-207. https:// doi. org/10. 1006/ jcat. 1995. 1247

Siddiqui, M. T. H., Nizamuddin, S., Baloch, H. A., Mubarak, N. M., Tunio, M. M., Riaz, S., Shirin, K., Ahmed, Z., & Hussain, M. (2018). Thermogravimetric pyrolysis for neem char using novel agricultural waste: A study of process optimization and statistical modeling. *Biomass Conversion and Biorefinery, 8*(4), 857-871. https:// doi. org/ 10. 1007/ s13399-018-0336-4

Silcox, G. D., Kramlich, J. C., & Pershing, D. W. (1989). A mathematical model for the flash calcination of dispersed calcium carbonate and calcium hydroxide particles. *Industrial & Engineering Chemistry Research, 28*(2), 155-160. https:// doi. org/ 10. 1021/ ie00086a005

Sing, K. S., Rouquerol, F., & Rouquerol, J. (1999). *Adsorption By Powders and Porous Solids: Principles, Methodology, and Applications*. Academic Press, London. https:// www. google. com

Sing, K. S. W. (1985). Reporting physisorption data for gas/solid systems with special reference to the determination of surface area and porosity (Recommendations 1984). *Pure and Applied Chemistry, 57*(4), 603-619. https:// doi. org/: 10. 1351/ pac198557040603

Singh, P., Singh, R. K., Gokul, P. V., Hasan, S. U., & Sawarkar, A. N. (2020). Thermal degradation and pyrolysis kinetics of two Indian rice husk varieties using thermogravimetric analysis. *Energy Sources, Part A: Recovery, Utilization, and Environmental Effects*, 2020, 1-12. https://doi.org/10.1080/15567036.2020.1736215

Snoeck, J. W., Froment, G. F., & Fowles, M. (2002). Steam/$CO_2$ Reforming of Methane. Carbon Formation and Gasification on Catalysts with Various Potassium Contents. *Industrial & Engineering Chemistry Research, 41*(15), 3548-3556. https:// doi. org/ 10. 1021/ ie010665p

Stanmore, B. R., & Gilot, P. (2005). Review: Calcination and carbonation of limestone during thermal cycling for $CO_2$ sequestration. *Fuel Processing Technology*, *86*(16), 1707-1743. https://doi.org/10.1016/j.fuproc.2005.01.023

Su, H., Kanchanatip, E., Wang, D., Zheng, R., Huang, Z., Chen, Y., Mubeen, I., & Yan, M. (2020). Production of $H_2$-rich syngas from gasification of unsorted food waste in supercritical water. *Waste Management*, *102*, 520-527. https:// doi. org/ 10. 1016/j. wasman. 2019.11.018

Su, W., Cai, C., Liu, P., Lin, W., Liang, B., Zhang, H., Ma, Z., Ma, H., Xing, Y., & Liu, W. (2020). Supercritical water gasification of food waste: Effect of parameters on hydrogen production. *International Journal of Hydrogen Energy*, *45*(29), 14744-14755. https://doi.org/10.1016/j.ijhydene.2020.03.190

Su, X., Jin, H., Guo, L., Guo, S., & Ge, Z. (2015). Experimental study on Zhundong coal gasification in supercritical water with a quartz reactor: Reaction kinetics and pathway. *International Journal of Hydrogen Energy*, *40*(24), 7424-7432. https:// doi. org/ 10. 1016/j. ijhydene.2015.02.110

Sullivan, N., Jensen, A., Glarborg, P., Day, M. S., Grcar, J. F., Bell, J. B., Pope, C. J., & Kee, R. J. (2002). Ammonia conversion and NOx formation in laminar coflowing nonpremixed methane-air flames. *Combustion and Flame, 131*(3), 285-298. https:// doi. org/ 10.1016/S0010-2180(02)00413-3

Sun, J., Xu, L., Dong, G. H., Nanda, S., Li, H., Fang, Z., Kozinski, J. A., & Dalai, A. K. (2020). Subcritical water gasification of lignocellulosic wastes for hydrogen production with Co modified $Ni/Al_2O_3$ catalysts. *The Journal of Supercritical Fluids*, *162*, 104863. https://doi.org/10.1016/j.supflu.2020.104863

Sun, S., Zhao, Y., Ling, F., & Su, F. (2009). Experimental research on air staged cyclone gasification of rice husk. *Fuel Processing Technology*, *90*(4), 465-471. https://doi.org/10.1016/j.fuproc.2009.02.003

Susanti, R. F., Dianningrum, L. W., Yum, T., Kim, Y., Lee, B. G., & Kim, J. (2012). High-yield hydrogen production from glucose by supercritical water gasification without added catalyst. *International Journal of Hydrogen Energy*, *37*(16), 11677-11690. https://doi.org/10.1016/j.ijhydene.2012.05.087

Susanti, R. F., Veriansyah, B., Kim, J. D., Kim, J., & Lee, Y. W. (2010). Continuous supercritical water gasification of isooctane: A promising reactor design. *International Journal of Hydrogen Energy, 35*(5), 1957-1970. https:// doi. org/ 10. 1016/j. ijhydene. 2009.12.157

Tamhankar, S. S., Tsuchiya, K., & Riggs, J. B. (1985). Catalytic cracking of benzene on iron oxide-silica: Catalyst activity and reaction mechanism. *Applied Catalysis, 16*(1), 103-121. https://doi.org/10.1016/S0166-9834(00)84073-7

Tan, R. S., Tuan, A. T. A., Johari, A., & Md Isa, K. (2020). Catalytic steam reforming of tar for enhancing hydrogen production from biomass gasification: A review. *Frontiers in Energy*, 2020, 1-25. https://doi.org/10.1007/s11708-020-0800-2

Thomsen, T., Hauggaard-Nielsen, H., Bruun, E., & Ahrenfeldt, J. (2011). *The potential of pyrolysis technology in climate change mitigation–influence of process design and–parameters, simulated in SuperPro Designer Software* (Risø-Report 1764, ISSN: 0106e2840, ISBN 978-87-550-3877-6). http:// orbit. dtu. dk/ get Resource% 3 FrecordId %3 D274130%26objectId%3D1%26versionId%3D1

Tilman, D., Hill, J., & Lehman, C. (2006). Carbon-negative biofuels from low-input high-diversity grassland biomass. *Journal of Science, 314*(5805), 1598-1600. https:// doi. org/ 10. 1126/ science.1133306

Tsai, W. T., Lee, M. K., & Chang, Y. M. (2007). Fast pyrolysis of rice husk: Product yields and compositions. *Bioresource Technology, 98*(1), 22-28. https:// doi. org/ 10. 1016/j. biortech. 2005.12.005

Tursun, Y., Xu, S., Abulikemu, A., & Dilinuer, T. (2019). Biomass gasification for hydrogen rich gas in a decoupled triple bed gasifier with olivine and NiO/olivine. *Bioresource Technology, 272*, 241-248. https://doi.org/10.1016/j.biortech.2018.10.008

Uddin, M. A., Tsuda, H., Wu, S., & Sasaoka, E. (2008). Catalytic decomposition of biomass tars with iron oxide catalysts. *Fuel, 87*(4-5), 451-459. https:// doi. org/ 10. 1016/j. fuel. 2007. 06.021

Uguru-Okorie, D. C., Ikpotokin, I., Ajiboye, M. O., & Ojediran, M. E. (2018). FTIR Investigation of the Effect of Storage on Ogogoro-Gasoline Blend's Stability. *IOP*

*Conference Series: Materials Science and Engineering, 413*, 012073. https:// doi. org/ 10. 1088/1757-899x/413/1/012073

Vicentini, R., De Maria, F. J., Dornelas, M. C., & Menossi, M. (2009). Characterization of a sugarcane (Saccharum spp.) gene homolog to the brassinosteroid insensitive1-associated receptor kinase 1 that is associated to sugar content. *Plant Cell Reports, 28*(3), 481-491. https://doi.org/10.1007/s00299-008-0656-0

Vieira, F. R., Romero, L. C. M., Arce, G. L. A. F., & Ávila, I. (2020). Optimization of slow pyrolysis process parameters using a fixed bed reactor for biochar yield from rice husk. *Biomass and Bioenergy, 132*, 105412. https://doi.org/10.1016/j.biombioe.2019.105412

Virginie, M., Adánez, J., Courson, C., De Diego, L. F., García-Labiano, F., Niznansky, D., Kiennemann, A., Gayán, P., & Abad, A. (2012). Effect of Fe–olivine on the tar content during biomass gasification in a dual fluidized bed. *Applied Catalysis B: Environmental, 121-122*, 214-222. https://doi.org/10.1016/j.apcatb.2012.04.005

Virginie, M., Courson, C., & Kiennemann, A. (2010). Toluene steam reforming as tar model molecule produced during biomass gasification with an iron/olivine catalyst. *Comptes Rendus Chimie, 13*(10), 1319-1325. https://doi.org/10.1016/j.crci.2010.03.022

Visconti, C. G., Lietti, L., Forzatti, P., & Zennaro, R. (2007). Fischer–Tropsch synthesis on sulphur poisoned $Co/Al_2O_3$ catalyst. *Applied Catalysis A: General, 330*, 49-56. https:// doi. org/10.1016/j.apcata.2007.07.009

Wagner, W., & Pruß, A. (2002). The IAPWS formulation 1995 for the thermodynamic properties of ordinary water substance for general and scientific use. *Journal of Physical and Chemical Reference Data, 31*(2), 387-535. https:// doi. org/ 10. 1063/1. 1461829

Wang, C., Jin, H., Feng, H., Wei, W., Cao, C., & Cao, W. (2020). Study on gasification mechanism of biomass waste in supercritical water based on product distribution. *International Journal of Hydrogen Energy*, 107, 2411-2502 https:// doi. org/ 10. 1016/j. ijhydene .2020. 02.146

Wang, C., Zhu, C., Cao, W., Wei, W., & Jin, H. (2021). Catalytic mechanism study on the gasification of depolymerizing slag in supercritical water for hydrogen production. *International Journal of Hydrogen Energy, 46*(3), 2917-2926. https:// doi. org/ 10. 1016/j. ijhydene. 2020.06.061

Wang, C., Zhu, C., Huang, J., Li, L., & Jin, H. (2021). Enhancement of depolymerization slag gasification in supercritical water and its gasification performance in fluidized bed reactor. *Renewable Energy, 168*, 829-837. https:// doi. org/ 10. 1016/j. renene. 2020. 12. 104

Wang, D., Montané, D., & Chornet, E. (1996). Catalytic steam reforming of biomass-derived oxygenates: Acetic acid and hydroxyacetaldehyde. *Applied Catalysis A: General, 143*(2), 245-270. https://doi.org/10.1016/0926-860X(96)00093-2

Wang, G., & Li, A. (2008). Thermal Decomposition and Kinetics of Mixtures of Polylactic Acid and Biomass during Copyrolysis. *Chinese Journal of Chemical Engineering, 16*(6), 929-933. https://doi.org/10.1016/S1004-9541(09)60018-5

Wang, H., Cao, Y., Li, D., Muhammad, U., Li, C., Li, Z., & Zhang, S. (2013). Catalytic hydrorefining of tar to liquid fuel over multi-metals (W-Mo-Ni) catalysts. *Journal of Renewable and Sustainable Energy, 5*(5), 053114. https://doi.org/10.1063/1.4822050

Wang, L., Weller, C. L., Jones, D. D., & Hanna, M. A. (2008). Contemporary issues in thermal gasification of biomass and its application to electricity and fuel production. *Biomass and Bioenergy, 32*(7), 573-581. https://doi.org/10.1016/j.biombioe.2007.12.007

Wang, S. H., & Griffiths, P. R. (1985). Resolution enhancement of diffuse reflectance i.r. spectra of coals by Fourier self-deconvolution: The C-H stretching and bending modes. *Fuel, 64*(2), 229-236. https://doi.org/10.1016/0016-2361(85)90223-6

Wang, T., Chang, J., Lv, P., & Zhu, J. (2005). Novel catalyst for cracking of biomass tar. *Energy & Fuels, 19*(1), 22-27. https://doi.org/10.1021/ef030116r

Wannapeera, J., Worasuwannarak, N., & Pipatmanomai, S. (2008). Product yields and characteristics of rice husk, rice straw and corncob during fast pyrolysis in a drop-tube/fixed-bed reactor. *Songklanakarin Journal of Science & Technology, 30*(3), 0125-3395

Watanabe, M., Inomata, H., & Arai, K. (2002). Catalytic hydrogen generation from biomass (glucose and cellulose) with $ZrO_2$ in supercritical water. *Biomass and Bioenergy, 22*(5), 405-410. https://doi.org/10.1016/S0961-9534(02)00017-X

Webb, P. A., & Orr, C. (1997). *Analytical methods in fine particle technology*. Micromeritics Instrument Corporation. https://www.google.com

Williams, P. T., & Onwudili, J. (2005). Composition of Products from the Supercritical Water Gasification of Glucose: A Model Biomass Compound. *Industrial & Engineering Chemistry Research, 44*(23), 8739-8749. https://doi.org/10.1021/ie050733y

Williams, P. T., & Onwudili, J. (2006). Subcritical and Supercritical Water Gasification of Cellulose, Starch, Glucose, and Biomass Waste. *Energy & Fuels, 20*(3), 1259-1265. ttps://doi.org/10.1021/ef0503055

Willis, H. A., Van der Maas, J., & Miller, R. G. (1987). *Laboratory methods in vibrational spectroscopy*. https://www.google.com

Wu, C., Huang, H., Zheng, S., & Yin, X. (2002). An economic analysis of biomass gasification and power generation in China. *Bioresource Technology, 83*(1), 65-70. https:// doi. org/ 10. 1016/S0960-8524(01)00116-X

Wu, C., & Williams, P. T. (2009). Hydrogen production by steam gasification of polypropylene with various nickel catalysts. *Applied Catalysis B: Environmental, 87*(3), 152-161. https://doi.org/10.1016/j.apcatb.2008.09.003

Xu, D., Wang, S., Hu, X., Chen, C., Zhang, Q., & Gong, Y. (2009). Catalytic gasification of glycine and glycerol in supercritical water. *International Journal of Hydrogen Energy, 34*(13), 5357-5364. https://doi.org/10.1016/j.ijhydene.2008.08.055

Xu, P., Cheng, S., Han, Y., Zhao, D., Li, H., Wang, Y., Zhang, G., & Chen, C. (2020). Natural Variation of Lignocellulosic Components in Miscanthus Biomass in China [Original Research]. *Frontiers in Chemistry, 8*(1028), 1-12. ttps:// doi. org/ 10. 3389/ fchem. 2020. 595143

Xu, Z. R., Zhu, W., Gong, M., & Zhang, H. W. (2013). Direct gasification of dewatered sewage sludge in supercritical water. Part 1: Effects of alkali salts. *International Journal of Hydrogen Energy, 38*(10), 3963-3972. https://doi.org/10.1016/j.ijhydene.2013.01.164

Yakaboylu, O., Harinck, J., Smit, K. G., & De Jong, W. (2015). Supercritical Water Gasification of Biomass: A Literature and Technology Overview. *Energies, 8*(2), 859-894. https://www.mdpi.com/1996-1073/8/2/859

Yan, M., Su, H., Zhou, Z., Hantoko, D., Liu, J., Wang, J., Wang, R., & Kanchanatip, E. (2020). Gasification of effluent from food waste treatment process in sub- and supercritical water: $H_2$-rich syngas production and pollutants management. *Science of the Total Environment, 730*, 138517. https://doi.org/10.1016/j.scitotenv.2020.138517

Yan, P., Xu, L., & He, N. (2018). Variation in the calorific values of different plants organs in China. *PLOS ONE, 13*(6), e0199762. https://doi.org/10.1371/journal.pone.0199762

Yang, F., Hanna, M. A., Marx, D. B., & Sun, R. (2013). Optimization of hydrogen production from supercritical water gasification of crude glycerol—byproduct of biodiesel production. *International Journal of Energy Research, 37*(13), 1600-1609. https:// doi. org/ 10. 1002/er.2969

Yang, H., Yan, R., Chen, H., Lee, D. H., & Zheng, C. (2007). Characteristics of hemicellulose, cellulose and lignin pyrolysis. *Fuel, 86*(12), 1781-1788. https:// doi. org/ 10. 1016/j. fuel. 2006.12.013

Yin, C. Y. (2011). Prediction of higher heating values of biomass from proximate and ultimate analyses. *Fuel, 90*(3), 1128-1132. https://doi.org/10.1016/j.fuel.2010.11.031

Yokoyama, C., Nishi, K., Nakajima, A., & Seino, K. (1998). Thermolysis of organosolv lignin in supercritical water and supercritical methanol. *Journal of the Japan Petroleum Institute, 41*(4), 243-250.

Yoshida, T., & Matsumura, Y. (2001). Gasification of Cellulose, Xylan, and Lignin Mixtures in Supercritical Water. *Industrial & Engineering Chemistry Research, 40*(23), 5469-5474. https://doi.org/10.1021/ie0101590

Yu, J., Tian, F. J., McKenzie, L., & Li, C. Z. (2006). Char-supported nano iron catalyst for water-gas-shift reaction: Hydrogen production from coal/biomass gasification. *Process Safety and Environmental Protection, 84*(2), 125-130. https:// doi. org/ 10. 1205/ psep. 05045

Yu, Q. Z., Brage, C., Nordgreen, T., & Sjöström, K. (2009). Effects of Chinese dolomites on tar cracking in gasification of birch. *Fuel, 88*(10), 1922-1926. https:// doi. org/ 10. 1016/j. fuel. 2009.04.020

Yusof, A. M., Nizam, N. A., & Rashid, N. A. A. (2010). Hydrothermal conversion of rice husk ash to faujasite-types and NaA-type of zeolites. *Journal of Porous Materials, 17*(1), 39-47. ttps://doi.org/10.1007/s10934-009-9262-y

Zając, G., Szyszlak-Bargłowicz, J., Gołębiowski, W., & Szczepanik, M. (2018). Chemical Characteristics of Biomass Ashes. *Energies, 11*(11), 2885. https:// www. mdpi. com/ 1996-1073/11/11/2885

Zhang, B., Von Keitz, M., & Valentas, K. (2009). Thermochemical liquefaction of high-diversity grassland perennials. *Journal of Analytical and Applied Pyrolysis, 84*(1), 18-24. https://doi.org/10.1016/j.jaap.2008.09.005

Zhang, F., Xu, D., Wang, Y., Argyle, M. D., & Fan, M. (2015). $CO_2$ gasification of Powder River Basin coal catalyzed by a cost-effective and environmentally friendly iron catalyst. *Applied Energy, 145*, 295-305. https:// doi. org/ 10. 1016/j. apenergy. 2015. 01. 098

Zhang, L., Champagne, P., & Xu, C. (2011). Screening of supported transition metal catalysts for hydrogen production from glucose via catalytic supercritical water gasification. *International Journal of Hydrogen Energy, 36*(16), 9591-9601. https:// doi. org/ 10. 1016/j. ijhydene.2011.05.077

Zhang, L., Xu, C., & Champagne, P. (2012). Activity and stability of a novel Ru modified Ni catalyst for hydrogen generation by supercritical water gasification of glucose. *Fuel, 96*, 541-545. https://doi.org/10.1016/j.fuel.2012.01.066

Zhao, J. (2013). *Enhancement of methane production from solid-state anaerobic digestion of yard trimmings by biological pretreatment* [The Ohio State University]. https://www.google.com

# APPENDIX

## Appendix 1: Geographical factors for different regions of Tanzania

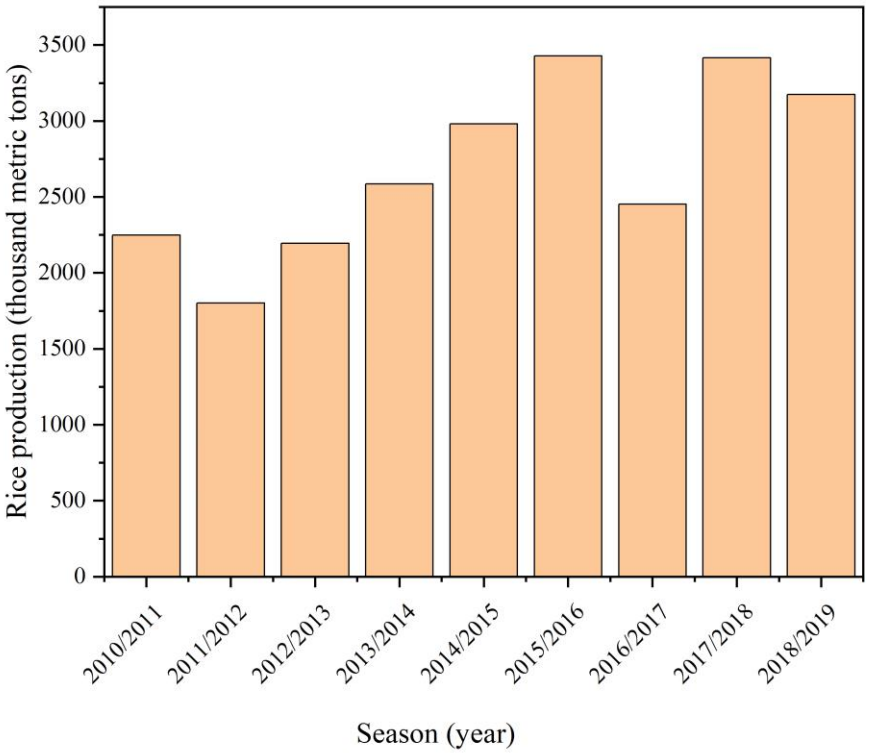


Data extracted from Faria (2021)

**Appendix 2: Geographical factors for different regions of Tanzania**

| Region | latitude | Longitude | altitude |
|---|---|---|---|
| Arusha | 3.38 | 36.68 | 1400 |
| Shinyanga | 3.68 | 33.42 | 1233 |
| Dodoma | 6.16 | 35.75 | 1120 |
| Morogoro | 6.82 | 37.65 | 509 |
| Iringa | 7.76 | 35.68 | 1550 |

**Appendix 3: The map of Tanzania showing the geographical location of the five regions reported in this study (colour code by altitude)**

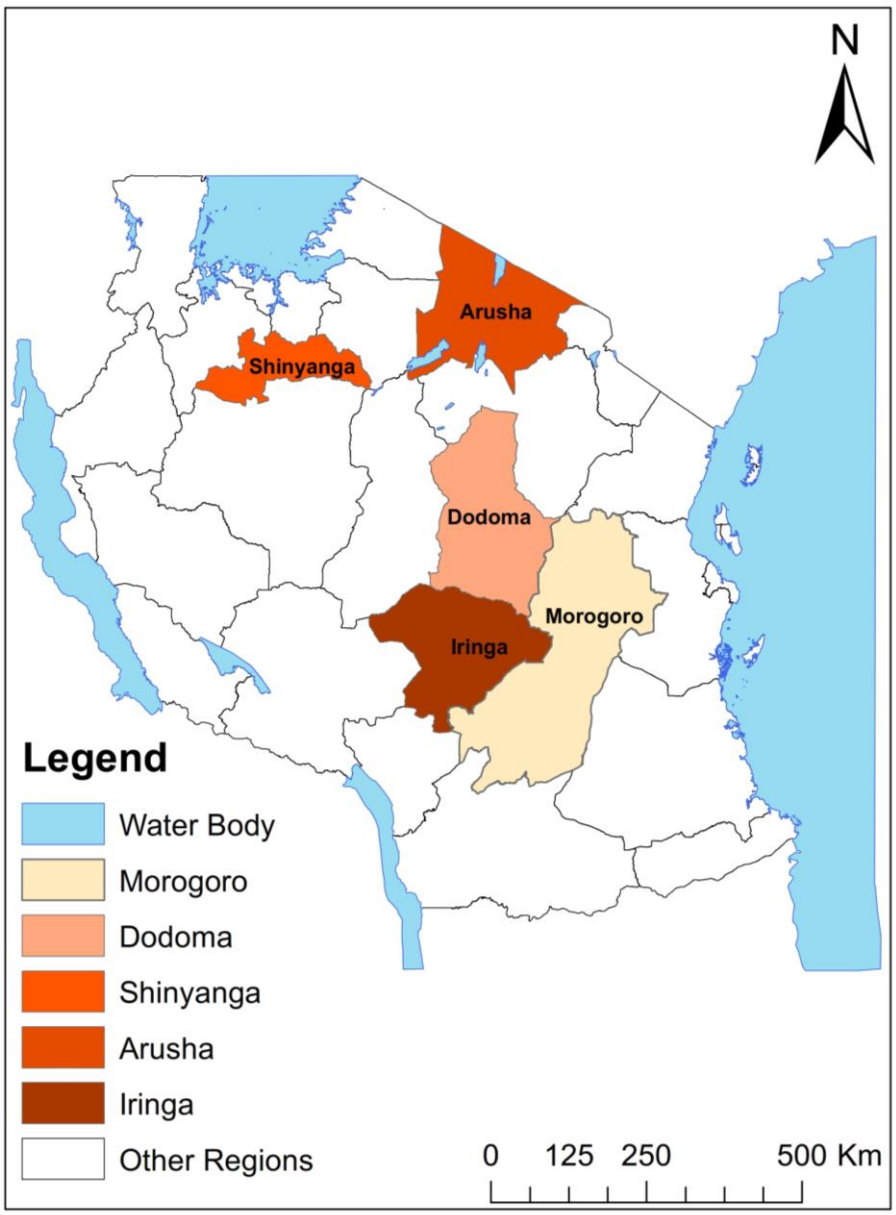

## RESEARCH OUTPUTS

### (i) Publications

Bakari, R., Kivevele, T., Huang, X., & Jande, Y. A. C. (2021). Sub- and Supercritical Water Gasification of Rice Husk: Parametric Optimization Using the I-Optimality Criterion. *ACS Omega*, 6(19), 12480-12499. https:// doi. org/ 10. 1021/ acsomega. 0c06318

Bakari, R., Kivevele, T., Huang, X., & Jande, Y. A. C. (2020). Simulation and optimisation of the pyrolysis of rice husk: Preliminary assessment for gasification applications. *Journal of Analytical and Applied Pyrolysis*, 150(5), 104891. https:// doi. org/ https:// doi. org/ 10.1016/j.jaap.2020.104891

Bakari, R., Kivevele, T., Kihedu, J. H., & Jande, Y. A. C. (2020). Catalytic tar conversion and the prospective use of iron-based catalyst in the future development of biomass gasification: A review. *Biomass Conversion and Biorefinery*, 12, 1369–1392. https:// doi. org/ 10. 1007/s 13399-020-00814-x

### (ii) Poster presentation

Bakari, R., Kivevele, T., & Jande, Y. A. C (2019). *Potential of rice husk as waste-to-energy resources for decentralized electricity generation systems in rural areas of Tanzania. Presented in the Community Engagement Event on Climate Change Conversations with an African Focus held on Wednesday May 8$^{th}$, 2019, at Ottawa Public Library, Ontario Canada*.